

Ionothermal Syntheses and Fundamental Properties of Selenido Metalates

Zur Erlangung des akademischen Grades eines

DOKTORS DER NATURWISSENSCHAFTEN

(Dr. rer. nat.)

von der KIT-Fakultät für Chemie und Biowissenschaften

des Karlsruher Instituts für Technologie (KIT)

genehmigte

DISSERTATION

von

M.Sc. Zhou Wu

aus

Anqing, China

Referentin: Prof. Dr. Stefanie Dehnen

Korreferentin: PD Dr. Masooma Ibrahim

Tag der mündlichen Prüfung: 05.12.2024

Abstract

Chalcogenido (semi)metalate clusters have been in the focus of inorganic chemistry and materials chemistry owing to their structural beauty and a variety of physical and chemical properties. Structurally, the tetrahedral coordination of their metal centers allows for the formation of zeolite-type framework compounds similar to zeolites, making them attractive from syntheses to application aspects. However, given these clusters are usually highly negatively charged, it is challenging to enable the formation of discrete cluster molecules in their solid-state. Understanding the molecular subunits and how they behave in solution has therefore been a hot topic in this field over the last decade. In addition, enriching the structural diversity of the chalcogenido metalate family, whether through variations in composition, connectivity between clusters, or the formation of new cluster types, provides valuable insights into the formation of these compounds and their potential applications.

To access discrete cluster molecules, and thus study their properties in solutions, strategies including a) incorporation of tetra-valent metal cations in the reaction system, b) charge reduction by neutral ligands, and c) alkylation of chalcogenido metalate clusters have been employed. In this thesis, a new cluster oligomerization strategy is presented. By oligomerizing $[\text{Ge}_4\text{Se}_{10}]^{4-}$ clusters into dimeric $[\text{Ge}_8\text{Se}_{19}]^{4-}$ and tetrameric $[\text{Ge}_{16}\text{Se}_{36}]^{8-}$ in their corresponding salts, these compounds were made soluble in DMF owing to a reduced local cation-anion electrostatic interactions; their undecomposed transfer into solutions was evidenced by mass spectrometry. The optical properties and size distribution of particles in solutions were studied by means of UV-visible spectroscopy and dynamic light scattering, respectively. Another salt comprising $[\text{Cs}@\text{Ge}^{\text{II}}_4(\text{Ge}^{\text{IV}}_4\text{Se}_{10})_4]^{7-}$ anions was also found soluble in DMF, and adds to the few examples of chalcogenido metalates capable of selectively capturing Cs^+ during crystallization, as monitored by mass spectrometry, energy-dispersive X-ray spectroscopy, and single crystal X-ray diffraction. Quantum chemical studies were also carried out to understand its exclusive preference for inclusion of Cs^+ compared to the lighter alkali metal ions.

For enriching the structural diversity of chalcogenido metalates, two strategies were introduced in this thesis, a) manipulating the anionic clusters *via* incorporation of Cu(I) atoms; and b) modifying the structure-directing agents during the formation of new cluster anions. The importance of Cu(I) atoms for tailoring the anionic clusters owing to the diverse coordination modes of Cu^+ with chalcogen atoms was highlighted by the isolation of four new compounds. All of them are narrow band-gap semiconductors. In comparison to a copper-free compound, the presence of Cu(I) allowed access to directly manipulate the chalcogenido metalate anions. The modification of the ionic liquid cations led to varied structure-directing agents, which in turn afforded the formation of two new compounds, their anisotropic conductivity along horizontal and vertical directions were also further investigated. Additionally, further structural expansions within the chalcogenido metalate family have been realized upon using different types of ionic liquids, or modifying the precursor salts.

In summary, within this thesis, a new oligomerization strategy towards isolating finite cluster oligomer-based compounds was introduced, thereby improving the solubility of chalcogenido metalates in standard solvents. In addition, the significance of the incorporation of copper ions, of the modification of ionic liquid cations and anions, and of the variation of the precursor salts for expanding the chalcogenido metalate family members was demonstrated. This thesis will help the community to better understand the controllable synthesis of new chalcogenido metalate compounds.

Table of contents

Abstract	iii
Table of contents	v
Abbreviations	ix
1 Introduction	1
1.1 General introduction to zeolites and polyoxometalates	1
1.2 General introduction to chalcogenido metalates.....	3
1.3 Towards structural design of compounds with molecular supertetrahedral chalcogenido metalate clusters	6
1.3.1 Incorporation of Tt^{4+} metal cations.....	7
1.3.2 Charge reduction by neutral ligands	9
1.3.3 Alkylation of supertetrahedral chalcogenido metalate clusters	10
1.4 Synthetic approaches to chalcogenido metalates.....	11
1.4.1 Solid-state syntheses.....	11
1.4.2 Solvothermal techniques	14
1.4.3 Ionothermal reactions	14
1.5 Applications of chalcogenido metalate compounds	22
2 Research objectives	26
3 Results and Discussion	27
3.1 Defined oligomers of supertetrahedra-based selenido germanate clusters	27
3.1.1 Introduction	27
3.1.2 Syntheses and crystal structures	29
3.1.3 Additional characterizations to compounds 1 – 4	37
3.1.4 Conclusions	43
3.2 Ion-selective assembly of supertetrahedral selenido germanate clusters for alkali metal ion capture.....	44
3.2.1 Introduction	44
3.2.2 Syntheses and crystal structures	46
3.2.3 Additional characterizations compounds 5 and 6.....	54
3.2.4 Conclusions	63
3.3 Structural expansion and enhanced photocurrent conversion of selenido stannates with Cu^+ ions.....	65
3.3.1 Introduction	65
3.3.2 Syntheses and crystal structures	67
3.3.3 Elemental analysis and PXRD measurement	77
3.3.4 Optical absorption properties and photocurrent measurement	79
3.3.5 Conclusions	83
3.4 Structural expansion of selenido stannates by modifying the ionic liquid cation and investigation of their conductivity properties	85

3.4.1	Introduction	85
3.4.2	Syntheses and crystal structures	85
3.4.3	Additional characterizations of compounds 12 and 13.....	88
3.4.4	Ion-exchange experiments of compounds 12 and 13.....	90
3.4.5	Conductivity measurements.....	95
3.4.6	Conclusions	102
3.5	Further structural expansion of selenido metalates <i>via</i> the above-mentioned strategies	103
3.5.1	Crystal structure of compound 14.....	103
3.5.2	Crystal structure of compound 15.....	104
3.5.3	Crystal structure of compound 16.....	106
3.5.4	Crystal structure of compound 17.....	107
3.5.5	Crystal structure of compound 18.....	108
3.5.6	Crystal structure of compound 19.....	109
3.5.7	Crystal structure of compound 20.....	110
3.5.8	Crystal structure of compound 21.....	111
4	Summary.....	113
5	Experimental sections	117
5.1	General	117
5.2	Characterizations	117
5.2.1	Light-microscopic images of the single crystals.....	117
5.2.2	Powder X-ray diffraction (PXRD).....	117
5.2.3	Energy dispersive X-ray (EDX) spectroscopy.....	118
5.2.4	Electrospray ionization mass spectrometry (ESI-MS).....	118
5.2.5	Dynamic light scattering (DLS).....	118
5.2.6	Raman spectroscopy	118
5.2.7	UV-visible spectroscopy.....	118
5.2.8	X-ray photoelectron spectroscopy (XPS)	119
5.2.9	Infrared Spectroscopy (IR)	119
5.2.10	Quantum chemical calculations	119
5.2.11	Photocurrent measurement	119
5.2.12	Ion-exchange experiments	120
5.2.13	<i>I</i> – <i>V</i> characteristic measurement	120
5.3	Syntheses of starting materials.....	121
5.4	Syntheses of compounds 1 – 21	122
5.4.1	Synthesis of (C ₂ C ₁ Im) ₄ [Ge ₄ Se ₁₀] (1).....	122
5.4.2	Synthesis of (C ₂ C ₁ Im) ₆ [Ge ₈ Se ₁₉] (2a and 2b)	122
5.4.3	Synthesis of (C ₂ C ₁ Im) ₈ [Ge ₁₆ Se ₃₆] (3)	122
5.4.4	Synthesis of (C ₂ C ₁ Im) ₆ [Ge ₁₂ Se ₂₇] (4)	122
5.4.5	Synthesis of (C ₂ C ₁ Im) ₇ [Cs@Ge ^{II} ₄ (Ge ^{IV} ₄ Se ₁₀) ₄] (5).....	123
5.4.6	Synthesis of (C ₂ C ₁ Im) ₁₀ [Na ₅ (CN) ₆ @Cu ₆ (Ge ₄ Se ₁₀) ₄ (Cu)] (6a and 6b) ..	123
5.4.7	Synthesis of (C ₂ C ₂ Im) ₉ Li[Cu ₁₀ Sn ₆ Se ₂₂] (7)	124
5.4.8	Synthesis of (C ₂ C ₂ Im) ₄ [Cu ₈ Sn ₆ Se ₁₈] (8)	124
5.4.9	Synthesis of (C ₂ C ₁ Im) ₃ [Cu ₅ Sn ₃ Se ₁₀] (9a and 9b).....	124

5.4.10 Synthesis of $(C_2C_2Im)_5[Cu_8Sn_6Se_{18}F] \cdot [C_2C_2Im][BF_4]$ (10)	125
5.4.11 Synthesis of $\{(C_2C_2Im)_2[Sn_3Se_7]\}_4 \cdot (C_2C_2Im)_2[BF_4]_2$ (11)	125
5.4.12 Synthesis of $(C_3C_1Im)_3(H^+ - DMMP)[Sn_3Se_7]_2$ (12)	126
5.4.13 Synthesis of $(H^+ - DMMP)_2[Sn_3Se_7] \cdot (H^+ - DMMP)[Sn_2Se_6]_{0.5}$ (13)	126
5.4.14 Synthesis of $\{(C_3C_1C_1Im)_2[Sn_3Se_7]\}_2 \cdot (C_3C_1C_1Im)Br$ (14)	126
5.4.15 Synthesis of $\{(C_2C_2Im)_2[Sn_3Se_7]\}_4 \cdot 2(C_2C_2Im)Br$ (15)	126
5.4.16 Synthesis of $(C_4C_1Pyrro)_8[Sn_{10}O_4Se_{20}]$ (16)	127
5.4.17 Synthesis of $(Cat)_{2x}[Sn_{4-x}Hg_xSe_8]$ (17)	127
5.4.18 Synthesis of $(C_2C_1Im)_6[Cu_8Sn_6Se_{18.7}S_{0.3}]$ (18)	127
5.4.19 Synthesis of $(C_2C_2Im)_{18}[Cu_6In_{16}Sn_4Se_{44}]$ (19)	128
5.4.20 Synthesis of $(H^+ - en)[Cu_3GeSe_4]$ (20)	128
5.4.21 Synthesis of $(C_2C_1Im)[Sb_3Se_5]$ (21)	128
6 Additional information	130
6.1 Additional information on compounds discussed in Chapter 3	130
6.1.1 High-resolution mass spectra of the cluster anion in 1, 2a, and 3	130
6.1.2 Stability study of solutions of the soluble compounds 1, 2a, and 3	133
6.1.3 UV-visible diffuse-reflectance spectra of compounds 1, 2a, and 3	134
6.1.4 Structural details of compound 5	135
6.1.5 Structural details of compound 6	136
6.1.6 Mass weight and yield of the cross-experiments for compound 5	138
6.1.7 Structural details of compound 7	138
6.1.8 Structural details of compound 8	139
6.1.9 Structural details of compound 9	140
6.1.10 Structural details of compound 10	141
6.1.11 Bond valence sum (BVS) of Cu atoms in compound 7 – 10	142
6.1.12 Optical properties of compounds 8 – 11	143
6.1.13 ESI(–) mass spectra of the solution upon extracting 13 with Cs^+	145
6.1.14 Crystal structure measurement and optical photographs of compounds 1 – 21	146
Bibliography	171
Declaration	183
Curriculum Vitae	184
Publications	185
Acknowledgement	186

Abbreviations

SDAs	structure-directing agents
POMs	polyoxometalates
TM	transition metal
Tt	Ge or Sn
Tr	Ga or In
AO	acridine orange
RhB	rhodamine B
DBN	1,5-diazabicyclo[4.3.0]non-5-ene
DBU	1-(2-aminoethyl)piperazine
AEP	1,8-diazabicyclo(5.4.0)undec-7-ene
DEM	4-[2-(dimethylamino)ethyl]morpholine
AB	2-amino-1-butanol
<i>im</i>	imidazole
Im	imidazolium
Ch	S or Se
A	alkali metal
Me	methyl
Pr	<i>n</i> -propyl
Bu	<i>n</i> -butyl
Pn	<i>n</i> -pentyl
Hex	<i>n</i> -hexyl
IL	ionic liquid
py	pyridine
DMA	dimethylamine
1-Mim	1-methylimidazole
PXRD	powder X-ray diffraction
<i>en</i>	ethylenediamine

<i>ma</i>	methylamine
DMMP	2,6-dimethylmorpholine
NMR	Nuclear Magnetic Resonance spectroscopy
ESI-MS	electrospray ionization mass spectroscopy
DMF	N,N-dimethylformamide
DLS	dynamic light scattering
SC-XRD	single-crystal X-ray diffraction
SEM	scanning electron microscope
EDX	energy dispersive X-ray spectroscopy
DMSO	dimethyl sulfoxide
R_H	hydrodynamic radius
DFT	Density functional theory
XPS	X-ray photoelectron spectroscopy
BVS	bond valence sum
CV	cyclic voltammograms
(C ₂ C ₁ Im)[B(CN) ₄]	1-ethyl-3-methyl-imidazolium tetracyanoborate
(C ₂ C ₁ Im)[BF ₄]	1-ethyl-3-methyl-imidazolium tetrafluoroborate
(C ₂ C ₂ Im)[BF ₄]	1,3-diethylimidazolium tetrafluoroborate
(C ₂ C ₂ Im)Br	1,3-diethylimidazolium bromide
(C ₃ C ₁ C ₁ Im)Br	1-propyl-2,3-dimethylimidazolium bromide
(C ₃ C ₁ Im)[BF ₄]	1-propyl-3-methylimidazolium bromide
(HOC ₂ C ₁ Im)[BF ₄]	1-(2-hydroxyethyl)-3-methylimidazolium tetrafluoroborate
(C ₄ C ₁ C ₁ Im)[BF ₄]	1-butyl-2,3-dimethylimidazolium tetrafluoroborate
(C ₄ C ₁ Pyrro)[N(CN) ₂]	1-butyl-1-methylpyrrolidinium dicyanamid

1 Introduction

1.1 General introduction to zeolites and polyoxometalates

Zeolites, a family of ordered porous crystalline materials, are formed by linking $\{\text{TO}_4\}$ tetrahedra (TO_4 , with oxygen atoms bonded to the central tetrahedral atoms, $\text{T} = \text{Si}/\text{Al}$) through O^{2-} bridges^[1,2]. These structures are templated by a wide spectrum of inorganic (especially Na^+ , K^+ , and Ca^{2+})^[3] or organic (ammonium, ionic liquid cation)^[4,5] or organic-inorganic hybrid (*e.g.* ($\text{Na}-\text{Crown ether}$)⁺ complexes)^[6] structure-directing agents (SDAs) in their cavities. The wide variety of these SDAs, especially the organic ones, offers great opportunities for the isolation of numerous zeolites with large pores which facilitates their application in areas ranging from ion-exchange^[7] to gas adsorption/separation^[8] and catalysis^[9]. Structurally speaking, the tetrahedral center of Si^{4+} and Al^{3+} can be partially substituted by other cations, such as Ge^{4+} , Ga^{3+} , Co^{2+} , without modifying the tetrahedral coordination geometries, but giving arise to specific properties owing to the incorporation of these heteroelements^[10]. Two examples of anionic zeolitic structures, comprising aluminosilicate^[11] or beryllophosphate^[12] architectures, are given in Figure 1.1 without showing the SDAs. These two anionic frameworks are established upon periodic assembly of the small $\{\text{TO}_4\}$ tetrahedral units, providing geometry-differing but large cavities for further applications in, but not limited to, catalysis and ion-exchange. Although there are successful cases of forming zeolitic structures without using Si^{4+} or Al^{3+} as a tetrahedral center (the latter beryllophosphate or $\text{Co}_x\text{Ga}_{1-x}\text{PO}_4$ and their analogues for instance), it is rather challenging and rare to fully replace them with elements from other groups while maintaining the anionic structure of zeolites. Doing so would mostly break the tetrahedral configuration of the central cations, leading to the formation of other structural units, like polyoxometalates (POMs), neutral or cationic metal oxido clusters, instead^[13].

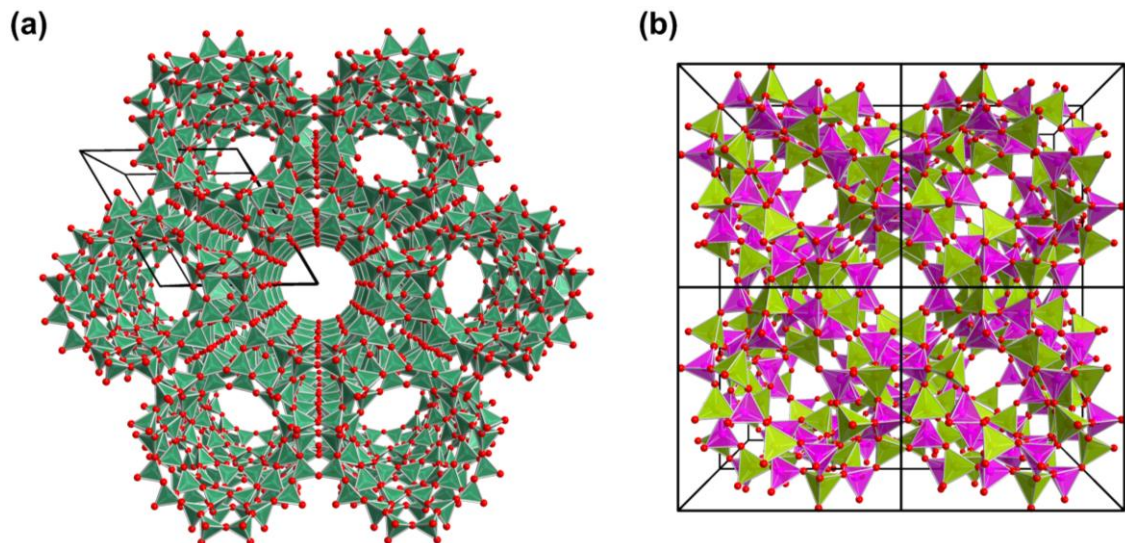


Figure 1.1: Zeolitic framework structures of aluminosilicate EMC-2, $[\text{Si}_{78}\text{Al}_{20}\text{O}_{192}]^{12-}$ (a), and beryllophosphate, $[\text{Be}_{24}\text{P}_{24}\text{O}_{96}]^{24-}$ (b). Counterions are not shown in their cavities for clarity. Color code: Al/Si—Sea green, P—Pink, O—Red, Be—Lime, $\{\text{Al/SiO}_4\}$, $\{\text{PO}_4\}$, and $\{\text{BeO}_4\}$ tetrahedra are shown in sea green, pink, and lime.

In comparison to the featured coordination configurations of the central atoms (tetrahedral) and ligand oxygen atoms of aluminates and silicates in zeolites, the use of their heavier congeners, such as Ge^{4+} , Sn^{4+} , Ga^{3+} and In^{3+} , commonly allows for more diverse coordination possibilities with oxygen in metal oxido clusters and POMs^[14,15]. As illustrated in Figure 1.2, these cations cannot only inherit the same tetrahedral geometry as those aluminates and silicates when bonding to oxygen ligands, but they can also form trigonal bipyramidal, as well as octahedral, coordination modes. Additionally, while oxygen atoms in zeolites typically serve as μ -ligands, in metal oxido clusters and POMs, $\mu_3\text{-O}$, $\mu_4\text{-O}$, or $\mu_5\text{-O}$ ligands are also observed^[13]. Therefore, given these considerations, synthesizing zeolitic structures, using the heavier congeners of Si^{4+} and Al^{3+} as the tetrahedral center atoms, presents a significant synthetic challenge, but are crucial for introducing specific structures and other properties beyond what zeolites can currently achieve.

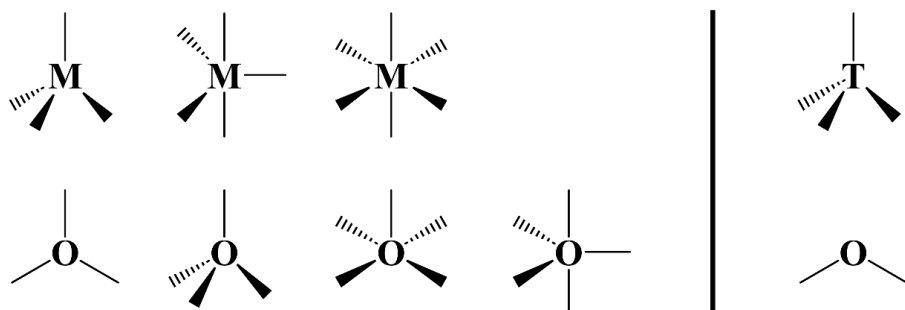


Figure 1.2: Coordination environments of Tl^{4+} , Tr^{3+} and O^{2-} in metal oxido clusters and POMs (Left) in comparison to those in zeolites (Right); M = central metal atoms, T = tetrahedral central atoms.

1.2 General introduction to chalcogenido metalates

To expand the structures and the properties of zeolites, it has been confirmed that further replacement of O^{2-} with S^{2-} or Se^{2-} is fruitful. This approach benefits from the size-matched characteristic between Ge^{4+} , Sn^{4+} , Ga^{3+} , In^{3+} and S^{2-} or Se^{2-} (Ch^{2-}) compared to O^{2-} ^[16,17]. Owing to the stronger polarization capability of chalcogen atoms, metal chalcogenides or chalcogenido metalates are normally semiconductor materials^[18]. Therefore, so-called “colored zeolites” can be isolated following this concept^[19]. In addition to this, the charge is better delocalized because of the longer T–Ch bond lengths compared to T–O, leading to more variable possibilities at the coordination spheres, and therefore new structure types.

In this introduction, a few zeolite-type framework compounds of chalcogenido metalates will be firstly introduced, focusing on their structures and applications, with an emphasis on the design and formation of the building blocks of each type of compound. Second, an introduction to the stabilization of discrete supertetrahedral clusters will be given, an elaborate consideration concerning the construction of size-differed cluster supertetrahedra have been fully presented. Third, the transformation of the alkali metal salts of such tetrahedra in ionic liquids (abbreviated as ILs, see below for a detailed introduction to ILs) and their reactivities towards transition metals compounds are presented. Both allow the formation of a wide spectrum of crystalline chalcogenido metalate-based compounds and application potential of corresponding products in different fields.

Bedard *et al.* first produced porous chalcogenido metalate architectures in 1989 by corner linking $[MS_4]^{x-}$ (M = transition metal, here, $M = Cu^{+}$; Zn^{2+} ; Mn^{2+} ; Co^{2+} ; Fe^{2+}) and $[Tt_4S_{10}]^{4-}$ ($Tt = Sn^{4+}$; Ge^{4+}) tetrahedra. The anionic networks are filled by organic SDAs^[20]. Their tetrahedral building units, $[MS_4]^{x-}$ and $[Tt_4S_{10}]^{4-}$, were later defined as T1 and T2 clusters by Yaghi *et al.* in 1999 (Tn refers to a tetrahedral cluster with n layers of metal atoms along the edges and all the metal centers being coordinated by four chalcogenide ligands, see Figure 1.3)^[21]. From there, they achieved giant porosities and channels in two T3- $\{In_{10}S_{20}\}$ -based zeolite-type structures (approximately 80% of voids for both). The T3- $\{In_{10}S_{20}\}$ unit can be regarded as the condensation of ten T1- $\{InS_4\}$ clusters *via* sharing their corner sulfur atoms. It is noteworthy that zeolites built by tetrahedral units larger than $\{TO_4\}$ have not been reported yet. Chalcogenido metalate framework compounds that are constructed by Tn units typically possess higher porosities than that of aluminosilicate zeolites, thus offering new possibilities for gas adsorption/separation, selective catalysis and ion-exchange process.

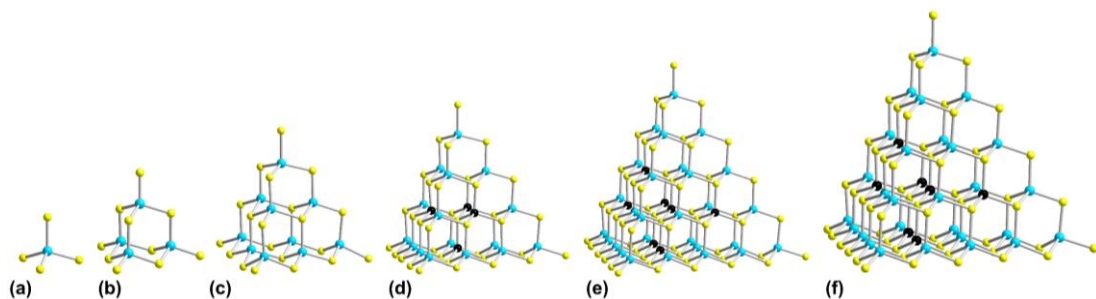


Figure 1.3: The known Tn -type cluster family members, ranging from T1 (a), to T2 (b), T3 (c), T4 (d), T5 (e), and T6 (f). Color code: Tr/Tt–Sky blue, transition metal–Black, chalcogen–Yellow.

From a mathematical perspective, to establish larger T_n clusters, one would theoretically need $[n(n+1)(n+2)]/6$ tetrahedral central metal atoms and $[(n+1)(n+2)(n+3)]/6$ chalcogen atoms^[16]. Structurally, for a discrete supertetrahedral cluster, a $T_2\{-Tt_4Ch_{10}\}$ anion comprises four terminating Ch_{term} , six bridging μ - Ch and four metal atoms^[22]. A $T_3\{-Tr_{10}Ch_{20}\}$ cluster contains four Ch_{term} , 12 μ - Ch , four μ_3 - Ch , and ten metal atoms. One may notice that there are μ_3 - Ch observed in a $T_3\{-[Tr_{10}Ch_{20}]^{10-}\}$ cluster unit^[23]. To balance the negative charges of these μ_3 - Ch , each adjacent In^{3+} would in theory contribute 0.75 relative positive charges to their neighboring chalcogen atoms and therefore, the $T_3\{-In_{10}Ch_{20}\}$ cluster can be chemically stabilized. The charge balance is much more challenging for (yet unknown) T_3 -type $\{Tt_{10}Ch_{20}\}$ or $\{M^{II}_{10}Ch_{20}\}$ clusters. T_3 -type $\{Sn_{20}O_4S_{20}\}$ ^[24,25] and $T_3\{-M_5Sn_5S_{20}\}$ ($M = Co, Mn, Zn, Cd, Hg$)^[26] are further examples, even though the first one is not an ideal supertetrahedral cluster, as interstitial O^{2-} ions are required for charge balancing. To build perfect discrete T_4 clusters, it is necessary to include low-valent metal atoms^[27]. A suitable selection of metal ions of certain charges is one of the most general concepts and means to push up the size of supertetrahedral chalcogenido metalate clusters, as detailed below (Chapter 1.3). This way, T_5 ^[28] and, especially, T_6 ^[29] clusters have been achieved. A few of the known zeolite-type chalcogenido metalate structures are illustrated in Figure 1.4, with a special focus on their corresponding building blocks ranging from T_2 to T_5 clusters. As shown in Figure 1.4a,b, in the anionic three-dimensional framework of $\{Tr_{4-x}Tt_xCh_8\}$ (denoted as UCR-20), Feng *et al.* achieved a sodalite-type topology structure upon regarding each T_2 cluster as a node^[19] (pink sphere). The sodalite-type chalcogenido metalate frameworks comprise large cavities (shown as a purple sphere in Figure 1.4b) which allows further use for pore-related applications. In a similar way, corner linking of T_3 -type $\{In_{10}S_{20}\}$ clusters afforded another porous structure in a CrB_4 -type topology^[21] (denoted as ASU-32, Figure 1.4c,d). In these two cases, all corner chalcogen atoms link two clusters each to form the networks. When the corner chalcogen atoms serve to link four identical T_4 -type $\{Zn_5In_{15}S_{35}\}$ clusters, an infinite *diamond*-type structure is formed upon treating each T_4 -type cluster as a node^[30], with a framework formula of $\{Zn_5In_{15}S_{32}\}$ (denoted as ITF-9, Figure 1.4e,f). Figure 1.4g,h displays the assembly of a T_5 -type $\{Cu_5In_{30}S_{56}\}$ -based cluster, forming a two-fold interpenetrated *diamond*-type anionic $\{Cu_5In_{30}S_{54}\}$ framework (denoted as UCR-17), upon sharing the four corner chalcogen atoms with adjacent clusters^[28]. Although a T_6 cluster is also reported^[29], there is no T_6 -based zeolite-type structure isolated yet, and it remains a synthetic challenge in this area.

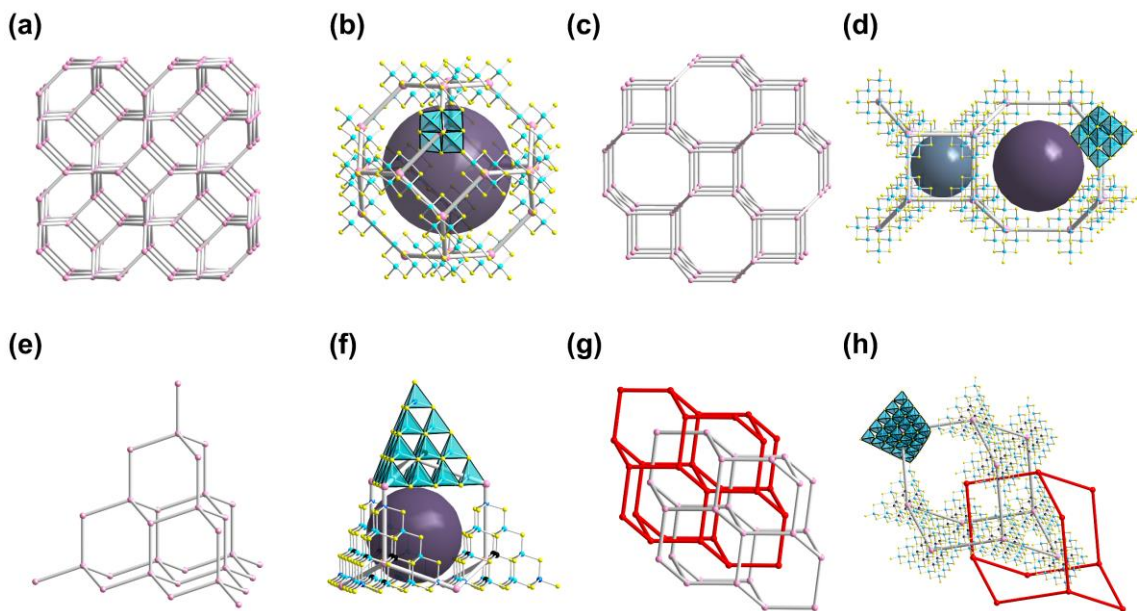


Figure 1.4: Examples of zeolite-type frameworks. UCR-20 with a sodalite-type topology, using T2 clusters as building units (a–b). ASU-32 with a CrB₄-type topology, using T3 clusters as building units (c–d). ITF-9 with a diamond topology, using T4 clusters as building units (e–f), and UCR-17 with a two-fold interpenetrated *diamond*-type topology, using T5 clusters as building units (g–h). Color code: Tr/Tt–Sky blue, TM–Black, chalcogen–Yellow. Small pink and red spheres represent the whole building units. Large purple and gray spheres represent the cavities of each network. The cavity of UCR-17 is not highlighted owing to its interpenetrated nature. Counterions are omitted for clarity.

Not only T_n-type clusters are observed in the tetrahedral chalcogenido metalate cluster family, pental-supertetrahedral (described as P_n) and capped-supertetrahedral (described as C_n), were also isolated. The latter two can be viewed as derivatives from parent T_n clusters. As illustrated in Figure 1.5a, a P1 cluster is formed through adding four T1 clusters onto the surfaces of an anti-T_n cluster, the anti-T_n cluster here is defined as a T_n cluster but with inversed cationic and anionic positions^[31]. Up to now, the largest P_n cluster is a P2 cluster, observed in its molecular and network versions, like $[\text{In}_{22}\text{Li}_4\text{S}_{44}]^{18-}$ anion in the network compound $[\text{Ca}_{1.5}\text{Li}_{11}(\text{H}_2\text{O})_{44}][\text{In}_{22}\text{Li}_4\text{S}_{42}]^{[32]}$. The C_n clusters are typically capped with thiolate ligands at the surfaces, and are constructed by covering a single sheet of atoms of the same composition as a T(*n*+1) cluster onto the four faces of a T_n core motif. A C1 cluster is shown as an example in Figure 1.5b^[33]. Table 1.1 serves to outline the differences in terms of the metal and chalcogen atom numbers in each type of clusters. However, this thesis targets on investigating the transformation of T_n clusters, therefore only T_n-type cluster-based structures and their reactivities are discussed.

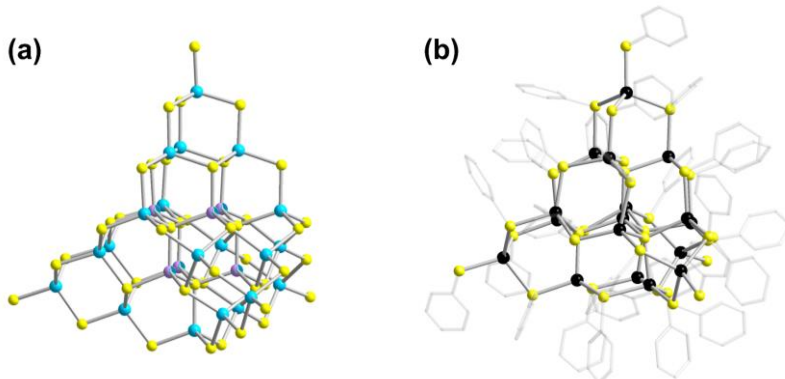


Figure 1.5: Molecular structure of P2-type cluster anion $[\text{In}_{22}\text{Li}_4\text{S}_{44}]^{18-}$ (a), and of C1-type cluster anion $[\text{Cd}_{17}\text{S}_4(\text{Ph})_{28}]^{2-}$ (b). Color code: In–Sky blue, In/Li–Blended purple and sky blue, Cd–Black, chalcogen–Yellow. H atoms are omitted for clarity.

Table 1.1: Summary of known T_n , P_n , and C_n clusters and their general formulas.

N	Compositions of T_n clusters (disregarding charge)	Compositions of P_n clusters (disregarding charge)	Compositions of C_n clusters (disregarding charge)
1	MCh_4	M_8Ch_{17}	$\text{M}_{17}\text{Ch}_{32}$
2	M_4Ch_{10}	$\text{M}_{26}\text{Ch}_{44}$	$\text{M}_{32}\text{Ch}_{54}$
3	$\text{M}_{10}\text{Ch}_{20}$		
4	$\text{M}_{20}\text{Ch}_{35}$		
5	$\text{M}_{35}\text{Ch}_{56}$		
6	$\text{M}_{56}\text{Ch}_{84}$		
n	$\text{M}_{x1}\text{Ch}_{y1}$ ^a	$\text{M}_{x2}\text{Ch}_{y2}$ ^b	$\text{M}_{x3}\text{Ch}_{y3}$ ^c

^a $x_1 = [n(n+1)(n+2)]/6$, $y_1 = [(n+1)(n+2)(n+3)]/6$
^b $x_2 = [4n(n+1)(n+2)]/6 + [(n+1)(n+2)(n+3)]/6$, $y_2 = [4(n+1)(n+2)(n+3)]/6 + [n(n+1)(n+2)]/6$
^c $x_3 = [n(n+1)(n+2)]/6 + [4(n+1)(n+2)]/2 + 4$, $y_3 = [(n+1)(n+2)(n+3)]/6 + [4(n+2)(n+3)]/2 + 4$

1.3 Towards structural design of compounds with molecular supertetrahedral chalcogenido metalate clusters

While a huge number of zeolite-type chalcogenido metalate framework compounds have been isolated and their physical and chemical properties have been extensively investigated over many years, a critical challenge in the study of these compounds has been the lack of control over assembling supertetrahedral cluster units. These units are known either as highly charged monomeric cluster anions^[34] or as extended anionic substructures of linked clusters with lower charge per cluster unit^[35]. The latter type is the predominant in applications of such materials, which is why most of them take part in a heterogeneous environment.

In contrast to the frequent observation of framework compounds, molecular cluster supertetrahedra have been reported far less, but allow an opportunity to study their aggregates in liquid and gas phases^[36], and, at the same time, provide a platform for investigating their reactivities at various reaction conditions^[37]. In the present thesis, the assembly of T_n clusters, and exploration of their reactivities have been focused on. T_n clusters tend to form porous framework compounds *via*

linking corner chalcogen atoms. This tendency results in lower reactivities and hinder further structural transformation. To address this challenge, it is of great importance to form compounds with molecular chalcogenido metalate anions, and several strategies, including, but not limited to, 1) incorporation of Tt^{4+} metal cations^[38,39], 2) charge reduction by neutral ligands^[40-42], and 3) alkylation of supertetrahedral clusters^[43-45] have been proposed in the past decade. A more detailed discussion of these three strategies is given below.

1.3.1 Incorporation of Tt^{4+} metal cations

As discussed earlier, the incorporation of transition metal cations, such as Zn^{2+} , facilitates the formation of larger cluster supertetrahedra^[29]. It has also been recently found that the *in-situ* inclusion of a significant amount of metal cations of a 4+ charge during the formation of these T_n clusters is helpful for terminating their extension into frameworks owing to intramolecular charge reduction. This approach enabled the isolation of a series of discrete tetrahedral clusters, ranging from T_2 to T_5 . Herein, a few examples of T_2 , T_3 , and T_4 clusters are shown to explain how the use of Tt^{4+} cations helps in the formation of discrete supertetrahedral clusters.

Feng *et al.* found that blending Tr^{3+} and Tt^{4+} typically results in T2-based zeolite-type framework compounds^[19]. Figure 1.6 illustrates a T2-type $\{\text{Tr}_x\text{Tt}_{4-x}\text{Ch}_{10}\}$ cluster ($0 \leq x \leq 4$). To date, no discrete T2-type $\{\text{Tr}_x\text{Tt}_{4-x}\text{Ch}_{10}\}$ cluster has been reported ($0 < x < 4$). There are only a few examples for the pure inorganic forms of T2-type cluster anions in $[\text{K}_8(\text{H}_2\text{O})_{16}][\text{Ga}_4\text{S}_{10}]$, $[\text{K}_8(\text{H}_2\text{O})_{16}][\text{In}_4\text{S}_{10}]$, and $[\text{K}_8(\text{H}_2\text{O})_{16}][\text{In}_4\text{Se}_{10}]$ ^[22]. The relatively small size of K^+ compared to that of organic cations might allow the stabilization and formation of the highly charged T2 clusters. $[\text{Tt}_4\text{Ch}_{10}]^{4-}$ clusters, in contrast, fewer charges need to be balanced, and consequently, discrete T2-type $\{\text{Tt}_4\text{Ch}_{10}\}$ clusters were obtained in a very wide spectrum of salts using different SDAs^[46,47,56,48-55].

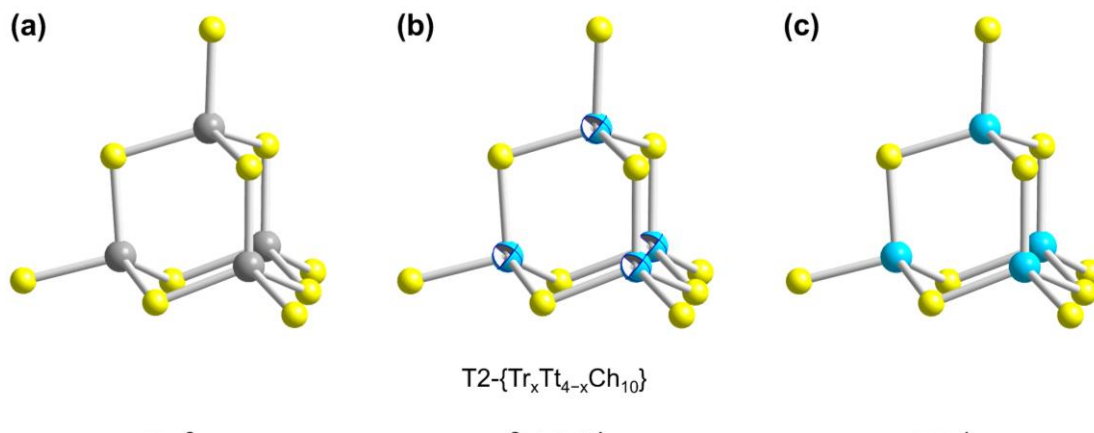


Figure 1.6: Illustration of pure or mixed T2-type $\{\text{Tr}_x\text{Tt}_{4-x}\text{Ch}_{10}\}$ clusters. Color code: Tt—Gray, Tr—Sky blue, Tt/Tr—Blended gray and sky blue, chlaogen, Yellow.

Ideal T3-type clusters, which typically are constructed by group 13 element atoms and chalcogen atoms for suitable charge balance^[57,58], can also be formed using a $\text{Ti}^{4+}/\text{M}^{2+}/\text{Ch}^{2-}$ combination^[26]. Here, Ti^{4+} atoms not only serve to compensate the negative charges in the presence of M^{2+} cations, but also serve to inhibit the aggregation of those T3-type clusters into networks. As depicted in Figure 1.7, in a T3-type $\{\text{M}^{\text{II}}_5\text{Sn}_5\text{Ch}_{20}\}$ cluster (here $\text{M}^{\text{II}} = \text{Zn}$ and Co), there are four $\mu_3\text{-Ch}$ observed at the surface of the cluster, twelve $\mu\text{-Ch}$ found along the cluster's edges, and the remaining four chalcogen atoms are arranged at the corners, with four Sn^{4+} atoms bridging to the corner chalcogen atoms. The last Sn^{4+} atom is disordered and assigned at a 1/6 occupancy at each of the six remaining metal atom positions. Especially, given that alkali metal ions acting as counter cations in various forms of the $[\text{M}^{\text{II}}_5\text{Sn}_5\text{Ch}_{20}]^{10-}$ anions, again, it is somehow also favorable for the formation of these cluster anions because of the smaller size of alkali metal ions in comparison to that of organic counterions.

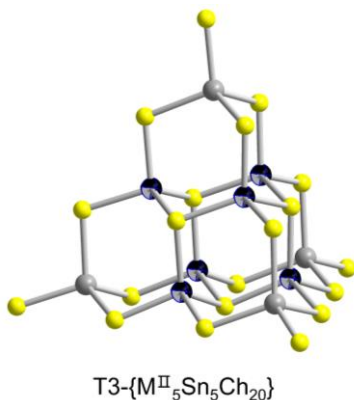


Figure 1.7: Molecular structure of a T3-type $[\text{M}^{\text{II}}_5\text{Sn}_5\text{Ch}_{20}]^{10-}$ anion. Color code: Sn—Gray, $\text{M}^{\text{II}}/\text{Sn}$ —Blended black and gray, chalcogen—Yellow.

Following the same idea on how to establish T2 and T3 clusters, discrete T4 clusters can also be stabilized. Known regular T4 clusters normally comprise of either $\text{Cu}^+ \text{--} \text{Tr}^{3+} \text{--} \text{Ch}^{2-}$ ^[34] or $\text{M}^{2+} \text{--} \text{Tr}^{3+} \text{--} \text{Ch}^{2-}$ ^[29,59-62] compositions (Figure 1.8), and in most cases, these clusters further serve as building blocks to form porous frameworks *via* sharing corner chalcogen atoms. To obtain discrete cluster molecules, it is necessary to compensate for the relative charges arising from the terminal chalcogen atoms of the clusters. Given that T4 clusters are approximately twice the size of T2 clusters, it is thus possible to congregate more counterions nearby the cluster's edges or surfaces, and to achieve the formation of T4 clusters, even in the presence of larger organic counterions^[39]. Additionally, the inclusion of a significant amount of Ti^{4+} also improve the possibilities to obtain isolated T4-type substructures, and T4-type clusters $\{\text{M}_2\text{Ga}_{16}\text{Sn}_2\text{Ch}_{35}\}$ are pointed to as examples.

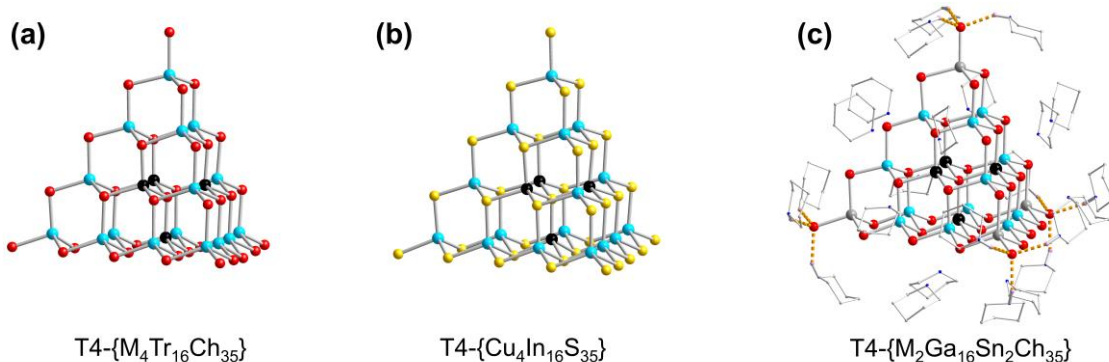


Figure 1.8: Molecular structure of a T4-type $\{M_4Tr_{16}Ch_{35}\}$ cluster (a), a T4-type $\{Cu_4In_{16}S_{35}\}$ cluster (b), a T4-type $\{M_2Ga_{16}Sn_2Ch_{35}\}$ cluster (c). Color code: M–Black, Tr–Sky blue, Tt–Gray, chalcogen–Yellow. H atoms are omitted for clarity.

1.3.2 Charge reduction by neutral ligands

In addition to the success achieved in forming discrete Tn clusters by inclusion of Tt^{4+} cations for reduction of the negative charge, another approach involving the attachment of ligands at their corner metal atoms has also been widely investigated. These neutral ligands replace the terminal chalcogen atoms, thereby effectively reducing the overall negative charges of the clusters and enhancing their stability. The first documented formation of a Tn cluster with neutral corner groups was reported in 2007 by Vaqueiro *et al.* In their work, a $[Ga_{10}S_{16}(S)_4]^{10-}$ cluster had its four terminal sulfur atoms substituted by four neutral coordinating 3,5-dimethylpyridine ligands, effectively reducing the overall charge from $10-$ to $2-$ and resulting in the isolated T3-type $[Ga_{10}S_{16}(NC_7H_9)_4]^{2-}$ cluster^[40] (Figure 1.9a). In comparison to the original $[Ga_{10}S_{16}(S)_4]^{10-}$ molecule, the functionalized version possesses only one fifth of the overall charge, providing both a higher thermal and chemical stability through the attachment of organic ligands. By finely tuning the reaction conditions, it was also possible to partially replace the corner chalcogen atoms by placing three 3,5-dimethylpyridine ligands at the corners while the last remaining one was a thiol. Additionally, 3,4-dimethylpyridine or 4-methylpyridine ligands are also capable of substituting the vertices of the T3 supertetrahedron and terminate its further extension to multidimensional substructures^[42,63]. By modifying the reaction medium, from pyridine-derivatives to 1,5-diazabicyclo[4.3.0]non-5-ene (DBN) or imidazolium-based ionic liquids, a family of DBN or imidazolate (im) functionalized cluster supertetrahedra were obtained. T3-type clusters of $[In_{10}S_{16}(DBN)_4]^{2-}$ and $[In_{10}Ch_{16}Cl_3(C_4im)]^{5-}$ are pointed to as examples^[42,64]. As discussed earlier, the incorporation of transition metals allows further pushing such clusters up to T4 and T5, such as T4-type $[Cd_4In_{16}S_{31}(DBN)_4]^{6-}$ or $[Co_4In_{16}Ch_{31}(DBN)_4]^{6-}$ (Figure 1.9b) and T5-type $[Cd_{13}In_{22}S_{52}(C_1im)_4]^{12-}$ or $[Cu_5Ga_{30}S_{52}(SH)_2(C_4C_1im)_2]^{11-}$ (Figure 1.9c) and many other similar supertetrahedra-based functionalized clusters have been reported recently^[65,66].

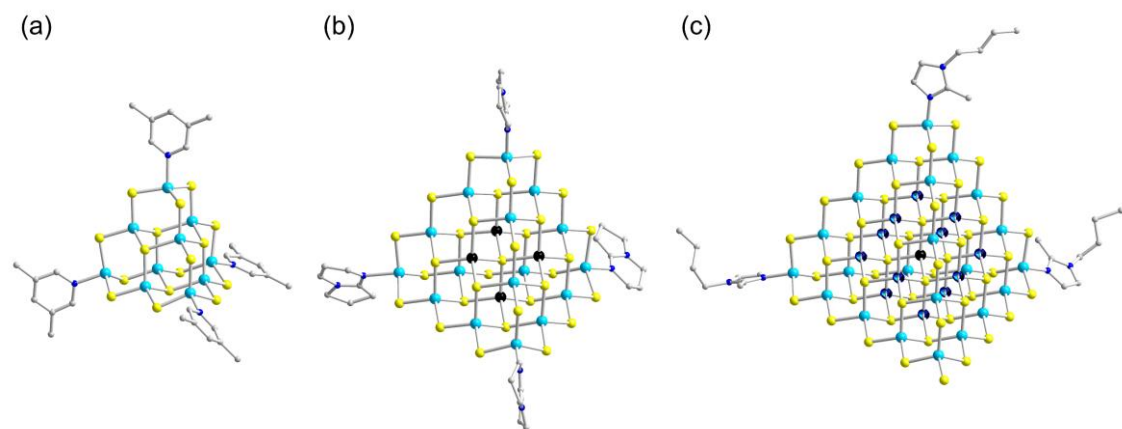


Figure 1.9: Molecular structure of a T3-type cluster $\{Ga_{10}S_{16}(NC_7H_9)_4\}$ (a), of a T4-type cluster $\{M_4In_{16}Ch_{31}(DBN)_4\}$ (b), and of a T5-type cluster $\{Cu_5Ga_{30}S_{52}(SH)_2(C_4C_1im)_2\}$ (c). Color code: Tr–Sky blue, M–Black, M/Tr–Blended sky blue and black, chalcogen–Yellow, C–Gray (25%), N–Blue. H atoms are omitted for clarity.

1.3.3 Alkylation of supertetrahedral chalcogenido metalate clusters

Most recently, *in-situ* alkylation has emerged as an alternative means towards forming discrete supertetrahedron-like cluster molecules through ionothermal reactions. In contrast to binding imidazolate or pyridine-based molecules to terminal metal atoms directly, as described above, this approach involves transferring one of the alkyl chains of the non-innocent ILs to the vertex chalcogen atoms, forming C–Ch bonds through *in-situ* alkylation reactions. This method effectively lowers the charges of the cluster anions, thereby potentially improving the solubility of such compounds in standard organic solvents as compared to their pure inorganic analogs. For instance, by adding $[A_4(H_2O)_x][SnS_4]$ (A = alkali metal) to imidazolium-based ILs, such as $(C_4C_1C_1Im)[BF_4]/Cl$ or $(C_mC_1C_mIm)Br$ ($m = 3; 4; 5; 6$), the selectively alkylated $[Sn_{10}O_4S_{16}(SMe)_4]^{4-}$ (Figure 1.10a), $[Sn_{10}O_4S_{16}(SPr)_4]^{4-}$ (Figure 1.10b), $[Sn_{10}O_4S_{16}(SBu)_4]^{4-}$ (Figure 1.10c), $[Sn_{10}O_4S_{16}(SPn)_4]^{4-}$, and $[Sn_{10}O_4S_{16}(SHex)_4]^{4-}$, were obtained ($Me =$ methyl group; $Pr =$ propyl group; $Bu =$ butyl group; $Pn =$ pentyl group; $Hex =$ hexyl group)^[43–45]. The negative charge of each cluster was thus reduced from 8^- for the non-decorated cluster core to 4^- . While the salt comprising $[Sn_{10}O_4S_{16}(SMe)_4]^{4-}$ anions is not soluble in standard solvent, the latter four compounds can be readily dissolved in MeCN and retain their structural features as well as compositions in liquid and gas phases as confirmed by electrospray ionization (ESI) mass spectroscopy and 1H and ^{119}Sn nuclear magnetic resonance (NMR). Although, these molecules are not ideal T_n clusters due to the incorporation of four oxygen atoms into their cores, this approach offers a new pathway towards obtaining discrete cluster supertetrahedra through *in-situ* alkylation at the corner chalcogen atoms. The alkylation of perfect T_n supertetrahedra is therefore feasible this way and is currently being investigated within this research group.

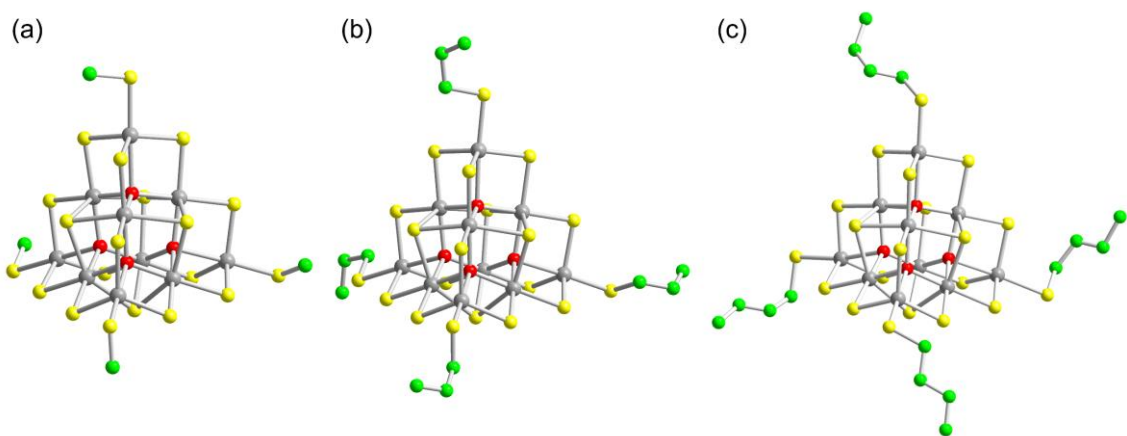


Figure 1.10: Molecular structure of *pseudo*-T3-type clusters $\{\text{Sn}_{10}\text{O}_4\text{S}_{16}(\text{SMe})_4\}$ (a), $\{\text{Sn}_{10}\text{O}_4\text{S}_{16}(\text{SPr})_4\}$ (b), and $\{\text{Sn}_{10}\text{O}_4\text{S}_{16}(\text{SBu})_4\}$ (c). Color code: Sn—Gray, O—Red, S—Yellow, C—Green. H atoms are omitted for clarity.

In general, the methods presented above are the three common ways for achieving isolated super-tetrahedral chalcogenido metalate clusters. For the latter two approaches, however, the protecting effect of organic ligands, endowing these compounds with good thermal and chemical stability, result in lower reactivities, and are unfavorable for their further chemical transformations. Taken together, in this thesis, the first method is employed to synthesize “naked” T1 or T2 clusters initially by a solid-state reaction. The investigation towards their structural transformation in ionic liquids is further carried out, leading to the formation of a wide spectrum of products, and the fundamental properties, including optical properties, photocurrent conversion, and electrical conductivity of these products, have been also explored.

1.4 Synthetic approaches to chalcogenido metalates

In the context of syntheses, there are several routes for targeting chalcogenido metalate compounds, which include, but are not limited to, a) solid-state syntheses^[67], b) solvothermal techniques^[68,69], c) ionothermal approaches^[70]. Given these three are the most popular approaches for accessing chalcogenido metalates, herein a brief introduction for each is given.

1.4.1 Solid-state syntheses

High temperature synthesis, including classical solid-state reactions and molten-salt flux methods, were among the most commonly used synthetic routes in chalcogenide chemistry two decades ago^[71,72]. These methods have been proven to yield products with high purity and unique structures that are not achievable under milder conditions.

Classical solid-state reactions typically occur at temperatures above 600 °C, while molten-flux reactions take place between 200–600 °C^[73]. With this method, reactants are mixed in stoichiometric ratios and heated to high temperatures to facilitate melting and diffusion of components. For these reactions, sealed tubes (for example quartz glass tubes) are used, and the reactions take

place in a furnace mostly under an inert atmosphere or vacuum to prevent oxidation. This approach serves as a platform to form new structure types or compositions that cannot be achieved at lower temperatures, which is attributed to the higher energy that can be provided using this method. Classical solid-state reactions are exemplified by the formation of binary and ternary chalcogenides, including materials with complex frameworks of high thermal stability. However, the high temperatures pose challenges for *in-situ* characterizations and therefore a challenge towards the elucidation of reaction pathways.

In typical solid-state syntheses for targeting chalcogenido metalates, the most common combinations of reagents include 1) A_2Ch/M_xCh_y ^[74] and 2) $A_2Ch/M/Ch$ ^[75] (A = alkali metals, M = metal elements) with varied stoichiometric ratios. The temperature and the duration of the reaction as well as the stoichiometry between the reactants are key factors to modify the product spectrum. By controlling the temperature, the diffusion of molecules at the interface can be modulated, thereby modifying the aggregation processes and ultimately, the substructure of the product. The duration of the reaction typically influences the yield and purity of target compounds. Adjusting the stoichiometry of the reactants changes the dimensionality and energy gap of resulting chalcogenido metalate compounds. Using chalcogenido cadmate-based compounds as an example to demonstrate the influence of stoichiometric ratios on the product formation in solid-state reactions, CdCh chalcogenides possess densely packed diamond-like structures, as that of sphalerite. As shown in Figure 1.11, reacting CdCh with a small amount of A_2Ch in a solid-state reaction can “break up” the dense parent structure and form three-dimensional (3D) porous networks with A^+ cations as intercalants and counterions, such as in $K_2[Cd_2Ch_3]$ ^[76]. By further increasing the amount of A_2Ch , the 3D dimensionality of $K_2[Cd_2Ch_3]$ can be reduced to 2D in $K_2[Cd_3Ch_4]$ ^[77] and to 1D in $K_2[CdCh_2]$ ^[78], and to molecular anions in $K_6[CdCh_4]$ ^[78]. This method not only allows for facile modification of the dimensionalities, but also enables the tuning of their optical gaps. The optical gaps are widened from dense phase *via* networks to molecular compounds.

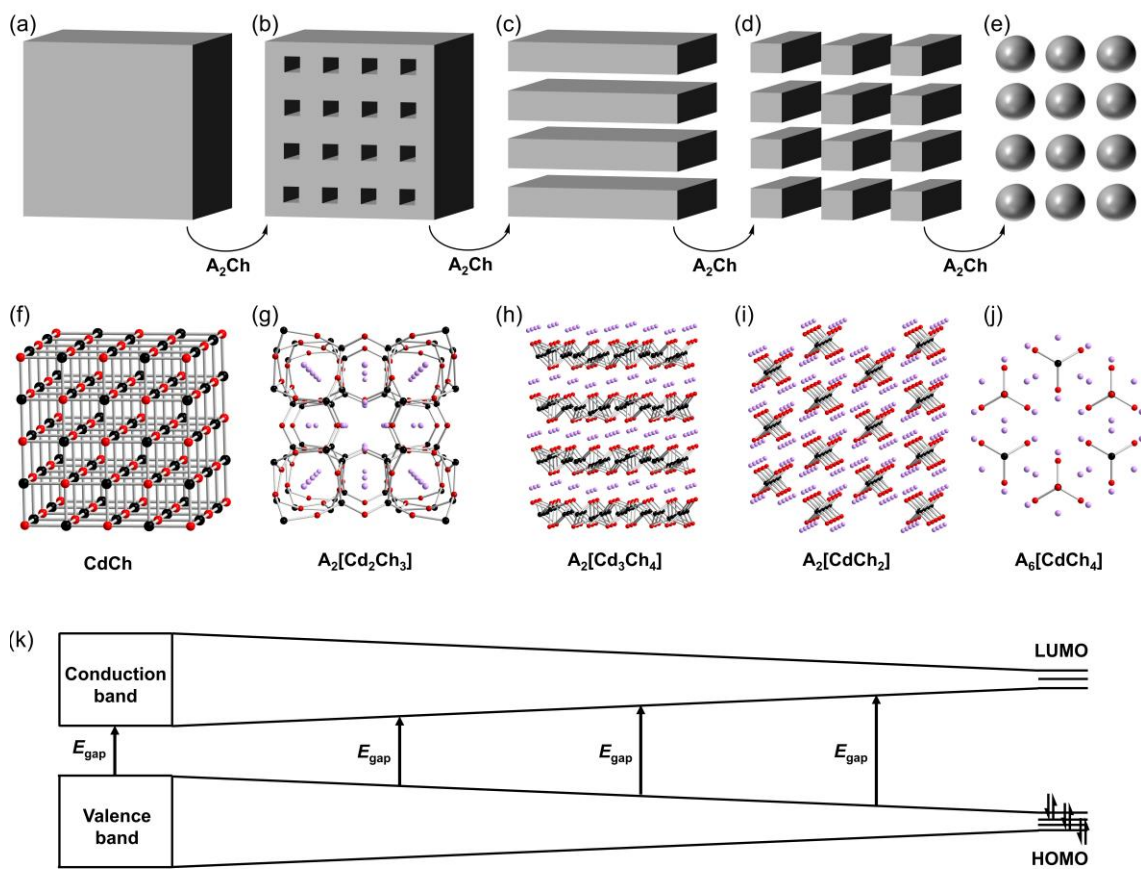


Figure 1.11: Approach for dimensionality reduction of chalcogenido cadmates from a 3D dense compound (a), or a 3D open-framework (b), *via* 2D layers (c), to 1D strands (d), and 0D molecular anions (e) in the A₂Ch/CdCh system through increasing the stoichiometric ratio of A₂Ch. Correspondingly, dense CdCh (f), 3D- $\{[Cd_2Ch_3]^{2-}\}$ in A₂[Cd₂Ch₃] (g), 2D- $\{[Cd_3Ch_4]^{2-}\}$ in A₂[Cd₃Ch₄] (h), 1D- $\{[CdCh_2]^{2-}\}$ in A₂[CdCh₂] (i), 0D- $\{[CdCh_4]^{6-}\}$ in A₆[CdCh₄] (j) were referred to as model examples, and the subsequent effect on the electronic properties of these compounds were illustrated (k).

Despite the fruitful set of compounds obtained from classic solid-state reactions, this approach favors the formation of the most thermodynamically stable compound. Molten-salt flux techniques have therefore become more popular in modern chemistry, due to the significantly lower melting point of the reactants, and because they allow to greatly decrease the reaction temperature in comparison to that of the former approach. This enables the isolation of kinetically stable compounds and intermediates^[79]. For instance, through replacing K₂S with the polysulfide salt K₂S₄ in a solid-state reaction, the reaction temperature can be reduced. This is attributed to the presence of polysulfide bonds in the latter, lowering the melting point to 145 °C compared to 850 °C for K₂S. Given the strong oxidizing nature of K₂S₄, it is highly reactive towards metals once it melts at 145 °C, thereby initiating the reactions^[73]. This way, the *in-situ* characterization of the reactions at relatively lower temperatures is feasible and thus offers possibilities to reveal the reaction mechanism of such so-called black-box syntheses with *in-situ* powder X-ray diffraction (PXRD), for instance.

1.4.2 Solvothermal techniques

Solvothermal techniques refer to reactions that take place in a sealed container and in a solvent that is heated to relatively high temperatures and pressures^[80]. These techniques have been the dominant synthetic approaches for targeting chalcogenido metalate-based compounds in the last twenty years^[81,82]. Unlike the diffusion at the interface in solid-state reactions, solvothermal techniques allow ions or molecules to react directly in the solvent. Therefore, it is also possible to isolate different products using the same reagents as those used in solid-state reactions.

Solvothermal techniques are defined as subcritical (below 240 °C) or supercritical (from 240 °C to 1000 °C)^[83]. The former route is most widely applied in laboratories and industry owing to the increased risk associated with higher temperatures and pressures. Nevertheless, variation in temperature is an important parameter used to modify the solubilities of reagents, and therefore, influence the product spectrum. Normally, not only the reaction temperature, but the used solvent and filling factor (*i.e.*, to the volume ratio of solvent to that of the reaction vessel) of the sealed reactor also influence the formation of different compounds^[84].

From a perspective of solvent choice, solvothermal synthesis can be further classified as hydrothermal synthesis, in particular, or solvothermal synthesis, in general. In the case of using water as a solvent, the surface tension, density and viscosity decreases at higher temperatures and pressures, while vapor pressure and ion production increase. This way, the reaction rate will be accelerated once the reaction system is heated above the boiling point of water, following to the Arrhenius equation:

$$d\ln k/dT = E/RT^2,$$

where k represents the reaction rate constant, T is the absolute temperature, E is the molar activation energy, and R is the universal gas constant. As the reaction temperature increases, k will exponentially increase simultaneously.

The large variety of organic solvents offer an even broader range of solvation properties, providing more possibilities in solvothermal reactions. Generally, solvents not only serve as a reaction medium for the mobility of reactants, but also help to dissolve or at least partially dissolve the reactants, which modifies the chemical conversion rate and affects the product spectrum. Selecting the appropriate organic solvent involves considering parameters such as density, melting point, boiling point, heat of evaporation, and solvent polarity. By choosing a suitable combination of these parameters, it is possible to effectively tune the dissolution behavior of reagents in different solvents and thus tailor the products out of solvothermal reactions^[85,86].

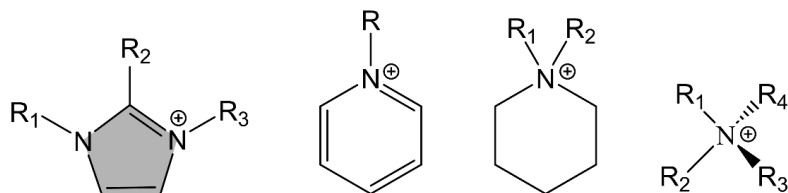
1.4.3 Ionothermal reactions

As a unique type of solvents, ionic liquids (ILs) have found extensive use in inorganic synthesis owing to their low melting points, nonflammability, excellent chemical and thermal stability, and many other advantages^[87]. Unlike other standard organic solvents, ILs resemble molten salts, making them suitable for ionothermal syntheses—a specialized method where reactions occur

under slightly elevated temperatures in sealed containers, yet clearly below supercritical conditions^[88]. Ionothermal syntheses have garnered significant attention in inorganic chemistry since the breakthrough discovery of ionothermally accessed zeolites in 2004^[89].

As shown in Figure 1.12, the cationic component of ILs typically includes imidazolium, pyridinium, piperidinium, or ammonium moieties, while the anionic part consists of weakly-interacting ions such as $[\text{BF}_4]^-$, $[\text{PF}_6]^-$, or $[\text{B}(\text{CN})_4]^-$, or of halides (abbreviated as X^-)^[90]. Notably, ILs not only act as solvents to dissolve reactants for allowing reactions in solution, they can also serve as counterions for templating the formation of anionic or cationic architectures^[91]. In this thesis, the transformation of chalcogenido metalate compounds with imidazolium-based ionic liquids as a reaction medium is focused on. For clarity, imidazolium-based cations will be abbreviated as $(\text{C}_l(\text{C}_m)\text{C}_n\text{Im})^+$, with Im representing the imidazolium cation, l , m , and n being the numbers of carbon atoms in the alkyl chains attached to the N1, C2, and N3 positions of the imidazolium ring, respectively. The alkyl group can also be replaced by other substituents like a tolyl or an isopropyl group. The wide variety of the substituents attached to the cations, and also their diverse combinations with different anions, creates a vast library of ILs, providing a great deal of variability regarding reaction conditions.

Cations:



Anions:

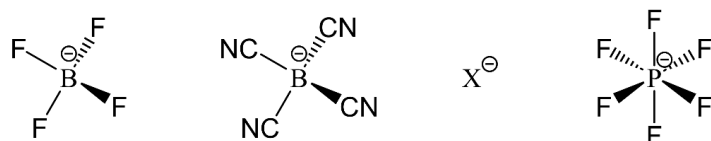
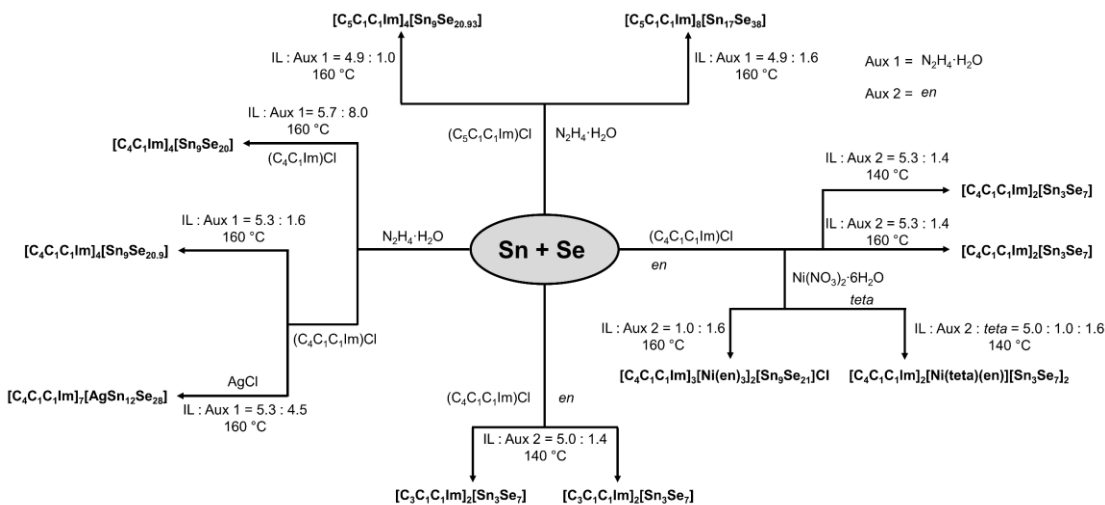


Figure 1.12: Examples of the cations (top) and anions (bottom) that have been combined in ionic liquids used for inorganic syntheses, with emphasis on the imidazolium-based ionic liquids used frequently for the access of chalcogenido metalate.

From a synthetic perspective, the Dehnen group first used ILs in the isolation of chalcogenido metalate-based compounds in 2011, exemplified by the framework structure of 3D- $\{[\text{Sn}_9\text{Se}_{20}]^{4-}\}$ through the transformation of $[\text{SnSe}_4]^{4-}$ in $(\text{C}_4\text{C}_1\text{Im})[\text{BF}_4]$ ^[92]. In the following, contemporary ionothermal approaches for targeting such compounds are presented, which can be categorized into three distinct methods by classifying the use of different kinds of precursors: 1) a combination of elemental chalcogens and metals or salts comprising such elements^[93]; 2) synthesis using microwave-activated precursors^[94]; 3) transformation of starting materials prepared by preceding solid-state-reactions^[95].

1.4.3.1 A combination between elemental chalcogens and metals or salts comprising such elements

In reactions involving elemental selenium and tin in ILs, a series of selenido stannate with different dimensionalities have been synthesized. For example, treating Sn and Se in (C₄C₁C₁Im)Cl or (C₄C₁Im)Cl with a small amount of N₂H₄·H₂O as an auxiliary reagent, various salts comprising new anionic substructures, such as 2D-{[Sn₁₇Se₃₈]⁸⁻}, 3D-{[Sn₉Se_{20.9}]⁴⁻}, and 3D-{[Sn₉Se₂₀]⁴⁻}, have been isolated in their corresponding salts with high yields^[96]. The *in-situ* oxidation of Sn to Sn⁴⁺ and reduction of Se to Se²⁻ under such basic reaction conditions allows for the formation of Sn–Se bonds and assembling complex architectures. In these reactions, N₂H₄·H₂O seems to play a crucial role by promoting the crystallization processes of chalcogenido metalates, as no target compounds were obtained in its absence. In addition, the used ratio of ILs and N₂H₄·H₂O is an important parameter for modifying the anionic substructures, which might be attributed to the varied basicity at different relative amounts of the auxiliary species. Furthermore, replacing N₂H₄·H₂O by organic amines, such as ethylenediamine, yielded six-membered-ring-based 1D-{[Sn₃Se₇]²⁻} or 2D-{[Sn₃Se₇]²⁻} in their respective compounds *via* varying the reaction temperature from 140 °C to 160 °C in (C₄C₁C₁Im)Cl (Scheme 1.1)^[97]. Incorporating Ni(NO₃)₂·6H₂O in the same reaction yielded the latter (C₄C₁C₁Im)₂[Sn₃Se₇]₂, a completely new lamellar substructure comprising [Sn₃Se₇]²⁻ as a building block in (C₄C₁C₁Im)₃[Ni(en)₃]₂[Sn₉Se₂₁]Cl. In this anionic substructure, the [Sn₃Se₇]²⁻ building block assembled into an eight-membered-ring-based network, rather than the most commonly observed six-membered-ring-based substructure, with (C₄C₁C₁Im)⁺ and [Ni(en)₃]²⁺ as cations. Further addition of triethylenetetramine (*teta*) to the reaction led to the isolation of another anionic 2D layer featuring a ten-membered-ring in (C₄C₁C₁Im)₂[Ni(*teta*)(en)][Sn₃Se₇]₂^[98]. Only a few compounds reported thus far out of this reaction system have been discussed (more shown in Scheme 1.1), yet indicating that varying the alkyl chains of ionic liquids, auxiliaries, different stoichiometric ratio of ionic liquids and auxiliaries, and incorporating transition metals are the keys for allowing the formation of new compounds comprising the same building blocks.



Scheme 1.1: Summary of the formation of selenido stannates from the transformation of Sn and Se in ionic liquids, which highlights the importance of different types of ionic liquids, auxiliaries, different stoichiometric ratio of ionic liquids and auxiliaries, temperature, and incorporation of transition metals for modifying the product spectrum.

To synthesize chalcogenido metalates, without the need of *in-situ* redox processes of elemental metals and chalcogens, the use of salts comprising these elements as starting materials has proven to be effective. By reacting In_2S_3 with CuI and thioacetamide in $(\text{C}_4\text{C}_1\text{C}_1\text{Im})\text{Cl}$, pyridine (py), and dimethylamine (DMA), for instance, the Huang group was able to form the largest isolated supertetrahedral cluster, $\text{T5-}[\text{Cu}_5\text{In}_{30}\text{S}_{52}(\text{SH})_2\text{Cl}_2]^{13-}$, in 2012. Detailed adjustments of reaction conditions yielded a set of imidazole-functionalized or purely inorganic T5 clusters, all of which exhibit fluorescence properties^[66].

However, a significant challenge lies in the low reactivity of these starting materials, which typically tend to form more stable bulk materials like M_xCh_y (SnSe or SnSe_2) instead of forming porous chalcogenido (semi)metalates. This inherent preference complicates the selective synthesis of chalcogenido metalates and requires strategic adjustments in reaction conditions to overcome^[96].

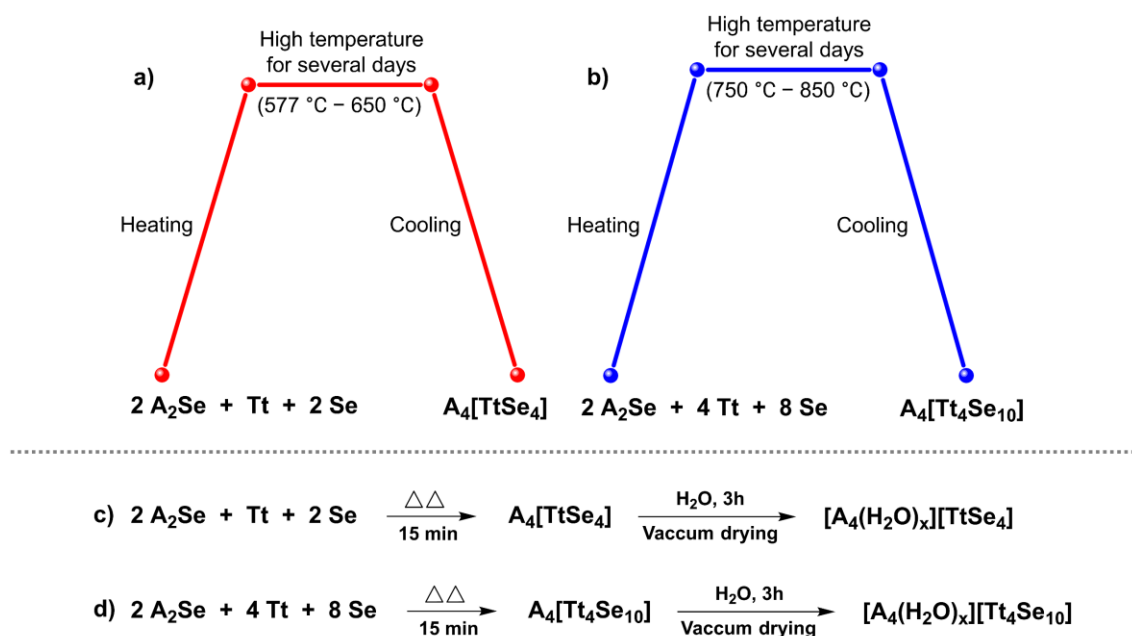
1.4.3.2 Synthesis using microwave-activated precursors

To improve the reactivity of starting materials and allow for a lower activation energy, therefore an accelerated and easier reaction pathway for obtaining chalcogenido metalates, Huang and coworkers employed a microwave-activated approach to prepare reaction precursors from elemental metals, chalcogens, and ILs. These precursors were further transformed into supertetrahedral cluster-based compounds in mixed solvents comprising ILs and amines. For instance, by heating In, S/Se, and $(\text{C}_4\text{C}_1\text{C}_1\text{Im})\text{Cl}$ at 150 °C for 5 min and follow-up treatment at 190 °C for 30 min, a dark-red gel-like precursor was formed. Its reactivity with CdCl_2 in 1-methylimidazole (1-Mim) and 1,5-diazabicyclo[4.3.0]non-5-ene (DBN) led to the formation of T4-type clusters $[\text{Cd}_3\text{In}_{17}\text{Ch}_{31}\text{Cl}_4]^{9-}$, shown to evolve H_2 in photocatalytic reactions^[94]. Replacement of DBN with thiourea in similar reactions, a family of compounds consisting of larger anions $[\text{Cd}_6\text{In}_{28}\text{Ch}_{52}\text{Cl}_{4-x}(\text{Mim})_x]^{q-}$ ($x = 1, q = 11; x = 3, q = 12$) were obtained; there is a metal atom

missing in the cluster core of these anions compared to an ideal T5 cluster, as a result of a charge-balancing effect^[65]. Using CuSCN as the transition metal source instead of CdCl₂, an ideal (without any deficient metal position) T5-[Cu₅In₃₀Ch₅₂Cl₃(im)]¹²⁻ cluster can be achieved. This is due to the fact that the incorporation of lower-valent Cu⁺ decreases the charge of the cluster core. In the absence of transition metals, one moves down from a T5 or T4 cluster to T3 as discussed above, hence a wide spectrum of [In₁₀Ch₁₆Cl₄]⁶⁻ clusters (with varied ratios between S and Se at the chalcogen atom positions) were isolated this way^[99-101]. While significant progress has been made, particularly in synthesizing discrete clusters, there still remains a number of avenues open for using this approach, such as the formation towards network compounds based on these clusters.

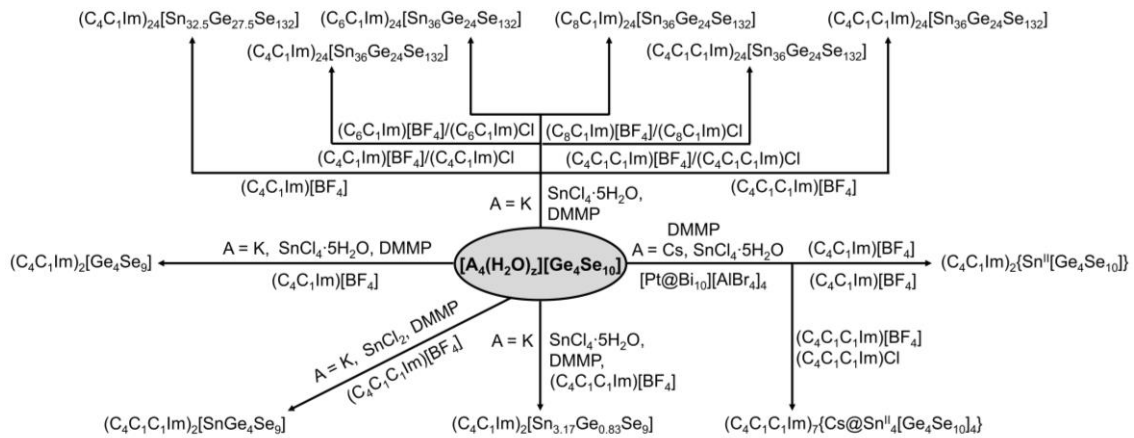
1.4.3.3 Transformation of starting materials prepared by preceding solid-state-reactions

Although the reactivity of the aforementioned microwave-activated precursors is significantly enhanced compared to their elemental counterparts—leading to the synthesis of a library of new compounds—their molecular structure and bonding situations remain unclear. To date, no crystals of these precursors have been isolated, which limits the understanding of their transformation mechanisms. To combine the advantages of these two approaches, it is necessary to find well-defined starting materials, which at the same time already have metal–chalcogen bonds formed. Following this, the third method for targeting supertetrahedral cluster-based chalcogenido metallocates from ILs focuses on using precursors that comprise either T1- or T2-type binary cluster anions and alkali metal cations, which can be dissolved in highly polar, protic solvents like MeOH, or in ILs^[102,103]. These salts are known and can be obtained from solid-state processes by reacting A₂Ch, elemental metal, and Ch in silica ampoules at a program-controlled temperature (Scheme 1.2a,b, with the synthesis of A₄[Tt₄Se₁₀] and A₄[Tt₄Se₁₀] as examples)^[52,104]. An alternative, but more efficient approach involves using an oxygen/propyl burner to melt the reagents and allow for their diffusion in the melt within 15 min. It can also be applied for synthesizing T1- or T2-cluster-based precursors (Scheme 1.2c,d). While single crystalline products are only rarely formed this way due to the rapid process and cooling rate, the materials are of a suitable crystallinity for powder X-ray diffraction (PXRD) to confirm the successful syntheses of the target compounds as well as their corresponding phase purity.



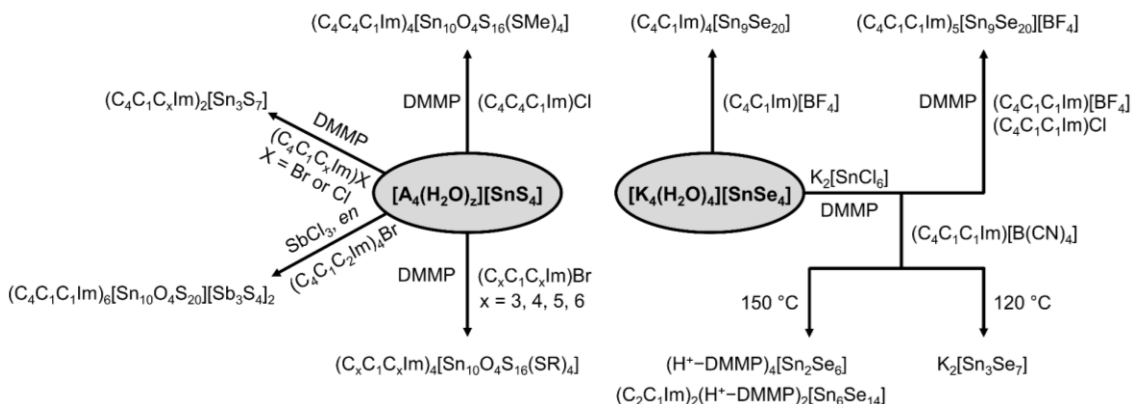
Scheme 1.2: Schematic illustration of the syntheses of well-defined salts $\text{A}_4[\text{TtSe}_4]$ and $\text{A}_4[\text{Tt}_4\text{Se}_{10}]$ via common solid-state reaction (a–b), and an alternative approach using an oxygen/propyl burner within a relatively shorter reaction duration (c–d).

To mimic the composition of zeolites, previous work in the research group has focused on utilizing salts containing group 14 and 16 elements as precursors, with a general formula of $\text{A}_x[\text{Tt}_y\text{Ch}_z]$. These salts and their reactivities in ILs were investigated at various conditions. For example, in $(\text{C}_4\text{C}_1\text{Im})[\text{BF}_4]$ or $(\text{C}_4\text{C}_1\text{C}_1\text{Im})[\text{BF}_4]$, treating $[\text{K}_4(\text{H}_2\text{O})_3][\text{Ge}_4\text{Se}_{10}]$ with $\text{SnCl}_4 \cdot 5\text{H}_2\text{O}$ in the presence of 2,6-dimethylmorpholine (DMMP) yielded the largest discrete main-group-element-based polyanions in $(\text{C}_4\text{C}_1\text{Im})_{24}[\text{Sn}_{36}\text{Ge}_{24}\text{Se}_{132}]$ and $(\text{C}_4\text{C}_1\text{C}_1\text{Im})_{24}[\text{Sn}_{36}\text{Ge}_{24}\text{Se}_{132}]^{[95]}$. By systematically varying the length of the alkyl chains of the imidazolium cations, the arrangement of the so-called “zeoball” anions can be altered within the unit cell and stabilized in different configurations. Examples for corresponding salts are $(\text{C}_6\text{C}_1\text{Im})_{24}[\text{Sn}_{36}\text{Ge}_{24}\text{Se}_{132}]$ and $(\text{C}_6\text{C}_1\text{Im})_{24}[\text{Sn}_{36}\text{Ge}_{24}\text{Se}_{132}]^{[105]}$. Further variations in reaction conditions, such as using other molar ratio of $\text{SnCl}_4 \cdot 5\text{H}_2\text{O} / [\text{K}_4(\text{H}_2\text{O})_3][\text{Ge}_4\text{Se}_{10}]$, employing different organic solvents or additives, like SnCl_2 instead of $\text{SnCl}_4 \cdot 5\text{H}_2\text{O}$, allowed for the formation of more diverse anionic substructures in $(\text{C}_4\text{C}_1\text{Im})_2[\text{Ge}_4\text{Se}_9]$, $(\text{C}_4\text{C}_1\text{C}_1\text{Im})_2[\text{Ge}_4\text{Sn}^{\text{II}}\text{Se}_{10}]$, $(\text{C}_4\text{C}_1\text{Im})_4[\text{Sn}_9\text{Se}_{20}]$, $(\text{C}_4\text{C}_1\text{C}_1\text{Im})_8[\text{Sn}_{18}\text{Se}_{40}]$, to name but a few (Scheme 1.3)^[106].



Scheme 1.3: Summary of the formation of selenido germanates by transformation of $[A_4(H_2O)_z][GeSe_{10}]$ ($A = K$ or Cs) in ionic liquids.

Treatment of the salts $[A_4(H_2O)_z][SnS_4]$ ($A = Li$, $z = 13$; $A = Na$, $z = 14$) in $(C_4C_1C_1)[BF_4]/Cl$ led to the first methylation of the known *pseudo*-T3-type cluster $[Sn_{10}O_4S_{20}]^{8-}$ in an ionothermal approach. The methylated versions of $[Sn_{10}O_4S_{16}(SMe)_4]^{4-}$ in a series of compounds $[C_4C_1C_1Im]_{4+x}[Sn_{10}O_4S_{16}(SMe)_4][An]_x$ (An = anion) possess only half of the charges of the purely inorganic analog, however, these compounds cannot be dissolved in any standard solvents^[45,107]. Considering that typically compounds of similar polarity dissolve in similarly polar substances, the research group has further propylated, butylated, pentylated, and hexylated the same cluster by using symmetrical ILs of the type $(C_lC_1C_1Im)Br$ ($l = 3; 4; 5; 6$) as solvents and alkylation agents. In these reactions, the alkyl chain at the N position is transferred to the corner S atoms and allowed the construction of $[Sn_{10}O_4S_{16}(SPr)_4]^{4-}$, $[Sn_{10}O_4S_{16}(SBu)_4]^{4-}$, $[Sn_{10}O_4S_{16}(SPn)_4]^{4-}$, and $[Sn_{10}O_4S_{16}(SHex)_4]^{4-}$, respectively (Scheme 1.4). The corresponding salts are soluble in CH_3CN and remain intact, not only in the liquid but also in the gas phase, as confirmed by Sn -NMR and ESI-MS^[43,44].



Scheme 1.4: Summary of the formation of selenido stannates by transformation of $[A_4(H_2O)_z][SnCh_4]$ ($A = Li, Na, or K, Ch = S, or Se$) in ionic liquids.

In contrast to the first two synthetic routes for the formation of chalcogenido metalates in ILs, there are several advantages using such salts as precursors, as illustrated in Figure 1.13a) these starting materials are all atomically well-defined and thus the reaction mechanism might possibly be revealed using *in-situ* characterizations; b) they are soluble in ionic liquids at subcritical pressure and relatively low temperature; c) Tt–Ch bonds are already formed in such salts, greatly reducing the activation energies for structural transformations; d) given that all these salts are charge-balanced by alkali metal cations, their use also serves as a platform to investigate the *in-situ* uptake of alkali metal ions by chalcogenido metalates. Considering these advantages, in the present thesis, the third route (as introduced in chapter 1.4.3.3) for transforming purely inorganic T1- or T2-type cluster-based salts into more complex chalcogenido metalate substructures in ionic liquids is focused on. The fundamental properties of the obtained products have been also studied from different perspectives.

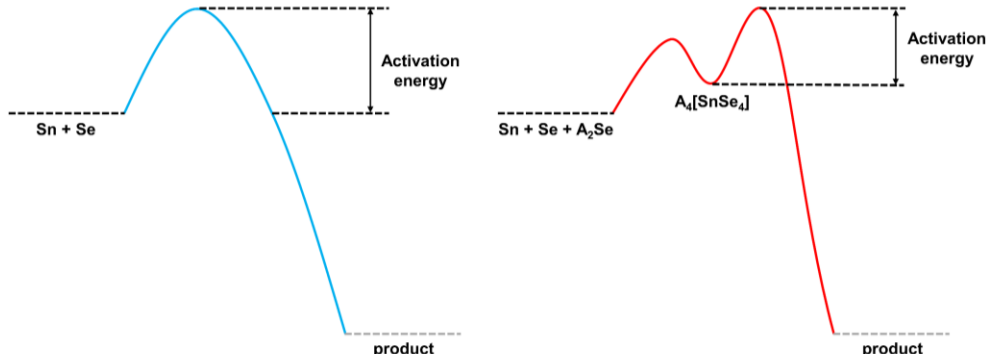
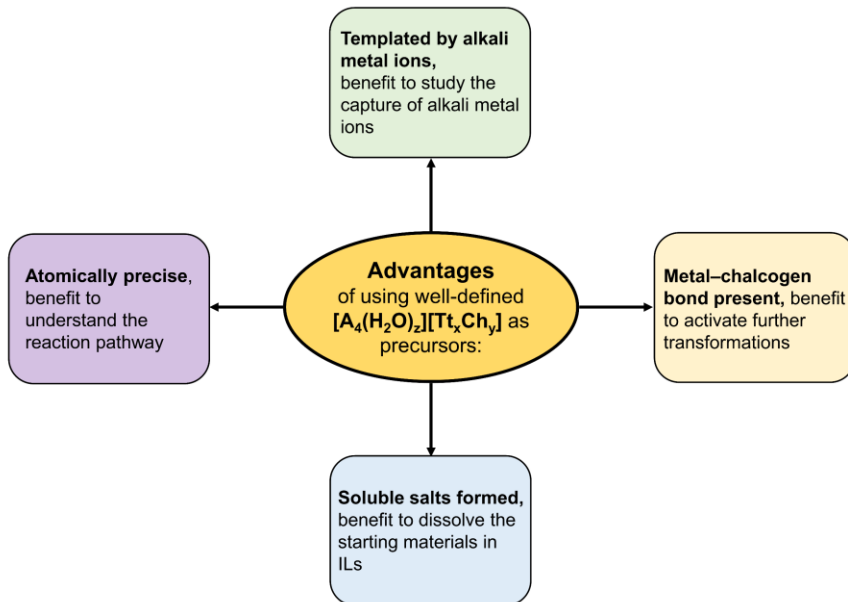


Figure 1.13: Summary of the advantages of using well-defined salts $[A_4(H_2O)_z][T_{tx}Ch_y]$ as starting materials in the syntheses of chalcogenido metalate compounds (top), with a particular emphasis on the reduction of the activation energy for structural transformation (bottom, with the schematic illustration of the differences of reacting elemental Sn and Se or a preformed single-source precursor $A_4[SnSe_4]$ as an example).

1.5 Applications of chalcogenido metalate compounds

In addition to their structural beauty, chalcogenido metalate compounds are also attractive in materials chemistry due to their application potential across diverse areas, such as ion-exchange, gas separation, ionic conductivity, and photocatalysis. Given the porous nature of compounds exhibiting chalcogenido metalate networks, for instance, the zeolitic T2- $\{Tr_{4-x}Tt_x\}$ -cluster-based UCR-20, is confirmed to be a potential ion-exchange material. The organic counterions of UCR-20 are exchangeable upon treating the solid sample with an aqueous solution of CsCl. Because of the relatively “soft” inner surfaces of zeolitic UCR-20, it exhibits high selectivity for capturing relatively “soft” alkali metal ions, like Cs^+ (the exchanged product is denoted as $Cs@UCR-20$), even

from solutions with very low Cs^+ concentrations (Figure 1.14a)^[108]. $\text{Cs}@\text{UCR-20}$ can further exchange Cs^+ with Na^+ , K^+ , and Rb^+ in their concentrated aqueous solutions, forming $\text{A}@\text{UCR-20}$ ($\text{A} = \text{Na}^+, \text{K}^+, \text{Rb}^+$). The latter effectively separate CO_2/N_2 due to the higher affinities of $\text{A}@\text{UCR-20}$ towards the polar $\text{C}=\text{O}$ bond in CO_2 as compared to the $\text{N}\equiv\text{N}$ bond in N_2 (Figure 1.14b,c)^[109]. Additionally, the size-matched windows of $\text{Cs}@\text{UCR-20}$ allows rapid encapsulation of smaller organic dye molecules, like acridine orange (AO) within its cavities, whereas larger molecules, like rhodamine B (RhB), can only be adsorbed onto the outer surface of $\text{Cs}@\text{UCR-20}$ ^[110]. Following this concept, composites of AO-encapsulated and RhB-covered UCR-20 was fabricated (denoted as [RhB-(AO@UCR-20)]). Given the semiconductor-derived nature of UCR-20, its host framework serves to absorb ultraviolet light and emits near the absorption wavelength of AO molecules, which in turn further excite the incorporated AO molecules. This leads to the emission of AO guests at around 525 nm, which serves to excite the RhB molecules (Figure 1.14d). Therefore, the supertetrahedral cluster-based framework serves as a platform for studying cascade-type fluorescence resonance-energy transfer processes. Such a phenomenon had not been observed in oxide zeolites due to their insulating nature stopping the (potential) energy-transfer process at the first step.

Furthermore, purely alkali metal cation templated supertetrahedral chalcogenido metalate architectures, such as compounds $\text{Na}_4[\text{In}_4\text{Se}_8]$ and $\text{Na}_{10}[\text{Cu}_3\text{In}_{17}\text{S}_{33}]$, were also isolated using Na_2Ch ($\text{Ch} = \text{S}$ or Se) as sources of inorganic SDAs. The highly polarized inner surfaces of 3D- $\{[\text{In}_4\text{Se}_8]^{4-}\}$ and 3D- $\{[\text{Cu}_3\text{In}_{17}\text{S}_{33}]^{10-}\}$ frameworks allow a smooth transport of “hard” Li^+ and Na^+ ions through ordered pores, achieving good ionic conductivities up to $0.018 \Omega^{-1} \text{ cm}^{-1}$ (Figure 1.14e)^[111]. The ionic conductivities of chalcogenido metalates embedding larger, “soft” alkali cations (*i.e.* K^+ , Rb^+ , and Cs^+) have been rarely investigated, because the relatively high affinity between the chalcogenido metalates’ inner surfaces and larger alkali cations would lead to low ionic conductivities.

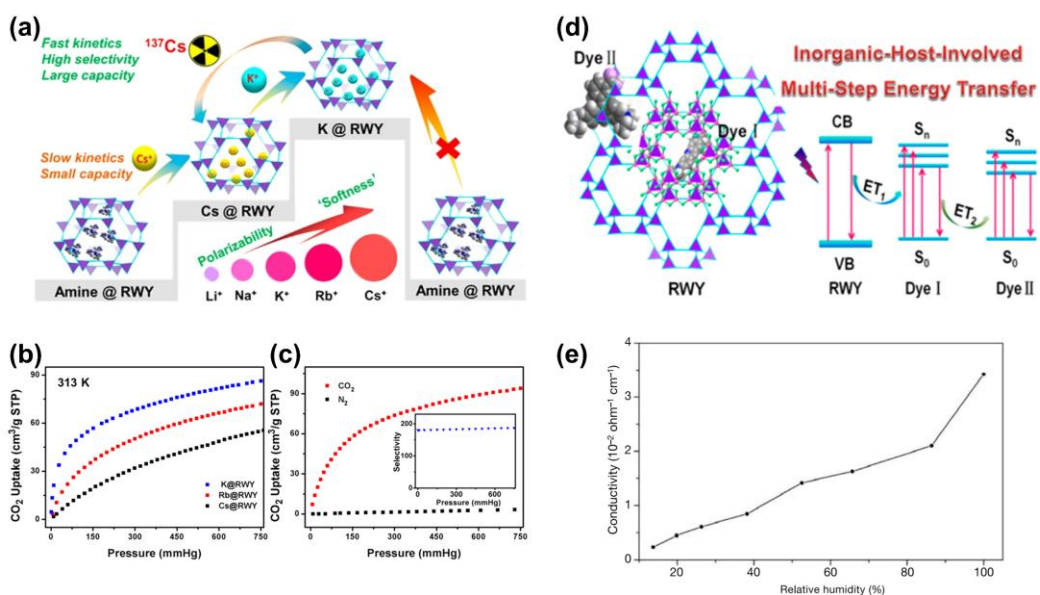


Figure 1.14: Applications of porous chalcogenido metalate-based framework compounds in the removal of Cs^+ (a), gas absorption/separation (b–c), host-guest chemistry for energy transfer (d), and fast-ion conduction (e).

In addition to exploring the applications of chalcogenido metalate framework compounds, studies on the applications of molecular chalcogenido metalates have also emerged. For instance, in the discrete core-missing T5-type cluster $[\text{Cd}_6\text{In}_{28}\text{S}_{52}(\text{SH})_4]^{12-}$, incorporation of a Cu(I) atom at the core-deficient position allows for the formation of a $[\text{CuCd}_6\text{In}_{28}\text{S}_{52}(\text{H}_2\text{O})_4]^{7-}$ molecule, resulting in significantly improved photoelectric properties of the solid state compared to the parent compound (Figure 1.15a)^[112]. Moreover, introducing a single Mn(II) into the core-missing location shifts the emission center from 490 nm of the parent compound to 630 nm of the Mn-doped variant, as evidenced by their photoluminescence spectra (Figure 1.15b)^[113]. Additionally, chalcogenido metalates also find applications in photocatalysis. For example, dissolving single crystals of a salt of the T5-type cluster $[\text{Cu}_5\text{In}_{30}\text{S}_{52}(\text{SH})_4]^{13-}$ in a DMF solution of LiBr results in a homogenous solution containing $[\text{Cu}_5\text{In}_{30}\text{S}_{52}(\text{SH})_4]^{13-}$; the undecomposed transfer of crystals to nanoparticles in solution was confirmed by ESI-MS. Importantly, these cluster-based aggregates can sensitize TiO_2 electrodes due to their excellent light absorption property, causing significantly improved photocurrent conversion efficiencies than that of unmodified TiO_2 electrodes (Figure 1.15c)^[114]. And this type of cluster-based compounds is also capable of producing H_2 *via* light irradiation. Crystals of compounds $(\text{C}_4\text{C}_1\text{C}_1\text{Im})_9[\text{Cd}_3\text{In}_{17}\text{S}_{31-x}\text{Se}_x\text{Cl}_4]$ ($x = 0, 18$, and 31) lead to a moderate photocatalytic H_2 production upon Xe-lamp irradiation. However, once the solid crystals are dissolved in DMSO and form homogenous solutions containing cluster-based aggregates, the H_2 evolution performance is improved due to larger number of exposed catalytic sites upon transitioning from micrometer-sized solid crystals to nanometer-sized dispersed aggregates (Figure 1.15d)^[94]. By loading these aggregates onto the surfaces of different materials, such as graphitic carbon nitride or a covalent organic framework, even better photocatalytic performance is achieved owing to the formation of a heterostructure between the two components that facilitates the electron-hole separation *via* irradiation^[115,116]. Overall, both network and molecular chalcogenido metalates are attractive because of their structural beauty and application potential in inorganic and materials chemistry.

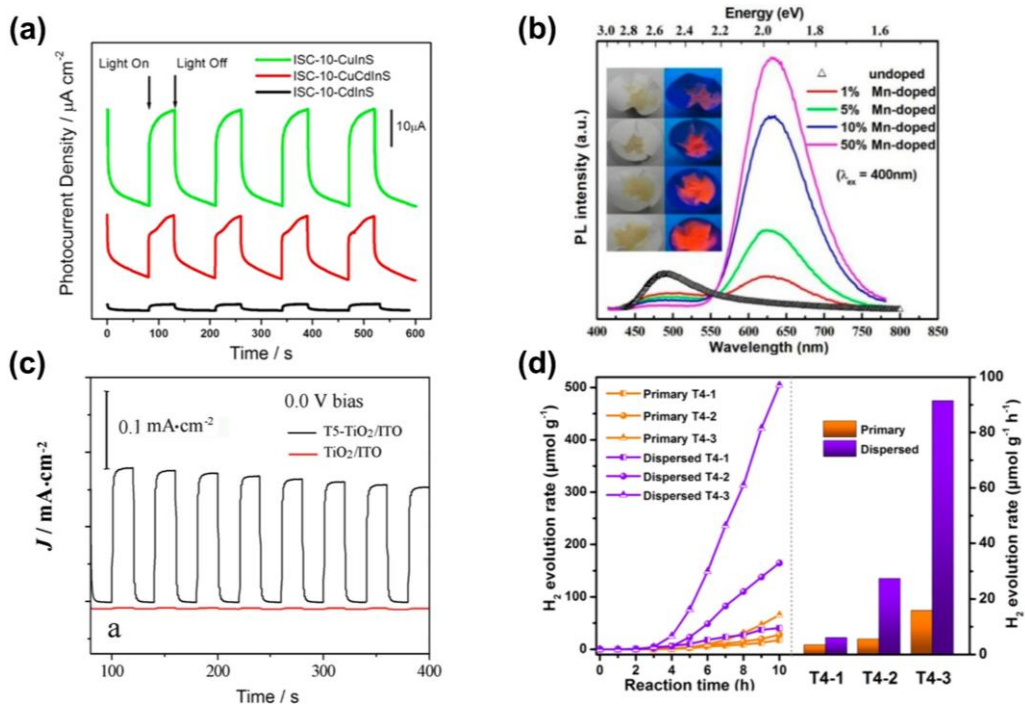


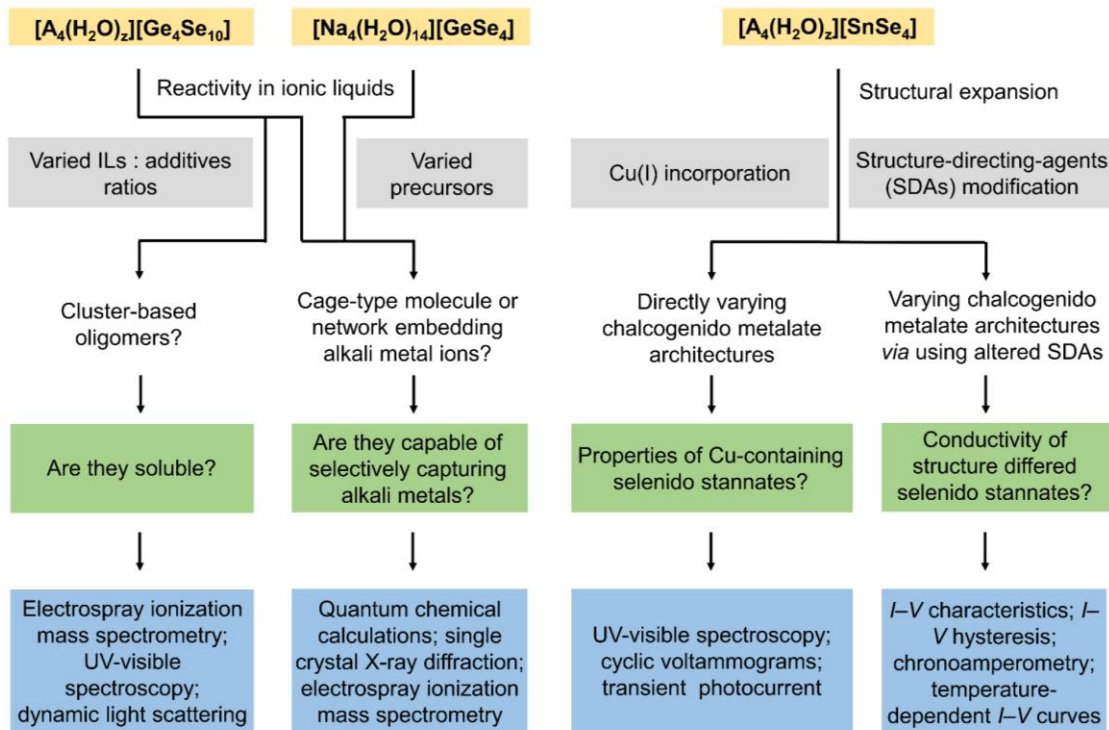
Figure 1.15: Applications of molecular chalcogenido metalates in solid-state or in their solution. Photoelectric response of compounds comprise $[\text{Cd}_6\text{In}_{28}\text{S}_{52}(\text{SH})_4]^{12-}$ or $[\text{CuCd}_6\text{In}_{28}\text{S}_{52}(\text{H}_2\text{O})_4]^{7-}$ cluster anions (a), emission spectra of compounds contain $[\text{Cd}_6\text{In}_{28}\text{S}_{52}(\text{SH})_4]^{12-}$ or Mn-doped anions (b), photoelectric response of TiO₂/ITO or T5 cluster decorated TiO₂/ITO (c), and H₂ evolution property catalyzed by compounds $(\text{C}_4\text{C}_1\text{C}_1\text{Im})_9[\text{Cd}_3\text{In}_{17}\text{S}_{31-x}\text{Se}_x\text{Cl}_4]$ or their aggregates in DMSO (d).

2 Research objectives

In the last three decades, a library of chalcogenido metalate network compounds has been obtained, however, there have been far fewer studies on chalcogenido metalate oligomers, leading to limited understanding on how these cluster subunits behave in solutions. Additionally, structural expansion of chalcogenido metalate family is desired for further extending their diversity and application potentials. This thesis aims to address these challenges with the following steps:

- 1) Syntheses of selenido germanate cluster-based oligomers *via* cluster condensation
- 2) Investigating the solubilities of salts comprising these oligomers in standard solvents (such as DMF), and their optical properties in solutions
- 3) Syntheses of oligomeric cage-type molecules embedding alkali metal ions for further charge reduction, and study the selectivity for different alkali metal ions
- 4) Variation of chalcogenido metalate architectures through manipulating anionic clusters with Cu(I) ions
- 5) Variation of chalcogenido metalate architectures through modifying the structure-directing agents
- 6) Comprehensive study of fundamental properties, such as photocurrent measurement, current-voltage characteristics, or optical properties of corresponding compounds

Scheme 2.1 illustrates the general considerations mentioned above.



Scheme 2.1: Schematic illustrations to the research objectives of this thesis.

3 Results and Discussion

3.1 Defined oligomers of supertetrahedra-based selenido germanate clusters

The results of this chapter are published in the following journal:

Zhou Wu, Isabell Nußbruch, Simon Nier, and Stefanie Dehnen*, Ionothermal Access to Defined Oligomers of Supertetrahedral Selenido Germanate Clusters. *JACS Au* **2022**, 2, 204–213.

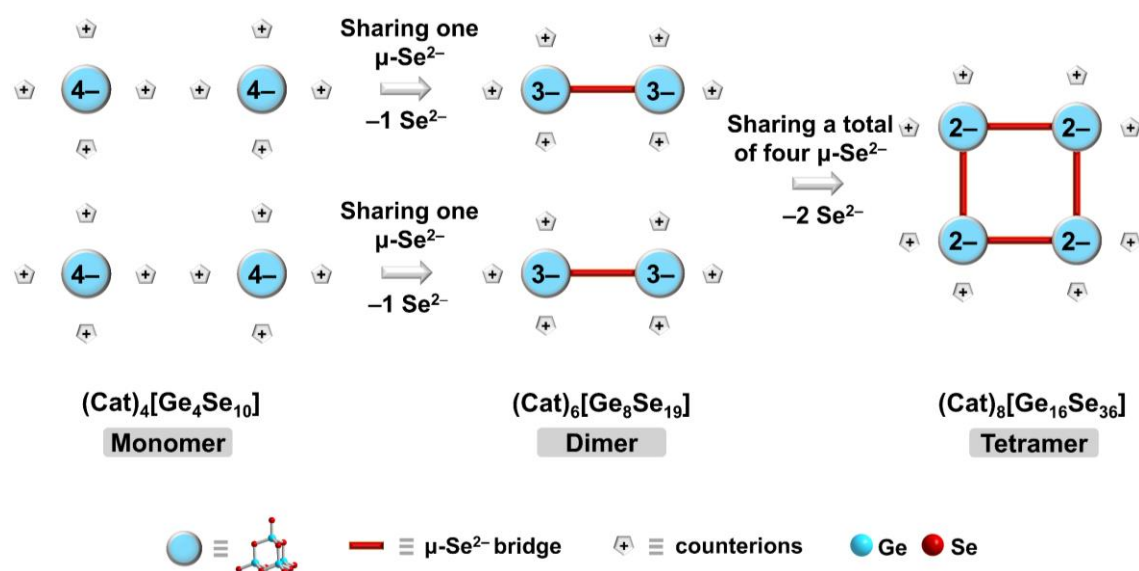
3.1.1 Introduction

Chapter 1 highlighted the enduring interest in supertetrahedral chalcogenido (semi)metalate clusters within inorganic and material chemistry for many years owing to their outstanding physical and chemical properties. However, a critical drawback of studying corresponding compounds has been the lack of control in assembling the supertetrahedral units, which are known as either highly charged monomeric cluster anions or lower charged, yet extended, anionic substructures of linked clusters. As a result, research and applications have largely focused on their behavior in the solid state or as suspensions^[117]—in many cases owing to the inherently high anionic charges and thus low solubility of salts of discrete (monomeric) clusters on the one hand^[118], and the inherent insolubility of one-, two- or three-dimensional cluster networks in their respective salts on the other hand^[119]. Oligomeric assemblies have not yet been realized for purely inorganic clusters. In order to fabricate functional nanomaterials, e.g., for opto-electronic devices, by processing such supertetrahedral clusters, there has been an increasing interest in dissolving such materials in standard solvents. However, only a few studies about dissolving ligand-free clusters have been reported, and most of them required the use of highly polar solvents like water or methanol owing to the relatively strong electrostatic interactions between anionic clusters and cationic counterions^[120]. Overcoming these interactions is crucial for dissolving such compounds in standard solvents, thus for expanding the applications of materials based on supertetrahedral chalcogenido (semi)metalate units, but at the same time challenging. As discussed in Chapter 1, alkylating supertetrahedral clusters or substituting “harder” sulfide atoms with “softer” selenide atoms in supertetrahedral chalcogenido metalate clusters allows better solubilities in standard solvents. While covering these clusters with organic ligands can increase their solubility^[121,122], it often comes at the cost of widening the bandgap or quenching luminescent properties—drawbacks that require new approaches.

As an approach to further increase the solubility of supertetrahedral selenide clusters, a strategy to (a) replace alkali metal cations with organic cations in an ionothermal approach and (b) apply conditions that allow a controlled and limited aggregation of the anionic molecules, as an alter-

native to the generation of (insoluble) extended networks was selected. The assembly of supertetrahedral clusters into oligomers of a finite size, with a corresponding decrease of the average negative charge per cluster unit, has not yet been reported in the literature to date.

Based on this strategy, a T2-type $[\text{Ge}_4\text{Se}_{10}]^{4-}$ cluster monomer is selected as a building unit, which was formed in ionic liquids and subsequently condensed into dimers or tetramers (Scheme 3.1) at distinct compositions of the reaction medium. Key to this was the thorough choice of an adequate relative amount of 2,6-dimethylmorpholine (DMMP) to be added as an auxiliary agent for the connection of chalcogenido germanate units. This approach highlights the innovative use of ILs to control the aggregation of supertetrahedral clusters, thereby expanding the potential applications by increasing their solubility in organic solvents.



Scheme 3.1: Schematic illustration of the concept of lowering the average charge of supertetrahedral chalcogenide cluster anions by formation of finite cluster oligomers.

In a first step, two of the $[\text{Ge}_4\text{Se}_{10}]^{4-}$ units form a dimer-like assembly by sharing one of the selenide ligands at the cluster corners as μ -bridges, under release of one Se^{2-} anions per newly formed dimer and a corresponding decrease of the anionic charge per cluster unit. Further condensation of two such dimers yields a tetramer-like assembly by sharing a total of four $\mu\text{-Se}^{2-}$ ligands upon release of another two Se^{2-} anions. This leads to a significantly lower charge per cluster building unit, and a moderate total negative charge of the tetrameric anions. The addition of an auxiliary such as DMMP controls this aggregation process. The optimal amount of DMMP leads to the formation of discrete cluster units rather than extended network structures. Under specific amounts of DMMP, an unprecedented large zigzag chain forms as an extended anionic substructure. These findings underscore the importance of precise reaction control for the targeted formation of cluster oligomers.

By following this approach, the first ligand-free chalcogenido (semi)metalate cluster-based dimer and its extension into a square-planar tetramer, $[\text{Ge}_{16}\text{Se}_{36}]^{8-}$, were obtained and the latter repre-

sents the largest discrete binary chalcogenido (semi)metalate cluster by now. It is also demonstrated that such oligomers readily dissolve in common solvents like DMF without decomposition, which was proven by mass spectrometry and optical absorption spectroscopy of crystals and their solutions.

3.1.2 Syntheses and crystal structures

The synthesis of five new selenido germanate compounds, including two polymorphs of the same anionic substructure, was achieved by the treatment of $[K_4(H_2O)_3][Ge_4Se_{10}]^{[52]}$ in the ionic liquid $(C_2C_1Im)[B(CN)_4]$ and DMMP (**2b**, **3**, **4**) or by the treatment of $[Na_4(H_2O)_{14}][GeSe_4]^{[123]}$ in a 10:1 mixture of $(C_2C_1Im)[B(CN)_4]$ and DMMP (**1**) or in a 1:1 mixture of $(C_2C_1Im)[B(CN)_4]$ and $(C_2C_1Im)[BF_4]$ (**2a**) at 150 °C for 3 days. It should be noted that all of the syntheses were sensitive to the reaction temperature: crystals were exclusively obtained upon treatment at 150°C, while no identifiable compounds were observed at lower (120 °C) or higher (180 °C) reaction temperatures. The most important parameters, however, to be varied for obtaining the different products was the amount of the auxiliary DMMP relative to the amount of ionic liquid used. The results are summarized in Figure 3.1, in comparison with reported products of similar reactions, of which highlighted the importance of using $(C_2C_1Im)[B(CN)_4]$ as solvent and source of the SDA in these reactions and at the same time clearly demonstrated the ratios of ILs relative to DMMP are the key to modifying the connection of T2-type selenido germanate cluster units.

As depicted in Figure 3.1, most reactions in this study were undertaken with $[K_4(H_2O)_3][Ge_4Se_{10}]$ as precursors. With the only exception being pale-yellow crystals of a new salt comprising the same discrete $[Ge_4Se_{10}]^{4-}$ anion, $(C_2C_1Im)_4[Ge_4Se_{10}]$ (**1**), by ionothermal treatment of $[Na_4(H_2O)_{14}][GeSe_4]$ in 500 μ L of $(C_2C_1Im)[B(CN)_4]$ in the presence of 50 μ L of DMMP. Increasing the relative amount of DMMP led to lower yields. The molecular structure of the anion with label scheme is shown in Figure 3.2.

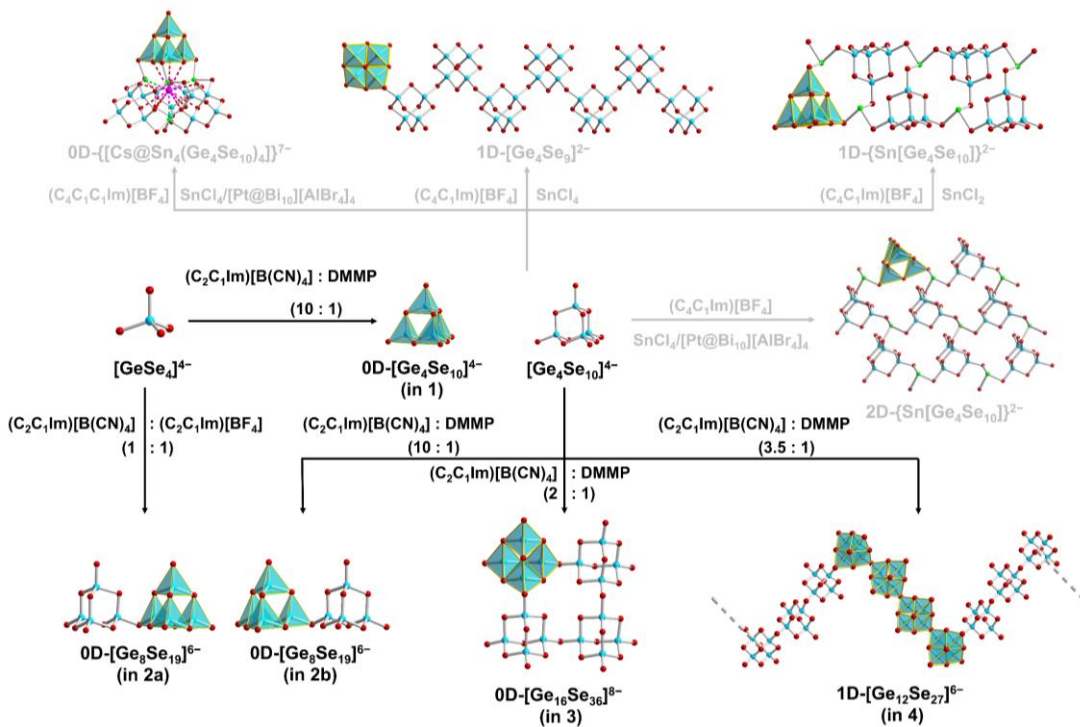


Figure 3.1: Survey of the formation and use of $[\text{Ge}_n\text{Se}_m]_n^{4-}$ anions for the synthesis of more complex anionic substructures in known compounds (top, gray arrows and formulas) and in compounds **1**, **2a**, **2b**, **3**, and **4** reported in this work (center and bottom, black arrows and formulas; all reactions done at 150°C). Relative amounts are given as v:v ratios. For more details, see the Experimental Section.
Crystallographically indistinguishable Ge and Se atoms were assigned based on their characteristic coordination modes.

Compound **1** crystallizes in the tetragonal crystal system, space group type $P4_2/n$ (No. 86) with two formula units per unit cell ($V = 2251.9(5)$ \AA^3 ; Figure 3.2). The asymmetric unit consists of one germanium atom, two and half selenium atoms, and one $(\text{C}_2\text{C}_1\text{Im})^+$ cation. Considering the anionic nature of the cluster units, the accessible void space is filled with the ionic liquid counterions. Structurally speaking, the $[\text{Ge}_4\text{Se}_{10}]^{4-}$ anion is condensed from four $[\text{GeSe}_4]^{4-}$ tetrahedrons by sharing three quarters of the Se^{2-} ligands, and therefore losing six Se^{2-} in total upon such a condensation procedure. Therefore, the negative charges of the four $[\text{GeSe}_4]^{4-}$ are well-reduced from 16^- to 4^- in a $[\text{Ge}_4\text{Se}_{10}]^{4-}$ anion. The $\text{Ge}-(\mu\text{-Se})$ bond lengths ($2.3674(12) - 2.3771(11)$ \AA) and $\text{Ge}-\text{Se}_{\text{terminal}}$ bond lengths ($2.2604(13)$ \AA) are within the range of reported values^[106,124,125].

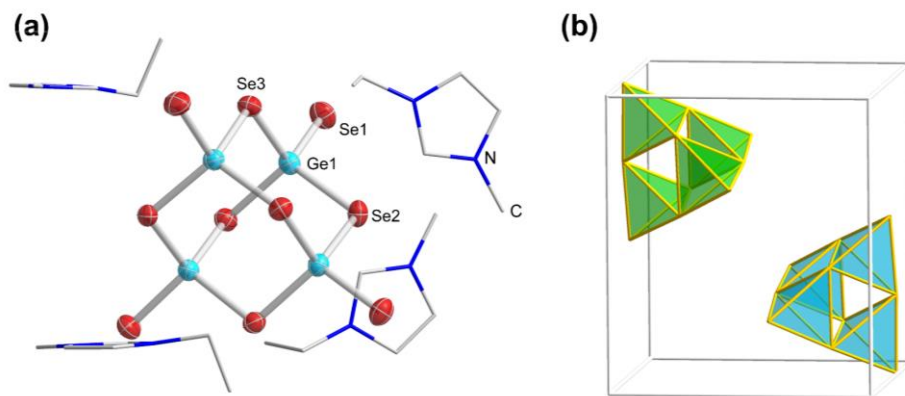


Figure 3.2: Structure of the anion and four nearest anions in compound **1** (a). View of the unit cell of compound **1** (ionic liquid counterions are omitted for clarity, the cluster tetrahedrons are shown in two different colors due to their altered orientations) (b). Ge and Se atoms (with atom labelling scheme) are shown as thermal ellipsoids at the 50% probability level; the atoms of the imidazolium counterions are given in wired-mode. H atoms are omitted for clarity.

By treatment of $[\text{Na}_4(\text{H}_2\text{O})_{14}][\text{GeSe}_4]$ in a mixture of $250 \mu\text{L}$ of $(\text{C}_2\text{C}_1\text{Im})[\text{B}(\text{CN})_4]$ and $250 \mu\text{L}$ of $(\text{C}_2\text{C}_1\text{Im})[\text{BF}_4]$ without addition of DMMP, the first dimeric structure of a ligand-free supertetrahedral cluster in $(\text{C}_2\text{C}_1\text{Im})_6[\text{Ge}_8\text{Se}_{19}]$ (**2a**; Figure 3.3a) was isolated. A polymorph of this compound was also generated starting from $[\text{K}_4(\text{H}_2\text{O})_3][\text{Ge}_4\text{Se}_{10}]$, by treatment in $(\text{C}_2\text{C}_1\text{Im})[\text{B}(\text{CN})_4]$ in the presence of a very small amount of DMMP (v:v = 10:1; Figure 3.3c). The polymorphs **2a** and **2b** crystallize in the triclinic crystal system, space group type $P\bar{1}$ (No. 2, **2a**) or in the monoclinic crystal system, space group type $P2_1/c$ (No. 14, **2b**) with two (**2a**, $V = 3735.5(3) \text{ \AA}^3$; Figure 3.3b) or four (**2b**, $V = 7524.9(9) \text{ \AA}^3$; Figure 3.3d) formula units per unit cell, respectively. As shown in Figure 3.3a,c, both anionic parts of the asymmetric unit of **2a** and **2b** contain eight germanium atoms, nineteen selenium atoms, charge balanced by six surrounding imidazolium cations. In the anionic substructures of **2a** and **2b**, two T2 clusters are linked *via* sharing one $\mu\text{-Se}^{2-}$ ligand, while three terminal Se^{2-} ligands are retained per building unit. Again, Ge–($\mu\text{-Se}$) bond lengths ($2.3296(19) - 2.4127(21) \text{ \AA}$) and Ge–Se_{terminal} bond lengths ($2.2388(21) - 2.2640(30) \text{ \AA}$) are close to the expected range. Another dimer of supertetrahedral clusters in $(\text{H}^+\text{-DBN})_6[\text{In}_{20}\text{S}_{33}(\text{DBN})_6]$ has recently been reported^[126,127]. However, in this case, six of the terminal cluster positions were occupied by organic substituents, while the dimeric assembly in **2** has a purely inorganic composition.

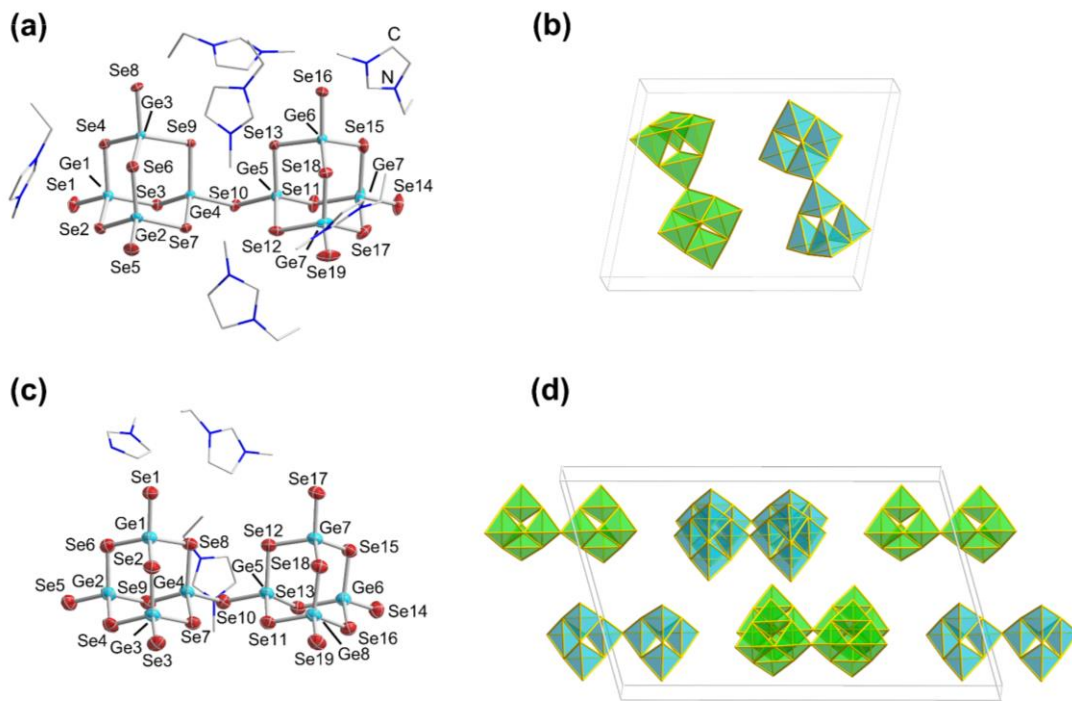


Figure 3.3: Molecular structure of the anion and nearest cations in compound **2a** (a). View of the unit cell of compound **2a** (b). Molecular structure of the anion and a part of the cations in compound **2b** (c). View of the unit cell of compound **2b** (d), given that those molecules are shared with the adjacent unit cells, only four of the anions observed within the unit cell in average. Ge and Se atoms (with atom labelling scheme) are shown as thermal ellipsoids at the 50% probability level; the atoms of the imidazolium counterions are given in wired-mode; the cluster tetrahedrons are shown in two different colors due to their altered orientations. H atoms are omitted for clarity.

By significantly increasing the amount DMMP relative to $(C_2C_1\text{Im})[B(\text{CN})_4]$ in the reaction mixture used for the preparation of compound **2b**, from 10% to 50% (v:v) and thus the largest relative amount of the auxiliary used in this study, it was possible to synthesize $(C_2C_1\text{Im})_8[\text{Ge}_{16}\text{Se}_{36}]$ (**3**). Compound **3** crystallizes in the monoclinic crystal system, space group type $C2/c$ (No. 15) with four formula units in the unit cell ($V = 11596.6(18) \text{ \AA}^3$; Figure 3.4). The anionic substructure of the asymmetric unit consists of eight germanium atoms, and eighteen selenium atoms. Compound **3** comprises an unprecedented tetramer of a chalcogenido (semi)metalate cluster and at the same time the largest discrete and ligand-free binary chalcogenido (semi)metalate cluster; larger species, like the T5-type $\{\text{In}_{34}\text{S}_{54}\}$ moiety^[128], were usually integrated in framework structures so far, and the only known (pseudo)-tetramer of T2-type clusters included linkage by Sn^{2+} ions and inclusion of a Cs^+ atom, $[\text{Cs}@\text{Sn}_4(\text{Ge}_4\text{Se}_{10})_4]^{7-}$ ^[124]. The molecular structure of the anion in compound **3** is illustrated in Figure 3.4. Ge–(μ -Se) bond lengths (2.3288(30) – 2.3978(33) \AA) and Ge–Se_{term} bond lengths (2.2296(35) – 2.2425(38) \AA) match those of the reported ones, and also the ones observed in compounds **1** and **2**.

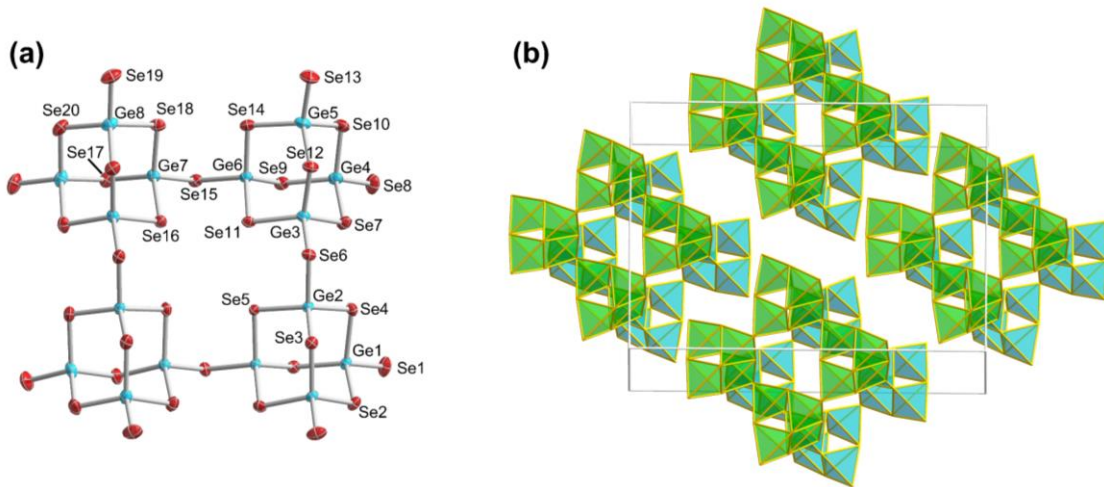


Figure 3.4: Molecular structure of the anion in compound **3** with atom labelling scheme (a). View of the unit cell of compound **3** (b), given that those molecules are shared with the adjacent unit cells, only four of the anions observed within the unit cell in average. Ge and Se atoms are shown as thermal ellipsoids at the 50% probability level; the imidazolium counterions are omitted for clarity; the cluster tetrahedrons are shown in two different colors due to their altered orientations.

To achieve the unique square-planar structure, one T2 cluster shares two corner Se^{2-} ligands with two neighboring clusters. However, instead of extending their corner-sharing with two further building units, both of these T2 units share corners with the same fourth cluster, which closes the macrocycle to form the tetrameric anion. This oligomer of four T2 supertetrahedra can also be regarded as the product of the dimerization of two preformed cluster dimers under release of two additional Se^{2-} anions (see also Scheme 3.1). This unprecedented assembly of T_n clusters represents a structural alternative to a supertetrahedral arrangement of T2 clusters that would be connected by sharing six (instead of four) corners, thus missing another two Se^{2-} anions and 4 negative charges. However, a corresponding defect T4-type anion “[$\text{Ge}_{16}\text{Se}_{34}]^{4-}$ ” (or any other group 14–group 16 cluster of this type) has not been described in the literature to date. While one might hypothesize that a corresponding structure could form, as known for organometallic chalcogenide clusters, the mismatch of the large size with the low charge has so evidently inhibited its crystallization so far. Indeed, another finite tetrameric assembly of (ternary) supertetrahedral clusters, $[\text{Cd}_{16}\text{In}_{64}\text{S}_{134}]^{44-}$, which was obtained in the ionic compound $[(\text{H}^+-\text{DBN})_{11}((\text{H}^+)_2-\text{DEM})_{11}][\text{Cd}_{16}\text{In}_{64}\text{S}_{134}] \cdot 50\text{H}_2\text{O}$ upon solvothermal treatment of $\text{Cd}(\text{CH}_3\text{CO}_2)_2 \cdot 2\text{H}_2\text{O}$, In, and S, shows this aggregation pattern but also comprises a much larger charge owing to the presence of di- and trivalent cations instead of tetravalent ones^[62]. In this cluster, four $\{\text{Cd}_4\text{In}_{16}\text{S}_{35}\}$ T4-type units are linked to form a hollow supertetrahedron by sharing six corners.

Another change of the ratio of $(\text{C}_2\text{C}_1\text{Im})[\text{B}(\text{CN})_4]$ to DMMP to an intermediate value (3.5:1; v:v) caused the linkage of the $[\text{Ge}_4\text{Se}_{10}]^{4-}$ cluster anions via $\mu\text{-Se}^{2-}$ ligands into infinite 1D zigzag chains in $(\text{C}_2\text{C}_1\text{Im})_6[\text{Ge}_{12}\text{Se}_{27}]$ (**4**). Compound **4** crystallizes in the monoclinic crystal system, space group type $P21/n$ (No. 14). As illustrated in Figure 3.5, the asymmetric unit of the zigzag arrangement comprises twelve germanium atoms and twenty-seven selenium atoms, in three T2-type building units. These are connected similarly to the three first T2 units in compound **3**, enclosing a near rectangular angle of 95.13° . However, instead of linking to the same fourth cluster

under formation of the four-membered macrocycle observed in compound **3**, the repeat unit is connected to identical units to both sides, thus extending into an infinite super-zigzag chain with four clusters in a straight row each. This structural motif has also been unprecedented in chalcogenido (semi)metalate chemistry to date.

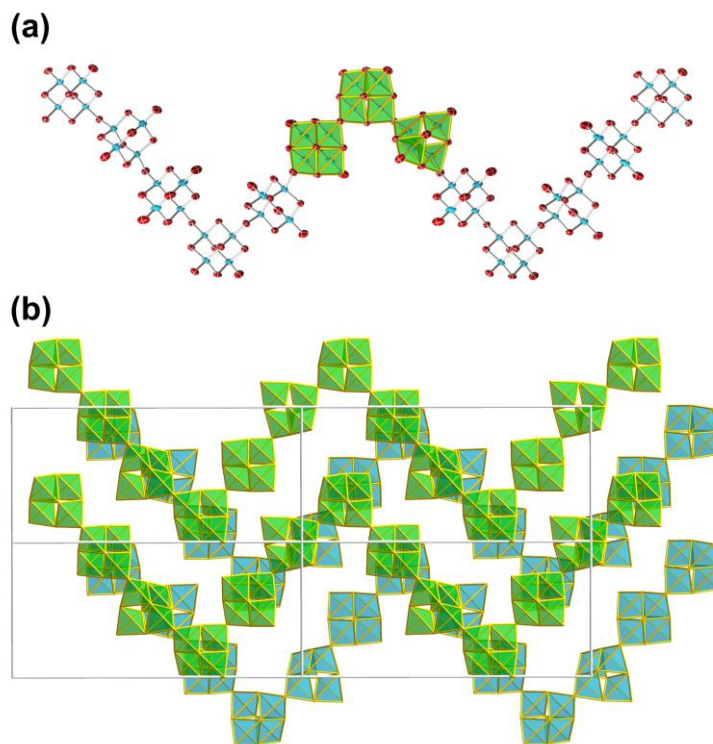


Figure 3.5: Anionic substructure of compound **4**, with the asymmetric unit display in polyhedron mode (a). View of the unit cell of compound **4** (b), given that those molecules are shared with the adjacent unit cells, only four of the anions observed within the unit cell in average. Ge and Se atoms are shown as thermal ellipsoids at the 50% probability level; the imidazolium counterions are omitted for clarity, the polyhedrons are highlighted in different colors to clearly illustrate the chains' arrangement. Color code: Ge–Sky blue; Se–Red.

So far, it has not been possible to gain detailed insight into the processes that lead to the formation of such complex compounds. However, it is evident that the relative amount of the auxiliary DMMP must play a crucial role. It is assumed that the basic molecules serve as mediators for the release of Se^{2-} anions (most probably as H_2Se) upon deprotonation of H_2O (from the reactant) and subsequent hydrogen bonding interactions with the selenido germanate anions. In the presence of a small amount of DMMP (1:10 relative to the ionic liquid), the T1-type $[\text{GeSe}_4]^{4-}$ anions assemble to the T2 cluster in **1**. Under the same conditions, if DMMP is replaced by $(\text{C}_2\text{C}_1\text{Im})[\text{BF}_4]$, the cluster dimerizes to form compound **2**. With a larger relative amount of DMMP (1:3.5 relative to the ionic liquid), the linkage extends to form the infinite zigzag chains in **4**, where all clusters share two corners with adjacent building units. This is also the case for the tetrameric anion in compound **3**, which forms at the highest relative amount of DMMP (1:2 relative to the ionic liquid). Hence, besides affecting the number of Se^{2-} anions released per cluster unit (which is the same as for **4**), the DMMP molecules likely have a more significant templating

effect here. It is assumed that they form H-bonded clusters that control the local tetramerization. These assumptions are based on plausibility considerations, as, to this date, there is no reliable method to study these reactions *in-situ*. The absence of suitable NMR nuclei for quick monitoring and the fact that the reactions take place in sealed ampules during a heating–cooling sequence inhibits corresponding studies. However, it is hypothesized that molecular dynamic simulations might one day bring us closer to understand the underlying mechanism.

The guest-accessible spaces of all described compounds are filled with counterions to balance the anions' negative charge. While this was fully proven for compound **1** *via* single crystal X-ray diffraction (SC-XRD), the assignment of some of the counterions' atoms was inhibited by heavy disorder. In order to avoid impairment of the refinement of the anionic substructures by an incomplete model, the influence of the electron density of atoms that could not be localized from the difference Fourier map was detracted from the data by application of the back Fourier transform method using the SQUEEZE program in PLATON^[129]. All refinement results are detailed in Tables 6.9–6.13. The precise Ge:Se ratios were additionally verified by means of energy dispersive X-ray (EDX) spectroscopy (Figure 3.6). Slight differences between calculated and simulated values (below ± 1 atom) are acceptable and caused by the overlap of Ge and Se signals in the EDX spectra. Phase purity was confirmed by powder X-ray diffraction (PXRD) measurement (Figure 3.7). Differences observed in the intensities of PXRD measurements are attributed to the crystals' random orientation during sample preparation, this is commonly observed in PXRD investigation due to the fact that we can never orient crystalline sample into the same arrangement as what they are in a single crystal.

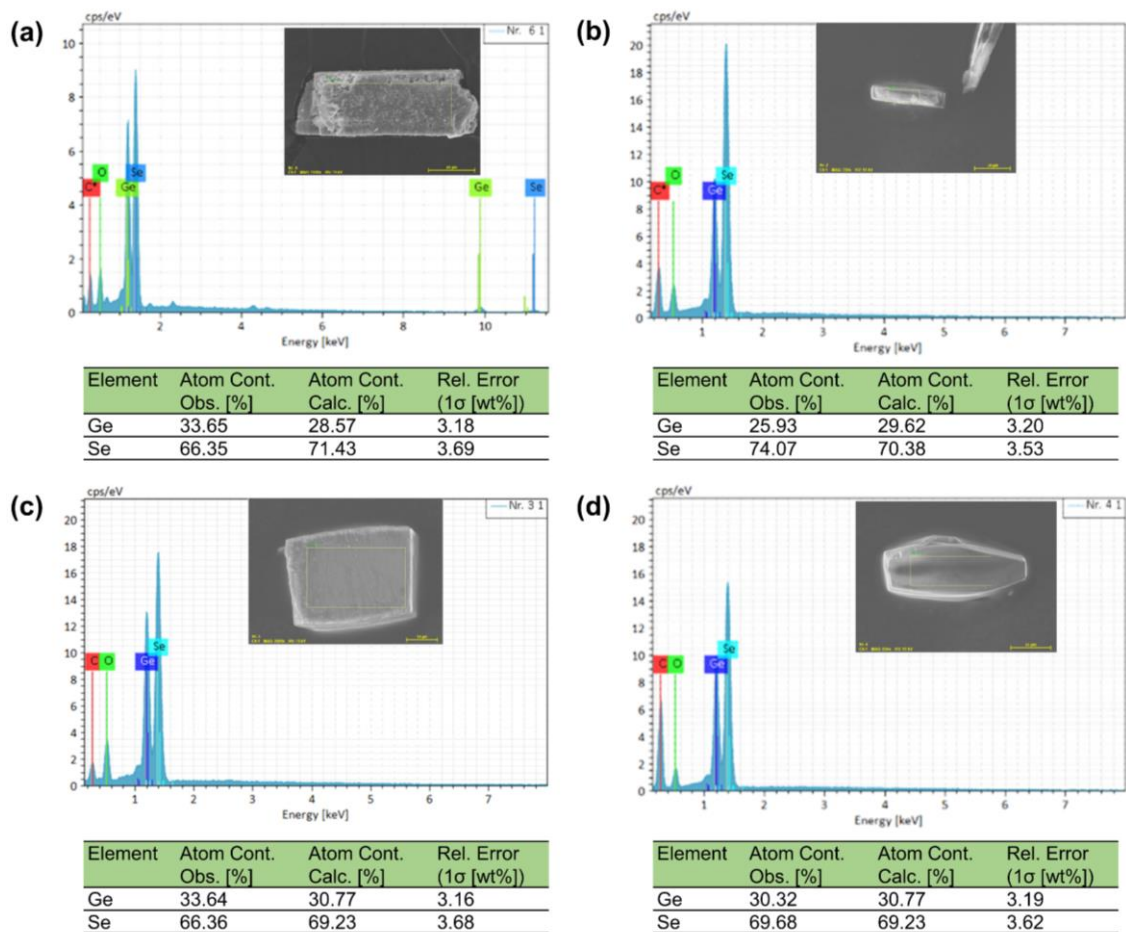


Figure 3.6: Scanning electron microscope (SEM) image and EDX spectrum of compound **1** (a); compound **2a** (b); compound **3** (c); compound **4** (d). Slight differences between calculated and simulated values (below ± 1 atom) are caused by the overlap of Ge and Se signals in the EDX spectra.

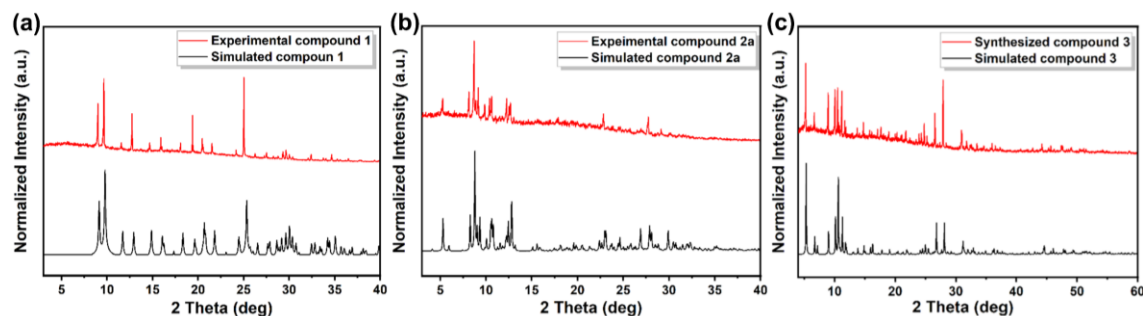


Figure 3.7: PXRD pattern of as-synthesized and simulated compound **1** (a); compound **2a** (b); and compound **3** (c). Notable differences in the intensities are attributed to texture effects.

As noted above, ligand-free supertetrahedral chalcogenido (semi)metalate clusters have only rarely been assembled into finite cluster oligomers, such as the anions of $[\text{Cd}_{16}\text{In}_{64}\text{S}_{134}]^{44-62}$, and $[\text{Cs}@\text{Sn}^{\text{II}}_4(\text{Ge}_4\text{Se}_{10})]^{7-124}$. This can be understood as the initial steps of the formation of extended structures in a bottom-up approach from isolated cluster units, as demonstrated with compounds

1, 2, 3, and 4. Hence, the first insights into corresponding materials formation with the example of $[\text{Ge}_4\text{Se}_{10}]^{4-}$ anions is provided.

As discussed above, this cluster assembly process serves to stepwise lower the charge per cluster unit: from 4⁻ in **1** to 3⁻ in **2**, and to 2⁻ in **3** (and **4**; which if the chains were interlinked would ultimately end up with a neutral network of all-corner-linked T2-clusters $[\text{Ge}_4\text{Se}_6\text{Se}_{4/2}]$ in a yet unknown modification of GeSe_2). It is therefore interesting to investigate the solubility of the crystals comprising molecular anions in a common organic solvent (DMF), and to probe their undecomposed transfer into solution by means of mass spectrometry, UV-visible spectroscopy, and dynamic light scattering experiments. The success of these experiments is documented in the following sections. Compounds **1** – **3** show excellent solubility in dry DMF, determined to be around 3.25 mg/mL, 2.75 mg/mL, and 3.13 mg/mL, respectively (1.3 mg of compound **1** in 0.4 mL of DMF; 1.1 mg of compound **1** in 0.4 mL of DMF; 2.5 mg of compound **1** in 0.8 mL of DMF), and they can be dispersed without visible change in other organic solvents and water. The decent solubility of compound **1**—despite possessing the highest charge per cluster unit—is attributed to its selenideic nature and the combination with $(\text{C}_2\text{C}_1\text{Im})^+$ counterions, both lower the lattice energy. These observations discriminate the compounds reported herein from salts of the T5-type supertetrahedral cluster $[\text{Cu}_5\text{In}_{30}\text{S}_{56}\text{H}_4]^{13-}$, which only dissolve upon addition of LiBr^[114].

3.1.3 Additional characterizations to compounds **1** – **4**

3.1.3.1 ESI mass spectroscopy

Electrospray ionization mass spectra recorded in negative ion mode, ESI(⁻), on a fresh DMF solution of single crystals of compound **1** display the signal of the cluster anion along with three counterions (Figure 3.8a). The experimental isotope pattern is in excellent agreement with the calculated isotopic distribution of the aggregate $\{(\text{C}_6\text{N}_2\text{H}_{11})_3[\text{Ge}_4\text{Se}_{10}]\}^-$ with a molecular mass of 1414.13 (Figure 3.8b). Besides this, further monoanionic complexes $\{(\text{C}_6\text{N}_2\text{H}_{11})_2\text{H}[\text{Ge}_4\text{Se}_{10}]\}^-$ and $\{(\text{C}_6\text{N}_2\text{H}_{11})_1\text{H}_2[\text{Ge}_4\text{Se}_{10}]\}^-$ (see also Figure 6.1 for more high-resolution mass spectra) and the aggregate $\{\text{H}_3[\text{Ge}_4\text{Se}_{10}]\}^-$ were transferred into the gas phase (Figure 3.8c). In addition, the signal of $\{(\text{C}_6\text{N}_2\text{H}_{11})_4\text{H}[\text{Ge}_4\text{Se}_{10}]\}^+$ was detected by means of ESI(⁺) mass spectrometry (Figure 3.8d), which has been unprecedented for a ligand free supertetrahedral chalcogenido (semi)metallate cluster and also is the only ESI(⁺) signal to be detected among the series of compounds reported herein. This and the identified aggregates, all of which survived the electrospray ionization treatment, confirmed the significant interaction between the cluster anions and ionic liquid cations in compound **1**. This is further supported by the mass spectrum of this compound, which is dominated by molecular peaks with a 1⁻ charge (Figure 3.8a). This behavior contrasts with that observed for the other compounds reported below this section.

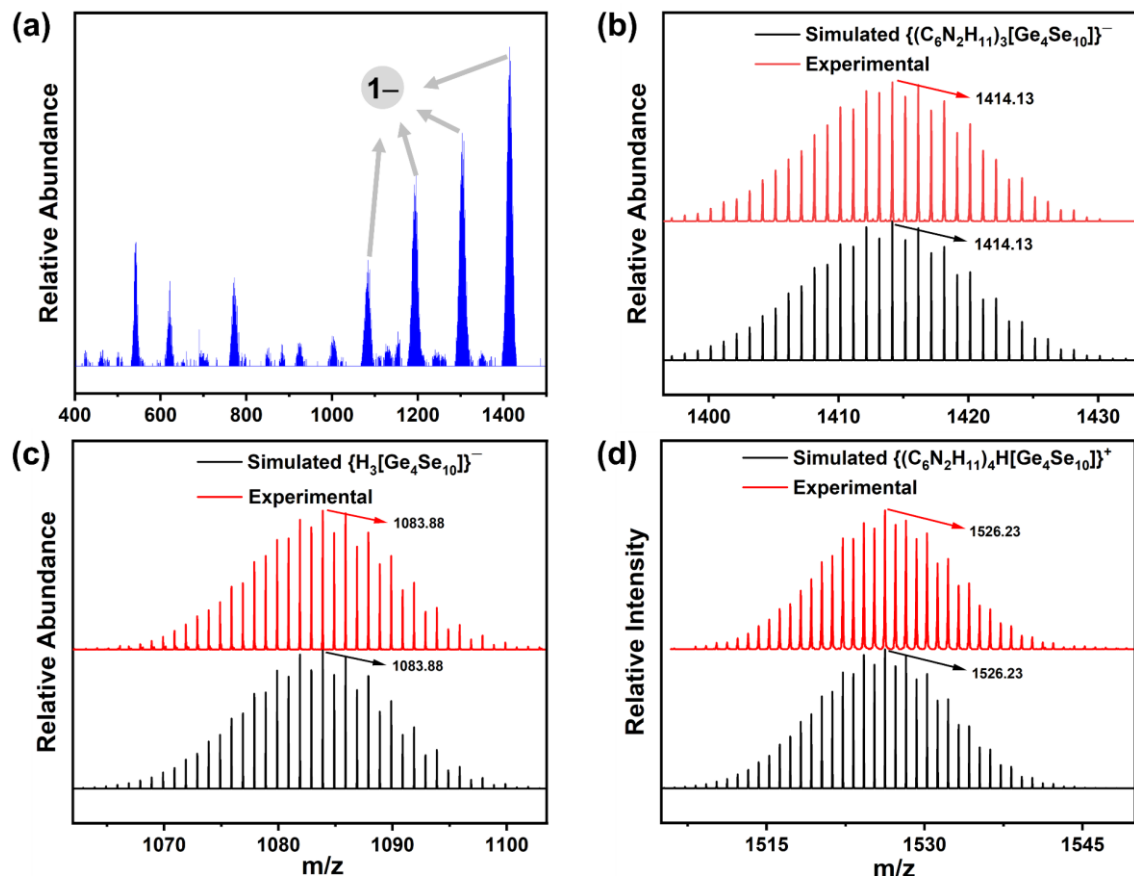


Figure 3.8: Overview of the ESI($-$) mass spectrum of a fresh solution of single-crystals of **1** in DMF (a). High-resolution ESI($-$) mass peak of the cluster anion of **1**, detected along with three ionic liquid counterions, formulated as $\{(C_6N_2H_{11})_3[Ge_4Se_{10}]\}^-$ (b); and with three protons $\{H_3[Ge_4Se_{10}]\}^-$ (c). High-resolution ESI($+$) mass peak of the cluster cation of **1** $\{(C_6N_2H_{11})_4H[Ge_4Se_{10}]\}^+$ (d), detected along with four ionic liquid counterions and one proton.

For compound **2a**, the mass spectrum revealed a series of signals corresponding to monoanionic and dianionic aggregates, where $(C_2C_1Im)^+$ and H^+ counterions served to decrease the charge. As shown in Figure 3.9, the dimeric cluster anion in compound **2a** along with different quantities of the mentioned cations was identified. The monoanionic aggregates were identified as $\{(C_6N_2H_{11})_5[Ge_8Se_{19}]\}^-$, $\{(C_6N_2H_{11})_4H_1[Ge_8Se_{19}]\}^-$, $\{(C_6N_2H_{11})_3H_2[Ge_8Se_{19}]\}^-$, $\{(C_6N_2H_{11})_2H_3[Ge_8Se_{19}]\}^-$, and $\{(C_6N_2H_{11})_1H_4[Ge_8Se_{19}]\}^-$. Additionally, three dianionic aggregates including $\{(C_6N_2H_{11})_4[Ge_8Se_{19}]\}^{2-}$, $\{(C_6N_2H_{11})_3H_1[Ge_8Se_{19}]\}^{2-}$, and $\{(C_6N_2H_{11})_2H_2[Ge_8Se_{19}]\}^{2-}$ were found (see Figure 6.2 for more high-resolution mass spectra). All of the measured isotope patterns agree very well with the simulated ones, which indicates a high stability of the species both in solution and in the gas phase. In addition, some fragments were identified, but their relative abundance is significantly smaller than that of the dimeric anions' signals. Most notably, the relative abundance of peaks with 2 $-$ charges is larger in this experiment compared to that of compound **1**. This observation confirms a reduced cation-anion interaction, which was expected and desirable due to the reduced average charge per cluster unit.

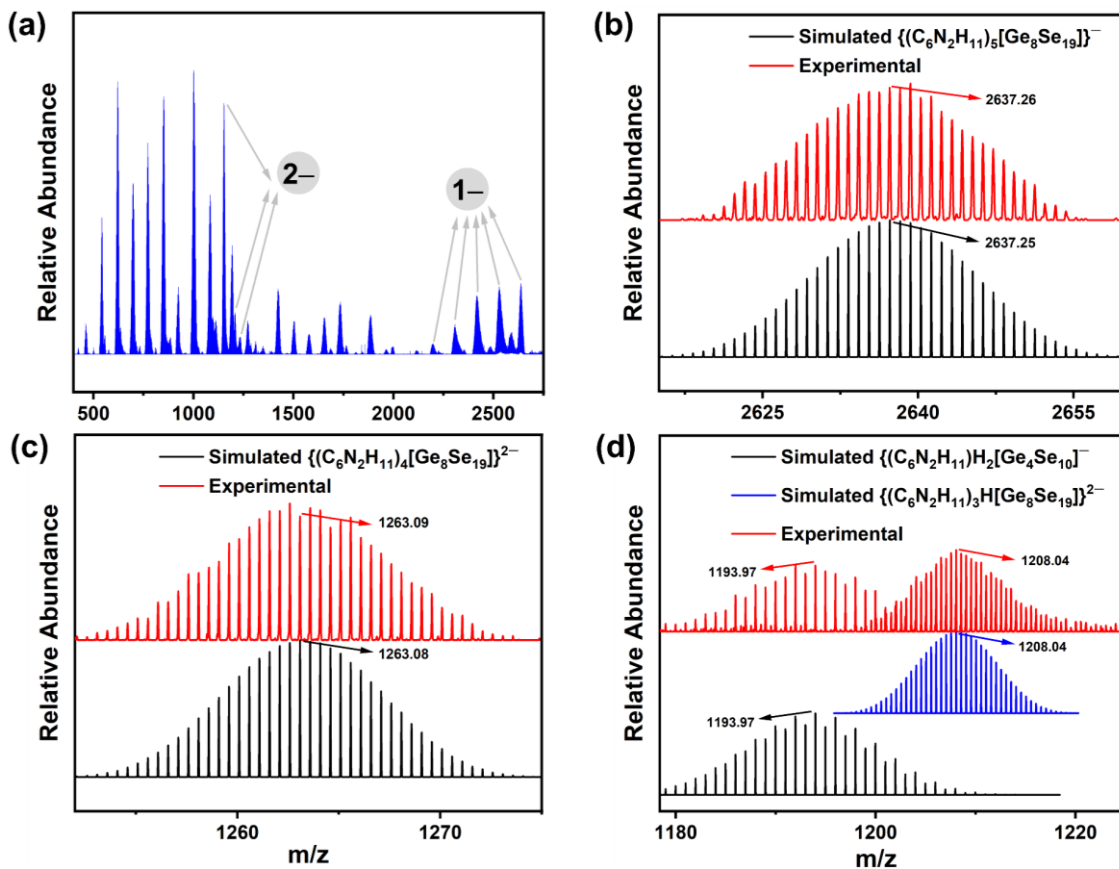


Figure 3.9: Overview of the ESI($-$) mass spectrum of a fresh solution of single-crystals of **2a** in DMF (a). High-resolution ESI($-$) mass peak of the cluster anion of **2**, detected along with five ionic liquid counterions, formulated as $\{(C_6N_2H_{11})_5[Ge_8Se_{19}]\}^-$ (b); and with four ionic liquid counterions, formulated as $\{(C_6N_2H_{11})_4[Ge_8Se_{19}]\}^{2-}$ (c), with three ionic liquid counterions and one proton, formulated as $\{(C_6N_2H_{11})_3H[Ge_8Se_{19}]\}^{2-}$, the overlay of the mass peak of $\{(C_6N_2H_{11})_3H[Ge_8Se_{19}]\}^{2-}$ with that of the fragment $\{(C_6N_2H_{11})_2H_2[Ge_4Se_{10}]\}^-$ formed during the ionization process (d).

For compound **3**, the mass spectra are even more complicated than those of compound **2a**. A series of peaks, with charges ranging from 2 $-$ and 3 $-$ to 4 $-$ were observed. The dominant peaks are found in the range of m/z = 1020 and 1130, and they correspond to species with the general composition $\{(C_6N_2H_{11})_{4-x}H_x[Ge_{16}Se_{36}]\}^{4-}$ ($x = 0-3$). The relative abundance of the species gradually decreases as H^+ replaces the ionic liquid counterions. In addition, cluster anions with a 3 $-$ or a 2 $-$ charge were also detected, but with lower relative abundance compared to those with a 4 $-$ charge. Notably, no monoanions were observed for solutions of compound **3**, which was attributed to both the large molecular mass and the reduced cation-anion interaction. This assumption is supported by the observed relative abundances of species with 4 $-$, 3 $-$, and 2 $-$ charges. High-resolution mass spectra for all of these anions are provided in Figure 3.10, all of which show excellent agreement of measured and simulated isotope patterns. Again, this is a strong indication for good solubility and fair stability of the compound in DMF. The clusters predominantly dissolve as a whole entity, in contrast to dispersions of $[Zn_4In_{16}S_{35}]^{14-}$ nanoclusters, which exhibit significant sulfide ligand loss and massive proton uptake in piperidine^[120]. However, some frag-

mentation was also observed in the studies of compound **3**, partially overlapping with the molecular peaks of the entire anion. As an example, Figure 3.10 demonstrates the coincidence of $\{(C_6N_2H_{11})_3[Ge_4Se_9]\}^-$ and $\{(C_6N_2H_{11})_6[Ge_{16}Se_{36}]\}^{2-}$ or of $\{(C_6N_2H_{11})_3[Ge_8Se_{18}]\}^-$ and $\{(C_6N_2H_{11})_6[Ge_{16}Se_{36}]\}^{2-}$ (see Figure 6.3–6.5 for more high-resolution spectra).

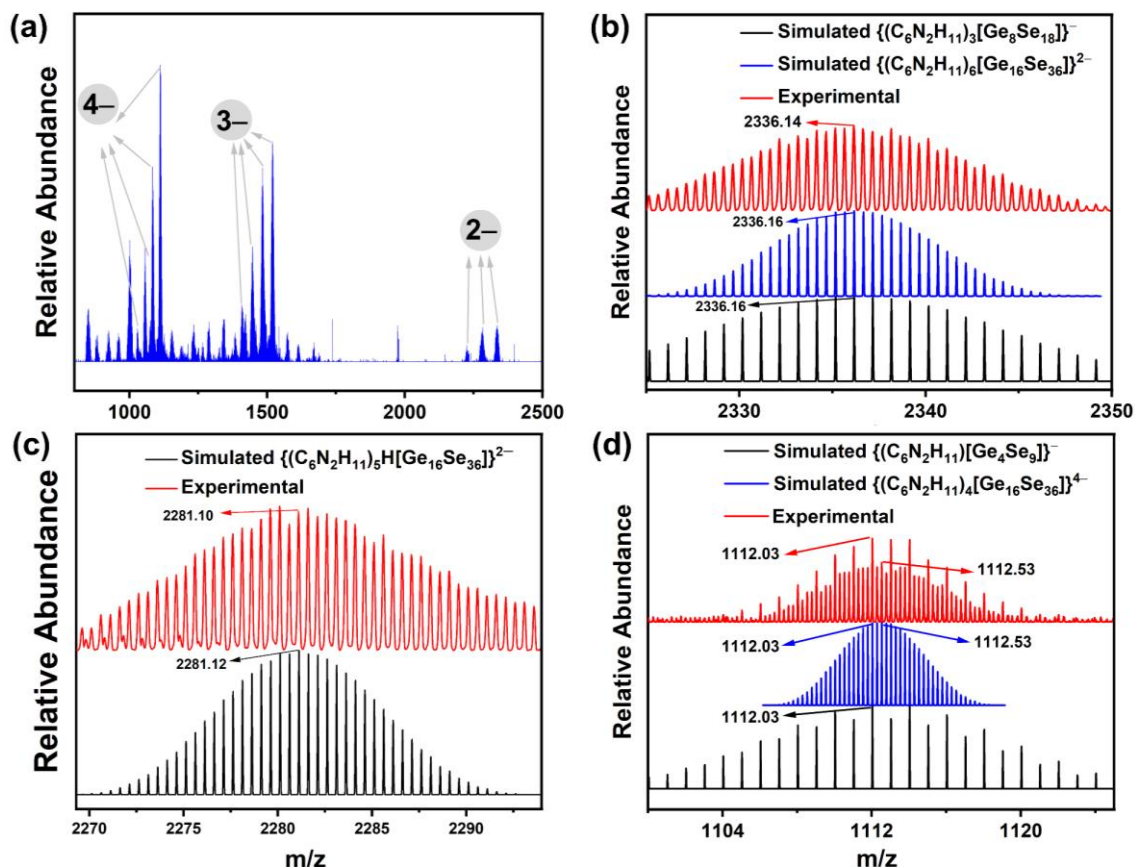


Figure 3.10: Overview of the ESI($-$) mass spectrum of a fresh solution of single-crystals of **3** in DMF (a) High-resolution ESI($-$) mass peak of the cluster anion of **3**, detected along with six ionic liquid counterions, formulated as $\{(C_6N_2H_{11})_6[Ge_{16}Se_{36}]\}^{2-}$, the overlay of the mass peak of $\{(C_6N_2H_{11})_6[Ge_{16}Se_{36}]\}^{2-}$ with that of the fragment $\{(C_6N_2H_{11})_3[Ge_8Se_{18}]\}^-$ formed during the ionization process (b), and with five ionic liquid counterions and one proton, formulated as $\{(C_6N_2H_{11})_5H[Ge_{16}Se_{36}]\}^{2-}$ (c), with four ionic liquid counterions, formulated as $\{(C_6N_2H_{11})_4[Ge_{16}Se_{36}]\}^{2-}$, the overlay of the mass peak of $\{(C_6N_2H_{11})_4[Ge_{16}Se_{36}]\}^{2-}$ with that of the fragment $\{(C_6N_2H_{11})[Ge_4Se_9]\}^-$ formed during the ionization process (d).

In addition, the stability of the solutions of all compounds was investigated. The color of the solutions remained unchanged over (at least) four weeks, indicating their good stability under inert conditions. However, the solutions decompose within two hours of exposure to air, as evidenced by a color change from yellow to transparent and the precipitation of a black solid (see Chapter 6, Figure 6.6).

3.1.3.2 Dynamic light scattering

The Tyndall effect demonstrated on these solutions (Figure 3.11) indicates that the solutes possess nanoparticle dimension. To study this in more detail and to determine the size distribution of the cluster anions in compounds **1–3**, dynamic light scattering (DLS) studies were carried out on DMF solutions of the single crystals. As shown in Figure 3.11, the hydrodynamic radius (R_H) was determined to fall in the ranges of 7.31–8.31 nm for compound **1**, 5.95–8.23 nm for compound **2a**, and 2.93–5.20 nm for compound **3**, respectively. The mean diameters of the cluster anions in compounds **1**, **2a**, and **3** (calculated as the largest Se···Se distance plus $2 \cdot R_{\text{cov}}(\text{Se}) = 2.0116 \text{ \AA}$) from the SC-XRD analyses are 0.99, 1.70, and 1.90 nm, respectively^[130]. This further confirms the notable decrease of the electrostatic interactions between anionic clusters and ionic liquid cations from compound **1** via compound **2a** to compound **3**: despite having the largest cluster diameter, compound **3** exhibits the smallest hydrodynamic radius, whereas compound **1** shows the largest hydrodynamic radius in DMF solution. This is comparable to the effective radii of alkali metal cations in aqueous solutions, which decrease from Li^+ to the heavier congeners owing to a significant drop in charge density^[131]. In summary, all studies performed on solutions of compounds **1**, **2a** and **3** confirm (a) the integrity of the cluster assemblies in solution and (b) the notably decreased interaction with counterions upon oligomerization.

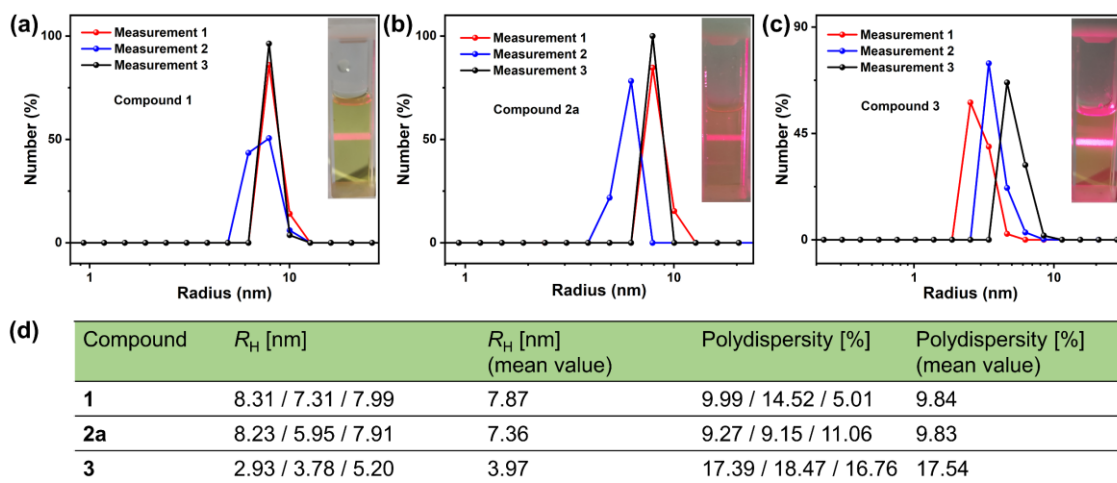


Figure 3.11: DLS measurements of fresh solution of compounds **1** (a), **2a** (b), and **3** (c), with the inset shows the solution and the Tyndall effect of each solution, summary of the hydrodynamic radii (R_H) and polydispersity on corresponding solutions (d).

3.1.3.3 Vibrational and optical absorption properties

Raman spectra were recorded on single crystals of **1**, **2a**, **3**, and **4**. As illustrated in Figure 3.12, all spectra exhibit almost identical vibrational modes (although with varied intensities), which indicates the identical bonding situations of these compounds. The most intensive peaks at around 145 cm^{-1} , 217 cm^{-1} , and 339 cm^{-1} are attributed to lattice vibrations of the cluster core, as compared with the reported value of $\text{Na}_8[\text{Ge}_4\text{Se}_{10}]$ ^[132], $\text{Na}_9\text{Sm}(\text{Ge}_2\text{Se}_6)_2$ ^[133], $\text{K}_2[\text{EuGeSe}_5]$ ^[134], $\text{Cs}_2[\text{Ge}_3\text{Ga}_6\text{Se}_{14}]$ ^[135], and $\text{Ge}_{24}\text{Se}_{76}$ ^[136]. The slight shifts observed in the spectra are attributed to

slight differences of bond lengths or the presence of heteroatoms in the reported cluster cores. Due to the relatively low resolutions of the Raman spectra, it was not possible to assign vibrational bands to the counterions.

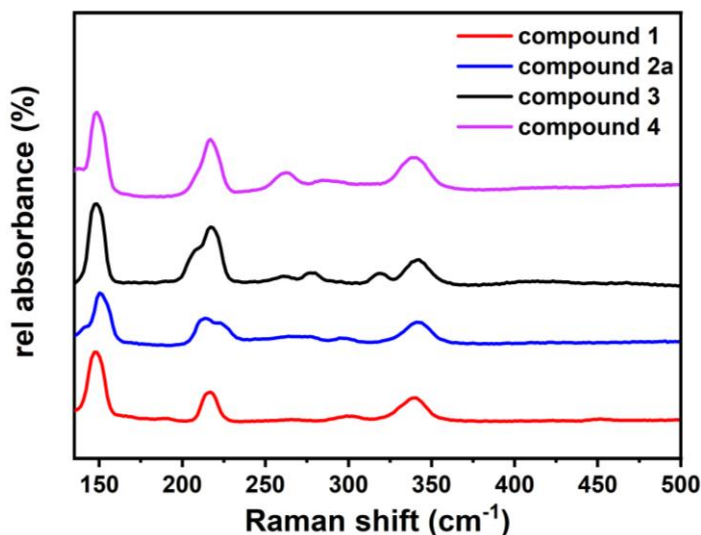


Figure 3.12: Raman spectra of compounds **1**, **2a**, **3**, and **4**. The peaks at 145 cm^{-1} and 339 cm^{-1} are assigned to the stretching modes of Ge–Se bond, the peaks at 217 cm^{-1} are attributed to the symmetric stretching mode of $[\text{GeSe}_4]^{4-}$ tetrahedron.

UV-visible spectra of crystalline samples (recorded in diffuse-reflectance mode, Figure 6.7) served to characterize the solid compounds **1**–**4** as narrow-band gap semiconductors. Figure 3.13a demonstrates a gradual red shift occurs for the lowest excitation energies from **1** to **4**. The optical bandgaps, determined by application of the Kubelka–Munk function, are 2.59 eV (479 nm; **1**), 2.42 eV (512 nm; **2a**), 2.15 eV (577 nm; **3**), and 2.02 eV (614 nm; **4**). It is noteworthy that the optical gaps of all four compounds are narrower than those reported for bulk GeSe_2 (2.74 eV)^[137] and also for GeSe_2 thin films ($\sim 1\text{ }\mu\text{m}$ thickness; 2.36 eV)^[138], even those with molecular selenido germanate anions. This indicates that the cluster-based chromophores are very effective in band gap narrowing.

The absorption spectra recorded on fresh solutions of the crystals in DMF solution (Figure 3.13b) show a similar red shift, with onsets of absorption at 2.98 eV (416 nm; **1**), 2.88 eV (431 nm; **2**), and 2.71 eV (457 nm; **3**). These values are blue-shifted by 0.4–0.6 eV relative to the solid samples but remain small in comparison with extended Ge–Se-based solids, indicating they stem from molecular anionic units in solution. Notably, the band gap of the dissolved molecular salt comprising the $[\text{Ge}_{16}\text{Se}_{36}]^{8-}$ anion in **3** is even smaller than that of bulk GeSe_2 . Owing to its inherent insolubility, it has so far not been possible to record an absorption spectrum of compound **4** in solution.

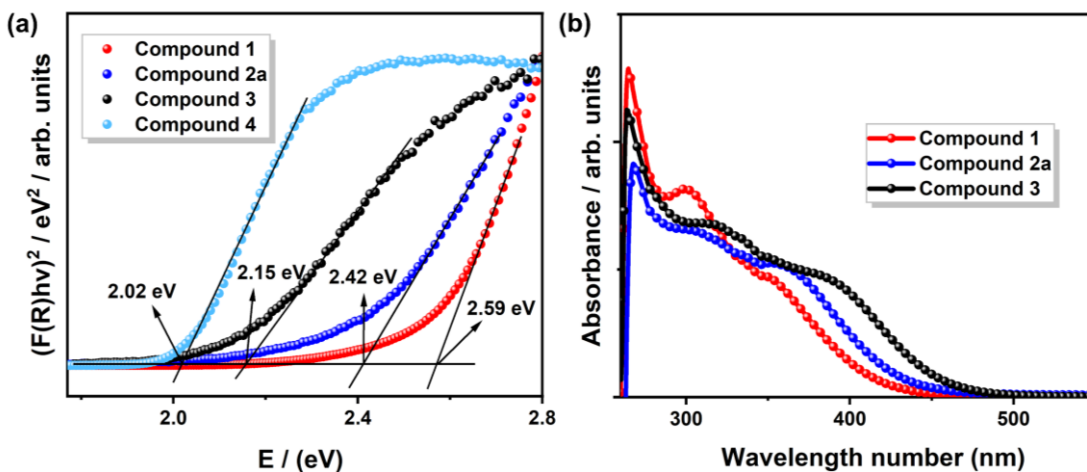


Figure 3.13: Tauc plots derived from the solid-state UV-visible diffuse-reflectance spectra of crystalline samples of **1**, **2a**, **3**, and **4**, and optical absorption spectra of fresh solutions of single crystals of **1**, **2a**, and **3** in dry DMF.

The investigations clearly demonstrate that although all compounds are based on the same building units (T2 clusters) composed of the same elements (Ge and Se) and even the same counterions, the stepwise oligomerization serves to finely tune the optical gap. This modification strategy is important crucial for a potential use of such oligomers in functional semiconductor-based arrays.

3.1.4 Conclusions

In summary, a series of narrow-band gap semiconductor clusters based on $[\text{Ge}_4\text{Se}_{10}]^{4-}$ have been presented, featuring the first purely inorganic dimers and a first square-shaped tetramer of chalcogenido (semi)metalate supertetrahedra. These compounds were obtained by thermal treatment of $[\text{Na}_4(\text{H}_2\text{O})_{14}][\text{GeSe}_4]$ or $[\text{K}_4(\text{H}_2\text{O})_3][\text{Ge}_4\text{Se}_{10}]$ in the ionic liquids 1-ethyl-3-methylimidazolium tetracyanoborate/tetrafluoroborate, $(\text{C}_2\text{C}_1\text{Im})[\text{BX}_4]$ ($\text{X} = \text{CN}, \text{F}$), at 150 °C. One of these compounds comprises the largest selenido germanate cluster anion, $[\text{Ge}_{16}\text{Se}_{36}]^{8-}$, reported to date. Oligomerization of these anions through sharing $\mu\text{-Se}^{2-}$ ligands reduces the charge per cluster unit compared to the monomeric clusters, resulting in a significantly reduced cation–anion interaction. Consequently, the compounds dissolve readily in DMF, which was demonstrated by means of ESI mass spectrometry and dynamic light scattering studies on corresponding solutions. UV–visible spectra of both the solid compounds and their solutions indicate remarkably small optical band gaps, similar to that of bulk GeSe_2 , or even smaller, which are finely tuned with the degree of aggregation. Future studies aim to extend this oligomerization strategy to other supertetrahedral chalcogenido metalate clusters, with the next logical step being the investigation of the related Ge/S and Ge/Te system.

3.2 Ion-selective assembly of supertetrahedral selenido germanate clusters for alkali metal ion capture

The results of this chapter are published in the following journal:

Zhou Wu, Florian Weigen, Dieter Fenske, Tim Naumann, J. Michael Gottfried, and Stefanie Dehnen*, Ion-Selective Assembly of Supertetrahedral Selenido Germanate Clusters for Alkali Metal Ion Capture and Separation. *J. Am. Chem. Soc.* **2023**, *145*, 3802–3811.

3.2.1 Introduction

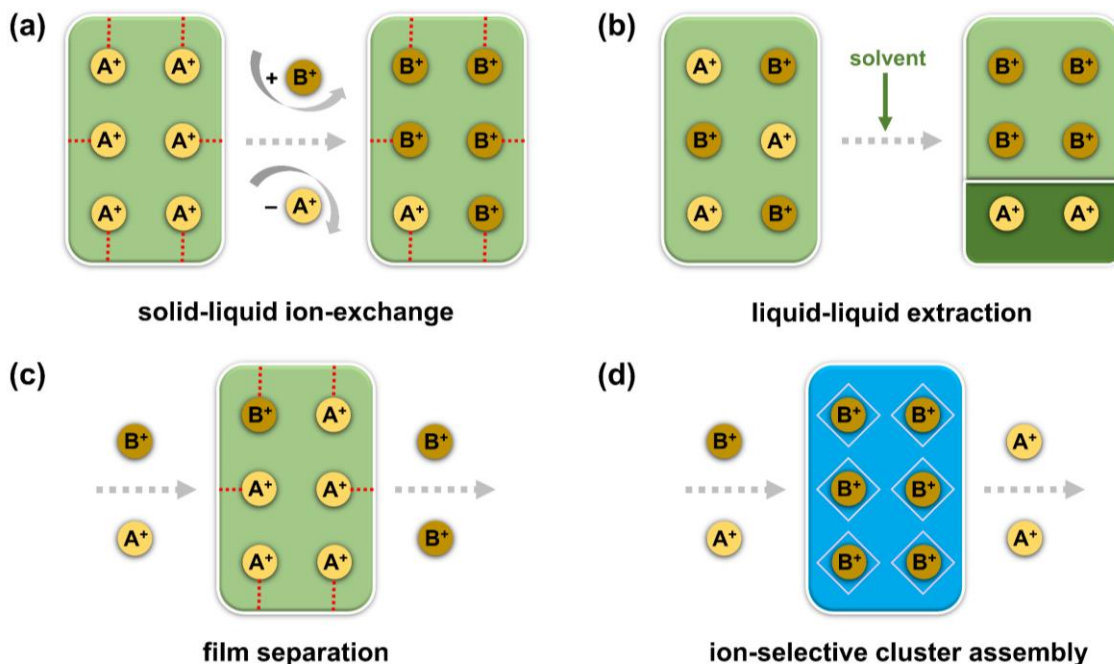
Supertetrahedral chalcogenido (semi)metalate cluster-based frameworks have demonstrated a high selectivity for alkali metal cations due to the specific charge density of their inner surfaces. This property has made them ideal ion-exchange materials towards various metal ions and have especially been investigated for separating Cs^+ ions over the last decades^[108,139–141].

The selective removal of Cs^+ ions and the recovery of other alkali metal ions (especially Li^+ , Na^+ , and K^+) from wastewater are crucial steps for solving the environmental crisis and achieving energy conversion. These issues have gained increasing significance and have been the focus of an advancing research topic during the past year^[142–144].

Due to their similar chemical properties, alkali metal cations often coexist in nature and industrial environment. Consequently, developing effective methods for their separation with high ion selectivity is both crucial and challenging. Various methods have been proposed to enhance these separation efficiencies, including ion-exchange^[145,146], liquid–liquid extraction^[147,148], solid–liquid extraction^[149,150], and film separation^[151,152]. Despite the small differences in ionic radii and charge densities of Na^+ , K^+ , and Ca^{2+} , an artificial Na^+ -selective ionic device based on crown-ether crystals was developed, for instance, which achieves a high selectivity of Na^+ toward K^+ and Ca^{2+} ^[153]. In addition, crystalline silicotitanate has shown exceptional high capacity and selectivity for Cs^+ in ion-exchange process, even in highly alkaline solutions (1–7 mol/L NaOH)^[154]. Additionally, zeolite-type chalcogenides have showed promising uptake rates for heavy ions^[108,140]. According to these findings, the slight yet notable differences in the ionic radii r_+ of the alkali metal ions (A^+) play the most important role in increasing the separation efficiency. Therefore, materials designed for alkali metal ion capture and separation can benefit from selective crystallization owing to the lattice energy’s general dependency from the cation’s charge Z^+ and the ionic radius as Z^+/r_+ .

Compounds comprising supertetrahedral chalcogenido metalate clusters have been extensively studied, from their synthesis to their application perspective, particularly in the selective removal of radionuclide or heavy metal elements^{[155][156]}. Corresponding salts have shown high selectivity for capturing relatively “soft” cations like Cs^+ and Sr^{2+} compared to “harder” alkali or alkaline earth ions. This selectivity is attributed to the stronger interaction of the former with the “soft” inner chalcogenide surface of such frameworks^[157,158]. However, none of these pioneering reports focused on selective crystallization of such compounds for separation of alkali metal cations.

Given the recent progress in chalcogenide cluster chemistry^[159–162], supertetrahedral chalcogenido metalate cluster compounds (or frameworks of such clusters) with suitable cavities, are considered as promising candidates for selective incorporation of A^+ ions. However, many of the reported compounds based on supertetrahedral chalcogenido metalate clusters are structurally templated by organic ammonium cations (from neutral amines or ionic liquid cations), which occupy the cavities and can hardly be replaced. In contrast, much fewer compounds have been known in which the clusters co-crystallized with A^+ counterions. To address this challenge, a method that allows a combination of both, and thus enabling A^+ -selective crystallization have therefore been proposed, on which is shown herein (Scheme 3.2).



Scheme 3.2: Summary of reported alkali metal ion separation approaches: solid–liquid ion-exchange (a). Ion separation by liquid–liquid extraction (b). Ion separation in films (c), and ion-selective cluster assembly (d, presented herein).

In this work, a new approach of ion-selective cluster assembly using two new compounds as examples is demonstrated. Both compounds are based on the supramolecular assembly of supertetrahedral selenido germanate clusters, forming *pseudo*-P2-type or T2,2-type superclusters. The first one, $(C_2C_1Im)_7[Cs@Ge^{II}_4(Ge^{IV}_4Se_{10})_4]$ (**5**), comprises the largest selenido germanate cluster reported to date. The anions features an enclosed tetrameric oligomers of $[Ge^{IV}_4Se_{10}]^{4-}$ interlinked by four Ge(II), and represents the first mixed-valent supertetrahedral anionic substructure incorporating both Ge(II) and Ge(IV) oxidation states. The second compound, $(C_2C_1Im)_{10}[Na_5(CN)_6@Cu_6(Ge_4Se_{10})_4(Cu)]$ (**6**), is based on a framework of related heterometallic supercluster anions. The title compounds were obtained by joint templating effects of A^+ ($= Cs^+$ in **5**, $= Na^+$ in **6**) and ionic liquid cations (C_2C_1Im) $^+$ ($=$ 1-ethyl-3-methyl-imidazolium). These salts exhibit high selectivity for either heavy (**5**) or light (**6**) types of A^+ cations, and as such show very promising *in-situ* separation characteristics. The exclusive crystallization with either Cs^+ or Na^+

was proven by corresponding cross experiments in combination with thorough analyses by means of SC-XRD, EDX spectroscopy, and ESI-MS, taking advantage of the good solubility of compound **5** in DMF. Moreover, comprehensive density functional theory (DFT) calculations on (hypothetic) series of clusters with Li^+ , Na^+ , K^+ , Rb^+ , or Cs^+ on the central position of the anion in compound **5** indicate that an isolated cluster would also allow for the inclusion of Rb^+ or even K^+ . However, the selective crystallization experiments demonstrate a clear preference for Cs^+ ions in the crystalline state, highlighting the influence on the formation of compound **5**. This work provides a comprehensive insight into the selective incorporation of specific alkali metal ions into supramolecular aggregates of supertetrahedral chalcogenide clusters, and are promising basis for new ion trapping techniques—especially for heavy alkali metal ions that pose environmental challenges.

3.2.2 Syntheses and crystal structures

The three title compounds were obtained from ionothermal reactions in the ionic liquid ($\text{C}_2\text{C}_1\text{Im}$)[B(CN)₄] in the presence of DMMP at 150 °C for three days. As shown in Scheme 5.3, crystals of compound **5** were obtained upon treating [Cs₄(H₂O)][Ge₄Se₁₀] in a 10:1 (v:v) mixture of ($\text{C}_2\text{C}_1\text{Im}$)[B(CN)₄] and DMMP. Red plate-like single crystals of compounds **6a** and **6b** were prepared under the same reaction conditions by using other starting materials. For preparing **6a**, [Na₄(H₂O)₁₄][GeSe₄] was reacted with CuCN. To explore whether the (CN)⁻ anions in the structure of **6a** originated from the copper salt alone or also from the complex ionic liquid anion, [B(CN)₄]⁻, an alternative approach was tested employing Cu(OAc)₂·H₂O. This treatment afforded the same compound, as polymorph **6b**, yet in lower yields than obtained for **6a**. An overview of the comprehensive investigations using ($\text{C}_2\text{C}_1\text{Im}$)[B(CN)₄] ionic liquids for targeting [Ge₄Se₁₀]-based compounds is provided in Figure 3.14, and the crystal structures of the new compounds are discussed below.

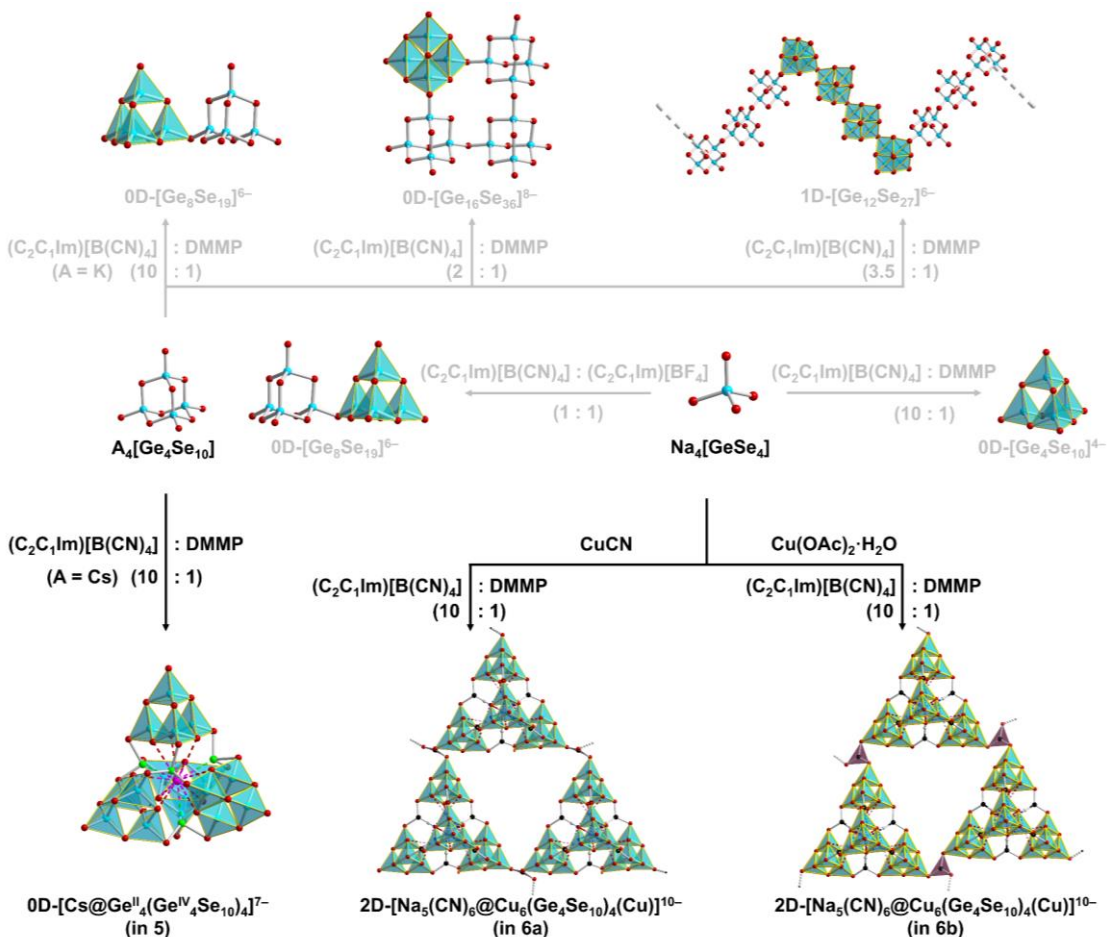


Figure 3.14: Overview of the formation of supertetrahedral $\{Ge_4Se_{10}\}$ -based anionic architectures *via* ionothermal reactions using $(C_2C_1Im)[B(CN)_4]$ ionic liquids, known compounds are summarized at the center and top with gray arrows and formulas; compounds **5**, **6a** and **6b** reported in this work at the bottom with black arrows and formulas, all reactions were performed at 150 °C for 3 days.

It is worth noting that the use of $[Cs_4(H_2O)][Ge_4Se_{10}]$ or $[Na_4(H_2O)_{14}][GeSe_4]$ is essential for successfully synthesizing the title compounds **5** and **6**, the compounds were not obtained upon replacement of these salts with $[Li_4(H_2O)_{20.33}][Ge_4Se_{10}]$, $Na_4[Ge_4Se_{10}]$, $[K_4(H_2O)_3][Ge_4Se_{10}]$, $Rb_4[Ge_4Se_{10}]$ or $[K_4(H_2O)_4][GeSe_4]$ as single source reactant, unless additional CsCl or NaCl was added in corresponding reactions. With these investigations, recent studies of the use of $[Ge_xSe_y]^{4-}$ anions in $(C_2C_1Im)[B(CN)_4]$ by exploring the effect of varied counterions on (a) their templating role and (b) the selectivity of the anionic substructures for the cations' incorporation in the finite cluster and the cluster network architectures were further expanded.

Compound **5** crystallizes in the orthorhombic crystal system, space group $P2_12_12_1$ with four formula units per unit cell [12307.8(8) Å³; Figure 3.15a]. The asymmetric unit of anionic substructure in **5** consists of one cesium, twenty germanium, forty selenium atoms (Figure 6.8). The crystallographically indistinguishable Ge and Se atoms were assigned according to their characteristic coordination modes; their relative amount was verified by means of EDX analyses and ESI-MS.

These analytical techniques help ensure the accuracy of the atomic positions within the crystal lattice of compound **5**.

As shown in Figure 3.15b,c, four T2-type $[\text{Ge}_4\text{Se}_{10}]^{4-}$ anions are connected by four Ge atoms. Corresponding to their pyramidal coordination, those four atoms represent (formal) Ge sites with a lone pair pointing toward the center of the supramolecular assembly. Compound **5** exhibits a structure related to supertetrahedral P2-type clusters like $[\text{Cu}_6\text{Tr}_{12}\text{Sn}_8\text{S}_{44}]^{14-}$ ($\text{Tr} = \text{Ga}$ and In)^[163,164], $[\text{Li}_4\text{In}_{22}\text{S}_{44}]^{14-}$ ^[32], or $[\text{Cu}_{11}\text{In}_{15}\text{Se}_{16}(\text{SePh})_{24}(\text{PPh}_3)_4]^{165}$. This structural motif deviates from the pristine P2-type architecture (Figure 3.15d), the inner moiety is not an anti-T2-supertetrahedron but consists of a central Cs^+ cation and the four Ge^{II} atoms. This defect- or *pseudo*-P2-type architecture was only described for a related Sn/Ge compound so far, $(\text{C}_4\text{C}_1\text{C}_1\text{Im})_7[\text{Cs}@\text{Sn}^{\text{II}}_4(\text{Ge}^{\text{IV}}_4\text{Se}_{10})_4]$ [with $(\text{C}_4\text{C}_1\text{C}_1\text{Im})^+$ representing 1-butyl-2,3-dimethylimidazolium cations].

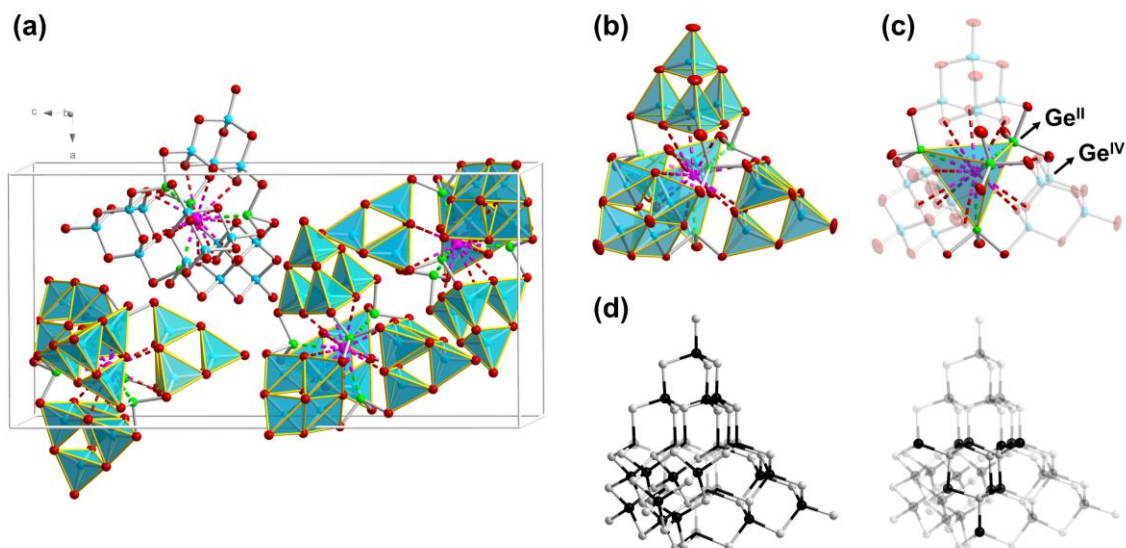


Figure 3.15: View of the (extended) unit cell of compound **5** (a). Molecular structure of the $[\text{Cs}@\text{Ge}^{\text{II}}_4(\text{Ge}^{\text{IV}}_4\text{Se}_{10})_4]^{7-}$ anion in compound **5** (b), atoms are shown as thermal ellipsoids with at the 50% probability level (color code: Ge^{II} —Turquoise, Ge^{IV} —Green, Se—Red, Cs—Pink). Highlight of the inner moiety comprising the Cs^+ ion, 4 Ge^{II} sites, and 12 Se atoms coordinating the latter; the connection of the Cs^+ ion to 12 Se atoms is illustrated by dash lines (c). Structure of the P2-type supertetrahedral cluster $[\text{Cu}_6\text{Tr}_{12}\text{Sn}_8\text{S}_{44}]^{12-}$ for comparison (d).

With a total composition of 20 Ge and 40 Se atoms, the anion in **5** is the largest binary selenido germanate cluster architecture reported to date. The co-existence of Ge^{II} and Ge^{IV} was unambiguously confirmed by high-resolution X-ray photoelectron spectroscopy (XPS) of **5** (Figure 3.16). The experimental ratio of $\text{Ge}^{\text{II}}:\text{Ge}^{\text{IV}}$ (1:3.5) obtained from the sum differs from the ratio according to the structural data (4:1), which is attributed to a surface effect upon sample preparation and measurement. However, the spectrum clearly indicates the presence of $\text{Ge}(\text{II})$ in the compound. In addition, the different valence states of the respective atomic positions were additionally rationalized by bond valence sum (BVS) calculations (Table 3.1)^[166,167]. Besides these, a comparison of the observed $\text{Ge}^{\text{II}}-\text{Se}$ and $\text{Ge}^{\text{IV}}-\text{Se}$ bond lengths with those of related compounds led to the

same conclusion (Table 3.2). Hence, the cluster also represents a rare example of an inorganic mixed-valent Ge(II/IV) compounds—and the first one observed in supertetrahedral chalcogenido metalate cluster chemistry to date.

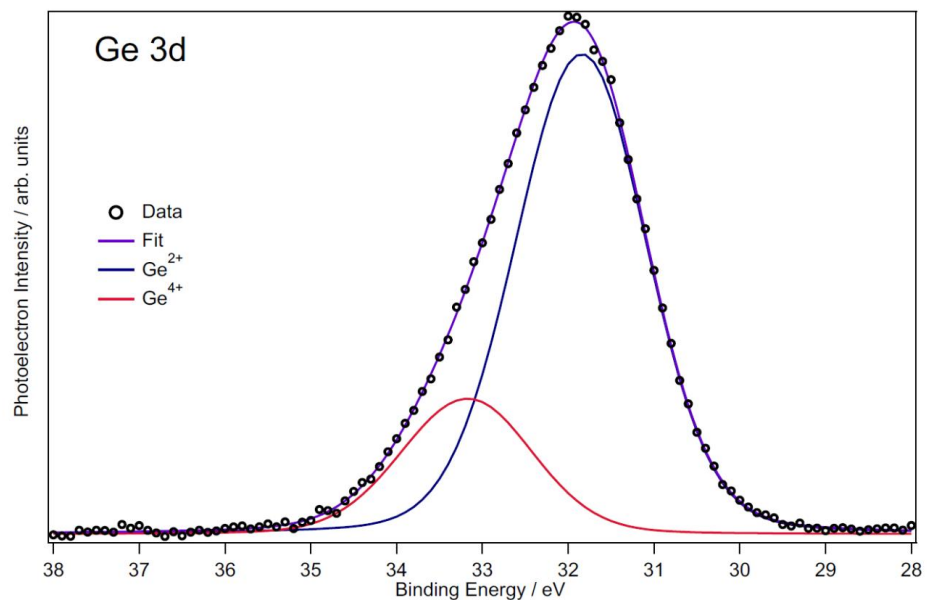


Figure 3.16: High-resolution Ge 3d XPS spectrum of compound 5. Open circles represent the measured data. The red line, centered around 33.2 eV, is assigned to Ge^{IV}. The blue line, centered around 31.8 eV, is assigned to Ge^{II}. The purple line is a sum of both Ge^{II} and Ge^{IV} as fitted to the measured data.

Table 3.1. Bond lengths (unit: Å) and results of a BVS calculation of the sixteen tetra-coordinated Ge atoms, and four tri-coordinated Ge atoms in the asymmetric unit of compound 5. The bond valence is defined as $S_{ij} = \exp[(R_0 - R_{ij})/B]$, where R_{ij} is the bond length between the two given atoms, R_0 and R_{ij} are empirical parameters as defined by Brown *et al.* The bond valence sum is defined as BVSs = $\sum S_{ij}$ for the sum of all the bond valences around a given atom *i*.

Tetra-coordinated Ge sites					
	Se1	Se2	Se3	Se4	BVSs
Ge1	2.2313	2.3786	2.4040	2.3703	4.1146
	Se2	Se5	Se6	Se7	BVSs
Ge2	2.3471	2.3225	2.3752	2.3499	4.0194
	Se3	Se6	Se8	Se9	BVSs
Ge3	2.3405	2.3516	2.3143	2.3669	4.0783
	Se4	Se7	Se9	Se10	BVSs
Ge4	2.3423	2.3643	2.3660	2.3120	4.0726
	Se11	Se12	Se13	Se14	BVSs
Ge6	2.3178	2.3720	2.3533	2.3462	4.0346
	Se12	Se17	Se18	Se40	BVSs
Ge7	2.3568	2.3429	2.3617	2.3321	4.0196
	Se14	Se15	Se16	Se17	BVSs
Ge8	2.3754	2.2518	2.3869	2.3820	4.0598
	Se13	Se16	Se18	Se19	BVSs
Ge9	2.3568	2.3509	2.3689	2.3193	4.0161
	Se20	Se21	Se23	Se27	BVSs
Ge11	2.3024	2.3532	2.3527	2.3645	4.0830
	Se21	Se22	Se24	Se28	BVSs
Ge12	2.3806	2.2439	2.3872	2.3733	4.0960

	Se23	Se24	Se25	Se26	BVSs
Ge13	2.3706	2.3462	2.3144	2.3503	4.0564
	Se26	Se27	Se28	Se29	BVSs
Ge14	2.3637	2.3585	2.3490	2.3175	4.0355
	Se30	Se31	Se32	Se33	BVSs
Ge16	2.3147	2.3515	2.3529	2.3660	4.0460
	Se31	Se34	Se35	Se37	BVSs
Ge17	2.3910	2.2357	2.3853	2.3699	4.1137
	Se33	Se35	Se36	Se38	BVSs
Ge18	2.3535	2.3408	2.3232	2.3698	4.0388
	Se32	Se37	Se38	Se39	BVSs
Ge19	2.3632	2.3432	2.3516	2.3254	4.0479
Tri-coordinated Ge sites					
	Se10	Se11	Se25	BVSs	
Ge5	2.5026	2.5208	2.5160	1.9308	Ge5
	Se19	Se20	Se36	BVSs	
Ge10	2.5075	2.5102	2.5327	1.9122	Ge10
	Se5	Se29	Se30	BVSs	
Ge15	2.5103	2.5325	2.5165	1.8967	Ge15
	Se8	Se39	Se40	BVSs	
Ge20	2.5219	2.5153	2.5128	1.9121	Ge20

Table 3.2: Comparison of Ge(II)–Se and Ge(IV)–Se bond lengths in typical supertetrahedral selenido germanate cluster compounds.

Compound	Ge(IV)–Se	Ge(II)–Se	Reference
5	2.2313 – 2.4040	2.5026 – 2.5307	This work
(C ₄ C ₁ C ₁ Im) ₇ [Cs@Sn ^{II} ₄ (Ge ^{IV} ₄ Se ₁₀) ₄]	2.3172(215) – 2.3598(54)	None	[124]
(C ₄ C ₁ C ₁ Im)[Sn ^{II} (Ge ^{IV} ₄ Se ₁₀)]	2.2465(9) – 2.3805(9)	None	[124]
(C ₃ NH ₁₀) ₂ [MnGe ₄ Se ₁₀]	2.2844(13) – 2.3700(13)	None	[168]
(C ₁₁ NH ₂₆) ₄ [Ge ₄ Se ₁₀]	2.2553(38) – 2.3809(20)	None	[52]
(C ₈ N ₂ H ₁₅) ₂ [Ge ₄ Se ₉]	2.2420(14) – 2.4086(13)	None	[106]
(C ₉ N ₂ H ₁₇) ₂ [Sn ^{II} (Ge ₄ Se ₁₀)]	2.2411(13) – 2.3802(13)	None	[106]
(C ₈ N ₂ H ₁₅) ₂₄ [Sn ₃₆ Ge ₂₄ Se ₁₃₂]	2.2886(54) – 2.3785(29)	None	[95]
(C ₆ N ₂ H ₁₁) ₆ [Ge ₈ Se ₁₉]	2.2388(21) – 2.4127(21)	None	[169]
(C ₆ N ₂ H ₁₁) ₈ [Ge ₁₆ Se ₃₆]	2.2296(35) – 2.3978(33)	None	[169]

Like the related Sn/Ge cluster, the [Ge^{II}₄(Ge^{IV}₄Se₁₀)₄]⁸⁻ cage embeds a Cs⁺ ion, which not only plays a significant structure-directing and structure-stabilizing role but also reduces the negative charges of the supercluster from 8- to 7-. The Cs⁺ ion is embedded in an inner cavity and stabilized by the lone pairs of the 4 Ge^{II} atoms [Cs···Ge 3.8208(1)–3.8557(1) Å] and 12 Se²⁻ anions [Cs···Se 4.1145(1)–4.3489(1) Å], see Figure 3.15b,c.

In contrast to the synthesis of (C₄C₁C₁Im)₇[Cs@Sn^{II}₄(Ge^{IV}₄Se₁₀)₄] by the ionothermal reaction of [Cs₄(H₂O)][Ge₄Se₁₀], SnCl₄, and [Pt@Bi₁₀][AlBr₄]₄, compound **5** was synthesized from a single-source precursor, [Cs₄(H₂O)][Ge₄Se₁₀]. The reduction of Ge^{IV} to Ge^{II} during this synthesis remains not fully elucidated, as either selenide or cyanide or both would be suitable for allowing the reduction of Ge^{IV}. Although, it is known that the presence of (C₂C₁Im)[B(CN)₄] is mandatory for obtaining the mixed-valent product. This is ascribed to the fact that (CN)⁻, which is released from the anion, is oxidized to cyanogen, C₂N₂, which under the basic condition (H₂O plus amine) disproportionates into cyanide and cyanate. In addition, the size of the ionic liquid cation seems to

subtly affect the crystallization since it was not possible to isolate a compound comprising this cluster anion from $(C_4C_1C_1Im)[BF_4]$ which in turn allowed the crystallization of the Sn/Ge/Se analogue. Apparently, the overall smaller size of the purely Ge- / Se-based anion (edge length $Se\cdots Se$ 15.78–16.01 Å) fits better to the smaller-size $(C_2C_1Im)^+$ cations, while the larger Sn/Ge/Se anion (edge length $Se\cdots Se$ 16.18 Å) is well accommodated within a $(C_4C_1C_1)^+$ counterion environment. Consequently, the packing schemes of the clusters in the crystals of the compounds differ (Figure 3.17). In compound **5**, the cluster anions settle into a diamond-like arrangement, and as of the latter reported compound, the clusters adopt a high symmetrical primitive cubic alignment.

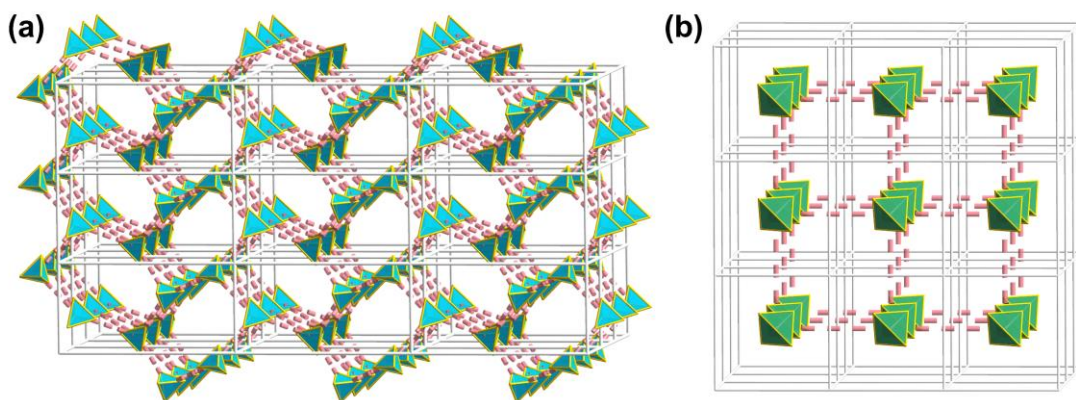


Figure 3.17. Arrangement of the crystal of compound **5**, each blue polyhedron represents one $[Cs@Ge^{II}_4(Se^{IV}_4Se_{10})_4]^{7-}$ cluster anion (a). Arrangement of the crystal of reported $(C_4C_1C_1Im)_7[Cs@Sn^{II}_4(Se^{IV}_4Se_{10})_4]$ compound, each green polyhedron represents one $[Cs@Sn^{II}_4(Se^{IV}_4Se_{10})_4]^{7-}$ cluster anion (b).

Compounds **6a** and **6b** crystallize in the triclinic crystal system, space group $P\bar{1}$, with unit cell volume of 7842.1(6) Å³ (**6a**) and 7822.6(5) Å³ (**6b**), respectively. As compounds **6a** and **6b** differ in structural details only, their general structural features will be discussed together here. The crystal structure of compound **6a** is displayed in Figure 3.18, as an example of both **6a** and **6b**.

Similar to the architecture of the anion in compound **5**, four T2-type $[Ge_4Se_{10}]^{4-}$ units are connected in compound **6** to form a supercluster assembly (Figure 3.18a). However, the way of connection is significantly different in several regards compared to the connectivity in **5**. In this case, not four Ge^{II} atoms, but six Cu^I atoms serve to connect the $[Ge_4Se_{10}]^{4-}$ moieties, which are thus arranged in a different way relative to each other: they are connected along the six edges of a T2,2-related architecture (Figure 3.18b, Tp,q -like clusters possess a defect Tn -type architecture, e.g., the T2,2-type is a defect T4-type architecture lacking a central T2-type cluster connecting four T2-type units) and not *via* the four faces of a P2-related one. Nevertheless, while the T2 units are linked *via* a single μ -bridging atom in a real T2,2-type cluster, the T2 moieties in the *pseudo*-T2,2 structure of the heterometallic cluster in **6** are connected *via* Se–Cu^I–Se bridges. The anion of **6** therefore represents the first superclusters with such triatomic bridges including transition metal atoms. The edge lengths of the superclusters are larger than they would be in a (hypothetical) Ge-/Se-based T2,2 cluster (Figure 6.12), being 18.3509(5)–18.7436(6) Å in compound **6a**.

and 18.4181(8)–18.7532(7) Å in compound **6b** (the edges of the Ge-/S-based T2,2 cluster in 3D- $\{\text{Ga}_{3.33}\text{Ge}_{0.67}\text{S}_8\}$ are 14.27–14.43 Å)^[19].

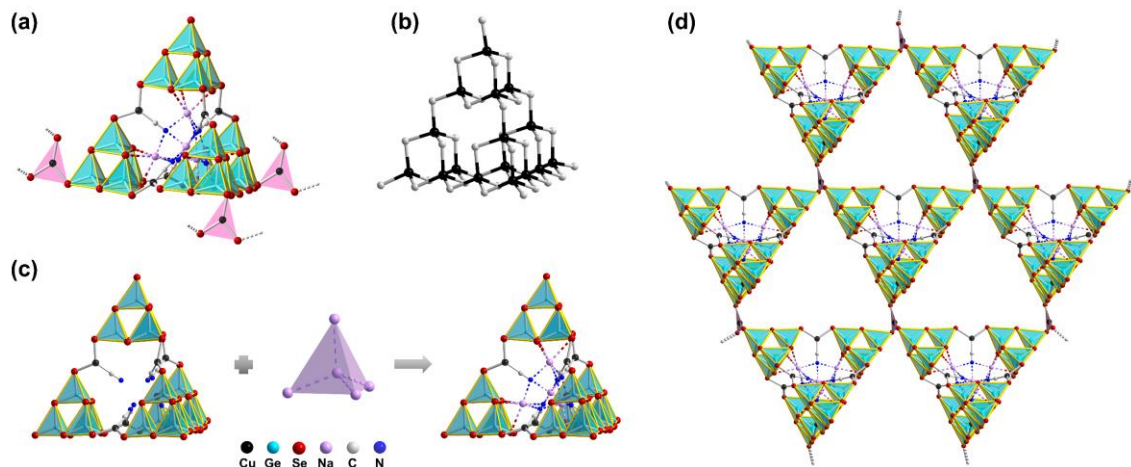


Figure 3.18: Molecular structure of one *pseudo*-T2,2-like $[\text{Na}_5(\text{CN})_6@\text{Cu}_6(\text{Ge}_4\text{Se}_{10})_4(\text{Cu})]^{10-}$ supercluster in compound **6a** (as an example for **6a** and **6b**) along with three $\{\text{CuSe}_3\}$ units connecting the supercluster with its neighbors (a). Structure of the T2,2 defect-supertetrahedral cluster in 3D- $\{\text{Ga}_{3.33}\text{Ge}_{0.67}\text{S}_8\}$ for comparison (b). Illustration of the architecture of the supercluster without (left) and with the inner $\{\text{Na}_5\}$ moiety for clarity (c). Fragment of the two-dimensional layer in compound **6a** (imidazolium counterions omitted for clarity) (d).

Compound **6** exhibits a complex structural arrangement where the Cu¹ atoms not only bridge $[\text{Ge}_4\text{Se}_{10}]^{4-}$ units but also coordinate with an inner unit filling the cluster cavity: besides the two Se²⁻ neighbors from two adjacent T2 clusters, the copper atoms are coordinated by a cyanide group, the presence of which has also been unprecedented in supertetrahedral chalcogenide cluster chemistry thus far. The (CN)⁻ anions serve as ambident ligands, coordinating to Na⁺ atoms with their second donor site. Specifically, the six cyanide ligands bridge the six edges of an inner Na₄ tetrahedron, which is centered by the fifth Na⁺ ion that is also coordinated by the six (CN)⁻ anions, each of which thus acts as an $\eta^1:\eta^3-\mu$ ligand (Figure 3.18c). The five Na⁺ ions, in turn, serve to balance a part of the overall negative charges of the anion, but at the same time provide us an opportunity to investigate the selectivity of the cluster formation toward Na⁺ as the stabilizing alkali metal ion and on a long term also the potential Na⁺ storage properties of such compounds.

As illustrated in Figure 3.18d, heterometallic superclusters coordinate to tri-connected Cu atoms with three of their four terminal Se atoms. This coordination leads to the formation of a 2D honeycomb (**hcb**) superlattice with an overall composition of 2D- $\{[\text{Na}_5(\text{CN})_6@\text{Cu}_6(\text{Ge}_4\text{Se}_{10})_4(\text{Cu})]^{10-}\}$. The slight structural differences between compounds **6a** and **6b** are caused by different relative orientations of the $\{\text{Cu}(\mu\text{-Se})_3\}$ groups that connect the *pseudo*-T2,2 clusters (Figure 3.19).

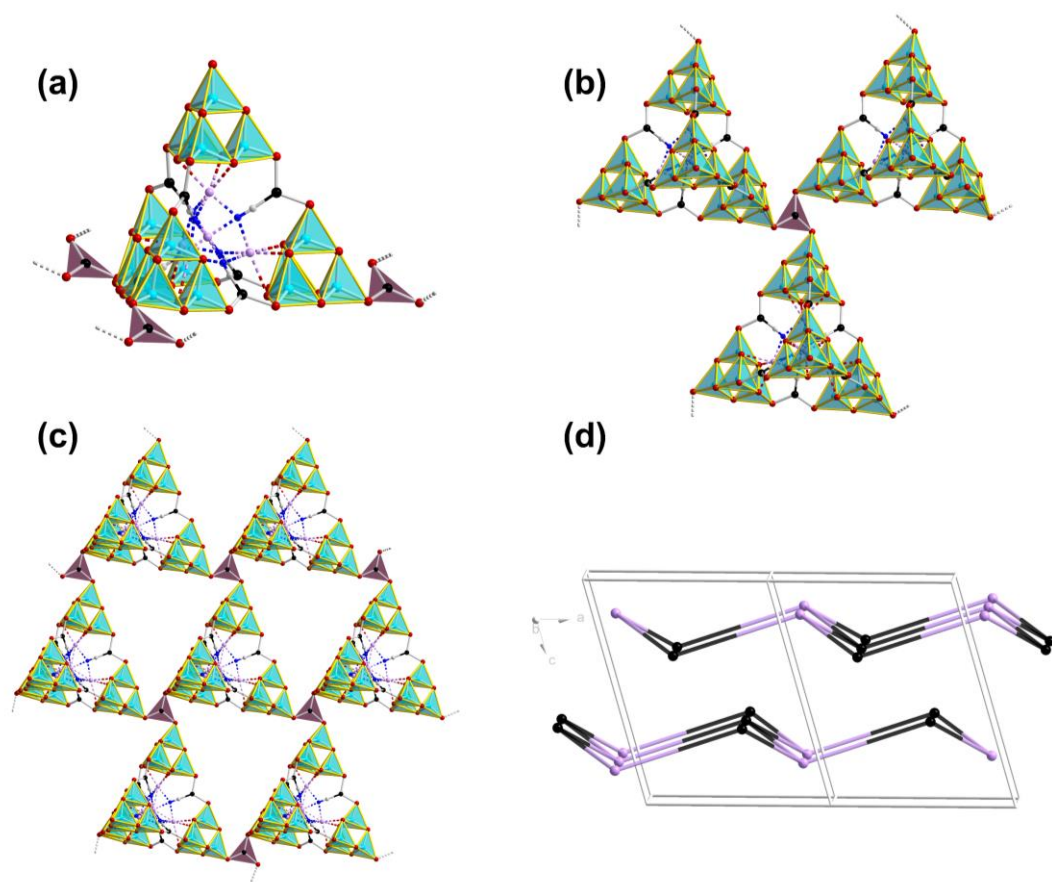


Figure 3.19: Linkage mode between single Cu^+ linker and *pseudo*-T2,2-type heterometallic supercluster in compound **6b**, each supercluster is connected with three copper linkers (a); and vice versa (b); two-dimensional layer structure of compound **6b** (c); and the arrangement of simplified layers in a $2 \times 1 \times 1$ supercell via treating each *pseudo*-T2,2-type heterometallic cluster (purple) and Cu^1 bridge (black) as a node (c – d). Counterions are not shown for clarity.

During structure refinement of **6a**, all ionic liquid cations could be localized from the difference Fourier map. In the case of **6b**, 8 of 10 counterions were localized and refined explicitly, while the electron density of the two remaining ones needed to be detracted from the data using the back Fourier transform algorithm. All refinement details are summarized in Table 6.15 and Table 6.16 in Chapter 6.

For reactions in supercritical solvents or ionic liquids, the most important templates are commonly ammonium cations or auxiliary amines applied in the reactions. Less attention has been spent on the alkali metal cations that were usually only part of the reactants. These findings show, however, that they do play a crucial role for certain compounds, which may be used for the targeted capture or separation of the alkali metal cations. It is thus interesting to explore the selectivity of the two compounds for the alkali metal cations stabilizing them in more detail, which was achieved by means of quantum chemical calculations using DFT methods, as well as doing corresponding cross-experiments followed by SC-XRD, EDX, and ESI-MS studies.

3.2.3 Additional characterizations compounds **5** and **6**

3.2.3.1 Quantum chemical studies

For the identification of metal types being preferred for the encapsulation, DFT calculations addressed the incorporation of A^+ into the discrete cluster assembly of compound **5** by a hypothetical reaction given as eq 1:



This reaction scheme models the uptake of an alkali metal cation in an empty supercluster (Figure 3.20, for $\text{A} = \text{Cs}$ as an example), thus delivering the binding energies of A^+ to the empty “[$\text{Ge}_4(\text{Ge}_4\text{Se}_{10})_4$]⁸⁻” supertetrahedron according to eq 2:

$$E_B = E([\text{A}@\text{Ge}_4(\text{Ge}_4\text{Se}_{10})_4]^{7-}) - E(\text{A}^+) - E(\text{“Ge}_4(\text{Ge}_4\text{Se}_{10})_4]^{8-}\text{”}) \quad (2)$$

The calculated bond energies provide insights into the stability of alkali metal cations within the pseudo-P2 type cluster architecture. The bond energies are as follows: E_B of -47.6 (Cs^+), -65.0 (Rb^+), -61.8 (K^+), -25.7 (Na^+), and -15.8 (Li^+) kJ/mol. The small differences between the energies obtained for Cs^+ , Rb^+ , and K^+ suggest that they could all potentially be accommodated within the cavity. This indicates that in theory, the cluster could selectively incorporate Cs^+ , Rb^+ , or K^+ cations, although the mode's accuracy does not significantly distinguish between these three due to the closeness in their bond energies. However, it is worth noting that all cations smaller than Cs^+ show an increasing tendency of adopting unsymmetrical off-center position. Distances from the center of gravity are 0.0 (Cs^+), 0.1 (Rb^+), 37.2 (K^+), 147.4 (Na^+), and 219.4 (Li^+) pm. The cavity thus seems to be perfectly adopted to the needs of a symmetrical Cs^+ inclusion, as a valuable precondition for crystallization.

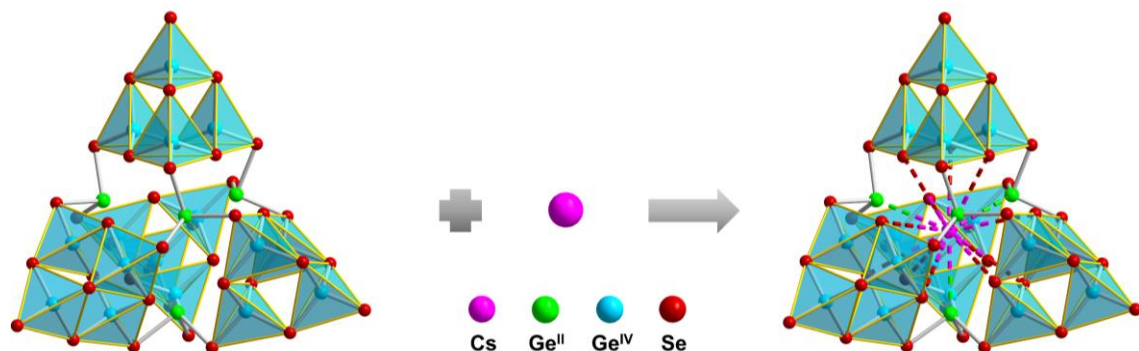


Figure 3.20: Illustration of the uptake of a Cs^+ ion by the surrounding “[$\text{Ge}_{20}\text{Se}_{40}$]⁸⁻” cage, according to eq 2. The calculated clusters symmetrize during geometry optimization.

3.2.3.2 Exchange Reaction, and Experimental Proof

To investigate the selectivity of compound **5** for Cs^+ cations, a series of cross-experiments were conducted as outlined in Scheme 3.3 and summarized in Table 3.3. The experimental conditions were the same as those for the preparation of compound **5**, except for variations in the alkali metal

salts of the $[\text{Ge}_4\text{Se}_{10}]^{4-}$ reactant. Namely, $[\text{Li}_4(\text{H}_2\text{O})_{20.33}][\text{Ge}_4\text{Se}_{10}]$, $\text{Na}_4[\text{Ge}_4\text{Se}_{10}]$, $[\text{K}_4(\text{H}_2\text{O})_3][\text{Ge}_4\text{Se}_{10}]$, or $\text{Rb}_4[\text{Ge}_4\text{Se}_{10}]$ were used, along with the addition of binary salts of other alkali metal salts, CsCl , NaCl , KCl , RbCl or $\text{NaCl} + \text{CsCl}$, to the original or modified reaction mixture.

Reproducibly, the use of $[\text{Li}_4(\text{H}_2\text{O})_{20.33}][\text{Ge}_4\text{Se}_{10}]$, $\text{Na}_4[\text{Ge}_4\text{Se}_{10}]$, $[\text{K}_4(\text{H}_2\text{O})_3][\text{Ge}_4\text{Se}_{10}]$, or $\text{Rb}_4[\text{Ge}_4\text{Se}_{10}]$ did not afford crystals of compound **5** (Scheme 3.3) but led to the crystallization of crystals of either compound $(\text{C}_2\text{C}_1\text{Im})_4[\text{Ge}_4\text{Se}_{10}]$ or $(\text{C}_2\text{C}_1\text{Im})_6[\text{Ge}_8\text{Se}_{19}]$ that have been discussed in chapter 3.1. As detailed in Scheme 3.3, the addition of CsCl to such a reaction mixture caused the formation of compound **5** in all cases, as verified by SC-XRD. In addition, the yield of **5** from all controlled combinations is close to the number of the single-source formed one and is listed in Table 6.2.



Scheme 3.3: Schematic illustration of the synthesis of the target compound $(\text{C}_2\text{C}_1\text{Im})_7[\text{A}@\text{Ge}^{\text{II}}_4(\text{Ge}^{\text{IV}}_4\text{Se}_{10})_4]$ by the use of $[\text{Li}_4(\text{H}_2\text{O})_{20.33}][\text{Ge}_4\text{Se}_{10}]$, $\text{Na}_4[\text{Ge}_4\text{Se}_{10}]$, $[\text{K}_4(\text{H}_2\text{O})_3][\text{Ge}_4\text{Se}_{10}]$, $\text{Rb}_4[\text{Ge}_4\text{Se}_{10}]$, and $[\text{Cs}_4(\text{H}_2\text{O})][\text{Ge}_4\text{Se}_{10}]$ as starting materials (a). Synthesis under addition of CsCl to the above-mentioned reaction mixtures (b). Synthesis under addition of NaCl to the above-mentioned reaction mixtures (c). Synthesis under addition of KCl to the above-mentioned reaction mixtures (d). Synthesis under addition of RbCl to the above-mentioned reaction mixtures (e). Synthesis under addition of NaCl and CsCl to the above-mentioned reaction mixtures (f).

Table 3.3: Summary of experiments undertaken to explore the selectivity of compound **5** for alkali metal ions, the yield of specific reactions that allow the formation of **5** is given in Table 6.2.

	no additional ACl	CsCl	NaCl	KCl	RbCl	NaCl + CsCl
[Li ₄ (H ₂ O) _{20.33}][Ge ₄ Se ₁₀]	×	√	×	×	×	√
Na ₄ [Ge ₄ Se ₁₀]	×	√	×	×	×	√
[K ₄ (H ₂ O) ₃][Ge ₄ Se ₁₀]	×	√	×	×	×	√
Rb ₄ [Ge ₄ Se ₁₀]	×	√	×	×	×	√
[Cs ₄ (H ₂ O)][Ge ₄ Se ₁₀]	√	√	√	√	√	√

^a√ denotes that it was possible to crystallize compound **5**; × denotes that it was not able to isolate compound **5**

As an example, in the case of using [K₄(H₂O)₃][Ge₄Se₁₀] and CsCl as the starting materials, detailed refinement procedures were employed to analyze the selectivity of compound **5** for Cs⁺ cations: in the first refinement procedure, the Q peak on the difference Fourier map representing the embedded cation was assigned the atom form factor of a K atom (Figure 3.21a), which yielded unacceptable *R*1 and *wR*2 values of 0.1176 and 0.3277, respectively (Figure 3.21b). In the second refinement procedure, the inner Q peak was assigned the atom form factor of a Cs atom instead (Figure 3.21c), which led to a significant improvement of the final *R*1 and *wR*2 values of 0.0814 and 0.2248, respectively (Figure 3.21d). The result is in agreement with the fact that the difference Fourier map after refinement indicates a clear under-assignment of electron density around the embedded site if it is considered to be a K atom (Figure 3.21a), whereas it is a perfect match regarded as a Cs atom (Figure 3.21c). The series of cross-experiments proved the high selectivity of the crystal structure of compound **5** for inclusion of Cs⁺ as compared to that of the lighter congeners (Scheme 3.3c–f).

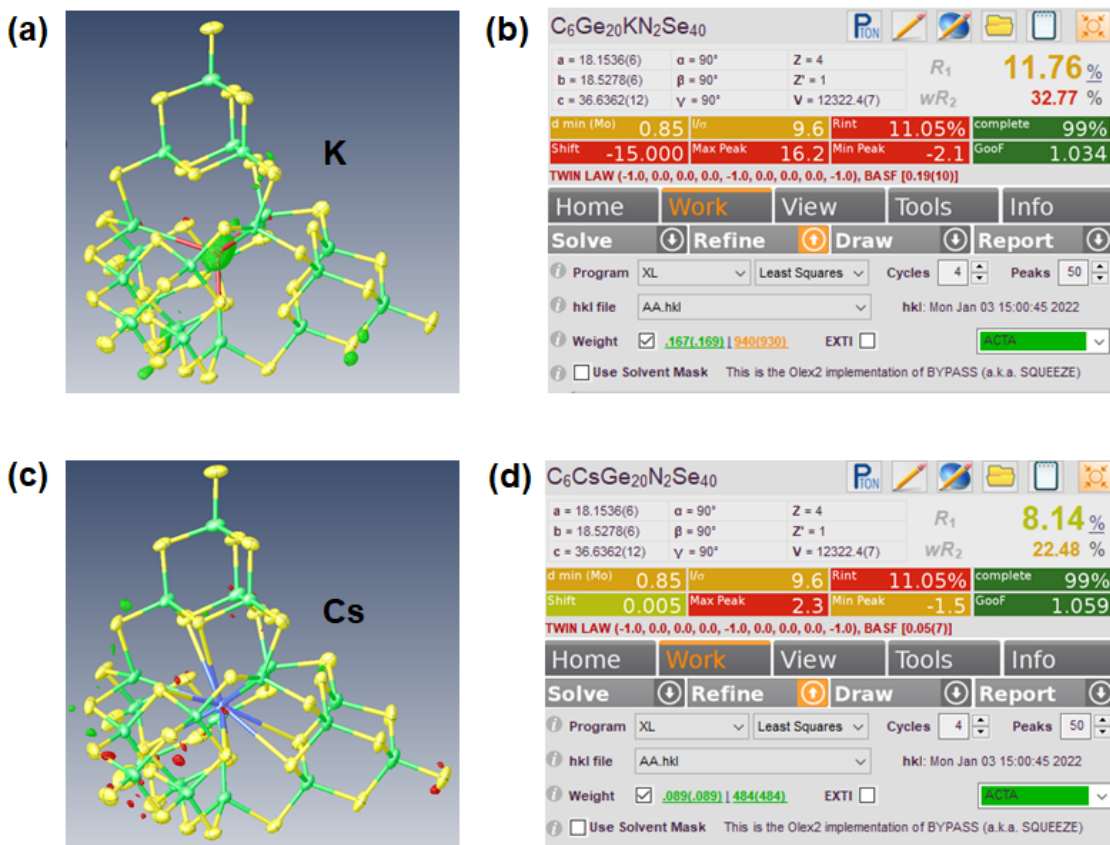


Figure 3.21: Electron density map and refinement details upon the X-ray diffraction experiment of compound **5** under assignment of the embedded atom as K (a – b) or as (c – d).

Furthermore, the preference for Cs^+ during the crystallization process was demonstrated by semi-quantitative EDX of the as-synthesized crystals (Figure 3.22). The data clearly indicate a predominance of Cs^+ in compound **5** across all combinations of reactants tested. In comparison with other alkali metals, the Cs^+ content is predominant in compound **5**; however, it was also possible to detect trace amounts of Li^+ , Na^+ , K^+ , or Rb^+ . Initially, it appears that the concentration of these alkali metals increases in the order of $\text{Li}^+ < \text{Na}^+ < \text{K}^+ < \text{Rb}^+$ (as expected with regard to the ion radius approaching the one of Cs^+). However, it's important to note that the accuracy of these measurements varies significantly, with larger errors associated with smaller amounts of the detected ions.

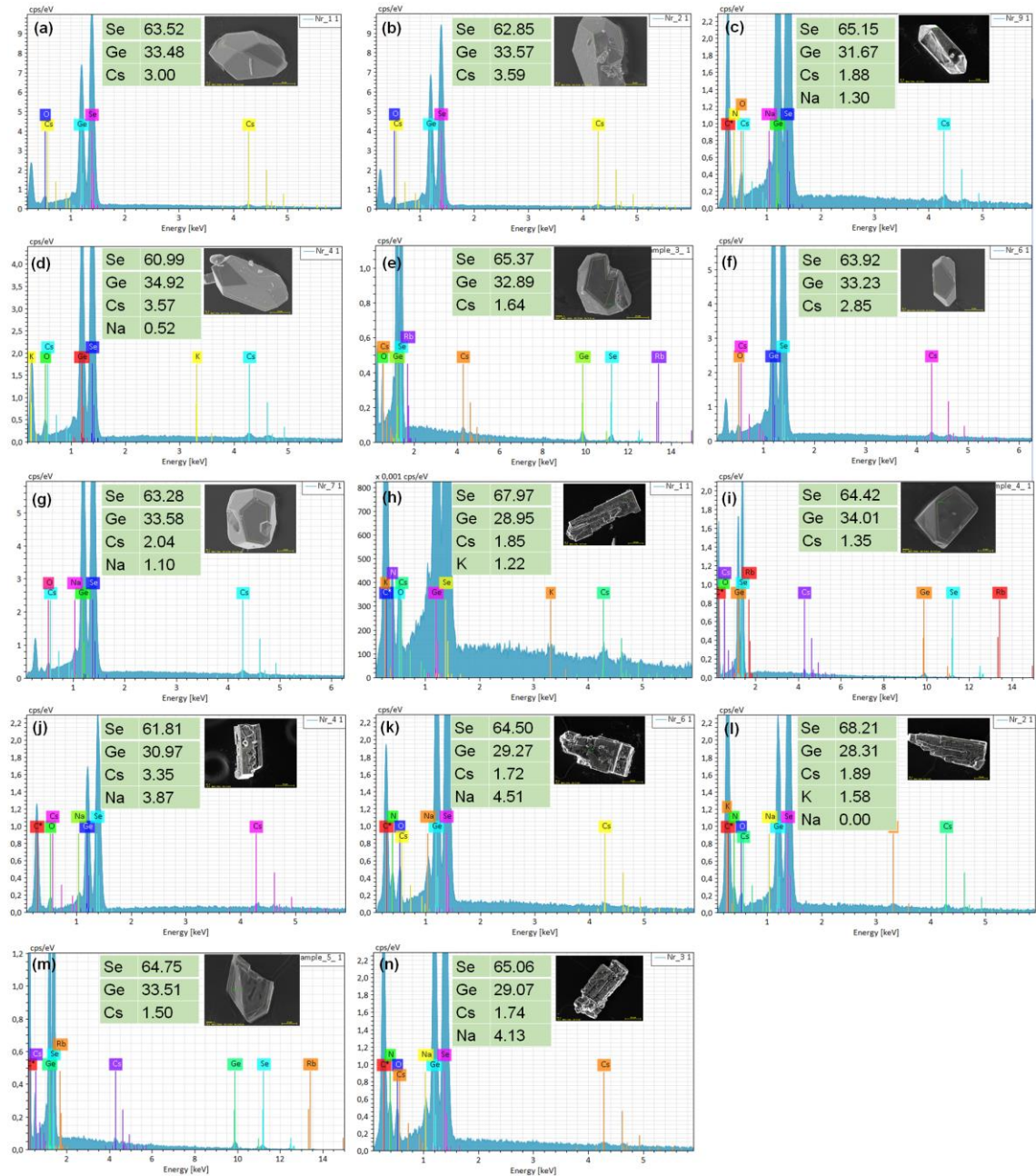


Figure 3.22: EDX spectra and analysis result of compound **5** crystallized from a series of cross experiments (see Table 3.3) along with an electron microscopy image of the investigated crystal individual from the respective ionothermal reaction, using different starting materials: $[\text{Cs}_4(\text{H}_2\text{O})][\text{Ge}_4\text{Se}_{10}]$ (a). $[\text{Li}_4(\text{H}_2\text{O})_{20.33}][\text{Ge}_4\text{Se}_{10}]$ and CsCl (b). $\text{Na}_4[\text{Ge}_4\text{Se}_{10}]$ (c). $[\text{K}_4(\text{H}_2\text{O})_3][\text{Ge}_4\text{Se}_{10}]$ (d). $\text{Rb}_4[\text{Ge}_4\text{Se}_{10}]$ and CsCl (e). $[\text{Cs}_4(\text{H}_2\text{O})][\text{Ge}_4\text{Se}_{10}]$ and CsCl (f). $[\text{Cs}_4(\text{H}_2\text{O})][\text{Ge}_4\text{Se}_{10}]$ and NaCl (g). $[\text{Cs}_4(\text{H}_2\text{O})][\text{Ge}_4\text{Se}_{10}]$ and KCl (h). $[\text{Cs}_4(\text{H}_2\text{O})][\text{Ge}_4\text{Se}_{10}]$ and RbCl (i). $[\text{Li}_4(\text{H}_2\text{O})_{20.33}][\text{Ge}_4\text{Se}_{10}]$, NaCl and CsCl (j). $\text{Na}_4[\text{Ge}_4\text{Se}_{10}]$, NaCl , and CsCl (k). $[\text{K}_4(\text{H}_2\text{O})_3][\text{Ge}_4\text{Se}_{10}]$, NaCl , and CsCl (l). $\text{Rb}_4[\text{Ge}_4\text{Se}_{10}]$, NaCl , and CsCl (m). $[\text{Cs}_4(\text{H}_2\text{O})][\text{Ge}_4\text{Se}_{10}]$, NaCl , and CsCl (n). Note that the detection of Li is impossible with this method.

This result aligns with the findings from the DFT study, indicating that while it is theoretically possible to include K^+ or Rb^+ , their incorporation is minimal. This supports the hypothesis that

the observed distortion in the crystal structure, which is only observed in the crystal structure (while the assembly relaxed into a higher symmetry during geometry optimization by quantum chemistry), causes the high selectivity for Cs^+ owing to a thus perfect match of the ionic radius of the inner ion with the cavity. In addition, this underscores the meaningfulness of actually crystallizing the compound for effective ion separation applications.

A final proof for the inclusion of Cs^+ in the cluster anion of isolated compound **5** was obtained by means of ESI-MS, as a powerful tool for the investigation of precise compositions. Isolated and washed single crystals obtained from the ionothermal reaction of $[\text{K}_4(\text{H}_2\text{O})_3][\text{Ge}_4\text{Se}_{10}]$ with CsCl were dissolved in DMF, and the fresh solutions were investigated. A series of signals of the $[\text{Cs}@\text{Ge}_4(\text{Ge}_4\text{Se}_{10})_4]^{q-}$ anion along with different numbers of counterions or H^+ and thus with charges ranging from 4 $-$ to 3 $-$ and 2 $-$ (Figure 3.23a) were detected. The experimental isotope patterns show perfect agreement with the simulated ones. The dominant signals can be assigned to species of the formulas $\{(\text{C}_6\text{N}_2\text{H}_{11})_{3-x}\text{H}_x\text{Cs}@\text{Ge}_4(\text{Ge}_4\text{Se}_{10})_4\}^{4-}$ ($x = 0-2$). An overlap with the isotope pattern of $\{(\text{C}_6\text{N}_2\text{H}_{11})_{3-x}\text{H}_x\text{K}@\text{Ge}_4(\text{Ge}_4\text{Se}_{10})_4\}^{4-}$ is coincidentally caused by the similar molecular weight of the $(\text{C}_2\text{C}_1\text{Im})^+$ cation and the difference between the atomic weight of Cs and K. As indicated in detail for the high-resolution mass peaks of $\{(\text{C}_6\text{N}_2\text{H}_{11})_2\text{H}_1\text{Cs}@\text{Ge}_4(\text{Ge}_4\text{Se}_{10})_4\}^{4-}$ and $\{(\text{C}_6\text{N}_2\text{H}_{11})_3\text{K}@\text{Ge}_4(\text{Ge}_4\text{Se}_{10})_4\}^{4-}$ (Figure 3.23b), the isotope patterns exhibit very similar m/z values, but that of $\{(\text{C}_6\text{N}_2\text{H}_{11})_3\text{K}@\text{Ge}_4(\text{Ge}_4\text{Se}_{10})_4\}^{4-}$ shows completely different relative abundances as compared to the experimental spectrum. In order to further distinguish the compositions, the mass spectra of the cluster anion with 3 $-$ charge, which amplifies the difference between simulated and experimental patterns due to the lower charge, are provided in Figure 3.23c,d.

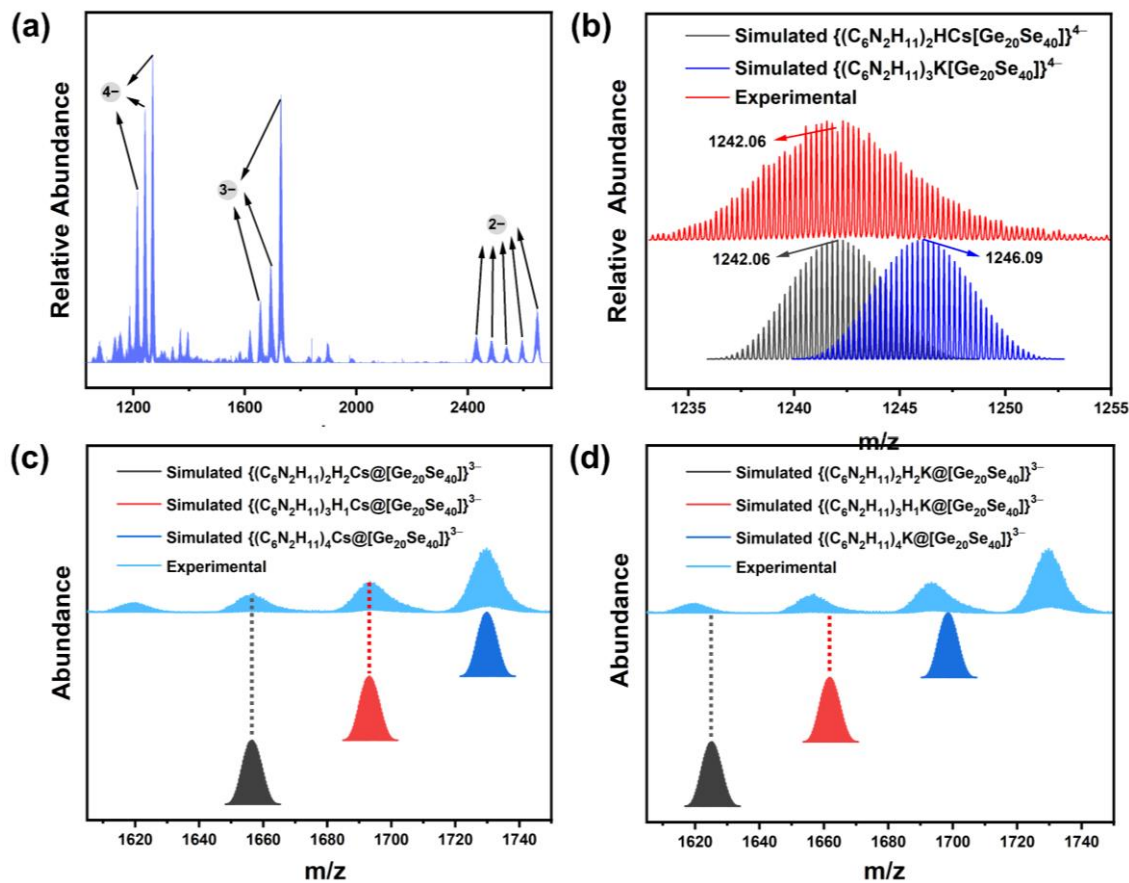


Figure 3.23. Overview of the ESI($-$) mass spectrum of a fresh solution of a single-crystal of compound **5** (upon ionothermal reaction of $[\text{K}_4(\text{H}_2\text{O})_3][\text{Ge}_4\text{Se}_{10}]$ with CsCl) in DMF. The cluster anion was detected with $2-$, $3-$ and $4-$ charges upon assembly with counterions $(\text{C}_2\text{ClIm})^+$ and H^+ (a). Comparison of the measured high-resolution mass peak around m/z 1242.06 (red) with the simulated spectra of $\{(\text{C}_6\text{N}_2\text{H}_{11})_2\text{H}_2\text{Cs}@[Ge_{20}\text{Se}_{40}]\}^{4-}$ (black) and $\{(\text{C}_6\text{N}_2\text{H}_{11})_3\text{K}@[Ge_{20}\text{Se}_{40}]\}^{4-}$ (blue) (b). Comparison of the experimental ESI-MS spectrum with the simulated spectra of $\{(\text{C}_6\text{N}_2\text{H}_{11})_2\text{H}_2\text{Cs}@[Ge_{20}\text{Se}_{40}]\}^{3-}$ (black), $\{(\text{C}_6\text{N}_2\text{H}_{11})_3\text{H}_1\text{Cs}@[Ge_{20}\text{Se}_{40}]\}^{3-}$ (red), and $\{(\text{C}_6\text{N}_2\text{H}_{11})_4\text{Cs}@[Ge_{20}\text{Se}_{40}]\}^{3-}$ (blue) (c). $\{(\text{C}_6\text{N}_2\text{H}_{11})_2\text{H}_2\text{K}@[Ge_{20}\text{Se}_{40}]\}^{3-}$ (black), $\{(\text{C}_6\text{N}_2\text{H}_{11})_3\text{H}_1\text{K}@[Ge_{20}\text{Se}_{40}]\}^{3-}$ (red), and $\{(\text{C}_6\text{N}_2\text{H}_{11})_3\text{H}_1\text{K}@[Ge_{20}\text{Se}_{40}]\}^{3-}$ (blue) (d), indicating the perfect fit if the presence of Cs^+ is assumed and the misfit if the presence of K^+ is assumed.

Clearly, the simulated mass peaks of the species $\{(\text{C}_6\text{N}_2\text{H}_{11})_{4-x}\text{H}_x\text{K}@\text{Ge}_4(\text{Ge}_4\text{Se}_{10})_4\}^{3-}$ (Figure 3.24c,d) differ from those appearing in the experimental spectrum, whereas the mass peaks of $\{(\text{C}_6\text{N}_2\text{H}_{11})_{4-x}\text{H}_x\text{Cs}@\text{Ge}_4(\text{Ge}_4\text{Se}_{10})_4\}^{3-}$ are an excellent match with the experimental ones. The mass spectra thus demonstrate both the integrity of the supramolecular cluster assembly (along with counterions) in solution and in the gas phase and the formation of $[\text{Cs}@\text{Ge}_4(\text{Ge}_4\text{Se}_{10})_4]^{7-}$ instead of $[\text{K}@\text{Ge}_4(\text{Ge}_4\text{Se}_{10})_4]^{7-}$ during crystallization. The comparison of measured mass spectrum with the simulated mass peaks of $\{(\text{C}_6\text{N}_2\text{H}_{11})_{5-x}\text{H}_x\text{Cs}@[Ge_{20}\text{Se}_{40}]\}^{2-}$ and $\{(\text{C}_6\text{N}_2\text{H}_{11})_{5-x}\text{H}_x\text{K}@[Ge_{20}\text{Se}_{40}]\}^{2-}$ species are also provided in Figure 3.24 for further amplifying the differences below.

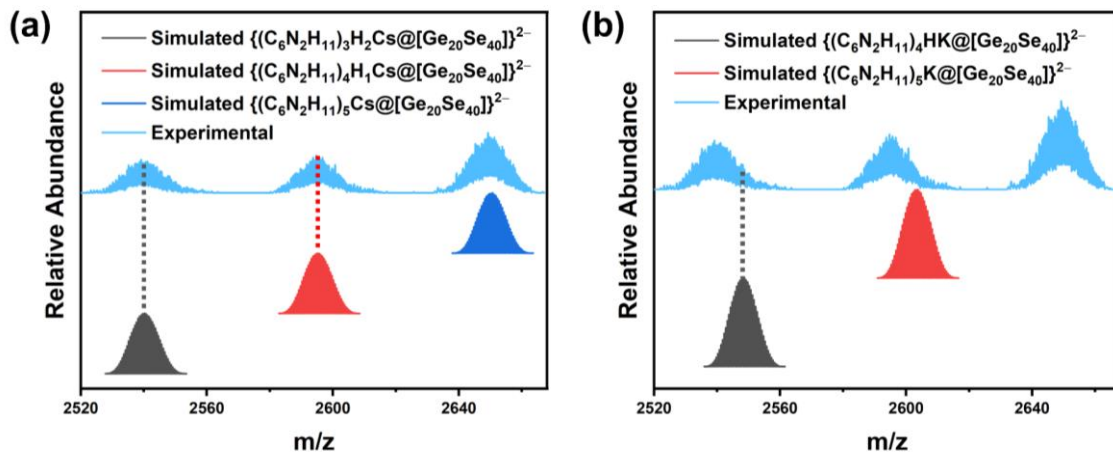
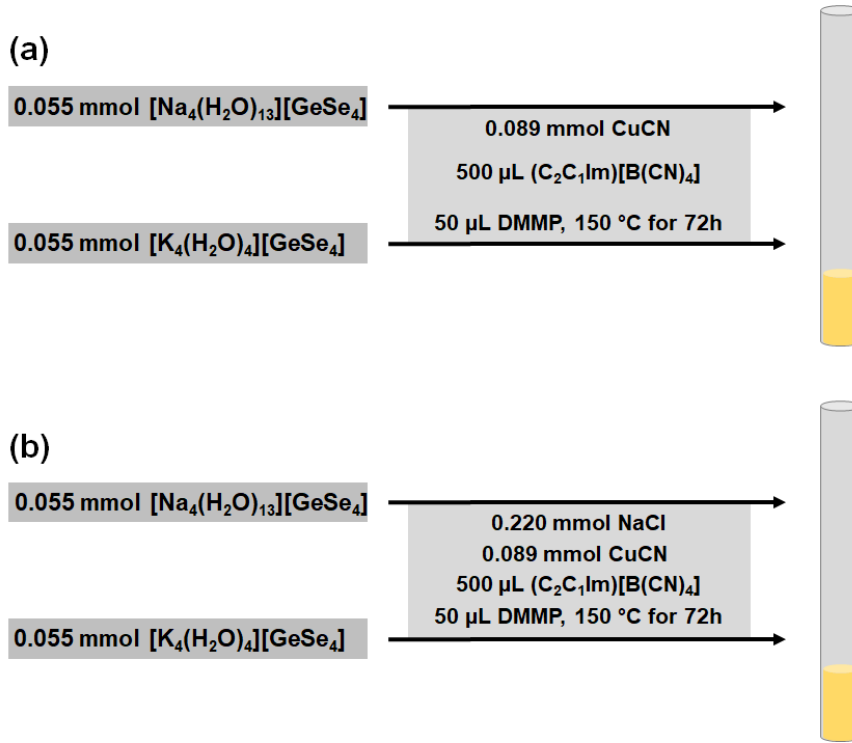


Figure 3.24: Comparison of the experimental ESI-MS spectrum with the simulated spectra of $\{(C_6N_2H_{11})_3H_2Cs@[Ge_{20}Se_{40}]\}^{2-}$ (black), $\{(C_6N_2H_{11})_4H_1Cs@[Ge_{20}Se_{40}]\}^{2-}$ (red), and $\{(C_6N_2H_{11})_5Cs@[Ge_{20}Se_{40}]\}^{2-}$ (blue) (a), $\{(C_6N_2H_{11})_4H_1K_1@[Ge_{20}Se_{40}]\}^{2-}$ (black), $\{(C_6N_2H_{11})_5K@[Ge_{20}Se_{40}]\}^{2-}$ (red) (b), indicating the perfect fit if the presence of Cs^+ is assumed.



Scheme 3.4: Schematic illustration of the synthesis of the target compound $(C_2C_1Im)_{10}[A_5(CN)_6@Cu_6(Ge_4Se_{10})_4(Cu)]$ by the simultaneous use of $[Na_4(H_2O)_{13}][GeSe_4]$, and $[K_4(H_2O)_4][GeSe_4]$ as starting materials (a). Synthesis under addition of NaCl to the reaction mixture comprising $[K_4(H_2O)_4][GeSe_4]$, but no $[Na_4(H_2O)_{13}][GeSe_4]$ (b).

Table 3.4: Summary of experiments undertaken to explore the selectivity of compound **6a** for alkali metal ions.^a

	no additional ACl	NaCl
[Na ₄ (H ₂ O) ₁₄][GeSe ₄]	✓	✓
[K ₄ (H ₂ O) ₄][GeSe ₄]	✗	✓

^a✓ denotes that it was possible to crystallize compound **6a**; ✗ denotes that it was not able to isolate compound **6a**

Another series of experiments were undertaken to investigate the selective incorporation of Na⁺ during crystallization of compound **6a**, which are summarized in Table 3.4 and Scheme 3.4. The study was restricted to a cross-check of the most closely related K⁺ as the competing ion during the crystallization process as this already ruled out the necessity to continue with the less similar ones. When the reaction conditions were replicated for the synthesis of compound **6a**, but with [K₄(H₂O)₄][GeSe₄] replacing [Na₄(H₂O)₁₄][GeSe₄], a crystal structure similar to **6a** with K⁺ embedded inside the heterometallic cage could not be obtained. (Table 3.4). However, crystals could be isolated upon the addition of NaCl and [K₄(H₂O)₄][GeSe₄], which was confirmed by means of SC-XRD measurements and corresponding refinement. According to the difference Fourier maps, all the embedded A⁺ atoms were determined to be exclusively Na⁺. As expected, R1 and wR2 values do not differ a lot, but still indicate a preference for the assignment of Na⁺ to the site of the A⁺ atom (0.0502 and 0.1243, respectively; Figure 3.25a,b) as compared to the assignment of K⁺ to this site (0.0545 and 0.1345, respectively; Figure 3.25c,d). These results are supported by EDX measurements (Figure 3.25e,f). Due to the polymeric nature of the anionic substructure, the compounds **6a** and **6b** exhibit low solubility, which precluded the use of mass spectrometric analyses and molecular quantum chemistry for further characterization. However, the experimental proofs given above are all aligned and clearly indicate that compounds **6a** and **6b** are based exclusively on the ion-selective cluster assembly with the aid of Na⁺ and Cu⁺.

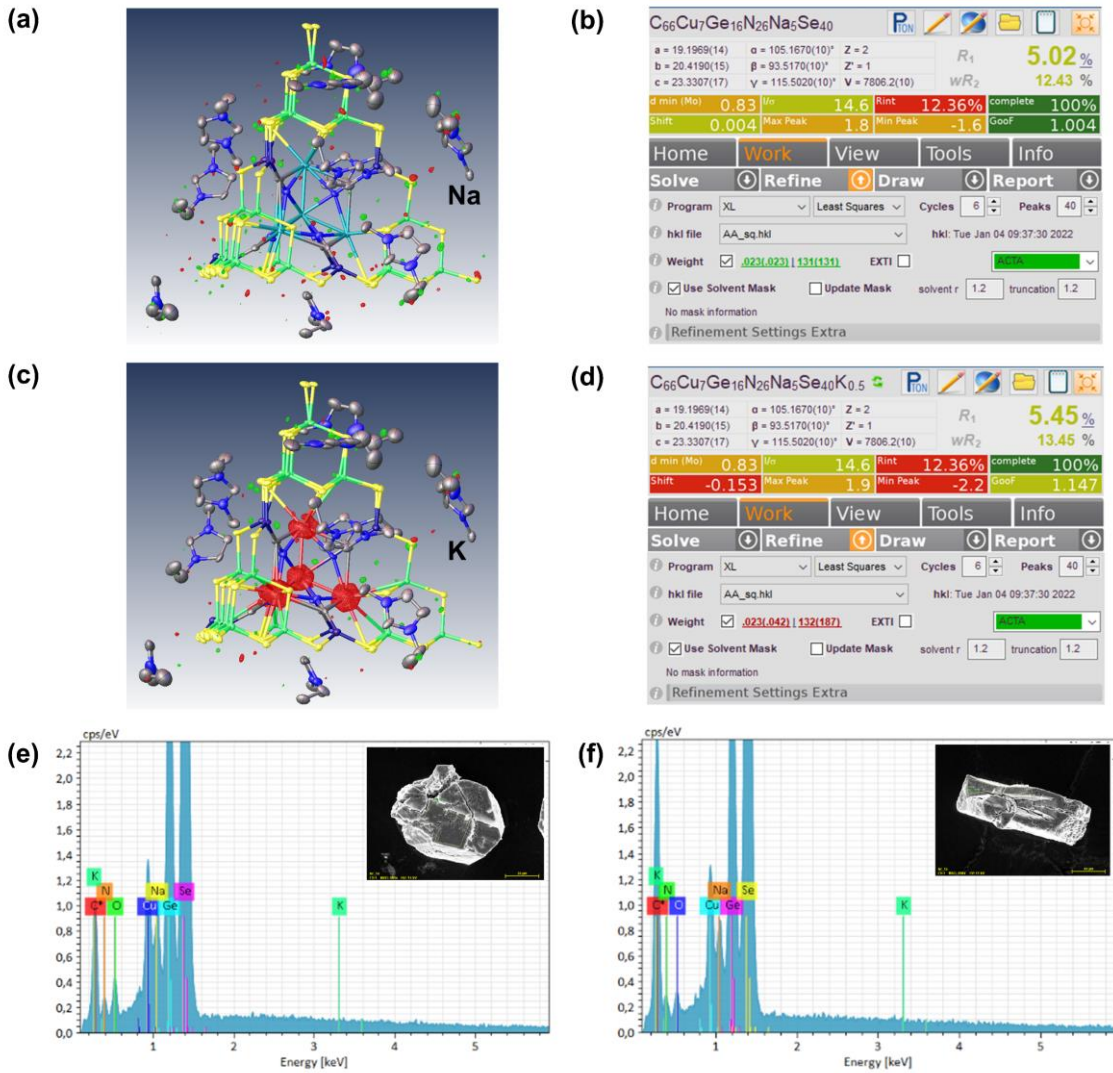


Figure 3.25: Electron density map and refinement details upon the X-ray diffraction experiment of compound **6a** under assignment of the embedded atom as Na (a – b); or as K (c – d), while the R_1 and wR_2 values do not differ significantly owing to the more similar characteristics of Na and K (as compared to the comparison of Na and Cs), but the electron density map clearly indicates a preference of Na over K on these positions. EDX spectra and analysis result of **6a** crystallized from different reaction mixtures using different starting materials $[\text{Na}_4(\text{H}_2\text{O})_{14}][\text{GeSe}_4]$ and NaCl (e), or $[\text{K}_4(\text{H}_2\text{O})_4][\text{GeSe}_4]$ and NaCl (f).

3.2.4 Conclusions

Through ionothermal reactions and subsequent crystallization, ion-selective assembly of supertetrahedral clusters into discrete or polyhedral supramolecular assemblies based on $[\text{Ge}_4\text{Se}_{10}]^{4-}$ anions were introduced. The discrete substructure, which represents a defect- or *pseudo*-P2-type architecture, is the largest supertetrahedral selenido germanate anion and the first one to feature Ge^{II} and Ge^{IV} co-existing in supertetrahedral chalcogenides. The polymeric substructures, which were isolated in two crystalline polymorphs, forming two dimensional layers. They are based on similar supramolecular cluster assemblies but differ in detail owing to the additional incorporation

of Cu⁺. Both types of compounds exhibit an exclusive selectivity for one specific type of alkali metal cations included in the crystalline compound. The anion in compound **5** shows high selectivity for Cs⁺, while the anionic substructure in compounds **6a** and **6b** selectively incorporate Na⁺. This selectivity has been confirmed by a variety of analytical methods. These compounds serve as models for further development of ion-selective cluster assemblies in crystalline phases. They hold promise as tools for targeted ion capture and separation applications, leveraging their unique structural and selectivity properties in environmental and chemical processes.

3.3 Structural expansion and enhanced photocurrent conversion of selenido stannates with Cu⁺ ions

The results of this chapter have been published in the following journal:

Zhou Wu, Benjamin Peerless, Panpan Wang, Wolfgang Schuhmann, and Stefanie Dehnen*, Structural Expansion and Enhanced Photocurrent Conversion of Selenido Stannates with Cu⁺ Ions. *JACS Au* **2024**, *4*, 3788–3799.

3.3.1 Introduction

Tin chalcogenides, particularly in ternary or quaternary forms with other metals, represent a crucial area of research in advanced materials for various high-end technologies. Examples include lead tin chalcogenides^[170,171], PbSnCh₂ (Ch = S or Se), copper tin chalcogenides^[172,173], Cu₂ShCh₃, or copper zinc tin chalcogenides^[174,175], Cu₂ZnSnCh₄. These materials are highly promising for thermoelectric or light-conversion technologies. The subtle impact of the admixture of Cu⁺ to tin selenide(s) has been intensively studied, and nanosized versions of the compounds in thin films were shown to be excellent materials for absorber layers in thin film solar cells^[176–178]. However, there are still many open questions regarding the synthetic access to such materials, especially in the context of new variations in compositions and their crystalline (nano)structures.

Multinary, cluster-based crystalline chalcogenido metalates, particularly those exhibiting micropores, have long been regarded as the “younger siblings” of zeolites^[21], as they share many commonalities in terms of the synthetic approaches^[27], of their structural subunits^[19], and also of functional applications^[155]. Anionic zeolite substructures are usually constructed from aluminates and silicates, in which ammonium or alkali or alkaline earth metal counter cations serve as structure-directing agents^[89,179,180] (see also chapter 1). Upon using the heavier congeners of these three main-group elements, typically Ga(III)/In(III), Ge(IV)/Sn(IV), and S(–II)/Se(–II), a wide spectrum of zeolite-type chalcogenido metalate structures can be prepared, all based on supertetrahedral subunits^[181]. Besides this, the *in-situ* reduction of tetrahedral Tt(IV) has also been employed, allowing for the formation of triangular pyramidal Tt(II) centers with the lone pair pointing towards the remaining direction of the tetrahedral geometry, thus achieving the isolation of a series of novel ternary and quaternary salts in this system^[106,182]. Even though, the coordination principle endows such chalcogenido metalate clusters with predictable and elegant structures, it simultaneously restricts the structural expansion of such compounds due to the limited types of operable cations and the geometric restrictions of their coordination by chalcogenide ligands.

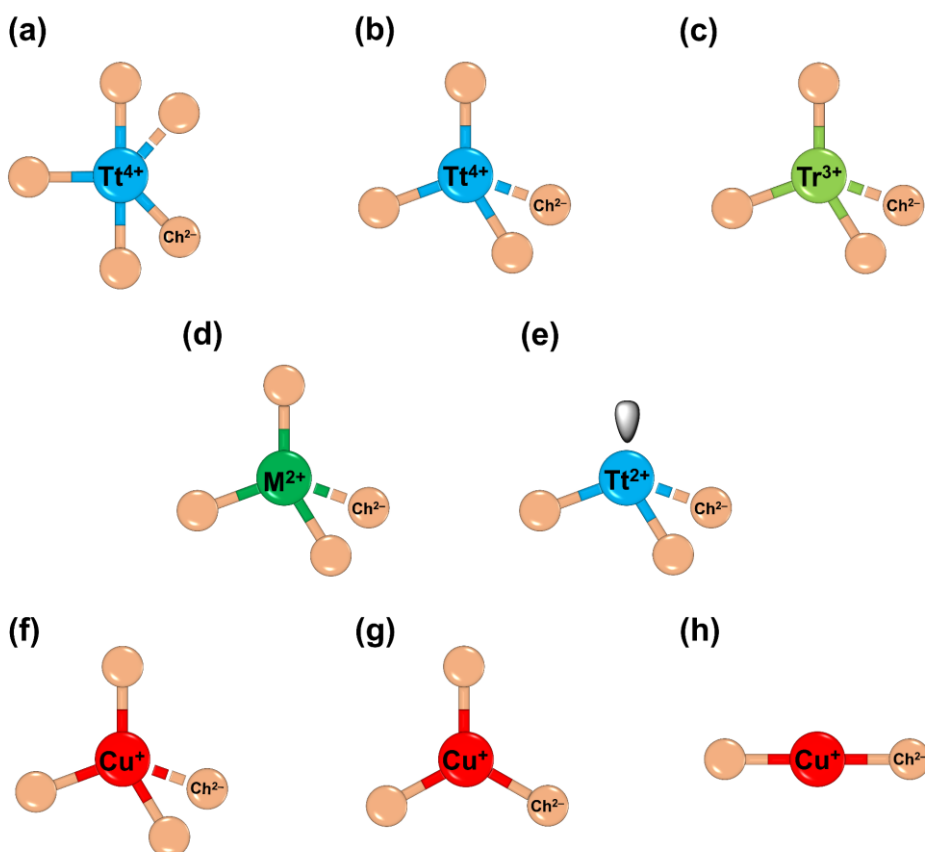
The inclusion of different atoms—similar to doping when added in small amounts—is generally recognized as an effective method for manipulating both structure and functional properties of crystalline compounds^[183,184], including supertetrahedral chalcogenido metalates^[185,186]. Other positive charges, in particular, cause modifications of the compositions and structures of the subunits in the crystal lattice. Therefore, the incorporation of M²⁺ cations like Zn²⁺, Cd²⁺, Mn²⁺, or Fe²⁺, into the Tt(IV)-Ch(–II) and Tr(III)-Ch(–II) systems has proven fruitful^[187,188]. However, the

coordination geometry of M^{2+} with chalcogenide ligands typically favors tetrahedral, which poses a barrier for further expansion of the family of such compounds to some extent.

As a last aspect, the synthesis conditions play another important role, with high-temperature approaches usually limiting the range of structural variations beyond the most stable versions, and solution-based approaches impacting the systems with solvent effects or solubility issues.

To expand the approaches clarified above, taking advantage of the multiple coordination modes of Cu^+ with chalcogenide ligands^[189–191], Cu^+ was introduced into chalcogenido metalate cluster architectures under mild ionothermal reaction conditions. This approach aimed to partially modify the coordination patterns to enable variations of the geometric as well as the electronic structures and, therefore, the physical properties. While this strategy has proven promising, predicting the crystal structures of final products remains challenging. Nonetheless, it opens new avenues for tailoring the properties of chalcogenido metalate clusters for advanced applications.

Scheme 3.5 illustrates the variety of coordination modes of the ions mentioned above.



Scheme 3.5: Summary of common coordination geometries of Tt^{4+} (Sn^{4+} and Ge^{4+}); Tt^{2+} (Sn^{2+} and Ge^{2+}); Tr^{3+} (Ga^{3+} and In^{3+}); M^{2+} (Zn^{2+} , Cd^{2+} , Mn^{2+} and Fe^{2+} etc.) and Cu^+ with Ch^{2-} (S^{2-} and Se^{2-}) observed in chalcogenido metalate compounds.

Selenido metalates were selected in this study for their higher reactivity than that of sulfido metalates and higher stability than that of tellurido metalates. In regard to the most sustainable materials, the use of selenido stannates stands out due to the greater annual production of tin with respect to that of gallium, indium and germanium, making them an economically viable choice for experimental investigation.

Thanks to the various coordination modes of $\{\text{CuSe}_x\}$ units within a ternary Cu/Sn/Se system, a wide spectrum of copper-selenido metalate compounds were obtained by slight variations of the synthesis protocols. These compounds include $(\text{C}_2\text{C}_2\text{Im})_9\text{Li}[\text{Cu}_{10}\text{Sn}_6\text{Se}_{22}]$ (**7**), $(\text{C}_2\text{C}_2\text{Im})_4[\text{Cu}_8\text{Sn}_6\text{Se}_{18}]$ (**8**), $(\text{C}_2\text{C}_1\text{Im})_3[\text{Cu}_5\text{Sn}_3\text{Se}_{10}]$ (**9**), and $(\text{C}_2\text{C}_2\text{Im})_5[\text{Cu}_8\text{Sn}_6\text{Se}_{18}\text{F}] \cdot (\text{C}_2\text{C}_2\text{Im})[\text{BF}_4]$ (**10**). For comparison, a compound based on a binary selenido metalate network, $\{(\text{C}_2\text{C}_2\text{Im})_2[\text{Sn}_3\text{Se}_7]\}_4 \cdot \{(\text{C}_2\text{C}_2\text{Im})[\text{BF}_4]\}_2$ (**11**) was also synthesized. A thorough analysis of these five new compounds illustrates the significance of Cu^+ for structural expansion, narrowing of the optical gap, and photocurrent conversion performance in relation to selenido stannate compounds.

3.3.2 Syntheses and crystal structures

In general, fewer copper-selenido stannates are reported than copper-sulfido stannates, typically due to the lower stability of the former and their corresponding intermediates, as well as the formation of side products such as CuSe or Cu_2Se during the reaction. To limit decomposition on the one hand, and inhibit the reactivity between copper and selenide reagents on the other hand, the salts of $[\text{Li}_4(\text{H}_2\text{O})_{13}][\text{SnSe}_4]$ and $[\text{K}_4(\text{H}_2\text{O})_4][\text{SnSe}_4]$ were first synthesized, and subsequently their reactivities with CuI were explored under inert conditions by an ionothermal approach. The preparation of $[\text{SnSe}_4]^{4-}$ salts offers a platform where Sn–Se bonds are already pre-formed before addition of copper reagents. This strategy helps avoid the formation of CuSe and Cu_2Se byproducts to some extent owing to the lower reactivity between Se^{2-} ligand atoms and Cu^+ . Additionally, it facilitates the formation of the target compounds.

Five new compounds were synthesized by reacting $[\text{Li}_4(\text{H}_2\text{O})_{13}][\text{SnSe}_4]$ ^[104] or $[\text{K}_4(\text{H}_2\text{O})_4][\text{SnSe}_4]$ ^[92] with CuI in the ionic liquids $(\text{C}_2\text{C}_x\text{Im})[\text{BF}_4]$ ($x = 2$ for compounds **7–8** and **10–11**; $x = 1$ for compound **9**) and DMMP at 120 °C or 150 °C for 3 days.

The reaction of $[\text{Li}_4(\text{H}_2\text{O})_{13}][\text{SnSe}_4]$ and CuI in $(\text{C}_2\text{C}_2\text{Im})[\text{BF}_4]$ and DMMP at 120 °C for 3 days yielded a few reddish-black crystals of the ternary anion of $[\text{Cu}_{10}\text{Sn}_6\text{Se}_{22}]^{10-}$ in **7**. This anion is stabilized by both $(\text{C}_2\text{C}_2\text{Im})^+$ and Li^+ counterions. When $[\text{K}_4(\text{H}_2\text{O})_4][\text{SnSe}_4]$ and LiCl salts were treated with CuI in the same solvents at 150 °C, compound **8** was obtained instead, with an approx. yield of 58% yield. Although neither Li^+/K^+ nor Cl^- were included in the product, their presence may have altered the solvation behavior of the ionothermal flux, leading to the formation of the different compounds. It has been previously reported, that modifications in the length of the alkyl chain of an imidazolium-based ionic liquid counterion can effectively modulate the structure of the anionic cluster units obtained from such reactions^[106]. By substituting one of the ethyl groups of $(\text{C}_2\text{C}_2\text{Im})^+$ in $(\text{C}_2\text{C}_2\text{Im})[\text{BF}_4]$ for targeting **7** with a methyl group, an inseparable mixture of enantiomeric-selenido metalate open-framework structures were obtained, compounds **9a** and **9b** (approx. 34% yield in total). Besides the nature of the ionic liquid counterion, the reaction tem-

perature is another significant parameter to modify solubility and thus the crystallization conditions of chalcogenido metalates in ionothermal environments. By raising the reaction temperature up from 120 °C, used for the formation of compound **7**, to 150 °C, black cubic crystals of **10** were obtained (the yield was not calculable due to the formation of a side product). In this reaction, compound **11** was identified as a minor side product and can also be obtained as a pure product (approx. 35% yield) if CuI is not present in the reaction mixture. It should be noted that the presence of $[\text{BF}_4]^-$ anions is essential for the successful synthesis of all compounds. Upon replacement of $[\text{BF}_4]^-$ by Br^- or Cl^- anions, none of the named products crystallized. This is understandable for compounds **10** and **11**, which contain $[\text{BF}_4]^-$ anions, but it is also attributed to the role of this anion in achieving optimal polarities and melting points of the corresponding reaction fluxes for all compounds. In addition, using CuI as a copper source turned out to be instrumental for the formation of copper-rich compounds **7–10**. No identifiable compounds were observed using CuCl , CuCl_2 or $\text{Cu}(\text{OAc})_2 \cdot \text{H}_2\text{O}$ instead. **8**, **10**, and **11** are also isolable from one batch by reacting $[\text{Li}_4(\text{H}_2\text{O})_{13}][\text{SnSe}_4]$ with CuBr at 150 °C, yet with very poor crystal quality due to heavily intergrown crystals. It is assumed that the solvation of Cu^+ and I^- ions and their solution dynamics in ionic liquids precisely meet the requirements for molecule or network formation and subsequent crystallization, while the other anions cause too high (Cl^-) or to low (OAc^-) reactivity under the given conditions. The use of bromides, exhibiting a reactivity between Cl^- and I^- , affords crystalline materials of lower quality owing to intergrown crystals.

Compound $(\text{C}_2\text{C}_2\text{Im})_9\text{Li}[\text{Cu}_{10}\text{Sn}_6\text{Se}_{22}]$ (**7**) crystallizes in the high symmetrical cubic space group $\text{Pa}\bar{3}$ (No. 206) with eight formula units per unit cell (Figure 3.26a). The asymmetric unit of the cluster anion, as shown in Figure 3.26b, contains four copper atoms, two tin atoms and eight selenium atoms. The relative atomic content was confirmed by means of EDX measurements. As pictured in Figure 3.26c, the cluster anion in **7** can be viewed as a molecular core-shell structure. The central fragment, $\{\text{Cu}_7\text{Se}\}$ (Figure 3.26d), is capped and stabilized by three dimeric $\{\text{Sn}_2\text{Se}_7\}$ anionic motifs (Figure 3.26e). Three additional copper atoms bridge the $\{\text{Sn}_2\text{Se}_7\}$ anions, forming a larger trigonal $\{\text{Cu}_3\text{Sn}_6\text{Se}_{21}\}$ shell. The $\{\text{Cu}_7\text{Se}\}$ core unit features a distorted cubane-type architecture. The distances between neighboring copper atoms range from 2.598(1) Å to 2.912(1) Å, which are longer than the interatomic distance in metallic copper (2.56 Å), indicating that bonding interactions between Cu atoms in **7** are negligible^[192]. The dashed lines in Figure 3.26d only demonstrate their arrangement. Nine copper atoms of the cluster anion adopt trigonal-planar coordination modes, while the remaining central tetra-coordinated Cu atom bridge three capping $\{\text{Sn}_2\text{Se}_7\}$ motifs and the remaining selenium atom of the anionic cluster (Figure 3.26f). The $[\text{Cu}_{10}\text{Sn}_6\text{Se}_{22}]^{10-}$ anion presented here has a larger cluster size (Figure 3.26g) and significantly higher charges compared to the reported $[\text{M}_7\text{As}_3\text{Ch}_{13}]^{4-}$ ($\text{M} = \text{Cu}$ or Ag , $\text{Ch} = \text{Se}$ or Te) anions^[193,194]. These differences can be attributed to the successful incorporation of tin atoms into the cluster anion. The local negative charges of the $\{\text{Sn}_2\text{Se}_7\}$ capping units in **7** are 6 $-$ (cf. the 3 $-$ charge of $\{\text{AsSe}_4\}$ in $\{\text{M}_7\text{As}_3\text{Ch}_{13}\}$), necessitating the introduction of more tri-coordinated Cu^+ atoms to balance a part of their negative charges and stabilize the cluster. Consequently, the cluster size increases from 9.11 – 9.95 Å in the $[\text{M}_7\text{As}_3\text{Ch}_{13}]^{4-}$ anions to 13.84 Å in the $[\text{Cu}_{10}\text{Sn}_6\text{Se}_{22}]^{10-}$ anion in **7**.

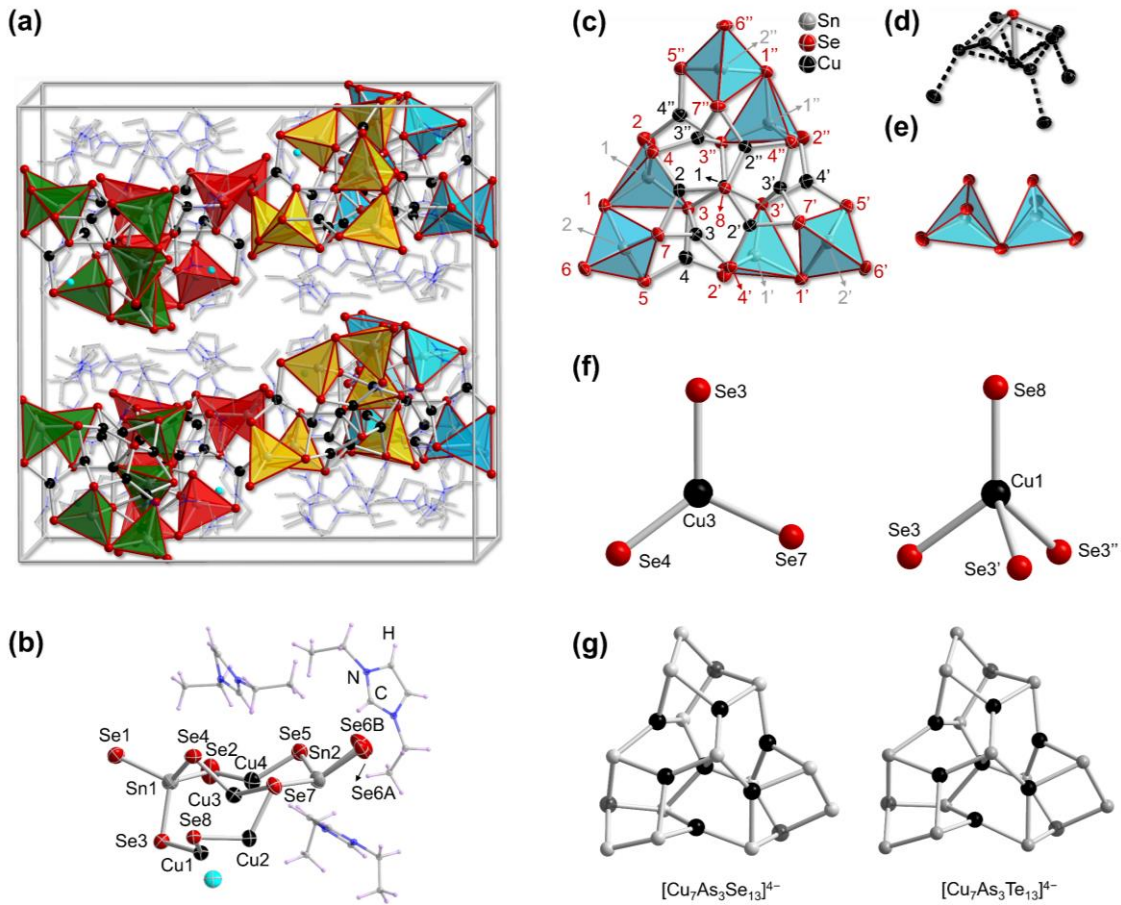


Figure 3.26: Illustration of the crystal structure of compound 7. View of the unit cell of compound 7. Ionic liquid cations are shown in wire mode; H atoms are omitted. For clarity, the $\{\text{Sn}_2\text{Se}_7\}$ units of different $[\text{Cu}_{10}\text{Sn}_6\text{Se}_{22}]^{10-}$ cluster anions are shown as polyhedral mode, to clearly clarify the quantity of anions in each unit, the polyhedrons are shown in different colors (a). Asymmetric unit of compound 7 (b). Molecular structure of the $[\text{Cu}_{10}\text{Sn}_6\text{Se}_{22}]^{10-}$ cluster anion in 7 (c). The $\{\text{Cu}_{10}\text{Se}\}$ core of $[\text{Cu}_{10}\text{Sn}_6\text{Se}_{22}]^{10-}$ (d). The dimeric $\{\text{Sn}_2\text{Se}_7\}$ capping motif in $[\text{Cu}_{10}\text{Sn}_6\text{Se}_{22}]^{10-}$ (e). Three- (left) and four-connected Cu^+ (right) in the asymmetric unit of 7, shown for atoms Cu3 and Cu1 as examples (f). Structures of the reported $[\text{Cu}_7\text{As}_3\text{Se}_{13}]^{4-}$ (left) and $[\text{Cu}_7\text{As}_3\text{Te}_{13}]^{4-}$ (right) cluster anions for comparison (g). Thermal ellipsoids are drawn at 50% probability level in Figures 3.26b–3.26e. A corresponding color code was used for the atom labels in Figure 3.26c. Color code for Figure 3.26g: Cu–Black; As–Gray (70%); Te–Gray (40%); and Se–Gray (10%).

Compound $(\text{C}_2\text{C}_2\text{Im})_4[\text{Cu}_8\text{Sn}_6\text{Se}_{18}]$ (8) crystallizes in the monoclinic crystal system, space group $P2_1/c$, (No. 14). As illustrated in Figure 3.27a, the asymmetric unit of 8 consists of eight crystallographically independent copper atoms, six tin atoms, and eighteen selenium atoms. The valence state of all copper atoms, which are found in trigonal-planar or tetrahedral coordination modes (Figure 3.27b), is assigned as +1 for charge balance, which is further demonstrated by BVS calculations (Table 6.4). The distances between neighboring copper atoms range from $2.6176(2)$ – $3.1850(2)$ Å, indicating negligible $\text{Cu}\cdots\text{Cu}$ bonding interactions. In terms of reticular chemistry^[195], two crystallographically independent $\{\text{Cu}_4\text{Sn}_2\text{Se}_6\}$ units represent the repeating motifs that extend into a backbone-type strand. These are bridged by a $\{\text{Sn}_2\text{Se}_6\}$ substructure, further

assembling into a two-dimensional polymeric structure (Figure 3.27c). The architecture of these layers accords with a honeycomb-type (*hcb*-type) net, considering each of the repeating units as a node. As displayed in Figure 3.27d, the crystal structure of **8** features two parallel anionic wave-shaped layers. Notably, all the ionic liquid cations could be localized in the crystal structure. Three quarters of these cations serve to separate the anionic components, being situated between the interlayers of the neighboring substructures. The remaining quarter of the cations are found within the six-membered rings of each single layer (Figure 3.27e), providing further charge compensation and internal stabilization of the anionic architecture.

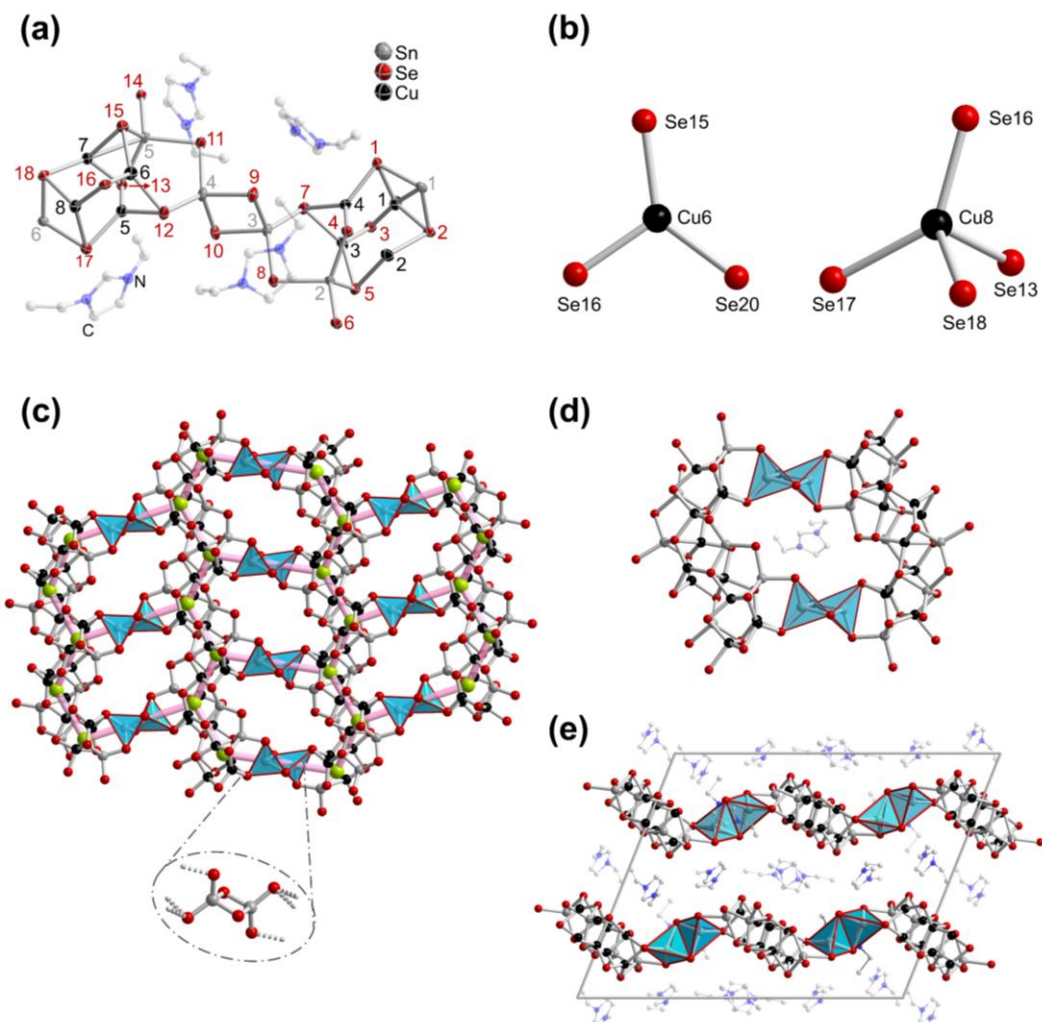


Figure 3.27: Asymmetric unit of compound **8** with labeling scheme (a), thermal ellipsoids are drawn at 50% probability level. A corresponding color code was used for the atom labels. Three- (right) and four-connected Cu⁺ (right) observed in the asymmetric unit of compound **8** (b). View onto the two-dimensional anionic substructure of compound **8** (c). Counterions are omitted for clarity. The simplified *hcb* net that is obtained when each repeating unit is regarded as a node (displayed as a lime sphere) is highlighted by sticks in rose color. The bridging {Sn₂Se₆} units are highlighted in polyhedral mode, and one of which is shown in bond and stick mode for clarity. Illustration of the cyclic substructure in the (distorted) honeycomb-like 2D network including one counterion (d). Side view of the corrugated 2D layers and the counterions in between them (e).

Compound $(C_2C_1Im)_3[Cu_5Sn_3Se_{10}]$ (**9**) crystallizes as a mixture of enantiomer-pure crystals, denoted as compounds **9a** and **9b**, in the trigonal crystal system in the two corresponding, chiral space groups $P3_2$ (No. 145) and $P3_1$ (No. 144), respectively. As displayed in Figure 3.28a,b, the asymmetric units of **9a** and **9b** contain five copper atoms, three tin atoms and ten selenium atoms (the Cu5 positions of both being split into Cu5A and Cu5B due to heavy disorder). The oxidation state of all copper atoms was assigned as +1 according to their trigonal-planar coordination geometry (Figure 3.28c) and as confirmed by BVS calculations (Table 6.5). As depicted in Figure 3.29a, the repeat units of **9a** and **9b** are connected to identical units *via* sharing tin atoms at four corners of the building blocks (Figure 3.29b,c), and further assemble into chiral quartz (*qtz*) networks (Figure 3.29d,e). Apart from the inverted chirality, compounds **9a** and **9b** possess the same anionic structures and are templated by the same counterions. The networks of **9a** and **9b** feature two different types of chirality: the naturally chiral *qtz* net, and the one-dimensional chirality of the M- and P-helix (Figure 3.29f,g). Most recently, similar anionic structure of both enantiomers, **COC-10-L** and **COC-10-D** with the formula $(H^+ - DBN)_3[Cu_5Sn_3Se_{10}]$, were obtained through solvothermal reactions^[196], with the difference being the chiral space groups of $P6_4$ and $P6_2$ in **COC-10-L** and **COC-10-D**. It is reasoned that the use of different structure directing agents, $(C_2C_1Im)^+$ for **9a** and **9b**, $(H^+ - DBN)$ for **COC-10-L** and **COC-10-D**, led to the formation of the same anionic frameworks but with altered chiral space groups, underscoring the importance of the reaction medium, and the cations originating from it, on the stereochemistry during product formation. Owing to heavy disorder of the ionic liquid counterions that located at the solvent accessible spaces, they were not able to be localized on the difference Fourier map. To avoid impairing of the refinement, the corresponding electron density was detracted from the data using the back-Fourier-transform method^[129]. The formula of **9a** and **9b** were determined to be $(C_2C_1Im)_3[Cu_5Sn_3Se_{10}]$ based on the SC-XRD measurements and charge balance rules.

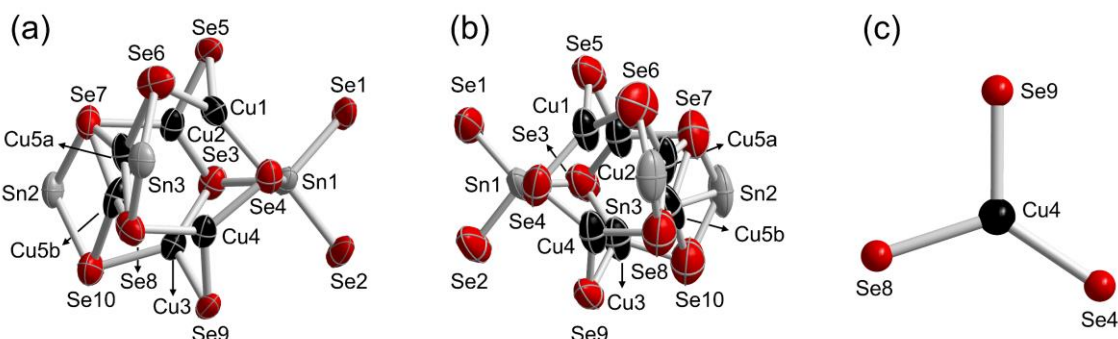


Figure 3.28: Asymmetric unit of compound **9a** (a); and compound **9b** (b). The thermal ellipsoids are drawn at 50% probability level, the imidazolium counterions were not able to be identified due to the poor crystal quality. Three-connected Cu⁺ of the asymmetric unit of compounds **9** shown for Cu4 as an example (c).

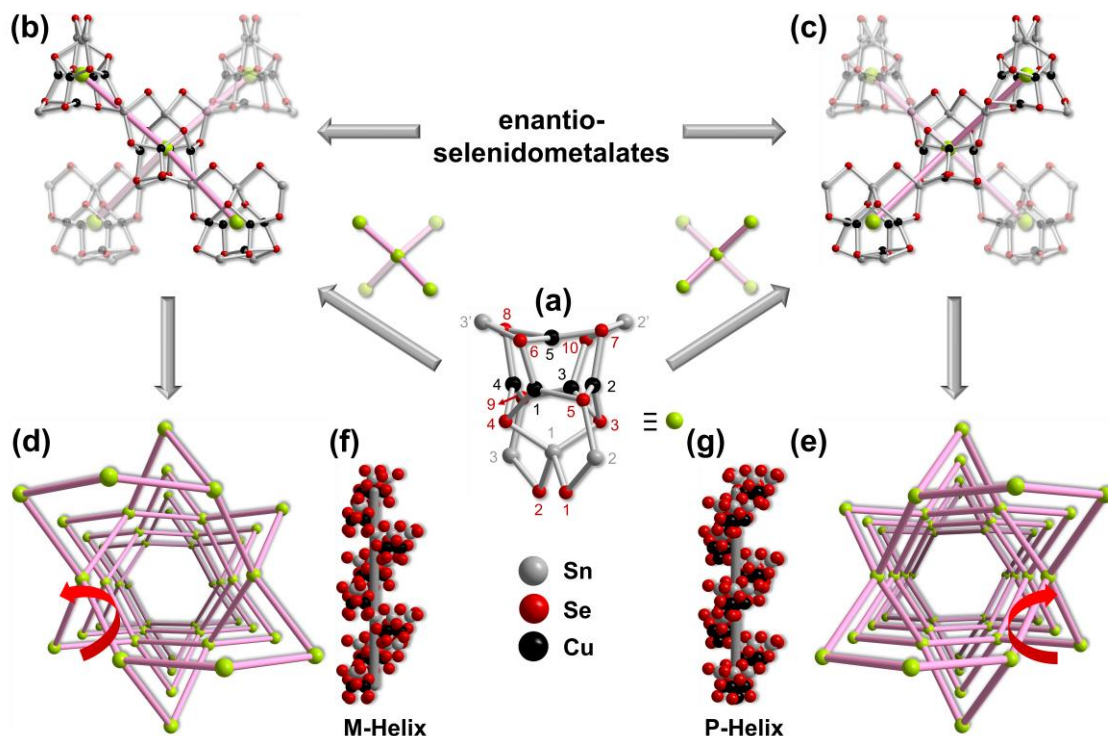


Figure 3.29: Structure of one secondary building unit in compound **9a** and **9b**, shown for **9a** as an example, a corresponding color code was used for the atom labels (a). Illustration of the enantiomeric linking mode between the second building units in **9a** (b) and **9b** (c), highlighted with increasing transparency as the units get more distant from the viewpoint of the viewer. Illustration of the simplified chiral *qtz* net of compounds **9a** (d) and **9b** (e) upon treating each building block as a node. The M-helix observed along axis *c* in **9a** (f). The P-helix observed along axis *c* in **9b** (g).

Compound $(C_2C_2Im)_5[Cu_8Sn_6Se_{18}F] \cdot (C_2C_2Im)[BF_4]$ (**10**) crystallizes in the highly symmetric cubic space group $Pm\bar{3}$ (No. 200) with one $\{FCu_8Sn_6Se_{12}Se_{12\times\frac{1}{2}}\}$ building block in the unit cell (Figure 3.30a). The Cu:Sn:Se ratio of **10** is the same as that for **8**, underpinning the key structure-directing role of the additional F^- and the impact of the slightly varied reaction conditions for altering product spectrum. The core of this building unit comprises a cubic array of copper atoms with the neighboring Cu…Cu distances being $3.3241(6)$ Å, indicating no significant interactions between adjacent copper atoms (Figure 3.30b). The $\{Cu_8\}$ cube accommodates a F^- anion, originating from the anion of the ionic liquid $(C_2C_1Im)[BF_4]$, its presence was further confirmed by EDX analysis. Twelve selenium atoms surround the core motif by bridging each edge of the $\{FCu_8\}$ cube, forming an icosahedral $\{FCu_8Se_{12}\}$ cluster unit. Bridging of the latter in compound **10** by six $\{Sn_2Se_2\}$ units finally affords a three-dimensional primitive cubic (*pcu*) network (Figure 3.30c,d). Although $\{Cu_8Ch_m\}$ ($Ch = S, Se; m = 12, 13$) clusters have been documented (Figure 31b-d), this is the first reported inclusion of F^- in $\{Cu_8\}$ cubes within a network structure. It has been known in the molecular cages of $[Cu_8(F)\{Se_2P(O^iPr)_2\}_6]$ and $[Cu_8(S)\{Se_2P(O^iPr)_2\}_6]^{[197]}$ (Figure 31e,f) exhibit slightly shorter Cu…Cu and Cu…F distances compared to those in compound **10**. The observed volume expansion of the building unit in the extended framework is attributed to the lack of terminal ligands, resulting in larger average coordination numbers of the involved atoms.

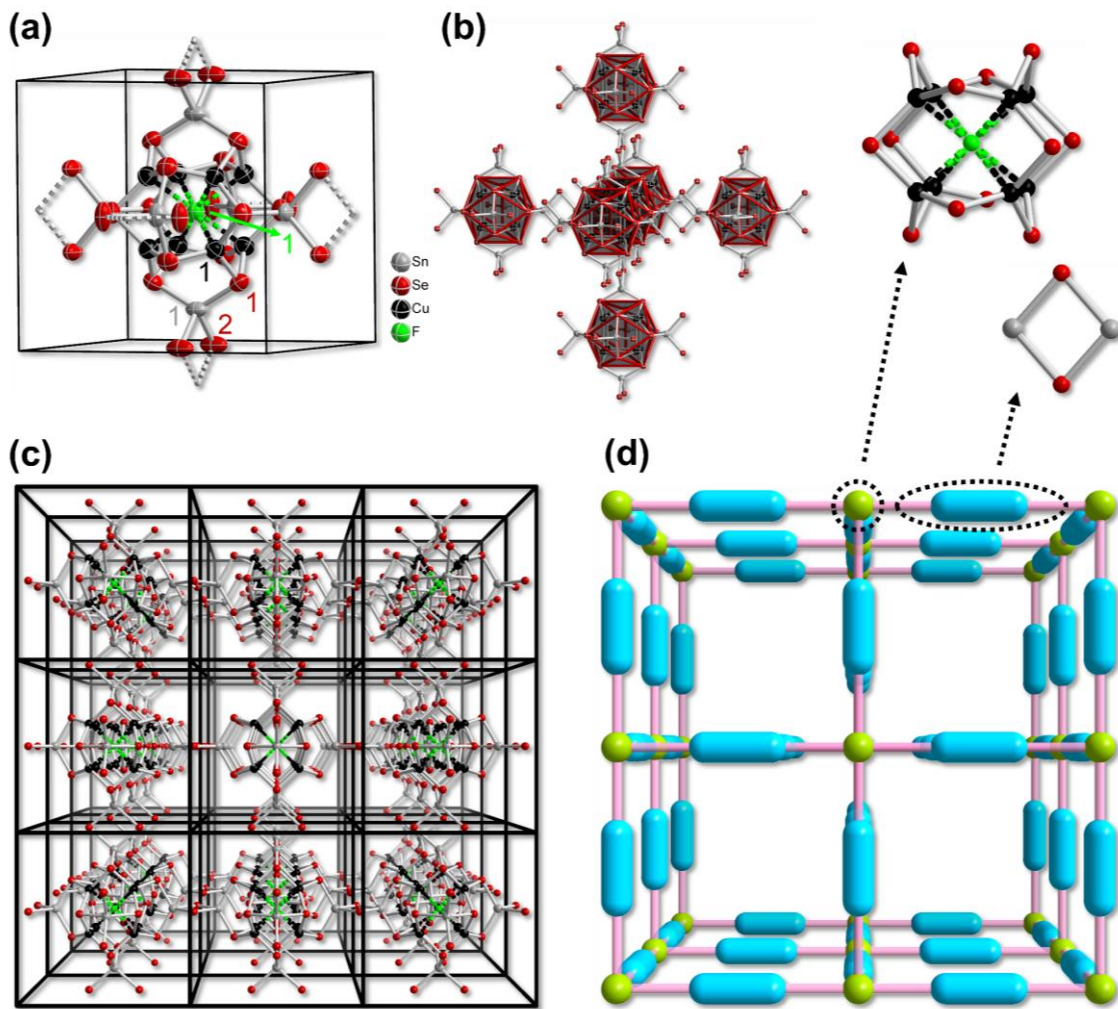


Figure 3.30: Structure of the building units in the unit cell in compound **10** (a). Thermal ellipsoids are drawn at 50% probability level. A corresponding color code was used for the atom labels. Illustration of the linkage of building units $\{\text{FCu}_8\text{Se}_{12}\}$ and $\{\text{Sn}_2\text{Se}_2\}$ in compound **10** (b). Extension of the anionic substructure in a $3 \times 3 \times 3$ supercell (c). The simplified *pcu* net of **10** upon treating each $\{\text{FCu}_8\text{Se}_{12}\}$ motif as a node and each $\{\text{Sn}_2\text{Se}_2\}$ unit as a linker (d). The disordered $[\text{BF}_4]^-$ anions are omitted for clarity.

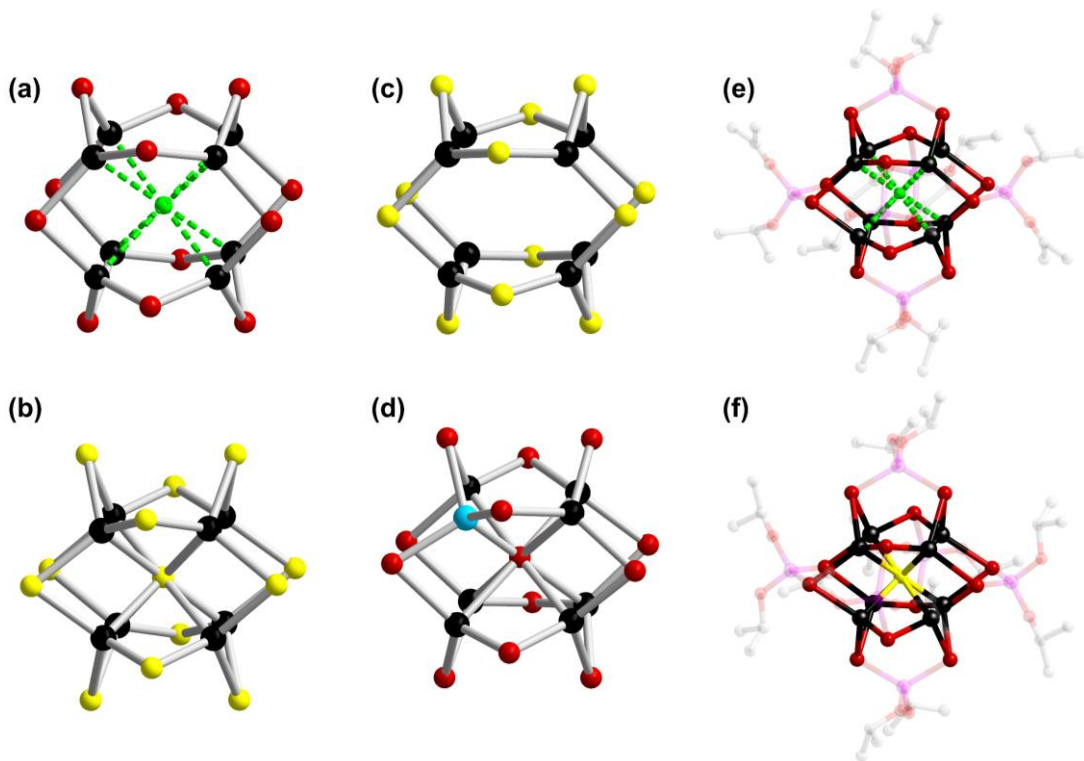


Figure 3.31: Structural comparison of embedded or hollow $\{\text{Cu}_{8-x}\text{TM}_x\text{Ch}_{12}\}$ motifs $\{\text{FCu}_8\text{Se}_{12}\}$ in compound **10** (a). Core-stuffed $\{\text{Cu}_8\text{Ch}_{13}\}$ (b); hollow $\{\text{Cu}_8\text{Ch}_{12}\}$ (c); and $(\text{Cu}_7\text{GeSe}_{13})$ in extended network compounds^[198–200] (d). $\{\text{FCu}_8\text{Se}_{12}\}$ (e); and $\{\text{SCu}_8\text{Se}_{12}\}$ (f) in reported molecular cage compounds of $[\text{Cu}_8(\text{F})\{\text{Se}_2\text{P}(\text{O}^{\prime}\text{Pr})_2\}_6]$ and $[\text{Cu}_8(\text{S})\{\text{Se}_2\text{P}(\text{O}^{\prime}\text{Pr})_2\}_6]^-$. The organic ligands are shown with transparency. Color code: Cu–Black; Se–Red; C–White; F–Green; N–Blue; Ch–Yellow.

The replacement of $[\text{BF}_4]^-$ anions of ionic liquids with Cl^- or Br^- did not yield the same compound, highlighting that $(\text{C}_2\text{C}_2\text{Im})[\text{BF}_4]$ acts not only as solvent and template for the ionothermal reactions, but is non-innocent and actively involved in the bottom-up construction of the cluster units. It is assumed that the $\{\text{Cu}_8\}$ cube cannot accommodate larger anions than F^- . As shown in Figure 3.32a, a disordered $[\text{BF}_4]^-$ anion from the ionic liquid is identified at the corner of each unit cell, supporting the important role of $(\text{C}_2\text{C}_2\text{Im})[\text{BF}_4]$ as reaction medium. The heavy disorder of the cations contributes to the high overall symmetry of the crystal structure, with the cations appearing as smeared electron density, making localization on the difference Fourier map challenging/impossible. Correspondingly, the SQUEEZE routine was applied again to account for this feature, which is typical for many structures of this kind. The solvent accessible voids, illustrated in Figure 3.32b, correspond to the accommodation of a total of six $(\text{C}_2\text{C}_2\text{Im})^+$ cations within the crystal structure of **10**.

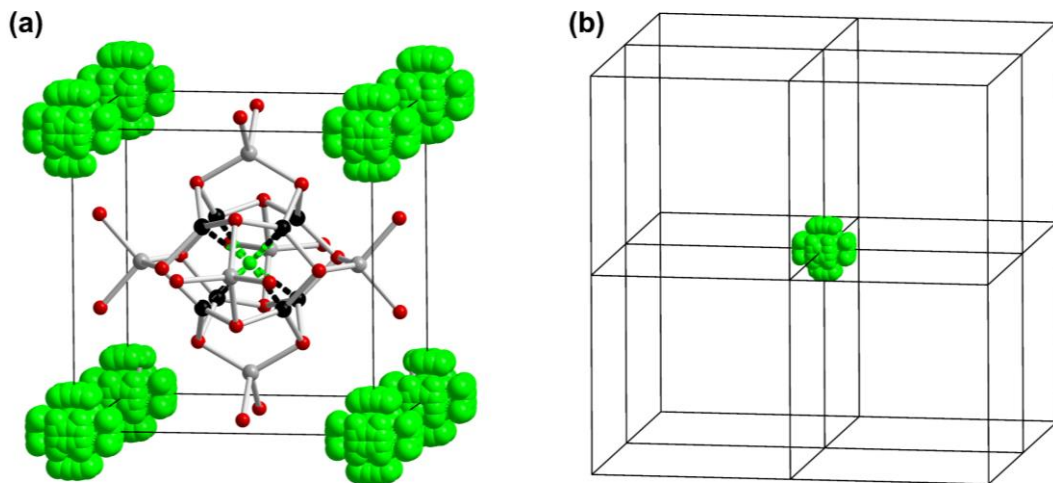


Figure 3.32: Disordered $[\text{BF}_4]^-$ anions at the corners of each unit cell (a); and centered at position of eight neighboring unit cells in compound **10** (b). Color code: Cu–Black; Se–Red; Sn–Gray; B–Pink; F–Green.

Compound $\{(C_2C_2\text{Im})_2[\text{Sn}_3\text{Se}_7]\}_4 \cdot \{(C_2C_2\text{Im})[\text{BF}_4]\}_2$ (**11**) crystallizes in the triclinic space group $P\bar{1}$ (No. 2) with a unit cell volume of 6667 \AA^3 . The asymmetric unit contains twelve crystallographically independent tin atoms and twenty-eight selenium atoms, forming the selenido stanate substructure, which is further surrounded by ten $(C_2C_2\text{Im})^+$ cations and two $[\text{BF}_4]^-$ anions (Figure 3.33a). The anionic substructure consists of the well-known honeycomb-like 2D layer, formed by repeating the $\{\text{Sn}_3\text{Se}_7\}$ unit *via* corner sharing of μ -Se atoms (Figure 3.33b,c). Two of the $(C_2C_2\text{Im})^+$ cations are located inside the hexagonal pores of the layer, six are intercalated between adjacent layers, and the remaining two cations balance the charges of two $[\text{BF}_4]^-$ anions within the crystal structure (Figure 3.34a–c). There is no interaction between the anionic substructures and the $[\text{BF}_4]^-$ anions, classifying this compound as a double salt. While compound **11** can form as a side product during the synthesis of compound **10**, it can also be obtained as a pure product in the absence of CuI.

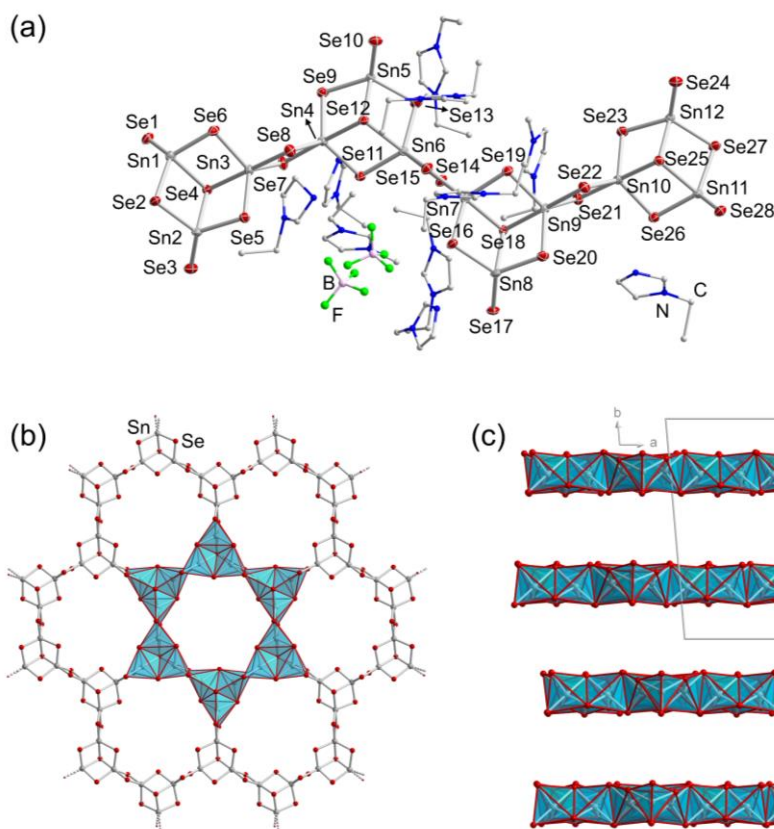


Figure 3.33: Asymmetric unit of compound **11** (a), thermal ellipsoids are drawn at 50% probability level. Top view of the two-dimensional, honeycomb-like anionic substructure of compound **11**, highlighting the six-membered ring motif in polyhedral mode (b). Side view of the stacking of the layers along the *b* axis in the crystal structure of **11** (c). Organic cations and $[\text{BF}_4]^-$ anions are omitted for clarity in (b) and (c). Color code: Se—Red; Sn—Gray (40%); B—Pink; F—Green; N—Blue; C—Gray (25%).

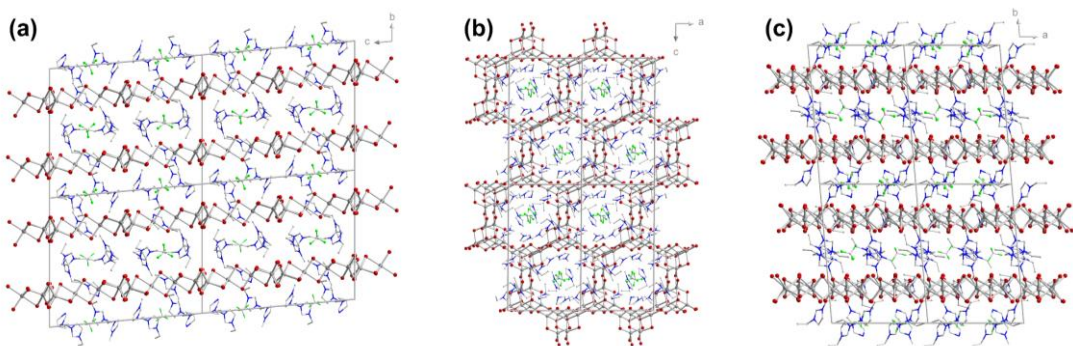


Figure 3.34: View of the arrangement of the infinite layers in the crystal structure of **11** along axis *a* (a); axis *b* (b); and axis *c* (c). Color code: Se—Red; Sn—Gray (40%); B—Pink; F—Green; N—Blue; C—Gray (25%).

It is emphasized that honeycomb-like binary substructures, similar as the one found in compound **11**, represent the most frequently observed structural motif in chalcogenido stannate compounds obtained under mild (solvothermal or ionothermal) reaction conditions—even in the presence of different structure-directing agents^[201–205]. Changing the reaction temperatures or crystallization

conditions allow access other motifs, but these variations remain somewhat limited. In contrast, the addition of Cu⁺ to the reaction system provides huge opportunities for structural diversity owing to the cation's diverse coordination modes by chalcogen ligands. This flexibility enables the formation of unprecedented anionic substructures, such as the ones observed for compounds **7–10** upon subtle modifications of reaction temperatures, precursor salts, as well as the use of different ionic liquid cations. Consequently, the spectrum of selenido stannate-based materials experiences a significant structural expansion despite the relatively similar atomic ratios of the involved elements Cu:Sn:Se of 10:6:22 (**7**), 8:6:18 = 10:7.5:22.5 (**8** and **10**), 5:3:10 = 10:6:20 (**9**).

3.3.3 Elemental analysis and PXRD measurement

3.3.3.1 Elemental analysis

To verify the precise atomic ratio between heavier elements, especially between Cu and Sn, in all compounds, EDX spectroscopy on the single crystals of compounds **7–11** were performed. Using the EDX analysis of compound **7** as an example, as shown in Figure 3.35a, the experimental atomic ratio of Cu:Sn:Se (0.2791:0.5456:0.1753) closely matches the calculated ratio (0.2632:0.5789:0.1579), with differences between observed and simulated values well below ± 1 atom. The light elements, such as C, N, H, and Li, were not investigated this way. The EDX measurement confirm the accurate compositions. Figure 3.35b–e depicted the SEM images and EDX spectra of single crystals of compounds **8–11**, they serve to support the atomic ratios as observed from the SC-XRD results, like the same case for compound **7**.

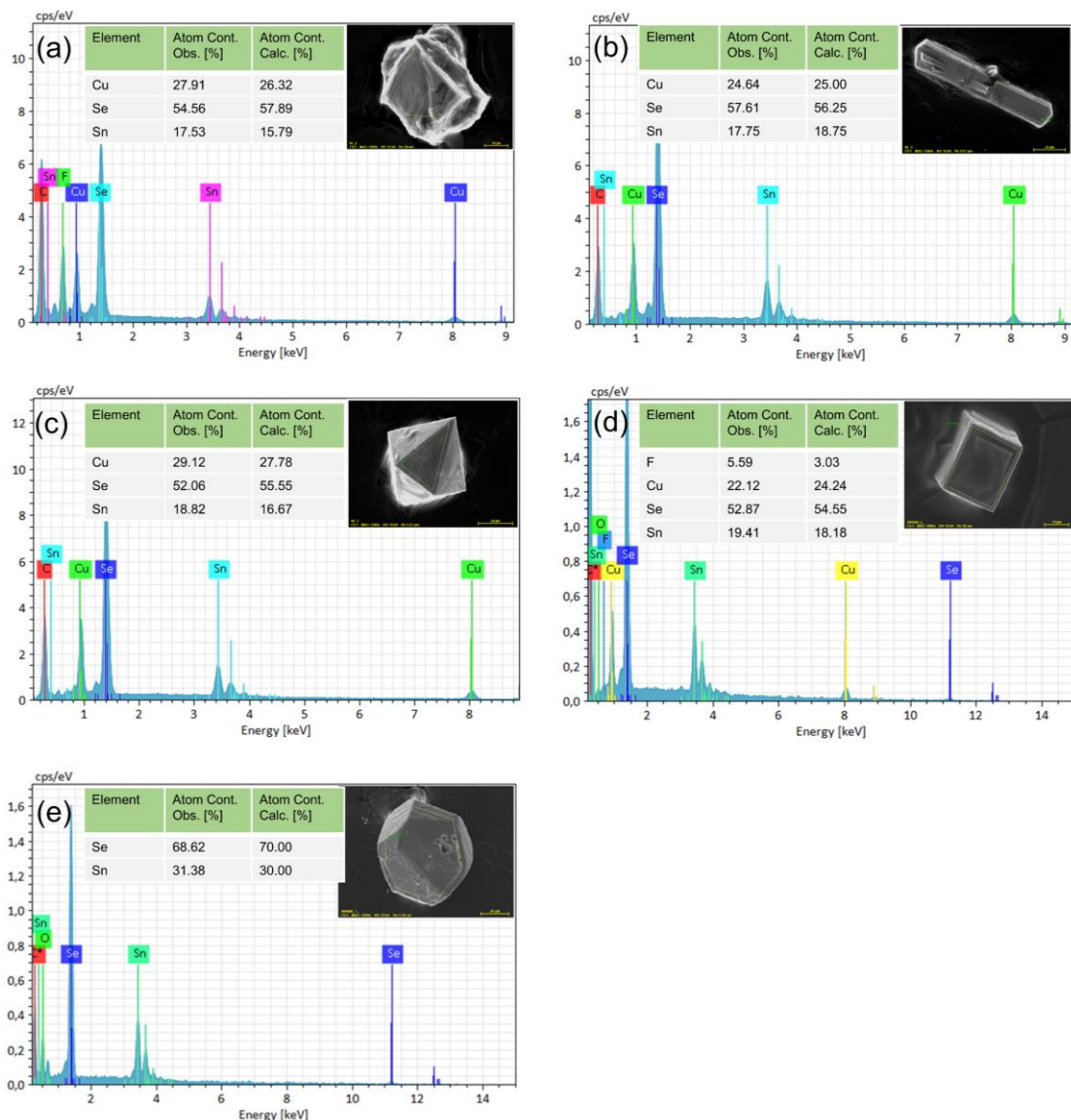


Figure 3.35: SEM images, EDX spectra and comparison of the differences between calculated and simulated atomic ratios of compound 7 (a); compound 8 (b); compound 9 (c); compound 10 (d); and compound 11 (e).

3.3.3.2 PXRD measurement

As an additional method to reveal crystal structures, and in turn to verify the as-solved crystal structures from SC-XRD technique, PXRD of compounds **8–11** were further investigated. Unfortunately, **7** could not be included in the PXRD analysis due to its limited yield. As depicted in Figure 3.36a–d, the experimental PXRD patterns of measured compounds **8–11** match the patterns simulated from SC-XRD. The differences in the intensity in **8** are attributed to texture effects (Figure 3.36a), while slight shifts towards the lower angle in all compounds are caused by the temperature effects. As the PXRD patterns were carried out at room temperature, the SC-XRD analyses were performed at 100 K. The sample measured for PXRD are more compressed compared to the crystals measured for SC-XRD, shifting the reflections in PXRD towards lower angles in comparison to that of the simulated pattern. The mixed phase of compounds **10** and **11**

were also identified by PXRD since they were not able to be separated, however, as it was mentioned above, phase-pure crystals of **11** were found without impurities as also verified by PXRD (Figure 3.36c–d).

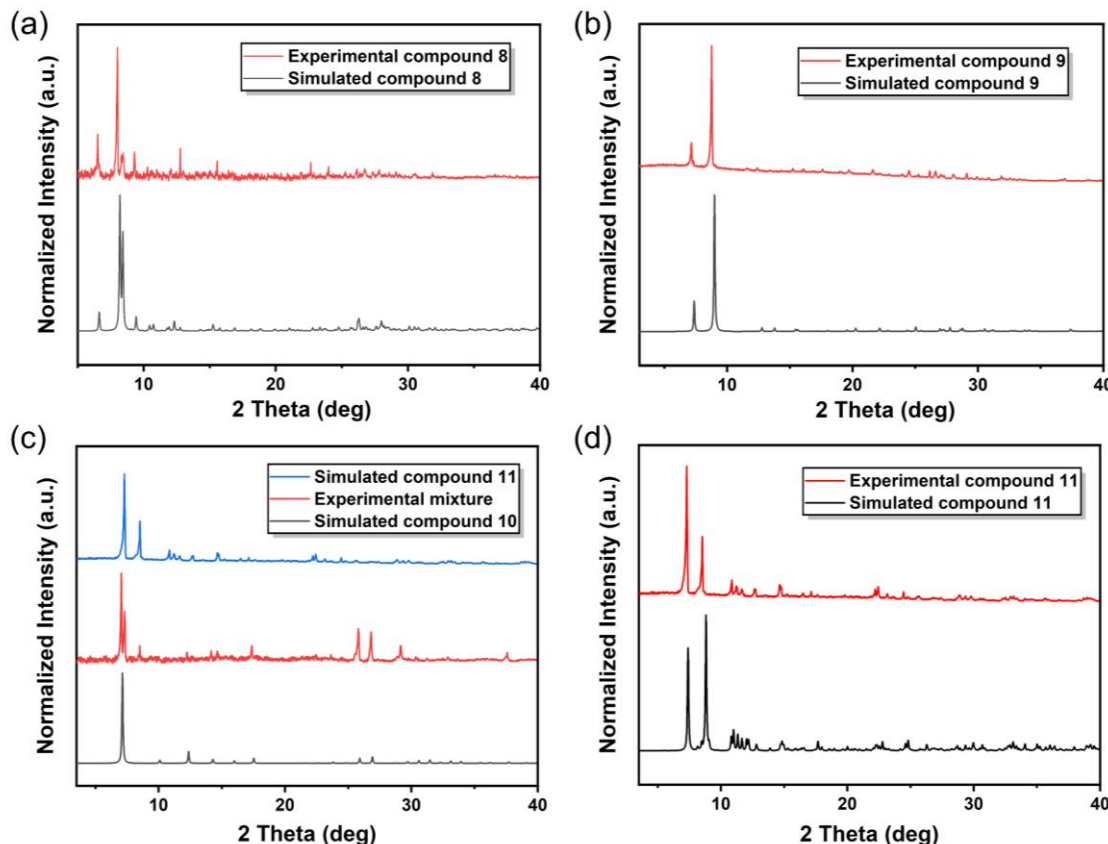


Figure 3.36: PXRD patterns of as-synthesized compound **8** and simulated one (a); as-synthesized compound **9** and simulated one (b); as-synthesized mixture of compound **10** and compound **11** and simulated patterns of **10** and **11** (c). as-synthesized compound **11** and simulated one (d).

3.3.4 Optical absorption properties and photocurrent measurement

3.3.4.1 Optical absorption properties

In addition to the structural expansion of such cluster assemblies, the introduction of Cu^+ was undertaken to modulate the electronic structures of corresponding compounds. Solid-state UV-vis diffuse-reflectance spectra were collected on crystalline samples of compounds **8** – **11** (the investigation of compound **7** was hampered by the small yield) to assess their optical properties (depicted in Figure 3.37a–c). It was found that all compounds, particularly **8** – **10**, are narrow band gap semiconductors with E_{gap} values similar to those of reported copper-rich cluster-based materials^[191,200,206] and those of the photovoltaic materials Cu_2SnCh_3 and $\text{Cu}_2\text{ZnSnCh}_4$ ^[207–209] (Table 6.8, Ch = S, Se, $E_{\text{gap}} = 1.33 – 1.88$ eV).

According to the corresponding Tauc plots shown in Figure 6.21, the optical band gap energies E_{gap} of compounds **8** – **11** were determined to be 1.39 eV (**8**), 1.75 eV (**9**), 1.83 eV (**10**), and 2.05

eV (**11**), respectively (Figure 3.37d). In comparison to the E_{gap} of **11**, a distinct red-shift of the UV-vis spectra of **8 – 11** is observed upon the introduction of Cu⁺ into the reaction system owing to the lower electronic excitation energy of copper(I) selenide (0.50 eV)^[210] as compared to tin(IV) selenide (1.07 eV)^[211].

Considering the ratios of “SnSe₂:Cu₂Se:Se²⁻” comprised in the four Cu/Sn/Se substructures (normalized to 6SnSe₂), hence 6SnSe₂:5Cu₂Se:5Se²⁻ in **7**, 6SnSe₂:4Cu₂Se:2Se²⁻ in **8** and **10**, and 6SnSe₂:5Cu₂Se:3Se²⁻ in **9** (cf. 6SnSe₂:2Se²⁻ in **11**), similar degrees of “Cu₂Se admixtures” relative to SnSe₂ in the new compounds **7 – 10** was observed. This explains the similar effect observed for **10** (1.83 eV) and **9** (1.75 eV) as compared to **11** (2.05 eV). The additional narrowing of the bandgap measured for **8** (1.39 eV), in spite of a slightly lower relative “Cu₂Se content”, is attributed to a denser anionic substructure – hence supporting the concerted effect on structures and electronic properties by incorporation of Cu⁺.

These findings indicate that the synthetic access reported herein provides a straight-forward and sustainable way of generating novel semiconductor materials with finely tunable geometric and electronic structures.

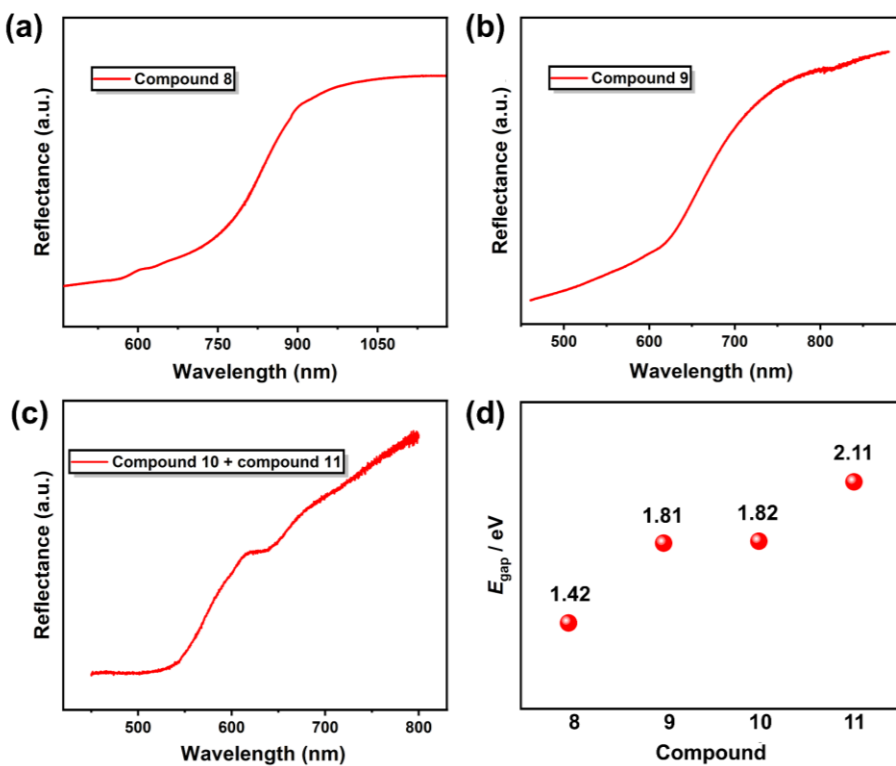


Figure 3.37: Solid-state UV-vis diffuse-reflectance spectra of compound **8** (a), compound **9** (b), compound **10** and compound **11** (c) and comparison of the differences between the optical band gap energies E_{gap} of compounds **8 – 11** (d). The tauc plots derived from the solid-state UV-vis diffuse-reflectance spectra are shown in Figure 6.21, and were generated using $(F(R\infty)hv)^{1/\gamma}$ function, with $\gamma = 0.5$, indicative for a direct allowed optical gap. And the corresponding measurement of compound **7** were hampered by its small yield.

3.3.4.2 Photocurrent measurement

Based on the distinct red-shift of the optical absorption energies of the compounds comprising Cu⁺ ions as compared to the Cu⁺-free compound, it was suspected that a corresponding effect on the photocurrent conversion efficiencies could also be found. Cyclic voltammograms (CV) were recorded on pulverized crystals of compounds **8**, **9**, **10** (with small amounts of side product **11**), or **11**. The compounds were deposited on carbon cloth under white-light irradiation and under exclusion of light (the corresponding characterization of **7** was hampered by its small yield). To ensure the accuracy of experimental results, CVs were measured under dark conditions first. As shown in Figure 3.38a–c, electrodes fabricated with compounds **8**, **9**, and **10** (plus **11**) present nearly two times the current densities during irradiation than in the dark over the applied potential range (*E*). The photocurrent density of the electron fabricated with **11** (Figure 3.38d) indicates that the photocurrent is only about 1.2 times the dark current, which indicates that copper-free selenido stannate improves the photocurrent conversion efficiency under the same irradiation condition, but at a relative moderate efficiency in comparison to the behavior of the copper-selenido stannates. Also, in terms of the absolute photocurrent and dark current density numbers, electrodes functionalized with Cu⁺-containing compounds **8** – **10** exhibit a superior conversion performance than electrode fabricated with compound **11**, which is attributed to the faster electron-hole separation during white-light illumination of the former three relative to the latter. In addition, the transient photocurrents of all electrodes were studied at a potential *E* of 250 mV vs Ag/AgCl/3 M KCl to amplify the differences in terms of their densities. As displayed in Figure 3.39, compound **11** modified electrode showcases almost negligible photocurrent response properties, while the electrode deposited with **8** achieves excellent current densities over 20 μ A/cm². Given the fact that the photocurrent and dark current keep decreasing owing to the moderate stability of these compounds, the photocurrent densities of electrodes fabricated with **8**, or a mixture of **10** and **11** decorated electrodes cannot be calculated. However, the increment of photocurrent in the first 30s after illumination of the sample was still observed.

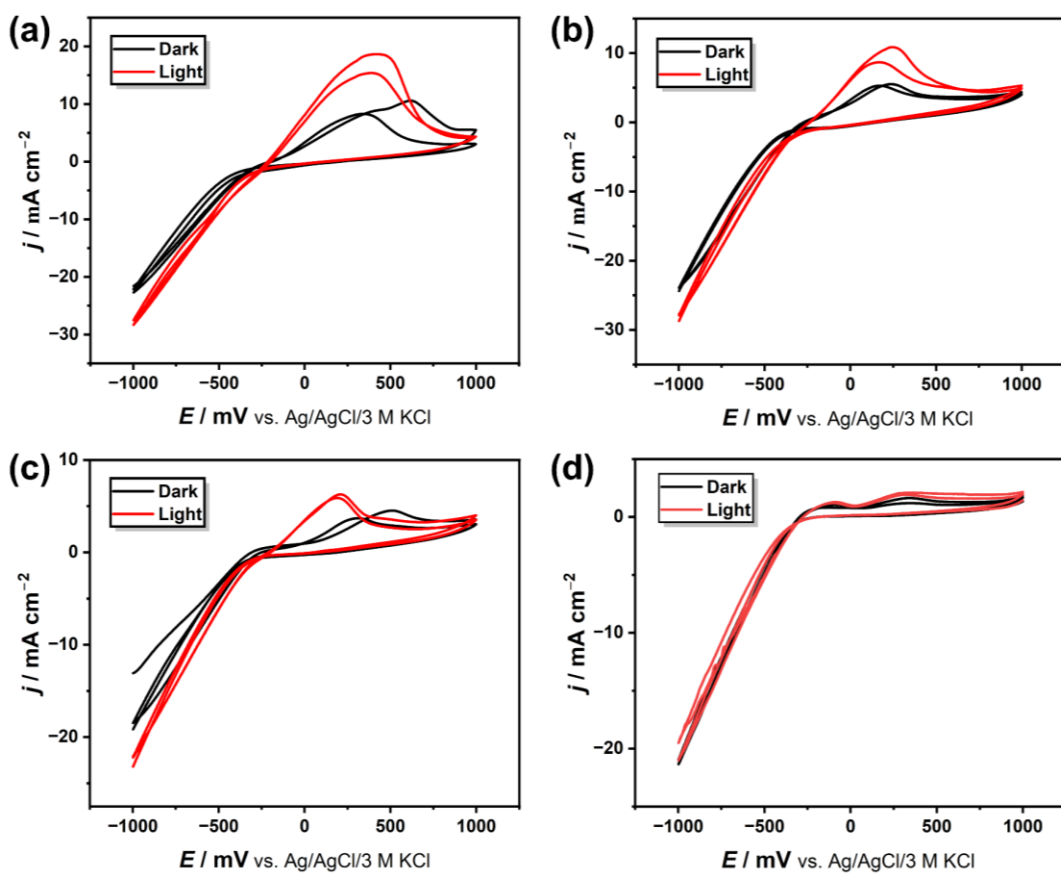


Figure 3.38: Photocurrent measurements of compounds **8** (a), **9** (b), **10** (with a small amounts of side product **11**; c), and **11** (d), given as cyclic voltammograms (CV) of pulverized crystals deposited on carbon cloth. Red curves represent measurements under white-light irradiation. Black curves were recorded under exclusion of light. Scan rate: 10 mV/s. An Ar-saturated phosphate buffer ($c = 0.1$ M) at pH = 7 was used as electrolyte, the electrode area is 0.246 cm^2 .

The study demonstrates that introducing Cu^+ into selenido stannate compounds allows for an increased photocurrent. The CVs also indicate that only oxidation peaks (Cu^+ to Cu^{2+}) of compounds **8–10** are observed on measurement, indicating that the redox reactions are irreversible and lead to degradation of the material under the given conditions. In order to improve the redox stability of such cluster-based materials, an *in-situ* anchoring of Cu^{2+} complexes around the Cu^+ in the ongoing materials development strategies is promising.

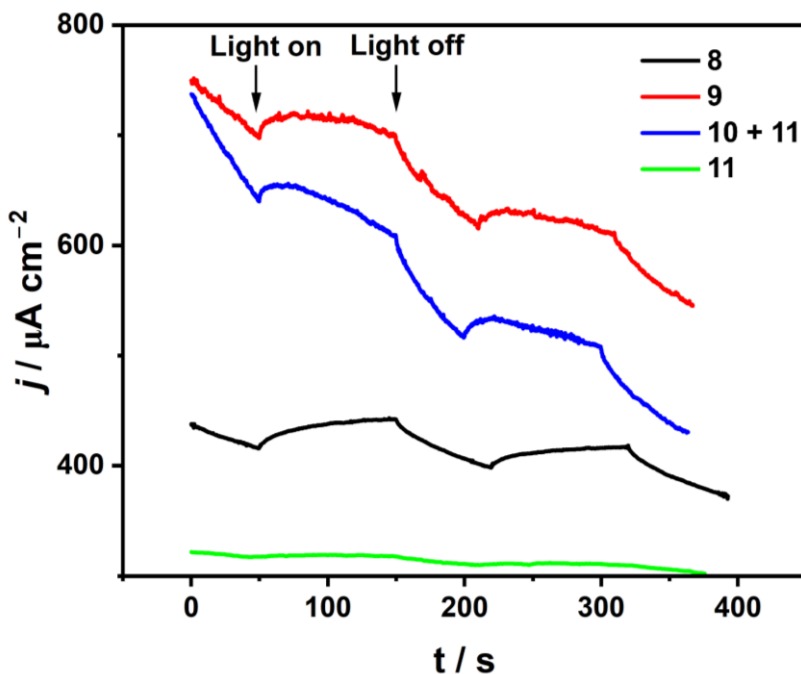


Figure 3.39: Comparison of transient amperometric response densities of **8**, **9**, a mixture of **10** and **11**, **11** fabricated working electrodes with an $E = 250$ mV by applying an on-off cycles with white light illumination.

3.3.5 Conclusions

In this work, the structural expansion of selenido stannates by introducing Cu^+ into the compounds was investigated. By reacting the salts $[\text{A}_4(\text{H}_2\text{O})_x][\text{SnSe}_4]$ ($\text{A} = \text{Li}^+$, $x = 13$; $\text{A} = \text{K}^+$, $x = 4$) with CuI in ionic liquids $(\text{C}_2\text{C}_2\text{Im})[\text{BF}_4]$ or $(\text{C}_2\text{C}_1\text{Im})[\text{BF}_4]$, a series of Cu^+ -containing anionic substructures, ranging from 0D- $\{[\text{Cu}_{10}\text{Sn}_6\text{Se}_{22}]^{10-}\}$ in **7** to 2D- $\{[\text{Cu}_8\text{Sn}_6\text{Se}_{18}]^{4-}\}$ in **8**, 3D- $\{[\text{Cu}_5\text{Sn}_3\text{Se}_{10}]^{3-}\}$ in **9**, and 3D- $\{[\text{Cu}_8\text{Sn}_6\text{Se}_{18}\text{F}]^5\}$ in **10** were accessed. Compound **7** demonstrates that this approach is suitable to push the size limit of this type of clusters, previously from 23 atoms in related ternary Cu/As/Ch assemblies ($\text{Ch} = \text{Se, Te}$) to 38 atoms in the Cu/Sn/Se combination. In compound **8**, an unprecedented 2D network which were observed—like **7**—has not been accessible by traditional synthetic approaches. Compound **9** serves to underpin the influence of reaction media that ultimately provide cations on the product formation, including the stereochemistry of complex 3D frameworks. With the observation of Compound **10**, the $\{\text{FCu}_8\text{Ch}_{12}\}$ cluster family were finally expanded from a molecular structure to an unprecedented 3D network—again inaccessible by traditional routes—with the concomitant consequence on the optical properties. With the formation of a fifth product, the importance of Cu^+ in enriching the family members of selenido metalates were underscored: in the absence of Cu^+ cations, yet under otherwise unchanged reaction conditions, compound **11** that is based on binary 2D- $\{[\text{Sn}_3\text{Se}_7]^{2-}\}$ layers is obtained.

Owing to the lower electronic transition energy of Cu^+ , its inclusion into the anionic substructures not only allows to expand the structures, but additionally and simultaneously serves to narrow the optical gaps of corresponding ternary compounds in comparison to that of binary ones as revealed by UV-vis spectroscopy. The excellent light-absorption capabilities therefore served to notably improve the photocurrent conversion efficiencies of such copper-selenido metalates.

In future investigations, the structural expansion of other chalcogenido metalates are to be investigated, like the related family of selenido germanates or homologous and mixed chalcogenides, utilizing this successful and straightforward strategy.

3.4 Structural expansion of selenido stannates by modifying the ionic liquid cation and investigation of their conductivity properties

3.4.1 Introduction

Chapter 3.3 served to understand the structural expansion of chalcogenido metalates *via* directly tailoring cluster anions through the incorporation of Cu⁺ ions. In Chapter 3.4, an alternative strategy, which involves modifying the nature of ionic liquid cation, is introduced.

In ionothermal reactions aiming at synthesizing new chalcogenido metalates, previous efforts have been focused on the modification of the length of alkyl chains, leading to anionic structures that differ in size or packing owing to the structure-directing effect of ionic liquid cations^[97,105]. In this chapter, a method towards substituting one of the alkyl groups of the imidazolium cation with a hydroxyl group is proposed. 1-propyl-3methyl-imidazolium tetrafluoroborate (abbreviated as (C₃C₁Im)[BF₄]) and 1-(2-hydroxyethyl)-3methyl-imidazolium tetrafluoroborate (abbreviated as (HOC₂C₁Im)[BF₄]) were selected as model ionic liquids for investigations. Structurally, the terminal –CH₃ of the propyl group in the former is replaced by a –OH group in the latter. Even if the hydroxy-functionalized ionic liquid cations were not found as (potentially) structure-directing counterions of chalcogenido metalates anions, they may serve as proton donors for regulation of the pH value of the reaction medium, resulting in the isolation of unprecedented compounds.

In addition to the structural expansion of chalcogenido metalates, in this chapter, anisotropic conductivity properties of four selenido stannate compounds have also been investigated. As also briefly outlined in Chapter 1, chalcogenido metalates are generally referred to semiconductor materials, yet their conductive properties, especially their anisotropic conductivity, have rarely been studied^[212,213]. Recent activities in this area, involving the conductivity measurements of (TMA)₂[MGe₄Ch₁₀], where TMA = tetramethyl ammonium, and M = Mn, Fe, Co, Ni, Zn, and Ch = S, Se, have demonstrated that (TMA)₂[FeGe₄Ch₁₀] behaves as a band-type electronic conductor^[214], while the other analogues display mixed ionic and electronic conductivities as revealed by direct-current conductivity measurement, impedance spectroscopy, and DFT modeling. However, given that [MGe₄Ch₁₀]²⁻ in (TMA)₂[MGe₄Ch₁₀] is a three-dimensional coordination polymer, it remains a challenge, but simultaneously an opportunity, to find and understand anisotropic phenomenon in chalcogenido metalates. To address this, compounds featuring two-dimensional anionic networks or one-dimensional strands are desired.

3.4.2 Syntheses and crystal structures

As mentioned in Chapter 3.3, the honeycomb-like binary substructure, 2D-{[Sn₃Ch₇]²⁻}, represents the most frequently observed anionic structural motif in chalcogenido stannate compounds^[201-205]. Their families were expanded by four new compounds *via* a Cu⁺-incorporation strategy (see Chapter 3.3), thereby manipulating the anionic substructures of the chalcogenido metalates.

Considering the structure-directing role of ionic liquid cations, in this chapter, the use of different ionic liquids for accessing compounds comprising 2D- $\{[Sn_3Ch_7]^{2-}\}$ is introduced. In the presence of DMMP, treatment of $[Li_4(H_2O)_{13}][SnSe_4]$ in 1-propyl-3-methyl-imidazolium tetrafluoroborate ($(C_3C_1Im)[BF_4]$) at 150 °C for 3 days afforded the frequently observed two-dimensional honeycomb-like substructure in $(C_3C_1Im)_3(H^+-DMMP)[Sn_3Se_7]_2$ (**12**). In this compound, three quarters of the counterions originate from the ionic liquids, and the remaining quarter are protonated DMMP molecules. By replacing the terminal $-CH_3$ of the propyl chain with a $-OH$ group in the imidazolium cation, while keeping the other reaction conditions unchanged, an unique heteroanionic substructure in $(H^+-DMMP)_2[Sn_3Se_7] \cdot (H^+-DMMP)_2[Sn_2Se_6]_{0.5}$ (**13**) was observed. In this case, all counterions are protonated DMMP, resulting in the different compound (see below for a detailed discussion of the structure). The formation of the latter is attributed to the introduction of a fairly protic hydroxyethyl group to the reaction media, serving to more effectively protonate DMMP molecules, and providing a chance to form an unprecedented compound compared to the former.

Compound **12** crystallizes in the monoclinic crystal system, space group *Cc* (No. 9), with a unit cell volume of 5806.8(7) Å³. As pictured in Figure 3.40a, the asymmetric unit comprises six crystallographically independent tin atoms, fourteen selenium atoms, three $(C_3C_1Im)^+$ and one (H^+-DMMP) counterion. Repeating the anionic substructure in the asymmetric unit through sharing Se1, Se3, Se10, and Se14 afforded the same honeycomb-type anionic substructure (Figure 3.40b) as what had been discussed in compound **11**. In compound **12**, however, not only imidazolium cations serve to balance the negative charges of the two-dimensional framework, but protonated DMMP also act as counterions. In this case, the protons are supposed to originate from water molecules present in the $[Li_4(H_2O)_{13}][SnSe_4]$ starting material. Figure 3.40c – e shows the arrangement of the layers in a $2 \times 2 \times 2$ supercell viewed from three different crystallographic directions. The protonated DMMP and imidazolium counterions are intercalated between neighboring layers.

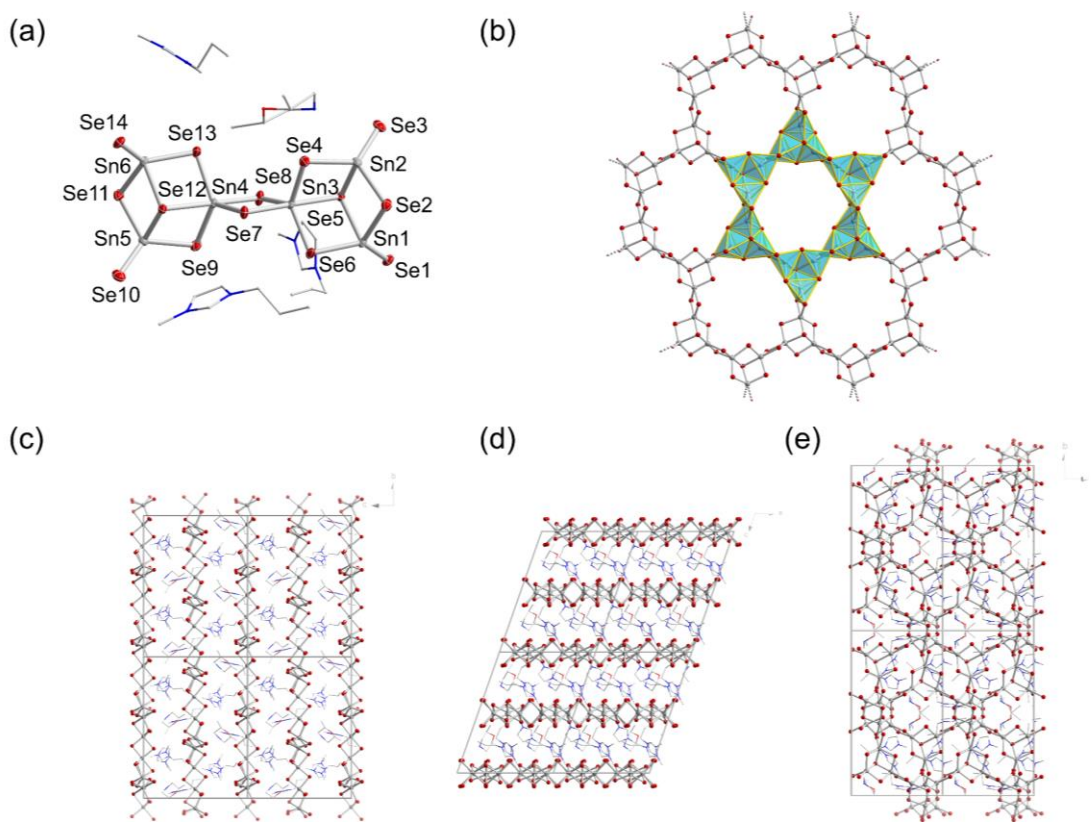


Figure 3.40: Asymmetric unit of compound **12**, Sn and Se atoms are shown as thermal ellipsoids at the 50% probability level (a). Fragment of the layer-type anion in compound **12** (b). Packing of the anions and cations in a $2 \times 2 \times 2$ supercell, the fragments that locate in the neighboring unit cell are shown with transparency (c – e).

Upon substituting the propyl group of the imidazolium cation in $(C_3C_1Im)[BF_4]$, which was used to form compound **12**, with a hydroxyethyl group, compound **13** was obtained. Compound **13** crystallizes in the triclinic crystal system, space group $P\bar{1}$ (No. 2), with a unit cell volume of $2337.5(7) \text{ \AA}^3$. As depicted in Figure 3.41a, the asymmetric unit comprises three different parts—the anionic $\{Sn_3Se_7\}$ and $\{SnSe_3\}$ units and (four) protonated DMMP counterions. In comparison to the anionic substructure in compound **12**, not only the formation of the same honeycomb-type network by repeating $\{Sn_3Se_7\}$ units can be observed, but in addition, there are dimeric $[Sn_2Se_6]^{4-}$ anions intercalated between the extended layers in this compound. While this type of anions has been known from various salts, their co-crystallization with the layer-type substructure has not yet been observed. Protonated DMMP counterions compensate for the charge of both anionic substructures (Figure 3.41b). The use of 1-(2-hydroxyethyl)-3-methylimidazolium tetrafluoroborate ionic liquid probably plays the role of proton donor in this case, as the proton is released relatively easily from a hydroxyl group. However, although only (H^+-DMMP) cations are observed as counterions in compound **13**, it cannot be excluded that the ionic liquid cations also help in the assembly of the selenido stannate substructures. Figure 3.41c – e displays the arrangement of the dimeric anions, the polymeric layer as well as the (H^+-DMMP) cations in a $1 \times 1 \times 2$ supercell viewed from different directions.

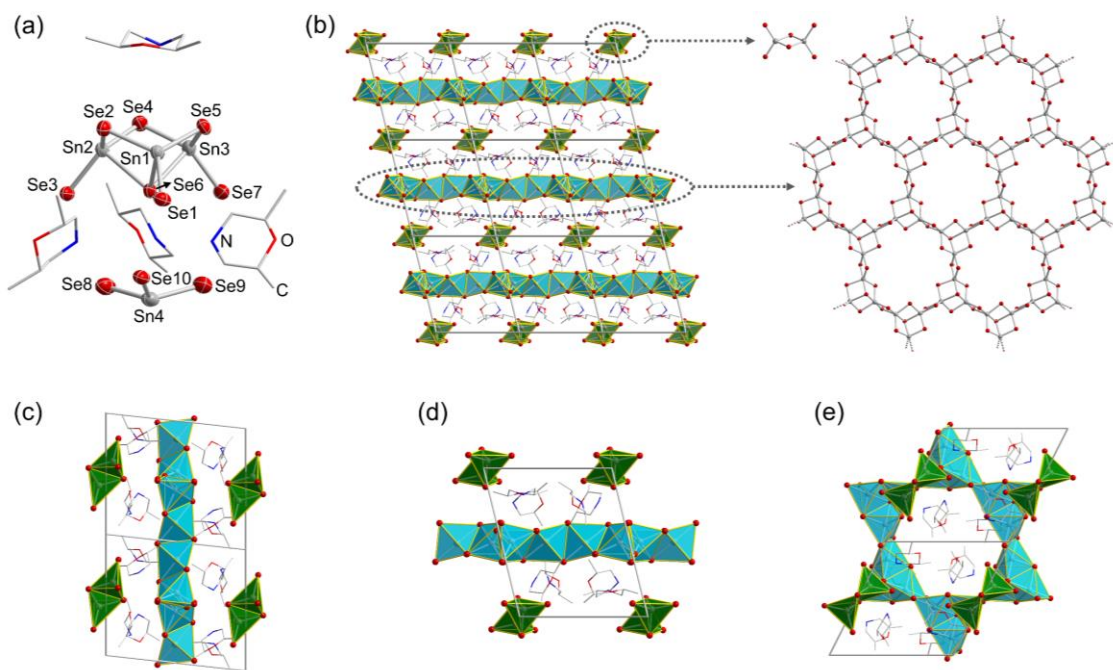


Figure 3.41: Asymmetric unit of compound **13**, Sn and Se atoms are shown as thermal ellipsoids at the 50% probability level (a). Packing of the layer-type anions and the dimeric anions in compound **13**. (b). Packing of the anions and cations in a $1 \times 1 \times 2$ supercell (c – e).

3.4.3 Additional characterizations of compounds **12** and **13**

3.4.3.1 Micro-X-ray fluorescence

Micro-X-ray fluorescence (μ -XRF) measurements were carried out on the single crystals of compounds **12** and **13** to verify the atomic ratio between Sn and Se. As illustrated in Figure 3.42, the experimental ratio of Sn:Se (0.7056:0.2941) matches well with the calculated value (0.7000:0.3000) of **12**, and the differences between measured and simulated values are below ± 1 atom, within an acceptable margin of error. For **13**, the experimental ratio of Sn:Se (0.7232:0.2768) also closely matches the calculated value (0.7143:0.2857) revealed by the SC-XRD measurement. The light elements of C, N, and H of both samples were not analyzed this way, but with SC-XRD analysis, it was possible to localize all the organic counterions, therefore, providing the accurate crystal structure and composition of both compounds.

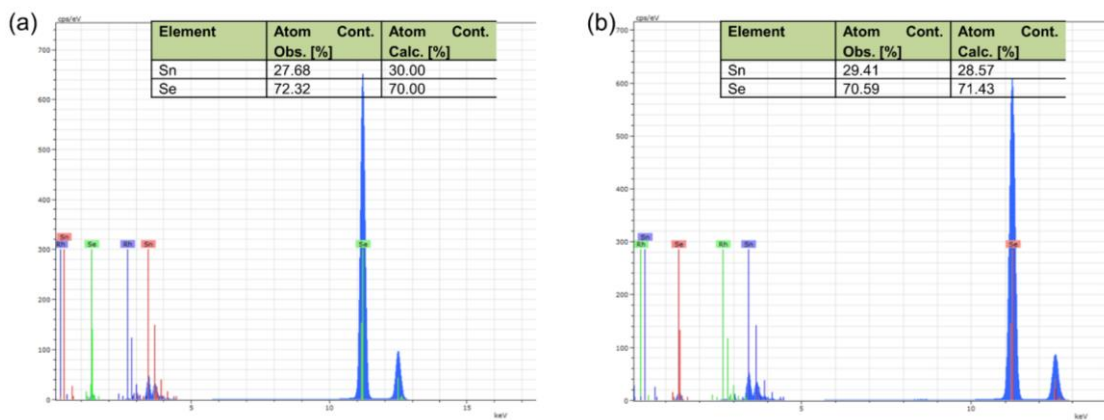


Figure 3.42: μ -XRF spectra and comparison of the differences between calculated and simulated atomic ratios of compound **12** (a), and compound **13** (b).

3.4.3.2 PXRD

As an additional characterization to verify the phase purity of of **12** and **13**, PXRD measurements were carried out on both samples. As illustrated in Figure 3.43, the measured PXRD patterns of **12** and **13** match the patterns simulated from SC-XRD analysis, confirming phase purity of both samples. Slight shifts of the measured PXRD reflections towards lower angles are caused by the effect of the temperature, as the PXRD measurements were carried out at room temperature, SC-XRD analyses were performed at 100 K. The sample measured at room temperature is more expanded than the compound measured at 100 K, therefore showing larger lattice spacing. The differences in the reflection intensities between measured and simulated patterns are attributed to texture effects, as both samples appear as hexagonal plates. This applies to compound **13** in particular.

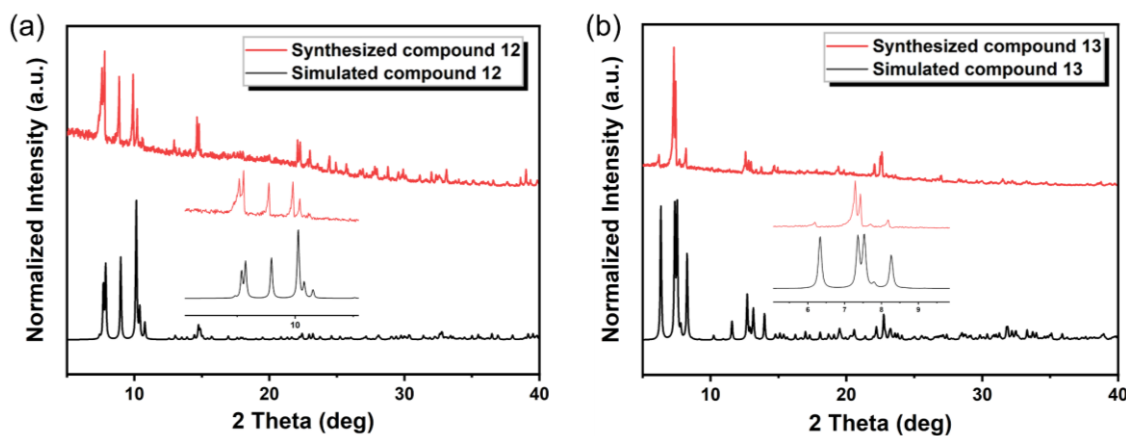


Figure 3.43: PXRD patterns of as-synthesized compound **12** along with the simulated diffractogram from SC-XRD analysis (a) and of as-synthesized **13** along with simulated from SC-XRD analysis (b); the insets display reflections at the small angle regions.

3.4.3.3 Optical properties

Solid-state UV-vis diffuse-reflectance spectroscopy, as a tool to investigate the energy gaps of semiconductor materials, was performed for compounds **12** and **13**. As shown in Figure 3.44a, the diffuse-reflectance spectrum of **12** was measured and plotted (in red) to an energy-gap-dependent absorption spectrum according to the Kubelka-Munk function^[215,216]:

$$(\alpha \cdot h\nu)^{1/n} = B(h\nu - E_g),$$

where α refers to the energy dependent absorbance, $h\nu = h \cdot c/\lambda$, E_g = energy gap, the exponent $1/n$ denotes the nature of the transitions, while $n = 2$, indicating for an indirect allowed transition, while $n = 0.5$, indicating for a direct allowed transition.

For compound **12**, in comparison to a direct energy gap value, the indirect energy gap value is closer to the energy gap calculated from the absorbance spectrum, therefore compound **12** is determined to be an indirect band gap semiconductor material. The energy gap was calculated to be 1.93 eV. Compound **13** was also determined to be an indirect band gap material, yet the replacement of half the honeycomb-type layers by $[\text{Sn}_2\text{Se}_6]^{4-}$ anions led to a slightly wider energy gap compared to that of **12**, and was determined to be 1.98 eV according to the Kubelka-Munk function (Figure 3.44b). The energy gaps of **12** and **13** are close to those of reported materials in the chalcogenido metalate family and of the well-known materials SnCh and SnCh_2 . They might therefore potentially be used as semiconducting materials, like SnCh and SnCh_2 which have been studied greatly in this regard over the last two decades^[217-219].

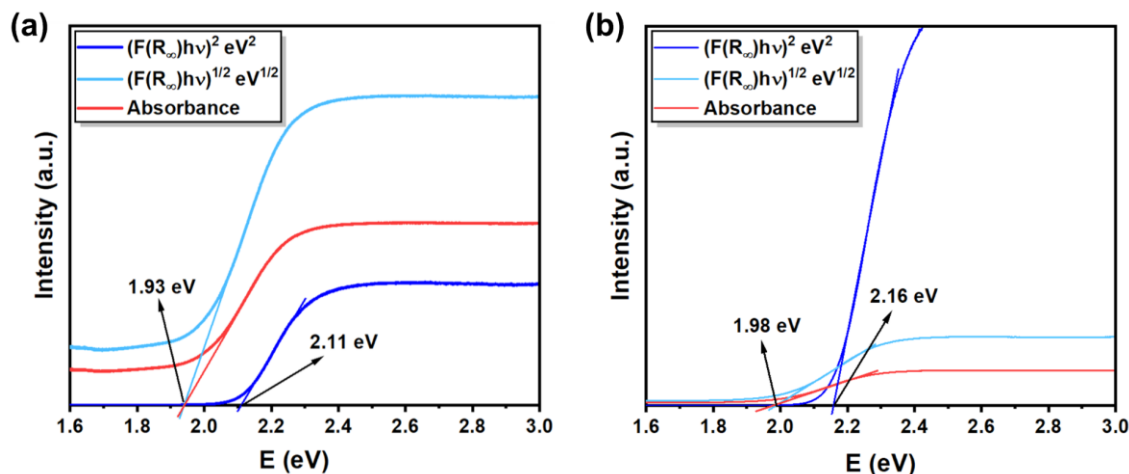


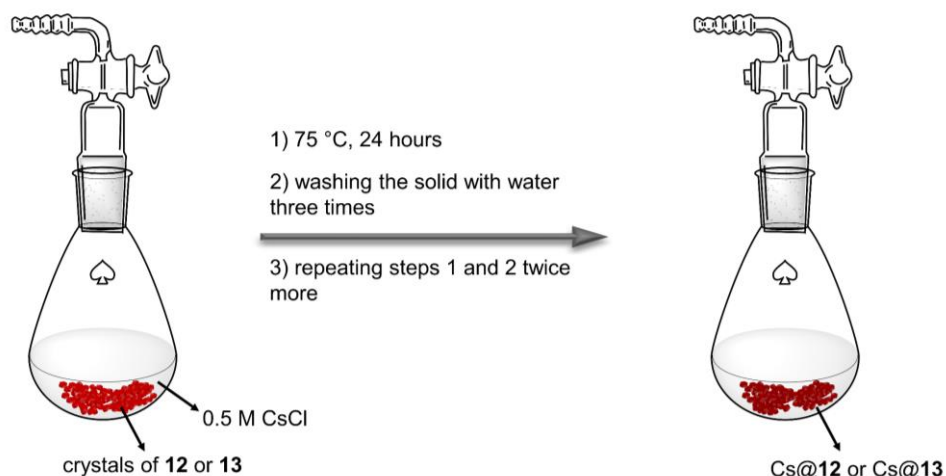
Figure 3.44: Solid-state UV-vis diffuse-reflectance spectra of compound **12** (a) and compound **13** (b). Both compounds were determined to be indirect band gap semiconductors.

3.4.4 Ion-exchange experiments of compounds **12** and **13**

The various salts of $[\text{Sn}_2\text{Ch}_6]^{4-}$ are soluble in water^[220,221], and the organic cations of chalcogenido stannates are exchangeable by soaking in concentrated aqueous solution of ACl (A = alkali metal ions)^[141,158,222,223]. The isolation of **12** and **13** therefore provides an opportunity to exchange the

organic cations of both and extract the molecular $[\text{Sn}_2\text{Se}_6]^{4-}$ anions of the latter out of the inter-layer spacings without decomposing the crystal structures themselves. By doing so, it is not only possible to study the properties of two more compounds, but also provides an opportunity to understand how the conductivities differ between inorganic or organic cation templated chalcogenido metalates.

The ion-exchange process was operated under Ar. As illustrated in Scheme 3.6, 10 mg crystals of **12** or **13** were immersed in 10 ml of an aqueous solution of CsCl (0.5 M) in a Schlenk flask, the flask was heated at 75 °C for 24 hours to allow the cation exchange and anion extraction process. After allowing the mixture to cool down to room temperature, the solution was filtered into another flask and analyzed by ESI-MS. The solid residue was washed three times with degassed water. The full process was repeated twice. The obtained solid samples are denoted as Cs@**12** and Cs@**13**, respectively.



Scheme 3.6: Schematic illustration to the ion-exchange reactions of **12** and **13** in aqueous solution of CsCl under inert condition.

ESI-MS was carried out to investigate the ion-exchange process. For the solution obtained after ion-exchange of **12**, as illustrated in Figure 3.45a–c, (H^+-DMMP) and $(\text{C}_3\text{C}_1\text{Im})^+$ cations were observed from high-resolution ESI(+) spectra, and the experimental isotope patterns are both in excellent agreement with the calculated isotopic distributions. Additionally, Cs^+ and hydrated (H^+-DMMP) were also detected in the ESI(+) spectrum. Elemental mapping was further performed on a single crystal to investigate the product obtained after ion-exchange. The even distribution of cesium, as shown by its elemental mapping images in Figure 3.45d, demonstrates the cation exchange took place in the whole crystal. Infrared spectroscopy (IR) was further carried out to detect any remaining organic counterions. As demonstrated in Figure 3.45e, this also corroborates an exchange of the organic cations, as the characteristic vibrations detected for **12** are considerably weaker in the IR spectrum of Cs@**12**, although a complete exchange was not achieved.

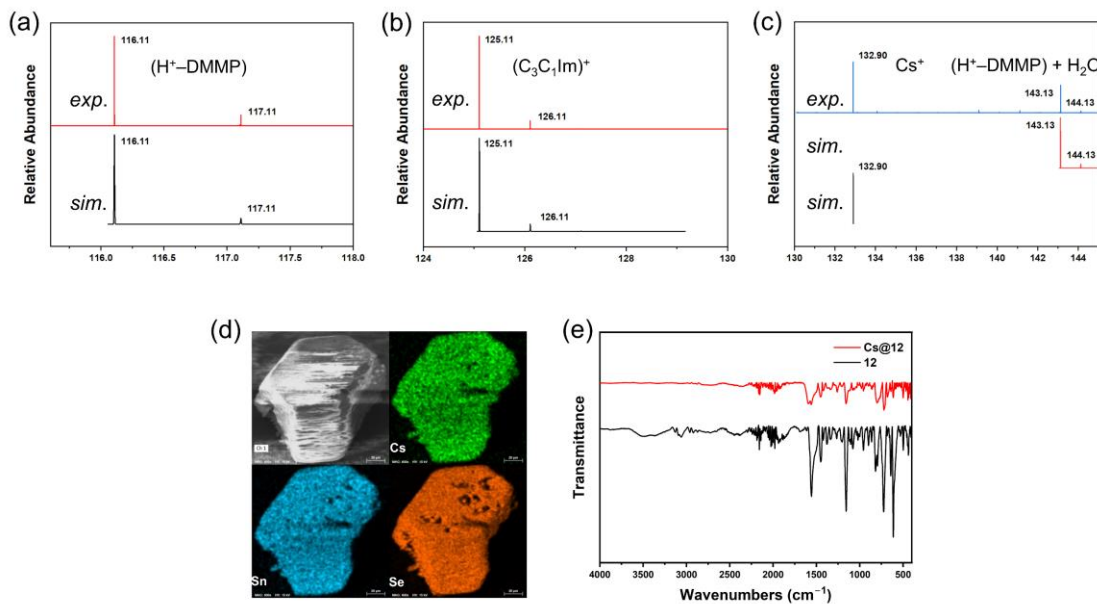


Figure 3.45: High resolution ESI(+) mass spectra of $(\text{H}^+ \text{--DMMP})$ (a), $(\text{C}_3\text{C}_1\text{Im})^+$ (b), and hydrated $(\text{H}^+ \text{--DMMP})$ (c) detected in the solution after ion-exchange process. Elemental mapping of **Cs@12**, showing even distribution of Cs, Sn, and Se (d); comparison of IR spectra of **12** and **Cs@12** (e).

PXRD measurements were additionally performed, as depicted in Figure 3.46a. The measured PXRD patterns of **Cs@12** and **12** serve to clarify the ion-exchange experiments by comparing the reflections' shifts at small scattering angle (2θ). There is no shift observed at $2\theta = 7.59^\circ$ between the PXRD patterns of **Cs@12** and **12**, indicating no obvious volume expansion or shrinking along the (1,1,0) lattice plane (Figure 3.46b). However, at scattering angles $2\theta = 7.83$ or $2\theta = 8.87$ in the diffractogram of **12**, corresponding to the (1,1,−1) or (0,2,1) lattice planes (Figure 3.46c–d), there is a slight shift towards smaller angles found in the PXRD pattern of **Cs@12**, demonstrating an expansion along those lattice planes upon the cation exchange process. This is attributed to the size differences of organic cations and hydrated Cs^+ ions, even though the shifts are small. As demonstrated in Figure 3.46a, the scattering angles $2\theta = 9.90$ in the PXRD pattern of **12** and at $2\theta = 9.83$ in the diffractogram of **Cs@12** correspond to the (0,0,2) lattice planes (Figure 3.46e) and further confirm the cation-exchange process. More notable differences between the scattering angles are caused by the more distinct distances along the (0,0,2) lattice planes as compared to the other lattice planes.

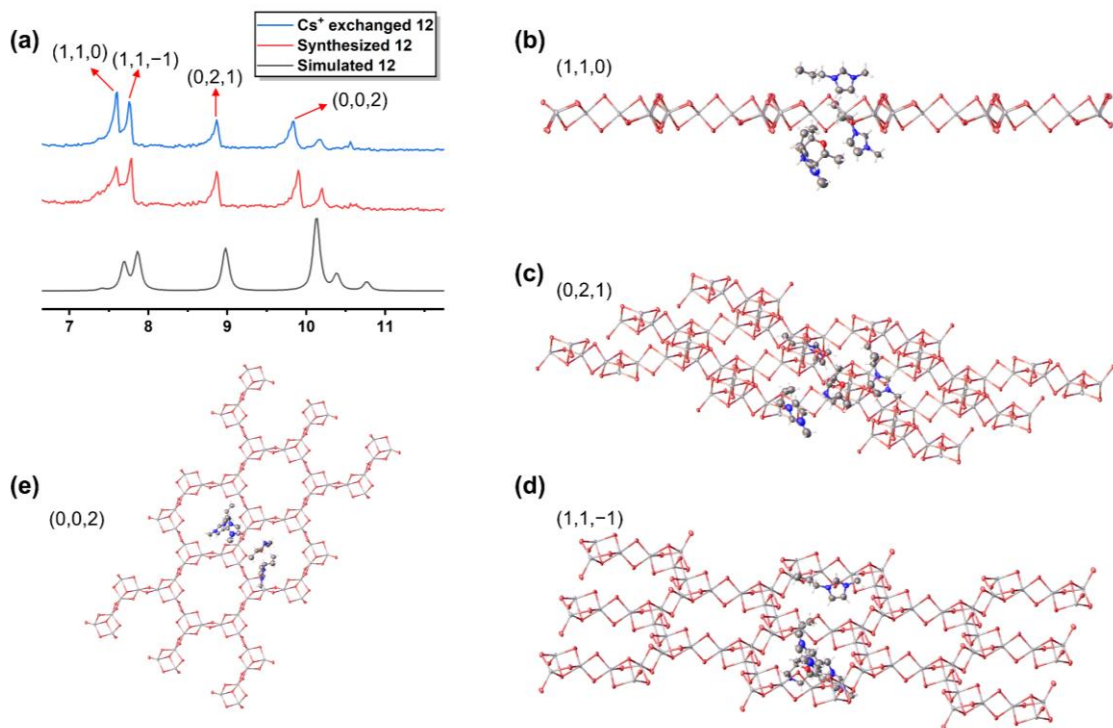


Figure 3.46: Comparison of the simulated PXRD pattern of **12** with its experimental pattern and with that of **Cs@12**
 (a). The anionic honeycomb layer viewed along various directions: (1,1,0) (b), (0,2,1) (c), (1,1,-1) (d), and (0,0,2) (e).

Similar characterizations were carried out to understand the ion-exchange process of **13**. The yellowish solution obtained after the ion-exchange process was investigated *via* ESI-MS. Figure 3.47a–b displays the high-resolution ESI(+) spectra of (H⁺-DMMP) and Cs⁺. Both experimental isotope patterns match well with the simulated distributions, indicating the successful cation-exchange of (H⁺-DMMP) with Cs⁺. Interestingly, a set signals of fragments {Cs₃[Sn₂Se₆]}⁻ (Figure 3.47c), {Cs[Sn₂Se₅]}⁻, {Cs[Sn₂Se₄]}⁻, and {H[Sn₂Se₅]}⁻ were also detected in the ESI(-) mass spectrum (see Chapter 6.1.13 for their high-resolution mass spectra), suggesting the extraction of [Sn₂Se₆]⁴⁻ units. EDX and elemental mapping were further performed on a single crystal to investigate the product upon ion exchange. The even distribution of cesium, as shown by elemental mapping images in Figure 3.47d, demonstrates that the cation exchange took place in the whole crystal. According to IR spectra of **13** and **Cs@13**, the (H⁺-DMMP) cations were not able to be completely exchanged, and not as effectively as for **Cs@12**, (Figure 3.47f).

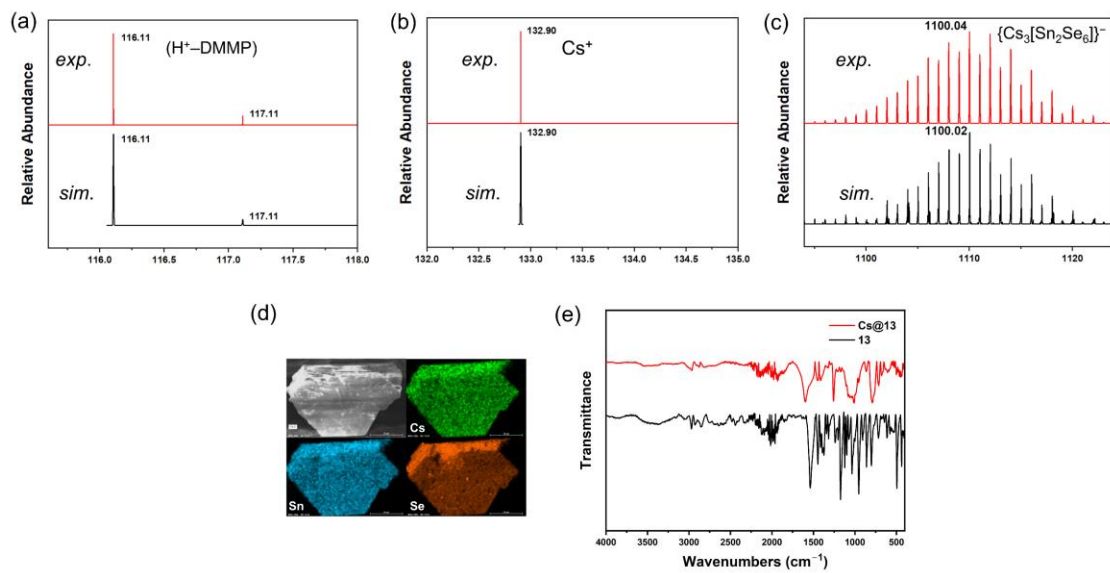


Figure 3.47: High resolution ESI(+) mass spectra of (H^+ -DMMP) (a) and Cs^+ (b); and high resolution ESI(-) mass spectrum of $\{\text{Cs}_3[\text{Sn}_2\text{Se}_6]\}^-$ (c) detected in the solution after the ion-exchange process. Elemental mapping of $\text{Cs}@\mathbf{13}$, showing even distribution of Cs, Sn, and Se (d); comparison of IR spectra of **13** and $\text{Cs}@\mathbf{13}$ (e).

PXRD was also performed to characterize **13** and $\text{Cs}@\mathbf{13}$ for demonstrating the cation-exchange and anion-extraction reactions. As shown in Figure 3.48a, the PXRD pattern of experimental **13** matches well with the one simulated from SC-XRD. For $\text{Cs}@\mathbf{13}$, the only two significant reflections observed at scattering angles $2\theta = 7.36^\circ$ and $2\theta = 7.56^\circ$, corresponding to lattice planes (1,0,0) and (0,1,0) (Figure 3.48b–c), indicate the long-range order along the two-dimensional networks. Slight shifts by 0.07° toward higher angles are attributed to the slight pore shrinking of the six-membered-rings of the anionic substructure. The diminished intensity of other reflections as compared to the PXRD pattern of parent **13**, for example the reflections representing the (0,0,1) (Figure 3.48d) and (1,1,1) planes, suggests no long-range order along these lattice planes. This is attributed to the successful extraction of some of the $[\text{Sn}_2\text{Se}_6]^{4-}$ units, leading to a rather random arrangement of the layers and remaining $[\text{Sn}_2\text{Se}_6]^{4-}$ anions along these lattice planes.

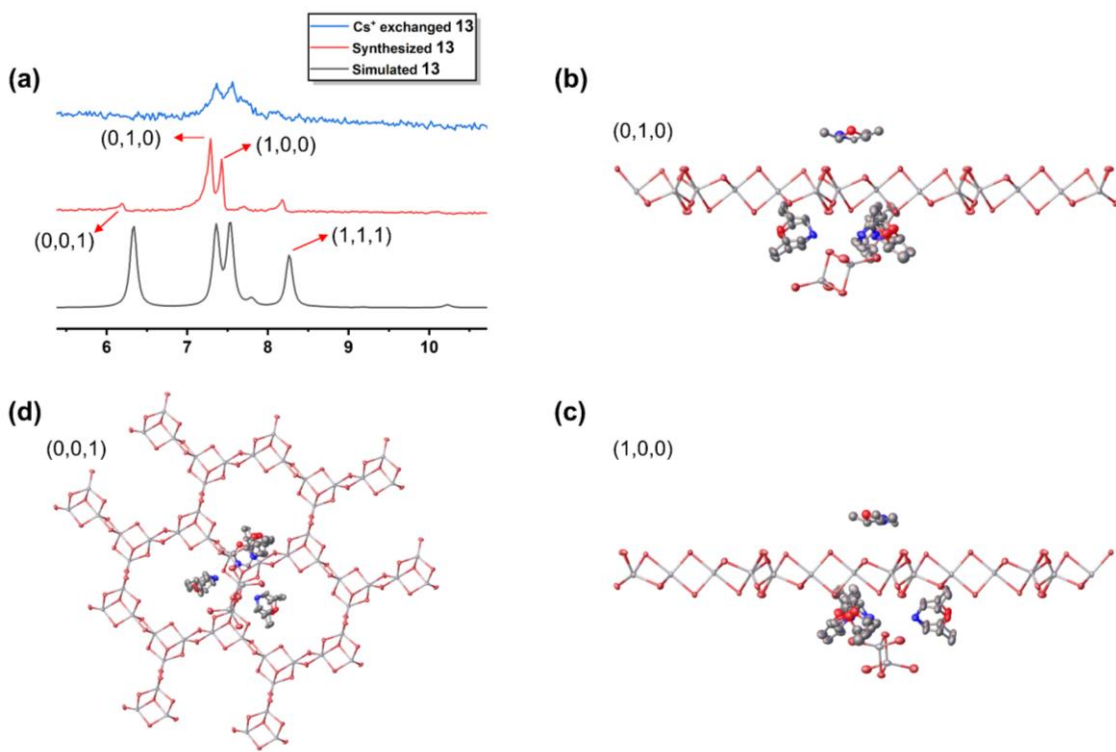
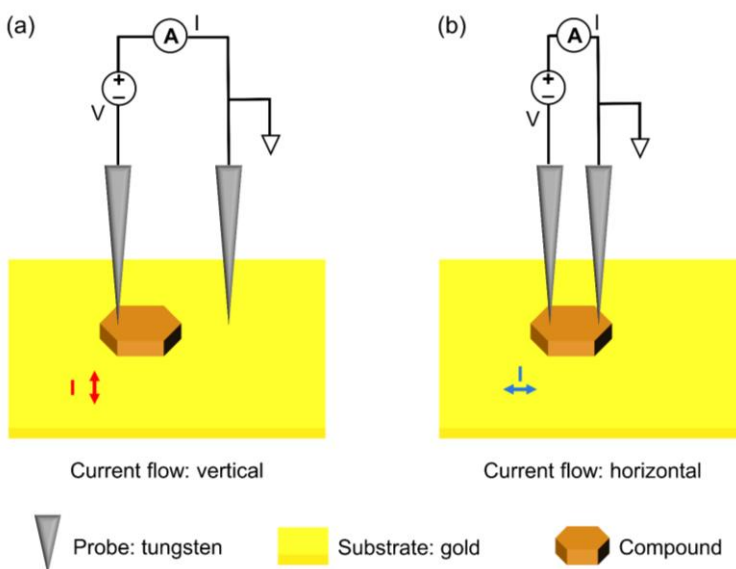


Figure 3.48: Comparison of the simulated PXRD pattern of **13** with its experimental pattern and with that of **Cs@13**
 (a). The anionic substructure viewed along various directions (0,1,0) (b), (1,0,0) (c), (0,0,1) (d).

3.4.5 Conductivity measurements

To understand the conductive nature of these compounds, a set of electrical measurements were performed on single crystals. As shown in Scheme 3.7, the hexagon-shaped crystals of **12**, **Cs@12**, **13**, and **Cs@13** were placed onto a gold-coated silicon wafer along the horizontal faces. The *I*-*V* characteristics were measured along horizontal or vertical directions of the crystals by varying the tungsten probes' positions. While one of the tungsten tips points towards the top surface of the crystal, and the other one situates at the gold substrate, the measured current flows vertically across the crystal. By placing both tungsten probes onto the top surfaces of the crystal, the current flow that crosses over the horizontal direction is obtained. This way, it provides a platform to investigate and understand the conducting behavior of this type of materials in different orientations.



Scheme 3.7: Schematic illustration of the two-terminal conductivity measurement along vertical (a) and horizontal (b) directions of the hexagon-shaped crystals.

The I - V characteristics were measured within an initial voltage sweep ($-10\text{ V} \rightarrow 10\text{ V}$) over a single crystal of compound **12**. As demonstrated in Figure 3.49, the voltage-dependent currents are nonlinear and asymmetric from both vertical and horizontal directions, revealing its semiconducting nature along the two different directions. However, the measured currents are small, even with a bias voltage at 10 V . As for Cs@12 , the I - V characteristics were recorded with a voltage sweep from -2 V to 2 V (denoted as forward sweeping), and from 2 V to -2 V (denoted as backward sweeping). As shown in Figure 3.50, the I - V curves, measured along vertical and horizontal directions, serve to demonstrate that the voltage-dependent currents improve by around ten times upon cation-exchange of **12**. More importantly, the I - V curves feature non-zero-crossing current, indicating a capacitor-like I - V characteristics. To better understand the non-zero-crossing nature, I - V hysteresis was investigated vertically and horizontally by applying sweeping voltage following a $0\text{ V} \rightarrow +2\text{ V} \rightarrow -2\text{ V} \rightarrow 0\text{ V}$ order. Figure 3.50c displays the hysteresis along the vertical direction of Cs@12 . At the initial stage, while no bias voltage was applied, there is no current flow observed. As the voltage sweeps from 0 V to $+2\text{ V}$, the current flow gradually increases. In the phase with a voltage sweeping from $+2\text{ V}$ to -2 V , an open circuit voltage (V_{OC}) at $+0.88\text{ V}$ is observed at where the current was determined to be zero but with 0.88 V voltage applied. While decreasing the voltage from -2 V to 0 V , a second V_{OC} at -0.68 V was obtained, indicating a pair of asymmetric V_{OC} s along the vertical direction of Cs@12 . During the voltage sweep direction transition from $+2\text{ V}$ to -2 V and -2 V to 0 V , two non-zero-crossing currents were observed at 0 V , suggesting a short circuit current (I_{SC}). This is attributed to the existence of a displacement current (I_{d}), which is a sum of voltage changes ($\text{V} \frac{dV}{dt}$) and capacitance changes ($\text{C} \frac{dC}{dt}$) over time. Yet, given that the former is a small number, the latter dominates the change and leads to the observation of I_{SC} at 0 V ^[224,225]. The same phenomenon has been found from the I - V hysteresis measured along the horizontal direction of Cs@12 (Figure 3.50d), although with altered V_{OC} (1.66 V and -0.54 V) and I_{SC} (-0.013 nA and 0.006 nA) values.

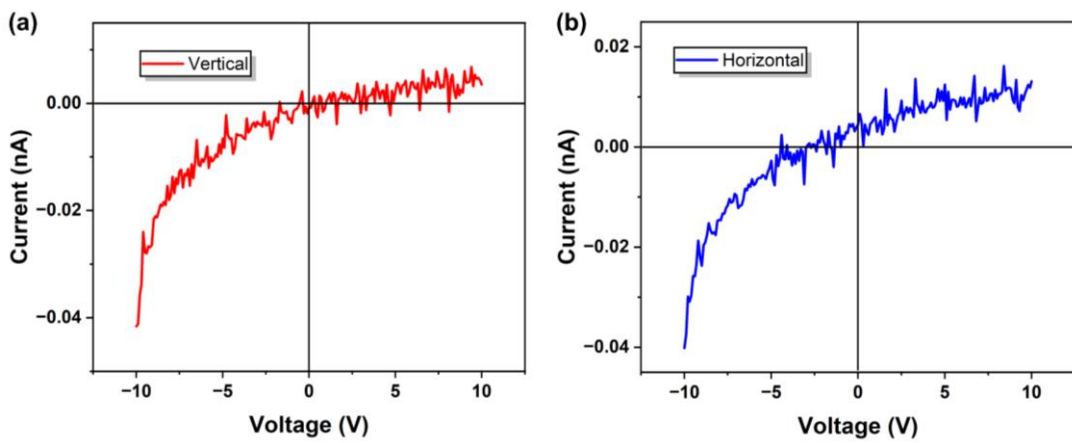


Figure 3.49: I - V characteristics of compound **12** measured over a single crystal, along vertical (a) and horizontal directions (b), within a voltage sweep from -10 V to $+10$ V.

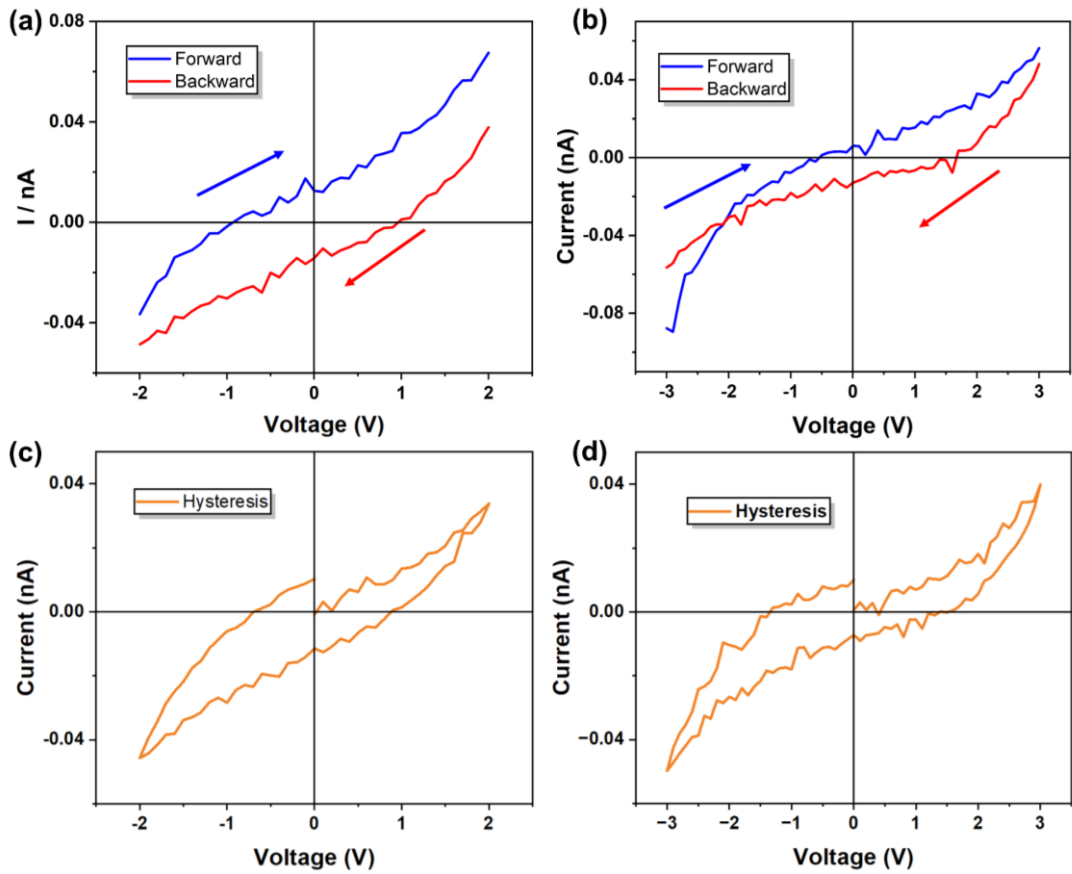


Figure 3.50: I - V curves of Cs@**12** measured over a single crystal along vertical (a) and horizontal (b) directions, both forward (blue) and backward (red) I - V curves are shown. I - V hysteresis of Cs@**12** measured over a consecutive voltage sweep (0 V \rightarrow $+2$ V \rightarrow -2 V \rightarrow 0 V) along vertical direction (c), and over a consecutive voltage sweep (0 V \rightarrow $+3$ V \rightarrow -3 V \rightarrow 0 V) along horizontal direction (d).

Chronoamperometry, as a tool for revealing conduction mechanisms of a material, were performed on single crystals of **Cs@12** along two directions. The current flows across vertical and horizontal directions of **Cs@12** were recorded while stepping the applied voltage by +0.5 V each 50 seconds between 0 V and 5 V. As illustrated in Figure 3.51a, at 0.0 – +1 V, the current flows are too small to be accurately distinguished from the background noise. However, by applying a higher voltage, at +1.5 – +5.0 V, it was found that the current flows decrease gradually at a steady biased voltage, indicating an ionic conductivity along the vertical direction; this is attributed to the movement of Cs^+ cations through the six-membered channels of the anionic substructure. As for the horizontal direction (Figure 3.51b), the currents are too small to determine the conduction mechanisms.

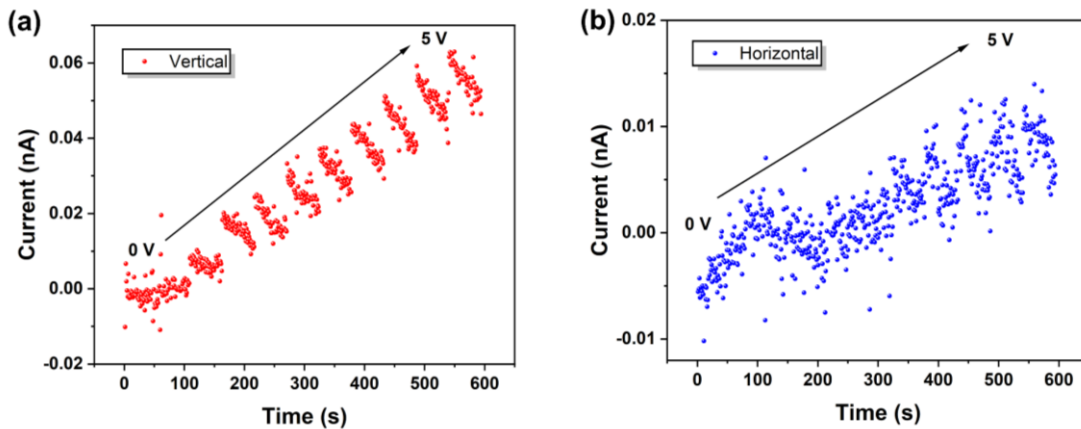


Figure 3.51: Chronoamperometry traces measured over single crystal of **Cs@12** along vertical (a) and horizontal (b) directions, under applied voltages ranging from 0 V to +5 V, with steps of 0.5 V.

Temperature-dependent I – V characteristics were additionally carried out to demonstrate temperature effects on the anisotropic conducting behavior of **Cs@12**. As depicted in Figure 3.52a, vertical I – V curves of **Cs@12** measured at four varied temperatures, room temperature, 313.75 K, 333.75 K and 353.75 K show that the higher the temperature, the lower the conductivity. This contrasts with the temperature-dependent conductivity of many reported ionic or electronic conductors, whose conductivity increase at higher temperature. It is possible that the structure of **12** becomes more flexible upon ion-exchange, and the anionic layers are more distant from one another upon raising the temperature up from room temperature to higher temperatures. This leads to a lower density of Cs^+ cations per unit volume and, consequently, reduces the conductivity compared to that at room temperature. Given the temperature-dependent I – V characteristics measured along the horizontal direction feature the same conduction behavior (Figure 3.52b), it is suggested that ionic conductivity also dominates the conductivity along the horizontal direction.

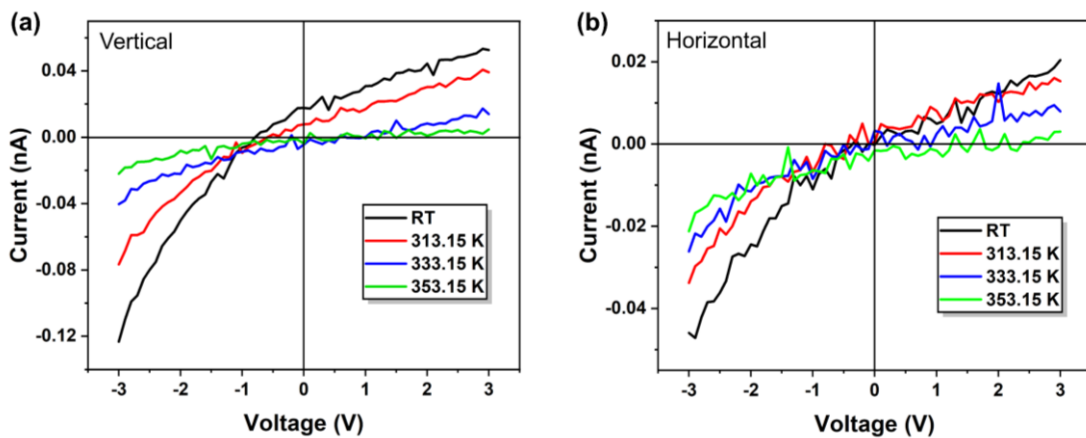


Figure 3.52: Temperature-dependent I – V curves of **Cs@12** measured along vertical (a) and horizontal (b) directions. I – V curves measured along both directions were carried out at room temperature, 313.15 K, 333.15 K, and 353.15 K.

The full set of I – V characteristics were also investigated over **13** and **Cs@13**. As shown in Figure 3.53, the I – V curves measured along both vertical and horizontal directions of **13** indicate its insulating behavior. For the horizontal direction, assuming that the topmost “layer” consists of $[\text{Sn}_2\text{Se}_6]^{4-}$ units, this leads to an open-circuit, and causes in an insulating characteristic. For the vertical direction, it is assumed a result of the substitution of the more mobile ionic liquid cations by the less mobile (H^+ –DMMP). However, for **Cs@13**, similar capacitor-like I – V characteristics were observed as for **Cs@12**, again suggesting a successful cation exchange. The forward (voltage scans from -2 V to $+2$ V) and backward (voltage scans from $+2$ V to -2 V) current flows along the two measured directions display non-linear characteristics, both exhibiting a pair of asymmetric V_{oc} and I_{sc} (Figure 3.54a–b).

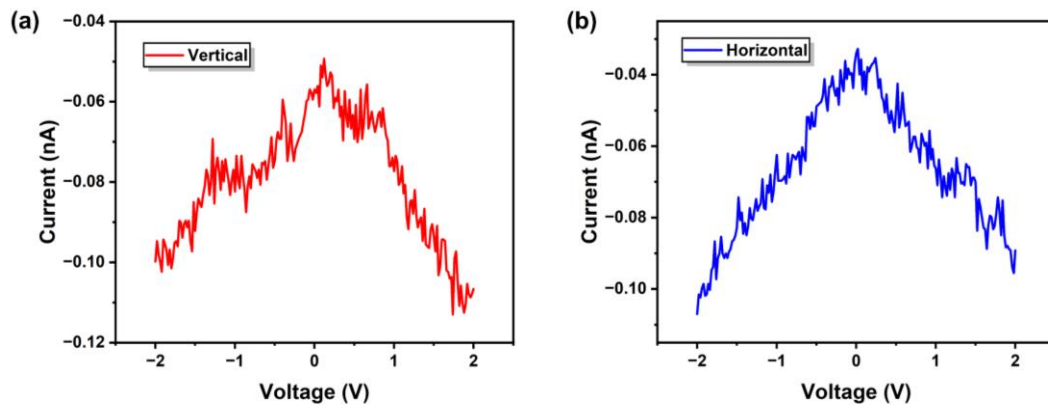


Figure 3.53: I – V characteristics of compound **13** measured over single crystal, along vertical (a) and horizontal directions (b), within a voltage sweep from -2 V to $+2$ V.

The I – V hysteresis was additionally investigated vertically and horizontally by applying a sweeping voltage following a $0\text{ V} \rightarrow +2\text{ V} \rightarrow -2\text{ V} \rightarrow 0\text{ V}$ order. Figure 3.54c displays the hysteresis along the vertical direction of Cs@13 . At the initial stage while no bias voltage is applied, the current is determined to be 0 nA . After scanning Cs@13 with a bias voltage from 0 V to $+2\text{ V}$ via -2 V to 0 V , the two V_{oc} are found at $+0.51$ and -0.98 V , respectively, and the two I_{sc} measured as -0.029 and $+0.048\text{ nA}$, slightly differing from the V_{oc} and I_{sc} numbers observed from the I – V hysteresis along vertical direction of Cs@12 . The horizontal I – V curve exhibits a similar hysteresis phenomenon but with V_{oc} being $+0.96$ and -0.84 V , and I_{sc} being -0.035 and $+0.021\text{ nA}$ (Figure 3.54d). Despite variations in the absolute V_{oc} and I_{sc} values, the hysteresis suggests capacitor-like I – V characteristics in both directions for compound Cs@13 .

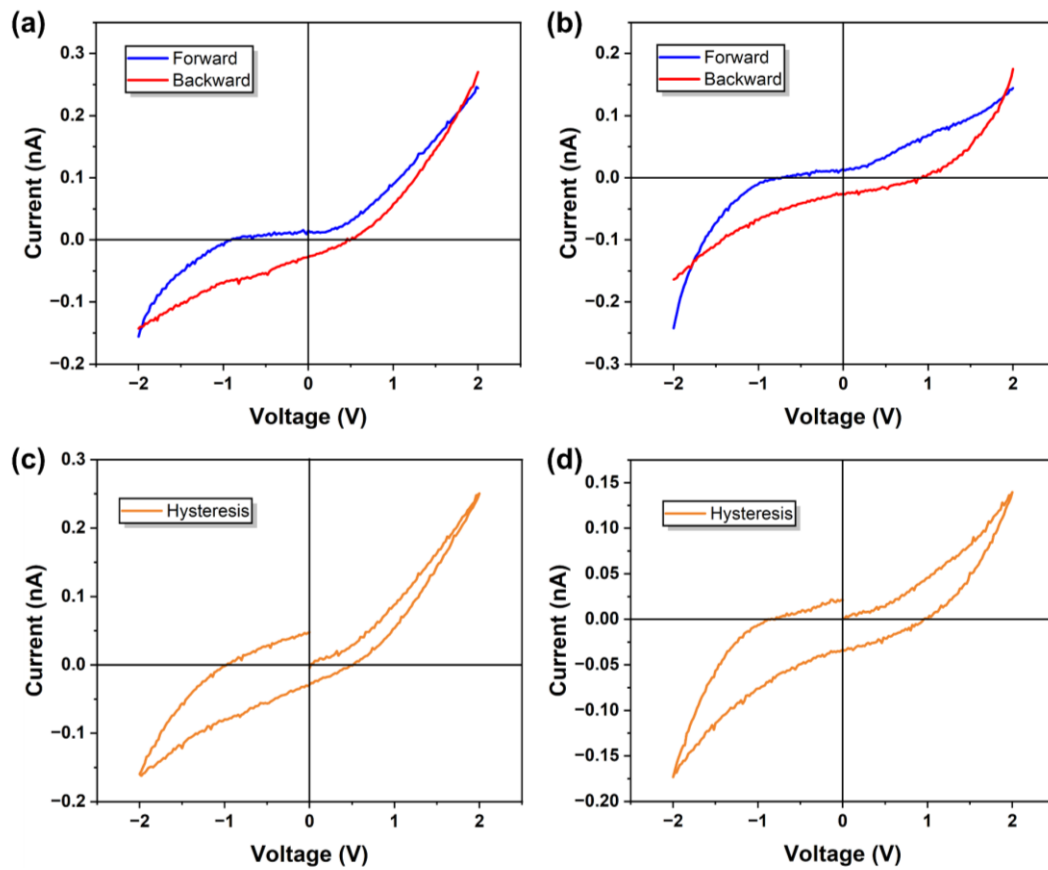


Figure 3.54: I – V curves of Cs@13 measured along vertical (a) and horizontal (b) directions, both forward (blue) and backward (red) I – V curves are shown. I – V hysteresis of Cs@12 measured over a consecutive voltage sweep ($0\text{ V} \rightarrow +2\text{ V} \rightarrow -2\text{ V} \rightarrow 0\text{ V}$) along vertical direction (c), and over a consecutive voltage sweep ($0\text{ V} \rightarrow +2\text{ V} \rightarrow -2\text{ V} \rightarrow 0\text{ V}$) along horizontal direction (d).

Chronoamperometry measurements were performed to elucidate the conduction mechanisms of Cs@13 along the two directions. As illustrated in Figure 3.55, at 0.0 – 1.0 V , the current flows are too small to yield reliable conclusions. At $+1.0$ – $+5.0\text{ V}$, the current flows decrease gradually at each steady bias voltage, indicating an ionic conductivity in both directions. This behavior is

attributed to the migration of Cs^+ cations through the six-membered channels of the anionic substructure in the vertical direction, and across the interlayer spacing of the network in the horizontal direction.

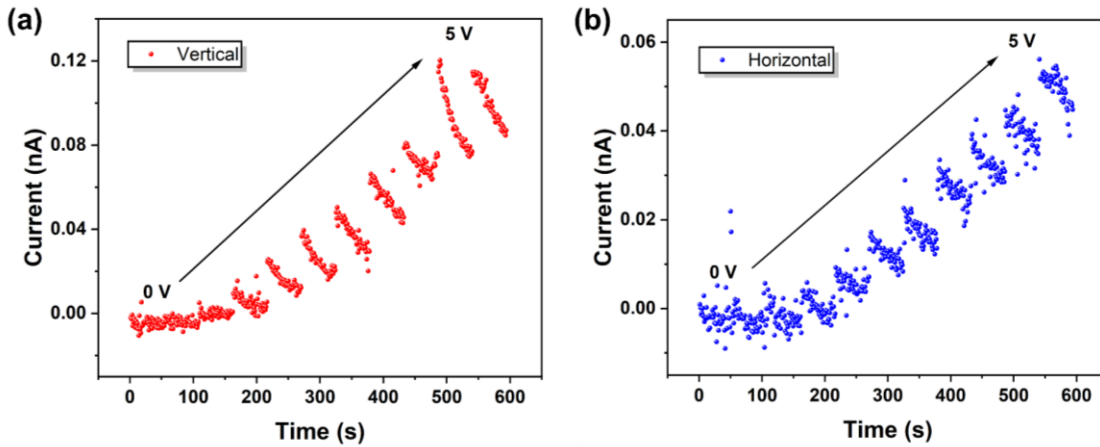


Figure 3.55: Chronoamperometry traces measured of $\text{Cs}@\mathbf{13}$ along vertical (a) and horizontal (b) directions, under applied voltages ranging from 0 V to +5 V, with steps of 0.5 V.

Temperature-dependent I – V characteristics were also investigated in order to further understand the anisotropic conducting behavior of $\text{Cs}@\mathbf{13}$. As demonstrated in Figure 3.56a, in the vertical direction, the current decreases with increasing temperature, displaying temperature-dependent I_{sc} and temperature-independent V_{oc} . In the horizontal direction, temperature-dependent I – V characteristics reveal similar conduction mechanisms, but with smaller I_{sc} and V_{oc} values (Figure 3.56b). It also suggests that increasing the temperature causes the anionic layers to separate further, leading to a lower density of Cs^+ cations per unit volume, and therefore a reduced conductivity.

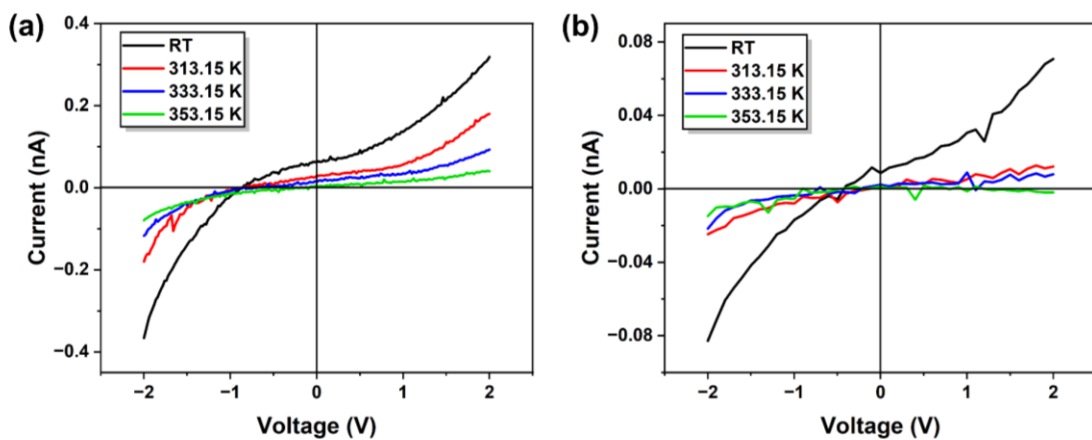


Figure 3.56: Temperature-dependent I – V curves of $\text{Cs}@\mathbf{13}$ measured along vertical (a) and horizontal (b) directions. I – V curves measured along both directions were carried out at room temperature, 313.15 K, 333.15 K, and 353.15 K.

3.4.6 Conclusions

In conclusion, two new compounds, $(C_3C_1Im)_3[H^+-DMMP][Sn_3Se_7]_2$ (**12**) and $(H^+-DMMP)_2[Sn_3Se_7] \cdot (H^+-DMMP)_2[Sn_2Se_6]_{0.5}$ (**13**), are presented in this chapter. The compounds were obtained by treating $[Li_4(H_2O)_{13}][SnSe_4]$ in 1-propyl-3-methylimidazolium tetrafluoroborate, $(C_3C_1Im)[BF_4]$, or in 1-(2-hydroxyethyl)-3-methylimidazolium tetrafluoroborate, $(HOC_2C_1Im)[BF_4]$, in the presence of DMMP. **12** comprises the well-known honeycomb-type 2D- $\{[Sn_3Se_7]^{2-}\}$ substructure, with three quarters of counterions being $(C_3C_1Im)^+$ cations and one quarter being (H^+-DMMP) . However, for the reaction that yields **13**, the hydroxyethyl group of the applied ionic liquid cation serves to more effectively protonate the DMMP molecules. With only (H^+-DMMP) counterions present, the unprecedented double-salt comprising $[Sn_2Se_6]^{4-}$ and 2D- $\{[Sn_3Se_7]^{2-}\}$ anionic substructures were formed. Further treatment of **12** and **13** in aqueous CsCl solution afforded cation-exchanged **12** (denoted as **Cs@12**), and cation-exchanged and $[Sn_2Se_6]^{4-}$ -anion-extracted **13** (denoted as **Cs@13**). *I*-*V* characteristics serve to reveal the semi-conducting nature along both vertical and horizontal directions of **12**. However, the incorporation of $[Sn_2Se_6]^{4-}$ anions in **13** creates an open circuit along the horizontal direction, thus leading to an insulating behavior. Upon a Cs^+ -exchange process, the conductivity increases along both directions, as revealed by forward and backward *I*-*V* curves. Additionally, the *I*-*V* hystereses feature non-zero-crossing currents, suggesting a capacitor-like conductive nature along both directions for **Cs@12** and **Cs@13**. Chronoamperometry traces show that Cs^+ migration dominates the conductivity in two directions of these compounds. Temperature-dependent *I*-*V* curves feature lower conductivity at higher temperature owing to a decreased Cs^+ density per unit cell upon increasing temperature. This work contributes on understanding and offering a platform to investigate the conductive nature of chalcogenido metalates.

3.5 Further structural expansion of selenido metalates via the above-mentioned strategies

In addition to the new compounds introduced in Chapter 3.3 and 3.4, which were obtained by a) heteroatom-incorporation or b) modification of the structure-directing agents, eight more new compounds (compounds **14** – **21**) were obtained following these two concepts. Their crystal structures are discussed below, information on the synthesis of these compounds is provided in Chapter 5.4. Further characterizations are yet to be performed.

3.5.1 Crystal structure of compound **14**

Compound **14** crystallizes in the triclinic crystal system, space group $P\bar{1}$ (No. 2), with a unit cell volume of $3552(2)$ Å³. As illustrated in Figure 3.57a, the asymmetric unit comprises six crystallographically independent tin atoms, fourteen selenium atoms, one bromine atom, and five (C₃C₁C₁Im)⁺ counterions; only four of the counterions refinable due to a heavy disorder of the remaining one. The two formula units in the asymmetric unit of **14** feature slight structural differences in terms of the bonding situation between Sn and Se atoms. While Se4 is bonded to three neighboring Sn atoms, the distance between Sn4 and Se11 is 3.1897(12) Å, indicating weak interactions only; therefore it is shown as a dashed line. Besides this, the Sn6–Se11 bond (2.5075(8) Å) is by nearly 0.7 Å shorter, and the terminal Sn6–Se12 bond length is 2.4181(10) Å. By repeating the asymmetric units *via* sharing Se1, Se3, and Se14, the 1D- $\{[Sn_3Se_7]_2^{4-}\}$ substructure is obtained (Figure 3.57b). A similar anionic substructure was reported in the (C₄C₁C₁Im)₄[Sn₃Se₇]₂^[97] and (C₄C₁C₁Im)₃(H⁺–DMMP)[Sn₃Se₇]₂^[226]. The smaller size of the propyl group of the ionic liquid cation in **14** in comparison to that of a butyl group in the published salts may cause the inclusion of the (C₃C₁C₁Im)Br ionic liquid to fulfill the steric needs. Apart from slightly modifying the structure of such compounds, the incorporation of (C₃C₁C₁Im)Br may serve to modulate the opto-electronic properties. Further efforts toward the replacement of Br[–] by other congener halide ions, like Cl[–] or I[–], is about to be investigated. More structural details of compound **14** are depicted in Figure 3.57c – e.

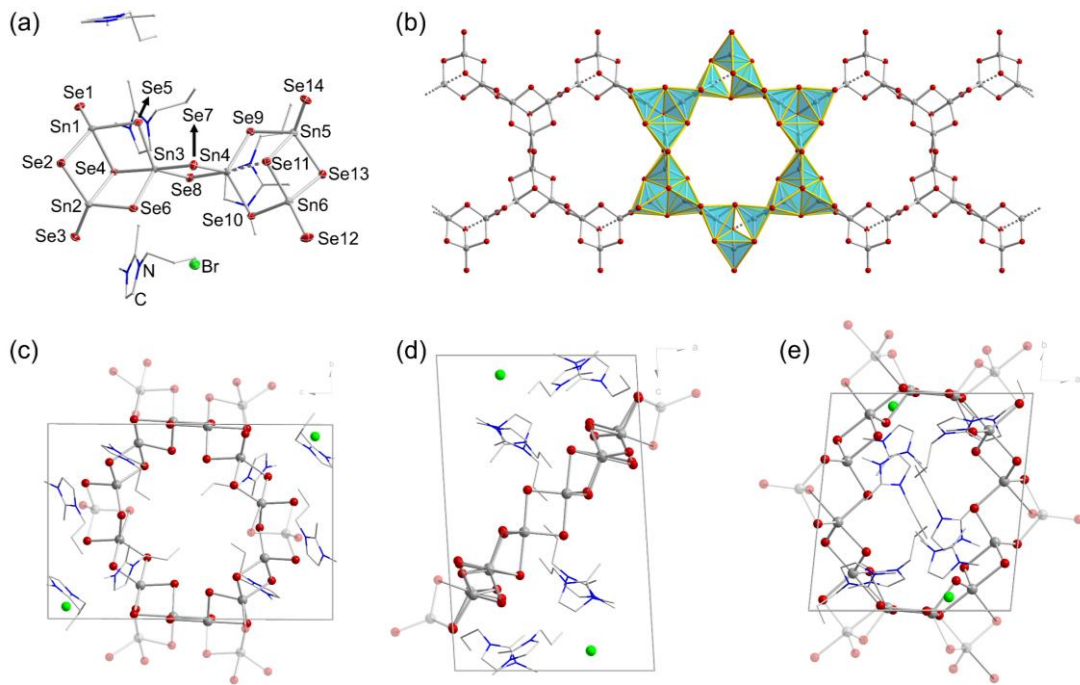


Figure 3.57: Asymmetric unit of compound **14**; Sn, Se, and Br are shown as thermal ellipsoids at the 50% probability level (a). Fragment of the strand-type substructure in compound **14** (b). Packing of the anions and cations in the unit cell; fragments that locate in the neighboring unit cell are shown with transparency (c – e).

3.5.2 Crystal structure of compound 15

Further modifications in term of the alkyl chain length at the imidazolium cation and the use of a different type of anion of the ionic liquids allow the isolation of similar substructures in some cases. Upon replacing the ionic liquid ($\text{HOC}_2\text{ClIm}^+ \text{BF}_4^-$) for forming **13** with $(\text{C}_2\text{C}_2\text{Im})\text{Br}$, and while keeping the other reaction conditions unchanged, compound **15** was obtained.

Compound **15** crystallizes in the monoclinic crystal system, space group $P21/n$ (No. 14), with a unit cell volume of $13446.5(4) \text{ \AA}^3$. As shown in Figure 3.58a, the asymmetric unit is more complex and comprises four $[\text{Sn}_3\text{Se}_7]^{8-}$ units, two Br atoms, and ten $(\text{C}_2\text{C}_2\text{Im})^+$ cations. By repeating the $[\text{Sn}_3\text{Se}_7]^{8-}$ units *via* sharing Se1, Se4, Se11, Se14 and Se15, Se18, Se27, Se28, the honeycomb-like substructure $2\text{D}-\{[\text{Sn}_3\text{Se}_7]^{8-}\}$ is obtained again (Figure 3.58b). All the Sn–Se bond lengths are within the reported range and similar to the values in compounds **12–13** and **15**. The use of Br^- as the anion of the ionic liquids slightly modifies the compositions of the compounds. One may notice that the asymmetric unit contains two additional units of the $(\text{C}_2\text{C}_2\text{Im})\text{Br}$ ionic liquid, which renders **15** a double-salt compound. And again, the incorporation of $(\text{C}_2\text{C}_2\text{Im})\text{Br}$ may serve to modify the optical properties of such compounds. Logically, the next step will include the substitution of Br^- by other halide anions as well as the exploration of their corresponding optical properties. Figure 3.58c – e displays the arrangement of anions and cations within the unit cell viewed from different directions.

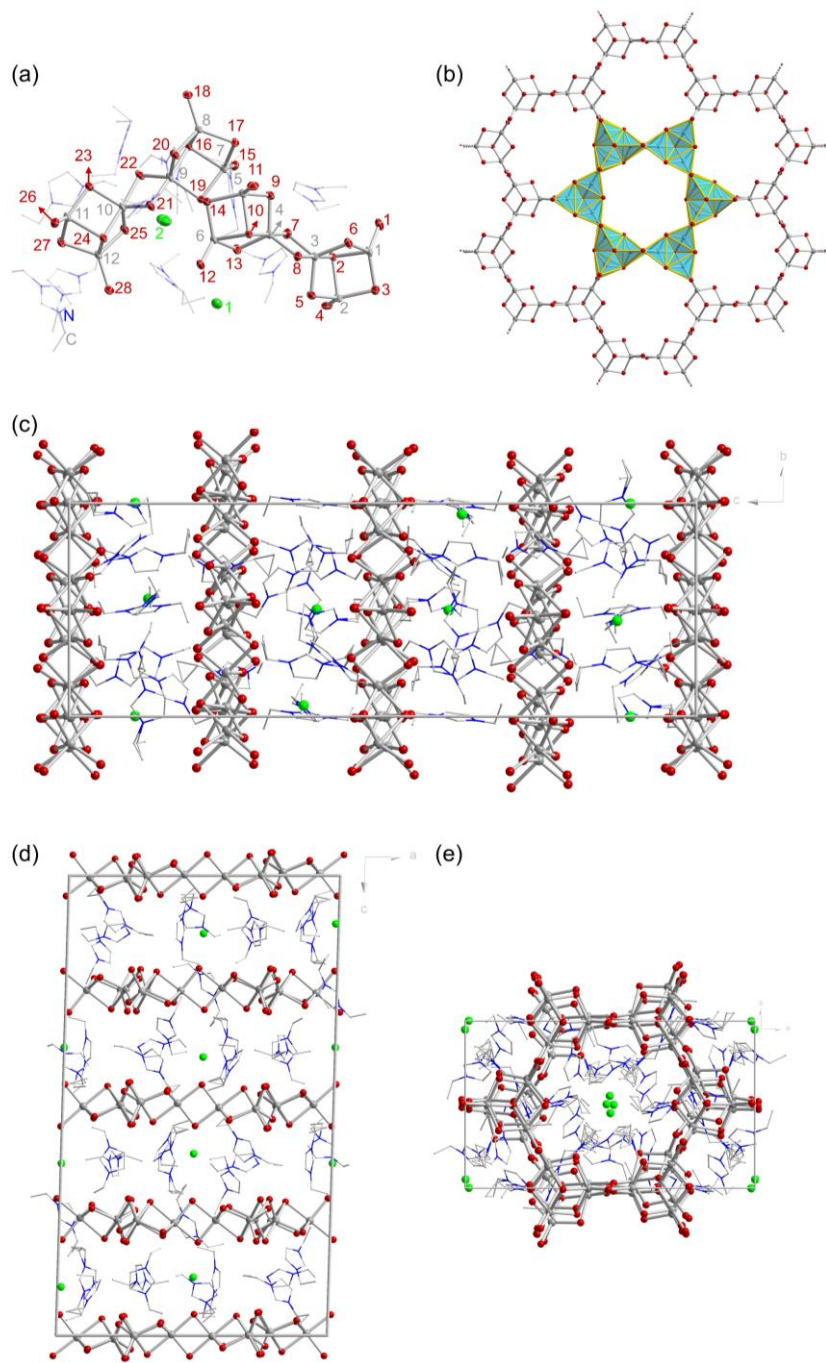


Figure 3.58: Asymmetric unit of compound **15**; Sn, Se and Br atoms are shown as thermal ellipsoids at the 50% probability level (a). Fragment of the layer-type substructure in compound **15** (b). Packing of the anionic layers, bromide atoms and counter cations in the unit cell (c – e).

Compounds **12–15** are all obtained under the same reaction conditions, but upon using slightly different ionic liquids through modifying the length or the nature of the attached alkyl chains or using different types of anions. The treatment of $\text{Li}_4[\text{SnSe}_4]$ in DMMP and a tri-alkylated imidazolium-based ionic liquid, $(\text{C}_3\text{C}_1\text{C}_1\text{Im})\text{Br}$, yielded a double-salt with the formula of

$(C_3C_1C_1Im)_4[Sn_3Se_7]_2 \cdot (C_3C_1C_1Im)Br$ (**14**). By using a di-alkylated imidazolium-based ionic liquid (C_3C_1Im)[BF_4], as the reaction medium and origins of the counterions, the strand-type substructure were further extended to a honeycomb-like anion (in **12**). Again, by using symmetrical 1,3-diethylimidazolium bromides as the reaction medium, the same anionic honeycomb-like 2D- $\{[Sn_3Se_7]^{2-}\}$ substructure was obtained in compound **15**, yet in this case, two more $(C_2C_2Im)Br$ crystallize in the asymmetric unit. The isolation of these compounds confirms once more that changing the length of the attached alkyl chains, the nature of the attached alkyl chains, and the use of different types of anions in ionic liquids can effectively modify the product spectrum of such selenido metalate compounds.

3.5.3 Crystal structure of compound **16**

Compound **16** crystallizes in the trigonal crystal system, space group $P31/c$ (No. 159), with a unit cell volume of $5242.8(10)$ \AA^3 . As shown in Figure 3.59a, the asymmetric unit comprises four tin atoms, two oxygen atoms and eight selenium atoms. All the Sn–Se bond lengths are within a reasonable range, yet for the Sn–O bonds, there are only weak interactions observed between Sn3 and O2 or Sn1 and O1, the connection is therefore illustrated by dashed lines. Figure 3.59b displays the known *pseudo*-T3-type $[Sn_{10}Se_{20}O_4]^{8-}$ cluster anion in compound **16**. Here, four oxygen atoms are accommodated in the four adamantine cages of a perfect T3-type “ $\{Sn_{10}Se_{20}\}$ ” cluster architecture. For targeting this cluster, the use of $[Li_4(H_2O)_{13}][SnSe_4]$ precursor is suitable, as it brings in O^{2-} ions. In contrast, treatment of $Li_4[SnSe_4]$ with ionic liquids under the same reaction condition does not afford the $[Sn_{10}Se_{20}O_4]^{8-}$ cluster. However, the counterions are unidentifiable due to heavy disorder, and therefore, the electron density of atoms that could not be localized from the difference Fourier map was detracted from the data by application of the back-Fourier transform method, using SQUEZZE tool in PLATON^[129]. Figure 3.59c – e shows different views of the unit cell. Each unit cell accommodates two *pseudo*-T3-type $[Sn_{10}Se_{20}O_4]^{8-}$ clusters.

With this compound, it is demonstrated that pyrrolidinium-based ionic liquids can also support the formation of selenido metalates. Therefore, further studies concerning the use of similar pyrrolidinium-based ionic liquids for the transformation of chalcogenido metalates should be performed.

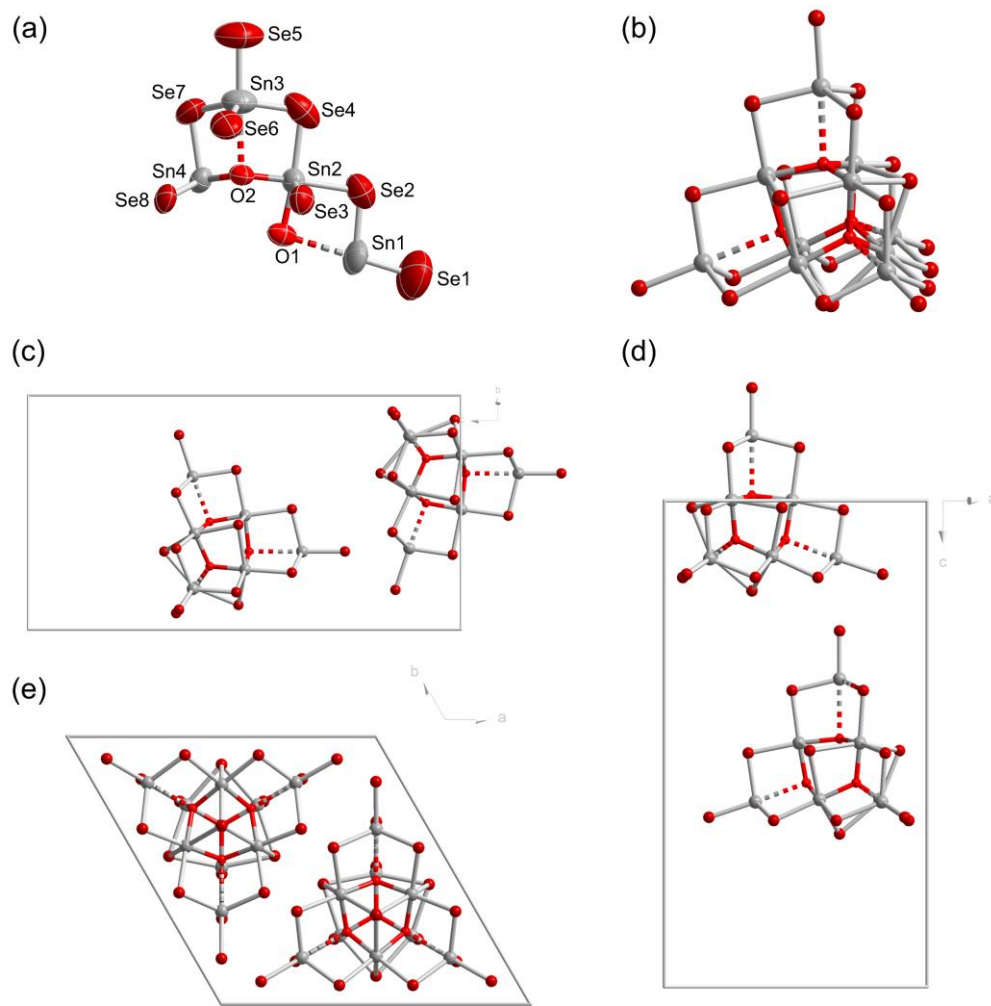


Figure 3.59: Asymmetric unit of compound **16**; Sn, Se and O atoms are shown as thermal ellipsoids at the 50% probability level (a). Molecular structure of the cluster anion in compound **16** (b). Packing of the two anions in compound **16** in the unit cell (c – e).

3.5.4 Crystal structure of compound 17

Compound **17** crystallizes in the tetragonal crystal system, space group *I*41/*a* (No. 88), with a unit cell volume of 2925.0(9) Å³. As shown in Figure 3.60a, the anion in the asymmetric unit comprises a central Sn1/Hg1 co-occupied metal atom position, and three Se ligand atoms. The further coordination assembly between Sn1/Hg1 and all Se atoms leads to the formation of a T2-type {Hg_xSn_{4-x}Se₁₀} architecture. By sharing the four corner Se atoms with adjacent clusters, an infinite layer-type substructure is formed, formulated as (Cat)_{2x}[Hg_xSn_{4-x}Se₈]. From a reticular chemistry perspective, the T2 cluster-based substructure can be simplified as a *sql* network by treating each T2-type cluster as a node (Figure 3.60b). In compound **17**, the Hg1/Sn1–Se2 bond lengths are close to the mean value of the overall Hg1/Sn1–Se bond lengths, as a consequence of the connection of the clusters. In Figure 3.60c – e, the substructure is illustrated in a 2 × 2 × 2 supercell from different crystallographic directions.

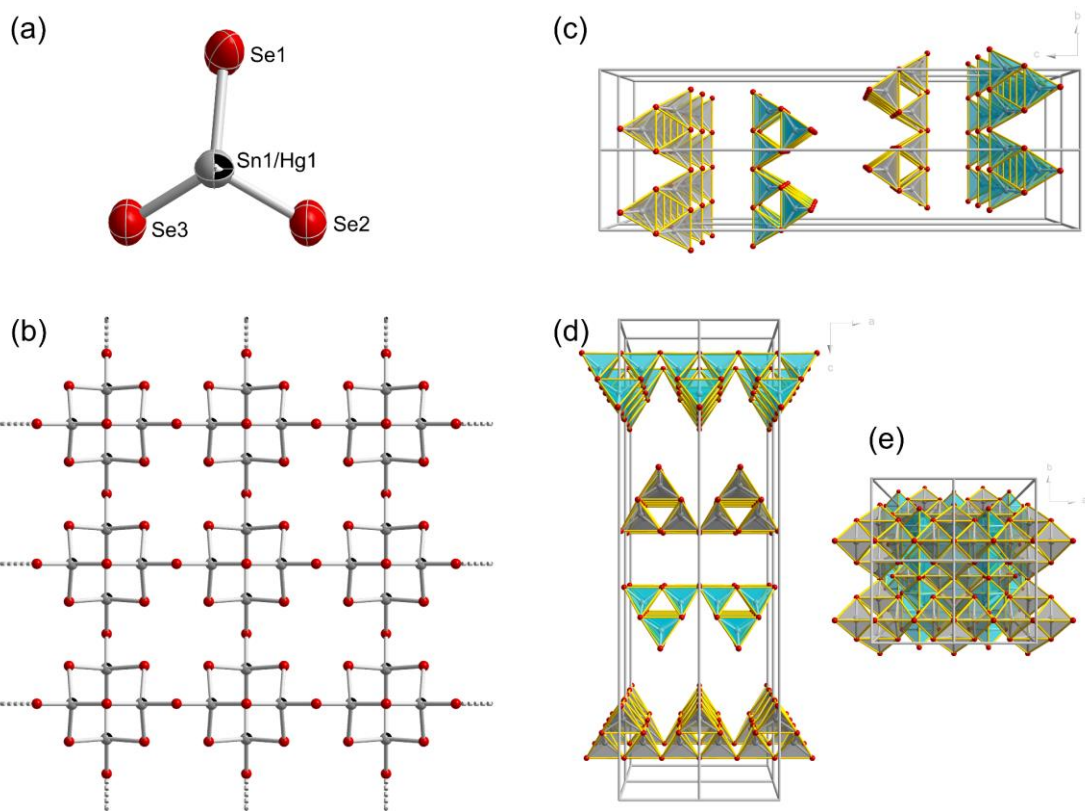


Figure 3.60: Asymmetric unit of compound **17**; Sn/Hg and Se atoms are shown as thermal ellipsoids at the 50% probability level (a). Fragment of the layer-type substructure in compound **17** (b). Packing of the polymeric layers in compound **17** in a $2 \times 2 \times 2$ supercell (c – e).

3.5.5 Crystal structure of compound **18**

As discussed in Chapter 3, incorporation of heteroatom, especially Cu^+ , is important for the structural expansion of chalcogenido metalate chemistry. Following the same strategy, another Cu/Sn/Se-based network was observed in compound **18**. Compound **18** crystallizes in the cubic crystal system, space group $Im\bar{3}$ (No. 204), with eight formula units in the unit cell. The anionic part of the asymmetric unit comprises two copper atoms, one tin atom, four selenium atoms, and the remaining site being co-occupied by selenium and sulfur from the CuSPh precursor (Figure 3.61a). The core of the building unit comprises a cubic array of copper atoms, with closest $\text{Cu} \cdots \text{Cu}$ distances being $3.0397(9)$ Å – $3.0407(9)$ Å, indicating no obvious interactions between the copper atoms (Figure 3.61b). The $\{\text{Cu}_8\}$ cube accommodates a Se_5/S_1 co-occupied atom. Twelve selenium atoms surround the core motif by bridging each edge of the $\{(\text{Se}/\text{S})\text{Cu}_8\}$ cube to form a polyhedral $\{\text{FCu}_8\text{Se}_{12}\}$ cluster unit. Bridging of the latter in compound **18** by six $\{\text{Sn}_2\text{Se}_2\}$ units finally affords a three-dimensional **pcu** network (Figure 3.61c – d). The bridging angles between those polyhedra get smaller in comparison to the ones observed in compound **10** (Figure 3.61b), as the cluster are slightly out of alignment with the neighboring clusters. This may be caused by the fact that the co-occupied Se_5/S_1 site yields a mismatch of the cluster sizes. The counterions are unidentifiable due to heavy disorder. The electron density of atoms that could not be localized

from the difference Fourier map was detracted from the data by application of the back-Fourier transform method using the SQUEZZE tool in PLATON^[129].

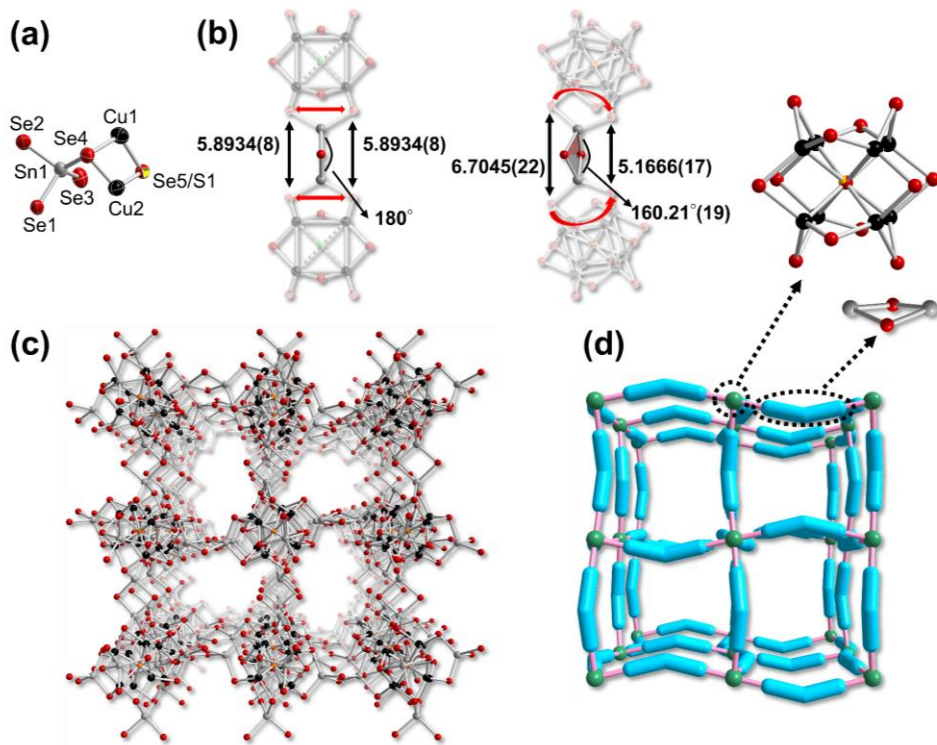


Figure 3.61: Asymmetric unit of compound **18**; Se/S, Cu, Sn and Se atoms are shown as thermal ellipsoids at the 50% probability level (a). Comparison of the bridging angles between the adjacent polyhedral clusters in compound **10** (left) and **18** (right) (b). Fragment of the framework structure in compound **18** (c). *pcu*-type topology of compound **18** by treating each $\{\text{Se/S/Cu}_8\text{Se}_{12}\}$ cluster as a node, and $\{\text{Sn}_2\text{Se}_2\}$ as a linker (d).

3.5.6 Crystal structure of compound **19**

Further investigations on the effect of incorporation of a third type of metal atoms in the Cu/Sn/Se, specifically, the introduction of In^{3+} , allowed for the formation of a P2-type cluster in compound **19**. Compound **19** crystallizes in the cubic crystal system, space group *P23* (No. 195), with one formula unit in the unit cell. The anionic part of the asymmetric unit consists of one tin atom, one copper atom, two indium atoms, and five selenium atoms (Figure 3.62a). The organic counterions are again unidentifiable due to heavy disorder. The electron density of atoms that could not be localized from the difference Fourier map was detracted from the data by application of the back-Fourier transform method using the SQUEZZE tool in PLATON^[129]. Figure 3.62b – d illustrates the structure of the P2-type cluster and the arrangement of those clusters in a $2 \times 2 \times 2$ supercell.

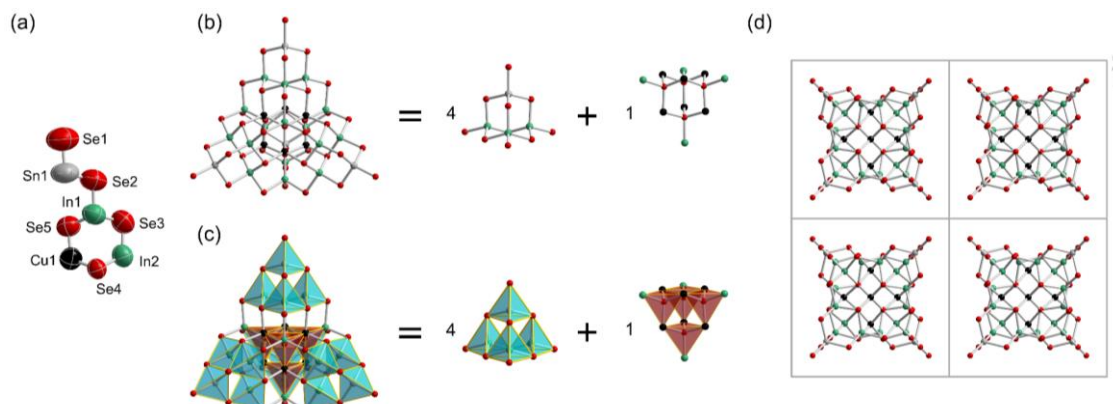


Figure 3.62: Asymmetric unit of compound **19**; Cu, In, Sn and Se atoms are shown as thermal ellipsoids at the 50% probability level (a). Molecular structure of the cluster anion in compound **19** and an illustration of its assembly (b). Molecular structure of the cluster anion in compound **19** shown in polyhedral mode (c). Packing of the P2-type anions in a $2 \times 2 \times 2$ supercell (d).

3.5.7 Crystal structure of compound **20**

In addition to expanding the families of selenido stannate compounds, Cu^+ also serves to enrich the structural types of selenido germanates. By reacting $\text{Li}_4[\text{GeSe}_4]$, instead of $[\text{Li}_4(\text{H}_2\text{O})_x][\text{SnSe}_4]$, with CuI in *en*, $(\text{H}^+ - \text{C}_2\text{N}_2\text{H}_{10})[\text{Cu}_3\text{GeSe}_4]$ (compound **20**) was formed. Figure 3.63a shows the asymmetric unit of compound **20**. The anionic substructure of **20** represents an infinite coordination assembly of selenium and metal atoms. As shown in Figure 3.63b, **20** comprises double honeycomb-type layers. The bottom and the top layer possess inverse chalcogen/metal positions and are coupled together *via* Cu_1-Se_3 and Ge_1-Se_2 bridges. The lighter organic counterions can be located in this case, although being affected by some disorder (indicated by transparency in Figure 3.63a). Figure 3.63c – e shows the arrangement of the anionic double-layer substructure accommodated in a $3 \times 5 \times 3$ supercell, viewed from three different directions. Counterions are not shown for clarity. Further variations regarding the reaction conditions may afford the crystallization of more new compounds in the Cu/Ge/Se system.

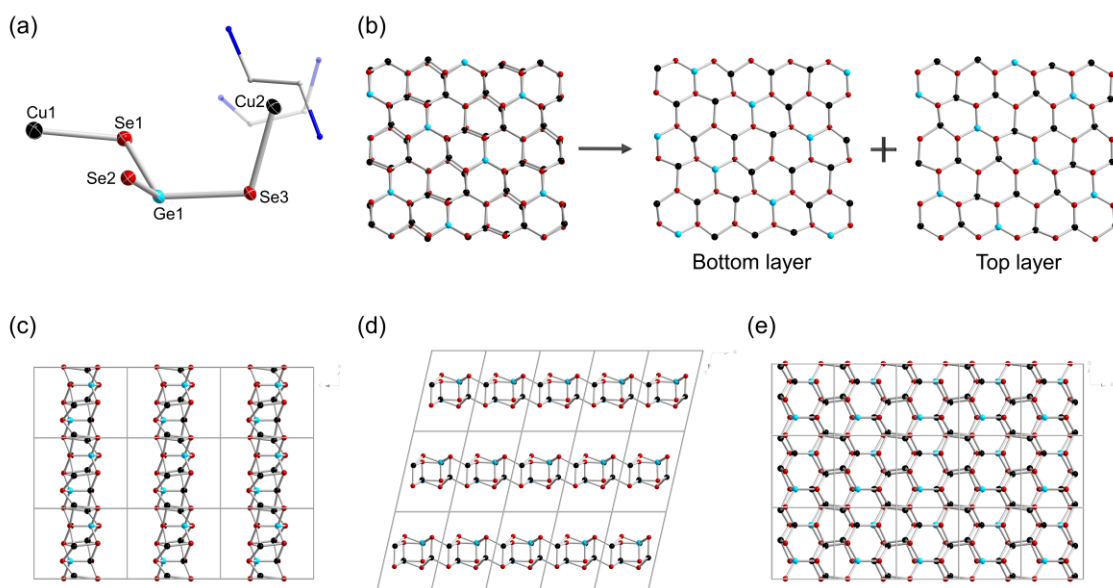


Figure 3.63: Asymmetric unit of compound **20**; Cu, Ge and Se atoms are shown as thermal ellipsoids at the 50% probability level (a). Substructure of the anionic substructure in compound **20**, and illustration of its construction by fusion of two layers (b). Packing of the layer-type anionic substructure in compound **20** in a $3 \times 5 \times 3$ supercell, viewed from crystallographic direction *a* (c), direction *b* (d), and direction *c* (e). Counterions are not shown for clarity.

As has been discussed in Chapter 3.3, the introduction of a heteroatom serves effectively to vary the structural types of selenido stannates. The compositional expansion strategy to widen the family members of such compounds is further studied. In compound **17**, through the incorporation of Hg^{2+} , a ternary T2-type $\{\text{Hg}_x\text{Sn}_{4-x}\text{Se}_{10}\}$ cluster-based 2D anionic network by sharing the corners of each cluster was isolated. Compound **18** features a similar cluster type and framework as that of compound **10** described in Chapter 3.3, with the only difference being the endohedral atom type. Instead of a F^- ion in compound **10**, a mixed occupation by S^{2-} and Se^{2-} was observed in this case. The incorporation of a third metal atom further serves to modify the cluster type. In the $\text{Cu}^+ \text{In}^{3+} \text{Sn}^{4+}$ reaction system, a rare, and the first P2-type cluster from ionothermal approach, was obtained. Further variations, like temperature, the use of a different ionic liquid, or the use of different additives, should be explored, which may afford network compounds by linking the P2-type cluster building units.

3.5.8 Crystal structure of compound **21**

In addition to the reactivities of selenido stannates or selenido germanates, the transformation of selenido antimonates in ionic liquids was studied. By treatment of (inseparable) salts $\text{K}_3[\text{SbSe}_4]$ and $\text{K}_3[\text{SbSe}_3]$ in $(\text{C}_2\text{C}_1\text{Im})[\text{BF}_4]$ and DMMP, $(\text{C}_2\text{C}_1\text{Im})[\text{Sb}_3\text{Se}_5]$ (compound **21**) was obtained. As shown in Figure 3.64a, the asymmetric unit is composed of three antimony atoms, five selenium atoms, and one $(\text{C}_2\text{C}_1\text{Im})^+$ cation. Secondary interactions are found between H atoms from the ionic liquid cations and atoms of the anionic substructure. Further assembly by repeating the asymmetric unit *via* sharing $\text{Sb}1$, $\text{Se}2$, $\text{Se}4$ and $\text{Se}5$ results in the formation of an infinite strand-

type substructure in **21** (Figure 3.64b). The lighter analogue, 1D- $\{[\text{Sb}_3\text{S}_5]_3^{3-}\}$, was documented in compound $(\text{H}^+ \text{--} \text{C}_7\text{N}_2\text{H}_{12})_3[\text{Sb}_9\text{S}_{15}]$ in 2004^[227], but this strategy allows us an opportunity to approach the family of selenido antimonates in ionic liquids, which may make a difference in terms of the structure types accessible in comparison to the ones that were synthesized through solvothermal reactions. Figure 3.64c – e displays the arrangement of the anionic strands accommodated in a $1 \times 5 \times 1$ supercell, viewed from three different directions. The orientation-dependent conductivity using single crystals is about to be investigated.

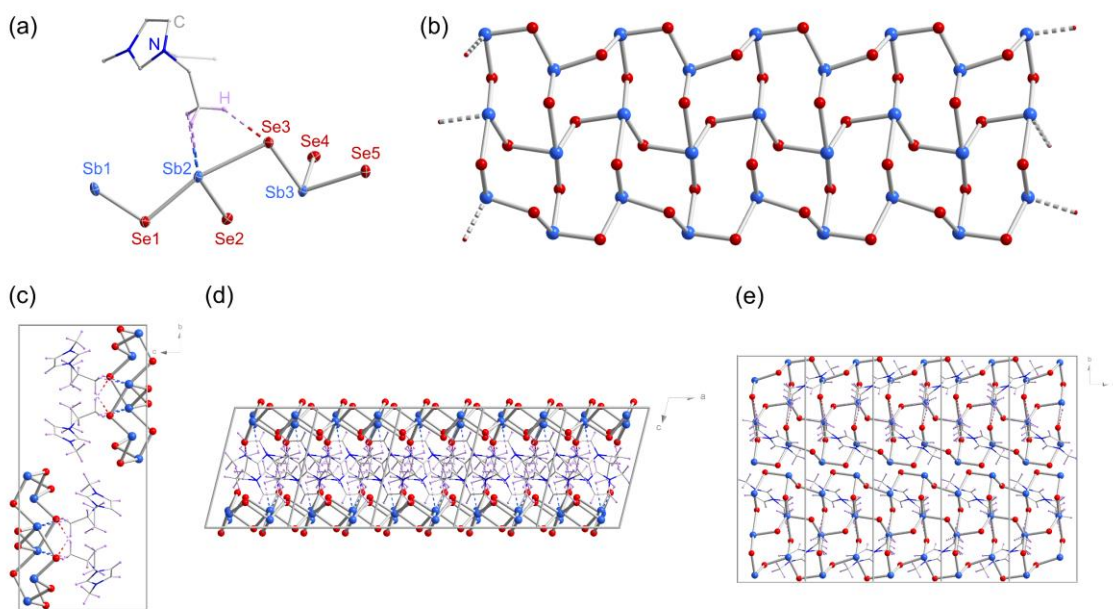
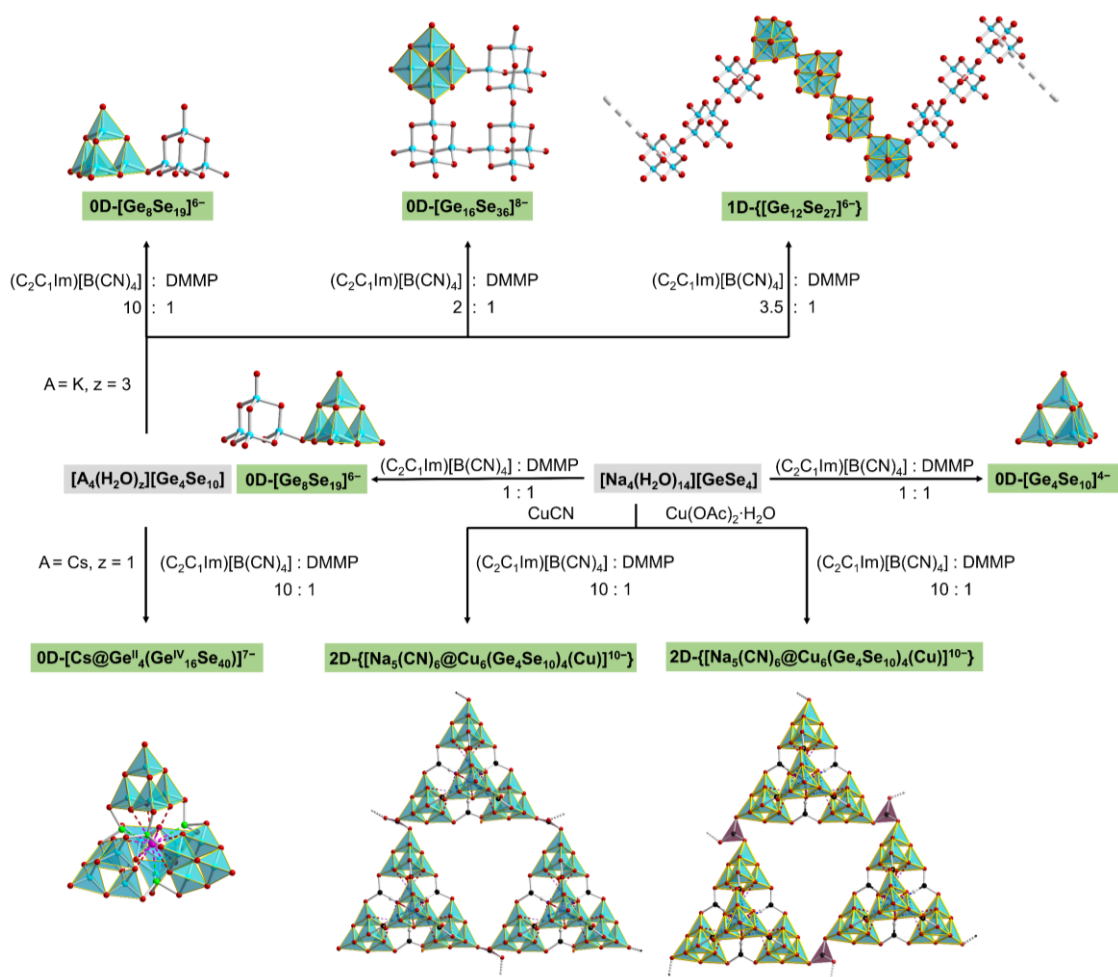


Figure 3.64: Asymmetric unit of compound **21**; Sb and Se atoms are shown as thermal ellipsoids at the 50% probability level (a). Substructure of the strand-type anionic substructure in compound **21** (b). Packing of two strands in compound **21** in a $1 \times 5 \times 1$ supercell, viewed from crystallographic direction *a* (c), direction *b* (d), and direction *c* (e), counterions are shown for illustrating their weak interaction with the strands.

4 Summary

This dissertation focuses on the transformation of salts of the general formula $[A_4(H_2O)_z][Tt_xSe_y]$ (A = alkali metal ions; Tt = Ge(IV) or Sn(IV)) into complex substructures in ionic liquids using three distinct strategies: a) oligomerization of $[Ge_4Se_{10}]^{4-}$ anion, b) Cu^+ incorporation in a Sn–Se reaction system, and c) modification of the imidazolium-based structure-directing agents.

(a) In Chapters 3.1 and 3.2, through an ionothermal approach, an effective route to target a family of oligomeric $\{Ge_4Se_{10}\}$ -based compounds was proposed. These compounds comprise the first dimeric anion of selenido metalate supertetrahedra in $(C_2C_1Im)_6[Ge_8Se_{19}]$ and the first square-shaped tetrameric anion in $(C_2C_1Im)_8[Ge_{16}Se_{36}]$. They can be readily dissolved in solvents like N,N-dimethylformamide (DMF) owing to a significantly decreased negative charges per cluster unit. Electrospray ionization mass spectrometry (ESI-MS) as well as dynamic light scattering (DLS) serve to demonstrate the alleviated interactions between each cluster unit and imidazolium counterions upon oligomerization of cluster supertetrahedra. By slightly modifying the reaction condition, a *pseudo*-P2-type cage-like molecule embedding a Cs^+ cation was observed. It is interesting not only because of its structural beauty, but also because of its selectivity towards Cs^+ ions in comparison to the lighter congeners during the crystallization process. A full set of characterization, including single-crystal X-ray diffraction (SC-XRD), energy dispersive X-ray spectroscopy (EDX), ESI-MS and quantum chemical calculations were applied to confirm its high selectivity for Cs^+ . Besides the *in-situ* capturing, and therefore potential separation of Cs^+ from its lighter congeners, another selenido metalate-based polymer compound was found selectively embedding Na^+ ions during crystallization. All these anionic substructures are summarized in Scheme 4.1.

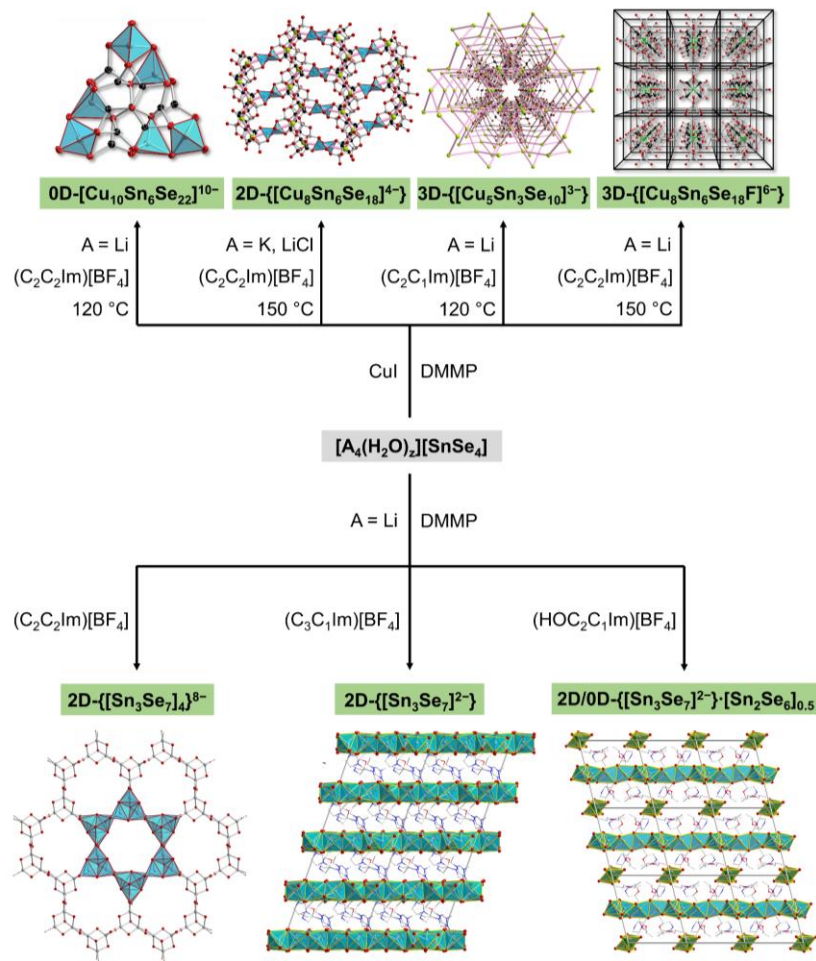


Scheme 4.1: Summary of the new supertetrahedra-based selenido germanate molecules or networks presented in Chapter 3.1 – 3.2.

(b) In Chapter 3.3, a Cu(I)-incorporation strategy was introduced to enrich the structural diversity of chalcogenido metalates. Owing to the multifaceted coordination environments of d^{10} Cu^+ ions with chalcogen atoms, the introduction of Cu(I) serves as an effective means to install a second or even a third kind of coordination mode of cations in such clusters. It allowed for the formation of a wide spectrum of copper-selenido stannate compounds, ranging from $(\text{C}_2\text{C}_1\text{Im})_9\text{Li}[\text{Cu}_{10}\text{Sn}_6\text{Se}_{22}]$, $(\text{C}_2\text{C}_1\text{Im})_4[\text{Cu}_8\text{Sn}_6\text{Se}_{18}]$, $(\text{C}_2\text{C}_1\text{Im})_3[\text{Cu}_5\text{Sn}_3\text{Se}_{10}]$ to $(\text{C}_2\text{C}_1\text{Im})_6[\text{Cu}_8\text{Sn}_6\text{Se}_{18}] \cdot (\text{C}_2\text{C}_1\text{Im})[\text{BF}_4]$. Their optical properties as well as photocurrent performance were investigated by UV-Vis spectroscopy and cyclic voltammograms. This underscored the impact of Cu(I) in chalcogenido metalate chemistry as compared to a copper-free compound.

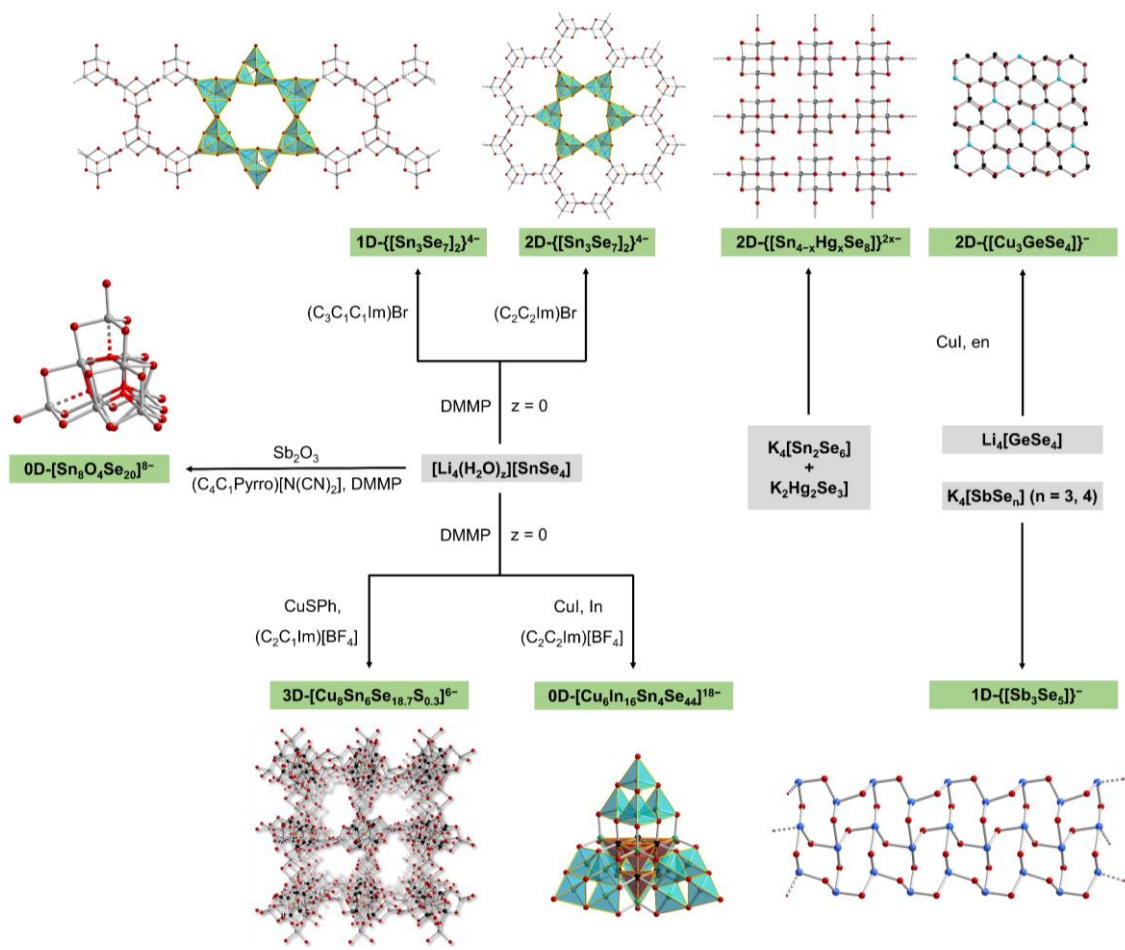
(c) Within Chapter 3.4, the structural expansion of selenido stannates *via* modifying the nature of the imidazolium cations' substituent was introduced. Treatment of $[\text{Li}_4(\text{H}_2\text{O})_{13}][\text{SnSe}_4]$ in 1-propyl-3-methyl-imidazolium tetrafluoroborate or 1-(2-hydroxyethyl)-3-methyl-imidazolium tetrafluoroborate and DMMP as auxiliary amine yielded two different selenido stannates,

$[\text{C}_3\text{C}_1\text{Im}]_3[\text{H}^+ - \text{DMMP}][\text{Sn}_3\text{Se}_7]_2$ and $[\text{H}^+ - \text{DMMP}]_2[\text{Sn}_3\text{Se}_7] \cdot [\text{H}^+ - \text{DMMP}]_2[\text{Sn}_2\text{Se}_6]_{0.5}$. The formation of the two different compounds is attributed to the proton donation effect of the hydroxyethyl group in the latter ionic liquid. Treatment of the two compounds in an aqueous solution of CsCl afforded cation-exchanged or cation-exchanged and anion-extracted selenido stannates. The anisotropic conductivity of the four compounds was studied by a full set of I - V measurement on single crystals. All the anionic substructures are summarized in Scheme 4.2.



Scheme 4.2: Summary of the new supertetrahedra-based selenido stannate molecules or networks presented in Chapters 3.3 – 3.4.

(d) In Chapter 3.5, the crystal structures of eight new compounds were presented, without results of further investigations of their additional properties. However, their isolation still allows to conclude that the length of alkyl chains of the ionic liquid cations and the nature of ionic liquid cations and anions in general can effectively modify the product spectrum upon transformation of chalcogenido metalates. It indicates that there is still room to be filled in this area. All the anionic substructures are summarized in Scheme 4.3.



Scheme 4.3: Summary of the new supertetrahedra-based selenido metalate molecules or networks presented in Chapter 3.5.

5 Experimental sections

5.1 General

All manipulations and reactions were performed in an argon atmosphere by using standard Schlenk or glovebox techniques. 2,6-Dimethylmorpholine (DMMP; Sigma-Aldrich, 99.8%) was dried over P_2O_5 , distilled and stored over molecular sieves (3 Å). 1-ethyl-3-methyl-imidazolium tetracyanoborate, $(C_2C_1Im)[B(CN)_4]$, from Sigma-Aldrich (99.5%); 1-ethyl-3-methyl-imidazolium tetrafluoroborate denoted, $(C_2C_1Im)[BF_4]$, from Sigma-Aldrich (99.5%); 1,3-diethylimidazolium tetrafluoroborate denoted as $(C_2C_2Im)[BF_4]$, from abcr GmbH (99%); 1,3-diethylimidazolium bromide denoted as $(C_2C_2Im)Br$, from Carl Roth GmbH (99%); 1-propyl-3-methyl-imidazolium tetrafluoroborate denoted as $(C_3C_1Im)[BF_4]$, from abcr GmbH (99%); 1-(2-hydroxyethyl)-3-methyl-imidazolium tetrafluoroborate denoted as $(HOC_2C_1Im)[BF_4]$, from abcr GmbH (99%); 1-propyl-2,3-dimethyl-imidazolium bromide, $(C_3C_1C_1Im)Br$, from Carl Roth GmbH (99%); 1-butyl-2,3-dimethyl-imidazolium tetrafluoroborate, $(C_4C_1C_1Im)[BF_4]$, from Alfa Aesar GmbH (99%); 1-butyl-3-methyl-purrolidinium dicyanamide, $(C_4C_1Pyrro)[N(CN)_2]$, from Carl Roth GmbH (99%); tin, Sn, from Sigma Aldrich (99%); selenium, Se, from Merck Millipore (99%); indium, In, from Sigma Aldrich (99%); antimony, Sb, from Sigma Aldrich (99%); copper(I) cyanide, CuCN, from Riedel-de-Haen (99%); copper(II) acetate monohydrate, $Cu(OAc)_2 \cdot H_2O$, from Fluka Chemika (99%); copper(I) iodide, CuI, from Sigma-Aldrich (98%); antimony(III) oxide, Sb_2O_3 , from Sigma Aldrich (99%), bought from Sigma-Aldrich with 99.5 % purity, and dried under vacuum before use. The gold-coated silicon wafer was bought from Sigma Aldrich. All reactions were carried out with ionothermal approaches, and the synthesis procedures of all compounds are detailed as below.

5.2 Characterizations

5.2.1 Light-microscopic images of the single crystals

Light microscopic investigation of crystals was performed on the stereo light microscope SteREO Discovery.V8 by Carl Zeiss. The microscope was equipped with a high-intensive cold-light source CL 1500 ECO, an Achromat S 0.63x objective (FWD 107 mm), a PL 10x/21 Br ocular, and the microscope camera AxioCam MRc 5 with the camera adapter 60N-C 2/3" 0,63x. The raw photo material was examined by the AxioVision40x64 4.9.1 SP1 software.

5.2.2 Powder X-ray diffraction (PXRD)

PXRD data were obtained with Cu- $K\alpha$ radiation in transmission mode on a Stoe StadiMP diffractometer using a Mythen detector system at room temperature. The data were examined by using WinXPOW.

5.2.3 Energy dispersive X-ray (EDX) spectroscopy

EDX analyses of single crystals were carried out using an EDX-device Voyager 4.0 of Noran Instruments coupled with an electron microscope CamScan CS 4DV. Data acquisition was performed with an acceleration voltage of 10 kV or 15 kV and 100 s accumulation time. All the EDX spectra were measured and analyzed by Michael Hellwig at Department of Physics Philipps-Universität Marburg.

5.2.4 Electrospray ionization mass spectrometry (ESI-MS)

ESI mass spectra were recorded with a Thermo Fisher Scientific Finnigan LTQ-FT spectrometer in negative ion mode. Single crystals of compounds were dissolved in freshly distilled DMF. The solutions were injected into the spectrometer with gas-tight 250 μ L Hamilton syringes by syringe pump infusion. ESI mass spectra were measured by the Service Department Mass Spectrometry at Philipps-Universität Marburg.

5.2.5 Dynamic light scattering (DLS)

A DynaPro NanoStar device from Wyatt Technology was used for the DLS measurement. Single crystals were dissolved in dry DMF under inert condition at low concentration. Three drops of the solutions were applied for the study, after equilibration for 1 min at 25 °C in the device prior to the measurements. The Dynals algorithm was used to calculate the size distributions from measured autocorrelation functions; the results are reported as number plots. Three independent measurements were performed on each sample. DLS measurement were measured and analyzed by Simon Nier from the Research Unit of Dehnen.

5.2.6 Raman spectroscopy

Raman spectra were recorded on an S&I Mono-Vista CRS+ device with a laser wavelength 633 nm and gratings of 300 and 1200 grooves mm^{-1} . The measurements had a duration of 25 s with 10 coadditions and 10 s with 25 coadditions. Raman spectra were measured by Gina Stuhrmann and Bertram Peters from the Research Unit of Dehnen.

5.2.7 UV-visible spectroscopy

Optical absorption spectra of all compounds were measured in diffuse-reflectance mode on single crystals and in absorption mode on a fresh solution of the crystals in DMF, employing a Varian Cary 5000 UV/VIS/NIR spectrometer from Agilent, equipped with a Praying Mantis accessory for the solid-state samples. For the measurement of solid-state sample, Tauc plots were generated using the Kubelka-Munk-function $(F(R_\infty)hv)^{1/\gamma}$, with $\gamma = 0.5$, indicative for a direct allowed optical gap, or with $\gamma = 2$, indicative for an indirect allowed optical gap.

5.2.8 X-ray photoelectron spectroscopy (XPS)

XPS was carried out on a SPECS Phoibos 150 electron energy analyzer, using monochromatized Al K α radiation operated at 30 keV pass energy. The spectrum was recorded in ultrahigh vacuum after cleaning the surface by sputtering with Ar $^+$ ions. The measurement was performed with low photon flux to avoid charging effects and beam damage. XPS were measured and analyzed by Tim Naumann and Prof. J. Michael Gottfried at Philipps-Universität Marburg.

5.2.9 Infrared Spectroscopy (IR)

Infrared spectra were performed on a Nicolet iS50 Fourier-transform infrared (FTIR) spectrometer with attenuated total reflection (ATR).

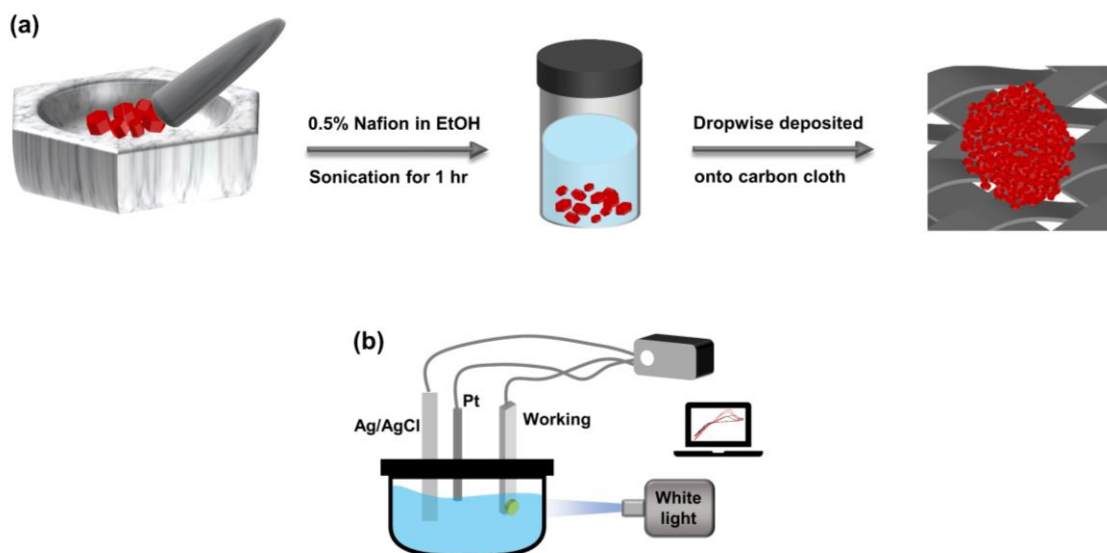
5.2.10 Quantum chemical calculations

The calculations were done at the DFT(PBE^[228]) level. The quasi-relativistic all-electron approach DLU-X2C^[229,230] in its scalar-relativistic variant was applied with optimized triple-zeta basis sets^[231]. The conductor-like screening model (COSMO^[232]) was used for charge compensation with default parameters throughout. All structures were fully optimized without symmetry restrictions. The calculations were performed and analyzed by Prof. Florian Weigend at Philipps-Universität Marburg.

5.2.11 Photocurrent measurement

Preparation of crystals modified carbon cloth working electrodes: 10 mg crystals of each sample was first ground in a mortar and subsequently the obtained powder was ultrasonicated in an ethanol solution that containing 0.5% Nafion for one hour, which was added dropwise to the surface of carbon cloth, the working electrodes were obtained after evaporation of ethanol thereupon, and the effective area was determined to be 0.246 cm².

Cyclic voltammograms and amperometric response of crystals decorated working electrodes were carried out using a PGU-BI 100 potentiostat (IPS Jaissle). Ag/AgCl in 3M KCl was used as the reference electrode; Pt plate was applied as an auxiliary electrode. Ar-saturated 0.1M phosphate buffer at pH = 7 was used as electrolyte. The preparation of working electrode and measurement of cyclic voltammograms are simplified as Scheme 5.1. The photocurrent measurements were carried out and analyzed by Panpan Wang and Prof. Wolfgang Schuhmann at Ruhr University Bochum.



Scheme 5.1: Schematic illustrations for the preparation of crystals deposited carbon cloth working electrode (a), and of a three-electrode photocurrent measurement setup (b).

5.2.12 Ion-exchange experiments

The ion-exchange process was operated under Ar condition. 10 mg crystals of **12** or **13** were soaked in 10 ml of 0.5 M CsCl aqueous solution in a Schlenk flask, the flask was heated at 75 °C for 24 hours to allow the cation exchange and anion extraction process. After cooling the Schlenk flask down to room temperature, the solid crystals were separated out of the solution and washed with degassed water three times. The full process was repeated twice, and the obtained solid samples are denoted as Cs@**12** and Cs@**13**, respectively.

5.2.13 *I*–*V* characteristic measurement

The *I*–*V* curves were measured over single crystals of **12**, **13**, Cs@**12**, and Cs@**13**. All the measurements were performed by applying voltage to one of the tungsten probes while grounding the other, and the induced current was measured with an ammeter accordingly. *I*–*V* hystereses were measured over a consecutive voltage sweep (0 V → +2 V → -2 V → 0 V) along both vertical and horizontal directions. The chronoamperometry traces were measured over single crystals, under applied voltages ranging from 0 V to +5 V, with steps of 0.5 V. Temperature-dependent *I*–*V* curves were collected after heating the crystal up from room temperature to certain temperatures, including 313.15 K, 333.15 K, and 353.15 K. *I*–*V* characteristics, *I*–*V* hysteresis, chronoamperometry traces, and temperature-dependent *I*–*V* curves were carried out and analyzed by Hongrong Hu and Prof. Jasmin Aghassi-Hagmann at Karlsruhe Institute of Technology.

5.3 Syntheses of starting materials

$[\text{Na}_4(\text{H}_2\text{O})_{14}][\text{GeSe}_4]$ ^[123], $[\text{K}_4(\text{H}_2\text{O})_4][\text{GeSe}_4]$ ^[233], and $[\text{Li}_4(\text{H}_2\text{O})_{20.33}][\text{Ge}_4\text{Se}_{10}]$ ^[234], $\text{Na}_4[\text{Ge}_4\text{Se}_{10}]$ ^[235], $[\text{K}_4(\text{H}_2\text{O})_3][\text{Ge}_4\text{Se}_{10}]$ ^[52], $\text{Rb}_4[\text{Ge}_4\text{Se}_{10}]$ ^[236], and $[\text{Cs}_4(\text{H}_2\text{O})][\text{Ge}_4\text{Se}_{10}]$ ^[236] were synthesized according to literature procedures. By fusion of stoichiometric of A_2Se , Ge, and Se in a sealed quartz ampoule and subsequently heated up in a temperature-programmed oven, $\text{A}_4[\text{GeSe}_4]$ and $\text{A}_4[\text{Ge}_4\text{Se}_{10}]$ are obtainable. To improve their solubilities, the salts were stirred in 25 mL degassed H_2O for 3 h in a Schlenk flask, and then the H_2O was removed under dynamic vacuum with warm-water bath during 8 h. Syntheses of $\text{Li}_4[\text{SnSe}_4]$ and $[\text{Li}_4(\text{H}_2\text{O})_{13}][\text{SnSe}_4]$ are given as examples as below.

Synthesis of $\text{Li}_4[\text{SnSe}_4]$: 20 mmol of Li_2Se , 10 mmol of Sn powder, and 20 mmol of Se powder were homogeneously mixed in a mortar and charged in a quartz ampoule. The quartz ampoule was heated by a propane/oxygen burner for 15 minutes under a dynamic Ar flow, the $\text{Li}_4[\text{SnSe}_4]$ salt was obtained by allowing the quartz ampoule to cool to room temperature.

Synthesis of $[\text{Li}_4(\text{H}_2\text{O})_{13}][\text{SnSe}_4]$: 1g of $\text{Li}_4[\text{SnSe}_4]$ salt and 25 mL of degassed water were charged in a 50 mL Schlenk flask, and being stirred at room temperature for 3 hours, the $[\text{Li}_4(\text{H}_2\text{O})_{13}][\text{SnSe}_4]$ formed upon removing the water by vacuum.

Synthesis of $\text{K}_2[\text{Sn}_2\text{Se}_6]$: 10 mmol of K_2Se , 20 mmol of Sn powder, and 40 mmol of Se powder were homogeneously mixed in a mortar and charged in a quartz ampoule. The quartz ampoule was heated by a propane/oxygen burner for 15 minutes under a dynamic Ar flow, the $\text{K}_2[\text{Sn}_2\text{Se}_6]$ salt was obtained by allowing the quartz ampoule to cool to room temperature thereupon.

Synthesis of $\text{K}_2\text{Hg}_2\text{Se}_3$: 10 mmol of K_2Se , 10 mmol of Hg, and 20 mmol of Se powder were homogeneously mixed in a mortar and charged in a quartz ampoule. The quartz ampoule was heated by a propane/oxygen burner for 15 minutes under a dynamic Ar flow, the $\text{K}_2\text{Hg}_2\text{Se}_3$ salt was obtained by allowing the quartz ampoule to cool to room temperature thereupon.

Synthesis of $\text{Li}_4[\text{GeSe}_4]$: 20 mmol of Li_2Se , 10 mmol of Ge powder, and 20 mmol of Se powder were homogeneously mixed in a mortar and fused in a quartz ampoule. The quartz ampoule was heated by a propane/oxygen burner for 15 minutes under dynamic Ar flow, the $\text{Li}_4[\text{GeSe}_4]$ salt was obtained by allowing the quartz ampoule to cool to room temperature thereupon.

Synthesis of $\text{K}_3[\text{SbSe}_n]$ ($n = 3$ or 4): 15 mmol of K_2Se_x , 10 mmol of Sb, and 15 mmol of Se powder were homogeneously mixed in a mortar and fused in a quartz ampoule. The quartz ampoule was heated by a propane/oxygen burner for 15 minutes under dynamic Ar flow, the mixed salts of $\text{K}_3[\text{SbSe}_3]$ and $\text{K}_3[\text{SbSe}_4]$ were obtained by allowing the quartz ampoule to cool to room temperature thereupon.

5.4 Syntheses of compounds 1 – 21

5.4.1 Synthesis of $(C_2C_1Im)_4[Ge_4Se_{10}]$ (1)

56 mg of $[Na_4(H_2O)_{14}][GeSe_4]$ (0.077 mmol), 500 μL (2.300 mmol) of $(C_2C_1Im)[B(CN_4)]$, and 50 μL (0.406 mmol) of DMMP were combined in a borosilicate glass ampoule, which was flash frozen in a liquid nitrogen filled dewar, evacuated to an internal pressure of 0.05 mbar and subsequently sealed air-tight thereupon. The ampoule was heated to 150 °C at a heating rate of 30 °C/h, kept at 150 °C for 72 h, and then cooled down to room temperature at a cooling rate of 5 °C/h. Pale yellow, needle-like crystals of **1** were obtained in approx. 33% yield.

5.4.2 Synthesis of $(C_2C_1Im)_6[Ge_8Se_{19}]$ (2a and 2b)

2a: 40 mg of $[Na_4(H_2O)_3][GeSe_4]$ (0.055 mmol), 250 μL (1.150 mmol) of $(C_2C_1Im)[B(CN_4)]$, and 250 μL (1.616 mmol) of $(C_2C_1Im)[BF_4]$ were combined in a borosilicate glass ampoule, which was flash frozen in a liquid nitrogen filled dewar, evacuated to an internal pressure of 0.05 mbar and subsequently sealed air-tight thereupon. The ampoule was heated to 150 °C at a heating rate of 30 °C/h, kept at 150 °C for 72 h, and then cooled down to room temperature at a cooling rate of 5 °C/h. Yellowish crystals of **2a** were obtained in approx. 42% yield; **2b:** 56 mg of $[K_4(H_2O)_3][Ge_4Se_{10}]$ (0.044 mmol), 500 μL (2.300 mmol) of $(C_2C_1Im)[B(CN_4)]$, and 50 μL of DMMP were combined in a borosilicate glass ampoule, which was flash frozen in a liquid nitrogen filled dewar, evacuated to an internal pressure of 0.05 mbar and subsequently sealed air-tight thereupon. The ampoule was heated to 150 °C at a heating rate of 30 °C/h, kept at 150 °C for 72 h, and then cooled down to room temperature at a cooling rate of 5 °C/h. Pale yellow needle-like crystals of **2b** were obtained in approx. 2.5% yield. The extremely low yield of this polymorph prevented access to further analytical data beyond the single-crystal structure; therefore, the other approach in the complete absence of DMMP was preferred, and all further data on compound **2** are based on the study of polymorph **2a**, which was accessible in good yield and purity (see above).

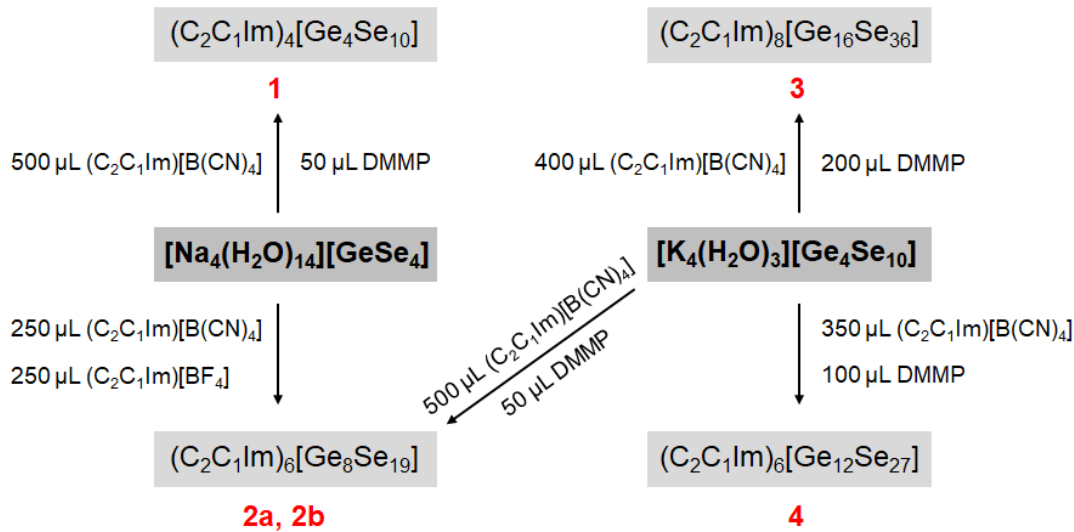
5.4.3 Synthesis of $(C_2C_1Im)_8[Ge_{16}Se_{36}]$ (3)

56 mg of $[K_4(H_2O)_3][Ge_4Se_{10}]$ (0.044 mmol), 400 μL (1.840 mmol) of $(C_2C_1Im)[B(CN_4)]$, and 200 μL (1.624 mmol) of DMMP were combined in a borosilicate glass ampoule, which was flash frozen in a liquid nitrogen filled dewar, evacuated to an internal pressure of 0.05 mbar and subsequently sealed air-tight thereupon. The ampoule was heated to 150 °C at a heating rate of 30 °C/h, kept at 150 °C for 72 h, and then cooled down to room temperature at a cooling rate of 5 °C/h. Yellow prismatic crystals of **3** were obtained in approx. 26% yield.

5.4.4 Synthesis of $(C_2C_1Im)_6[Ge_{12}Se_{27}]$ (4)

56 mg of $[K_4(H_2O)_3][Ge_4Se_{10}]$ (0.044 mmol), 350 μL (1.610 mmol) of $(C_2C_1Im)[B(CN_4)]$, and 100 μL (0.812 mmol) of DMMP were combined in a borosilicate glass ampoule, which was flash

frozen in a liquid nitrogen filled dewar, evacuated to an internal pressure of 0.05 mbar and subsequently sealed air-tight thereupon. The ampoule was heated to 150 °C at a heating rate of 30 °C/h, kept at 150 °C for 72 h, and then cooled down to room temperature at a cooling rate of 5 °C/h. Red plate-like crystals of **4** were obtained in approx. 7% yield.



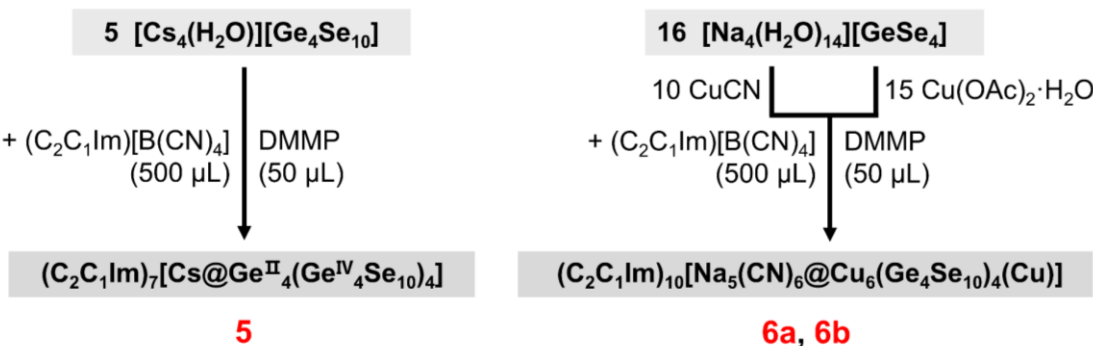
Scheme 5.2: Summary of the reactions yielding compounds **1** – **4**. All steps were carried out at 150 °C.

5.4.5 Synthesis of $(C_2C_1Im)_7[Cs@Ge^{II}4(Ge^{IV}4Se_{10})_4]$ (**5**)

40 mg of $[Cs_4(H_2O)][Ge_4Se_{10}]$ (0.025 mmol), 500 μ L of $(C_2C_1Im)[B(CN)_4]$ (2.300 mmol), and 50 μ L of DMMP (0.406 mmol) were combined in a borosilicate glass ampoule, which was flash frozen in a liquid nitrogen filled dewar, evacuated to an internal pressure of 0.05 mbar and subsequently sealed air-tight thereupon. The ampoule was heated to 150 °C at a heating rate of 30 °C/h, kept at 150 °C for 72 h, and then cooled down to room temperature at a cooling rate of 5 °C/h. Yellow, block-shaped crystals of **5** were obtained in approx. 72.9% yield (20.1 mg) with respect to $[Cs_4(H_2O)][Ge_4Se_{10}]$.

5.4.6 Synthesis of $(C_2C_1Im)_{10}[Na_5(CN)_6@Cu_6(Ge_4Se_{10})_4(Cu)]$ (**6a** and **6b**)

40 mg of $[Na_4(H_2O)_3][GeSe_4]$ (0.055 mmol), 8 mg of CuCN (0.089 mmol; for polymorph **6a**) or 10 mg of $Cu(OAc)_2 \cdot H_2O$ (0.050 mmol; for polymorph **6b**), 500 μ L of $(C_2C_1Im)[B(CN)_4]$ (2.300 mmol), and 50 μ L of DMMP (0.406 mmol) were combined in a borosilicate glass ampoule, which was flash frozen in a liquid nitrogen filled dewar, evacuated to an internal pressure of 0.05 mbar and subsequently sealed air-tight thereupon. The ampoule was heated to 150 °C at a heating rate of 30 °C/h, kept at 150 °C for 72 h, and then cooled down to room temperature at a cooling rate of 5 °C/h. A few red plate-like crystals of **6a** or **6b**, respectively, were obtained.



Scheme 5.3: Summary of the reactions yielding compounds **5**, **6a**, and **6b**. All steps were carried out at 150 °C.

5.4.7 Synthesis of $(C_2C_2Im)_9Li[Cu_{10}Sn_6Se_{22}]$ (7)

27 mg of $[Li_4(H_2O)_{13}][SnSe_4]$ (0.039 mmol), 10 mg of CuI (0.053 mmol), 500 mg of $(C_2C_2Im)[BF_4]$ (2.36 mmol), and 100 μ L of DMMP (0.812 mmol) were combined in a borosilicate glass ampoule, which was flash frozen in a liquid nitrogen filled dewar, evacuated to an internal pressure of 0.05 mbar and subsequently flame-sealed. After standing in a sand bowl for an hour, the sealed ampoule was heated to 120 °C from room temperature at a heating rate of 30 °C/h, kept at 120 °C for 72 h, and then cooled down to room temperature at a cooling rate of 5 °C/h. A few black, cubic-shaped crystals of **7** were obtained.

5.4.8 Synthesis of $(C_2C_2Im)_4[Cu_8Sn_6Se_{18}]$ (8)

27 mg of $[K_4(H_2O)_4][SnSe_4]$ (0.040 mmol), 10 mg of CuI (0.053 mmol), 10 mg of LiCl (0.236 mmol), 500 mg of $(C_2C_2Im)[BF_4]$ (2.36 mmol), and 100 μ L of DMMP (0.812 mmol) were combined in a borosilicate glass ampoule, which was flash frozen in a liquid nitrogen filled dewar, evacuated to an internal pressure of 0.05 mbar and subsequently flame-sealed. After standing in a sand bowl for an hour, the sealed ampoule was heated to 150 °C from room temperature at a heating rate of 30 °C/h, kept at 150 °C for 72 h, and then cooled down to room temperature at a cooling rate of 5 °C/h. Black, rod-shaped crystals of **8** were obtained in a 58% yield (12 mg) with respect to $[K_4(H_2O)_4][SnSe_4]$.

5.4.9 Synthesis of $(C_2C_1Im)_3[Cu_5Sn_3Se_{10}]$ (9a and 9b)

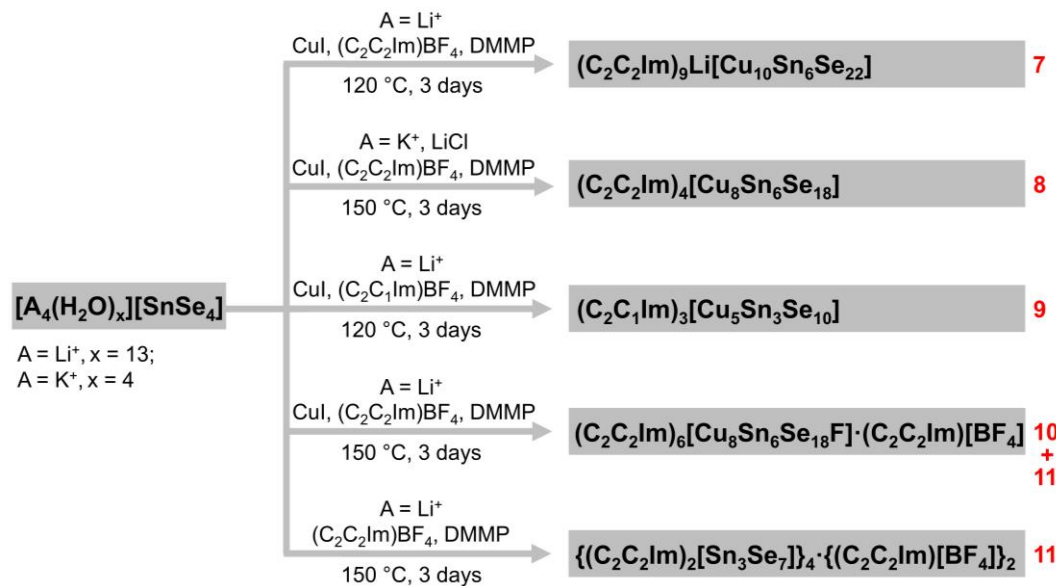
27 mg of $[Li_4(H_2O)_{13}][SnSe_4]$ (0.039 mmol), 10 mg of CuI (0.053 mmol), 500 mg of $(C_2C_1Im)[BF_4]$ (2.53 mmol), and 100 μ L of DMMP (0.812 mmol) were combined in a borosilicate glass ampoule, which was flash frozen in a liquid nitrogen dewar, evacuated to an internal pressure of 0.05 mbar and subsequently flame-sealed. After standing in a sand bowl for an hour, the sealed ampoule was heated to 120 °C from room temperature at a heating rate of 30 °C/h, kept at 120 °C for 72 h, and then cooled down to room temperature at a cooling rate of 5 °C/h. Black, octahedron-shaped crystals of inseparable **9a** and **9b** were obtained in a 34% yield (8 mg) with respect to $[Li_4(H_2O)_{13}][SnSe_4]$.

5.4.10 Synthesis of $(C_2C_2Im)_5[Cu_8Sn_6Se_{18}F] \cdot [C_2C_2Im][BF_4]$ (10)

27 mg of $[Li_4(H_2O)_{13}][SnSe_4]$ (0.039 mmol), 10 mg of CuI (0.053 mmol), 500 mg of $(C_2C_2Im)[BF_4]$ (2.36 mmol), and 100 μ L of DMMP (0.812 mmol) were combined in a borosilicate glass ampoule, which was flash frozen in a liquid nitrogen dewar, evacuated to an internal pressure of 0.05 mbar and subsequently flame-sealed. After standing in a sand bowl for an hour, the sealed ampoule was heated to 150 °C from room temperature at a heating rate of 30 °C/h, kept at 150 °C for 72 h, and then cooled down to room temperature at a cooling rate of 5 °C/h. Black, cubic-shaped crystals of **10** were obtained. However, the yield of **10** was not calculable since the co-crystallization of **11** in this reaction.

5.4.11 Synthesis of $\{(C_2C_2Im)_2[Sn_3Se_7]\}_4 \cdot (C_2C_2Im)_2[BF_4]_2$ (11)

27 mg of $[Li_4(H_2O)_{13}][SnSe_4]$ (0.039 mmol), 500 mg of $(C_2C_2Im)[BF_4]$ (2.36 mmol), and 100 μ L of DMMP (0.812 mmol) were combined in a borosilicate glass ampoule, which was flash frozen in a liquid nitrogen dewar, evacuated to an internal pressure of 0.05 mbar and subsequently flame-sealed. After standing in a sand bowl for an hour, the sealed ampoule was heated to 150 °C from room temperature at a heating rate of 30 °C/h, kept at 150 °C for 72 h, and then cooled down to room temperature at a cooling rate of 5 °C/h. Red, hexagonal-shaped crystals of **5** were obtained in a 35% yield (23 mg) with respect to $[Li_4(H_2O)_{13}][SnSe_4]$. Compound **11** is also a byproduct of the reaction yielding **10**.



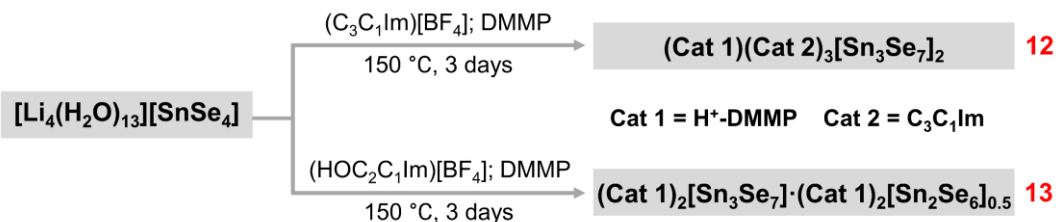
Scheme 5.4: Summary of the syntheses of compounds **7**–**11**. Compounds **7** and **9**–**11** were prepared by the use of $[Li_4(H_2O)_{13}][SnSe_4]$ in ionic liquids; compound **8** was formed by mixing $[K_4(H_2O)_4][SnSe_4]$ and LiCl salts as starting materials instead. The use of CuI is necessary for the formation of compounds **7**–**10**, and the DMMP auxiliary is needed for all syntheses.

5.4.12 Synthesis of $(C_3C_1Im)_3(H^+-DMMP)[Sn_3Se_7]_2$ (12)

30 mg of $[Li_4(H_2O)_{13}][SnSe_4]$ (0.043 mmol), 500 μ L (2.358 mmol) of $(C_3C_1Im)[BF_4]$, and 100 μ L (0.812 mmol) of DMMP were combined in a borosilicate glass ampoule, which was flash frozen in a liquid nitrogen filled dewar, evacuated to an internal pressure of 0.05 mbar and subsequently sealed air-tight thereupon. The ampoule was heated to 150 °C at a heating rate of 30 °C/h, kept at 150 °C for 72 h, and then cooled down to room temperature at a cooling rate of 5 °C/h. Orange, plate crystals of **12** were obtained.

5.4.13 Synthesis of $(H^+-DMMP)_2[Sn_3Se_7] \cdot (H^+-DMMP)[Sn_2Se_6]_{0.5}$ (13)

30 mg of $[Li_4(H_2O)_{13}][SnSe_4]$ (0.043 mmol), 500 μ L (2.337 mmol) of $(HOC_2C_1Im)[BF_4]$, and 100 μ L (0.812 mmol) of DMMP were combined in a borosilicate glass ampoule, which was flash frozen in a liquid nitrogen filled dewar, evacuated to an internal pressure of 0.05 mbar and subsequently sealed air-tight thereupon. The ampoule was heated to 150 °C at a heating rate of 30 °C/h, kept at 150 °C for 72 h, and then cooled down to room temperature at a cooling rate of 5 °C/h. Orange, plate crystals of **13** were obtained.



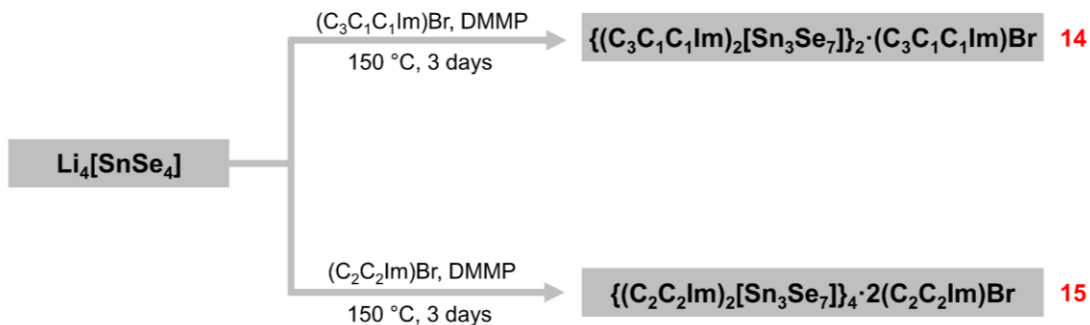
Scheme 5.5: Summary of the syntheses of compounds **12** and **13**. Cat 1 represents protonated DMMP molecules and Cat 2 represents $(C_3C_1Im)^+$. The use of DMMP auxiliary is needed for both syntheses.

5.4.14 Synthesis of $\{(C_3C_1C_1Im)_2[Sn_3Se_7]\}_2 \cdot (C_3C_1C_1Im)Br$ (14)

30 mg of $Li_4[SnSe_4]$ (0.065 mmol), 500 mg (2.283 mmol) of $(C_3C_1C_1Im)Br$, and 100 μ L (0.812 mmol) of DMMP were combined in a borosilicate glass ampoule, which was flash frozen in a liquid nitrogen filled dewar, evacuated to an internal pressure of 0.05 mbar and subsequently sealed air-tight thereupon. The ampoule was heated to 150 °C at a heating rate of 30 °C/h, kept at 150 °C for 72 h, and then cooled down to room temperature at a cooling rate of 5 °C/h. Pale yellow, plate crystals of **14** were obtained.

5.4.15 Synthesis of $\{(C_2C_2Im)_2[Sn_3Se_7]\}_4 \cdot 2(C_2C_2Im)Br$ (15)

30 mg of $Li_4[SnSe_4]$ (0.065 mmol), 500 μ L (2.439 mmol) of $(C_2C_2Im)Br$, and 100 μ L (0.812 mmol) of DMMP were combined in a borosilicate glass ampoule, which was flash frozen in a liquid nitrogen filled dewar, evacuated to an internal pressure of 0.05 mbar and subsequently sealed air-tight thereupon. The ampoule was heated to 150 °C at a heating rate of 30 °C/h, kept at 150 °C for 72 h, and then cooled down to room temperature at a cooling rate of 5 °C/h. Orange, plate crystals of **15** were obtained.

Scheme 5.6: Summary of the syntheses of compounds **14** and **15**.

5.4.16 Synthesis of $(C_4C_1Pyrro)_8[Sn_{10}O_4Se_{20}]$ (16)

30 mg of $[Li_4(H_2O)_{13}][SnSe_4]$ (0.043 mmol), 15 mg (0.0515 mmol) of Sb_2O_3 , 500 μ L (2.400 mmol) of $(C_4C_1Pyrro)[N(CN)_2]$, and 100 μ L (0.812 mmol) of DMMP were combined in a borosilicate glass ampoule, which was flash frozen in a liquid nitrogen filled dewar, evacuated to an internal pressure of 0.05 mbar and subsequently sealed air-tight thereupon. The ampoule was heated to 120 °C at a heating rate of 30 °C/h, kept at 120 °C for 72 h, and then cooled down to room temperature at a cooling rate of 5 °C/h. Orange, octahedral crystals of **16** were obtained.

Scheme 5.7: Syntheses of compound **16**.

5.4.17 Synthesis of $(Cat)_{2x}[Sn_{4-x}Hg_xSe_8]$ (17)

20 mg of $K_2[Sn_2Se_6]$ (0.025 mmol), 20 mg of $K_2Hg_2Se_3$ (0.028 mmol), 500 μ L (2.358 mmol) of $(C_2C_2Im)[BF_4]$ or 500 μ L (2.526 mmol) of $(C_2C_1Im)[BF_4]$ or 500 μ L (2.083 mmol) of $(C_4C_1C_1Im)[BF_4]$, and 100 μ L (0.812 mmol) of DMMP were combined in a borosilicate glass ampoule, which was flash frozen in a liquid nitrogen filled dewar, evacuated to an internal pressure of 0.05 mbar and subsequently sealed air-tight thereupon. The ampoule was heated to 150 °C at a heating rate of 30 °C/h, kept at 150 °C for 72 h, and then cooled down to room temperature at a cooling rate of 5 °C/h. Orange, square-plate crystals of **17** were obtained.

5.4.18 Synthesis of $(C_2C_1Im)_6[Cu_8Sn_6Se_{18.7}S_{0.3}]$ (18)

27 mg (0.058 mmol) of $Li_4[SnSe_4]$, 6 mg of (0.035 mmol) $CuSPh$, 500 μ L (2.526 mmol) of $(C_2C_1Im)[BF_4]$, and 100 μ L (0.812 mmol) of DMMP were combined in a borosilicate glass ampoule, which was flash frozen in a liquid nitrogen filled dewar, evacuated to an internal pressure of 0.05 mbar and subsequently sealed air-tight thereupon. The ampoule was heated to 150 °C at

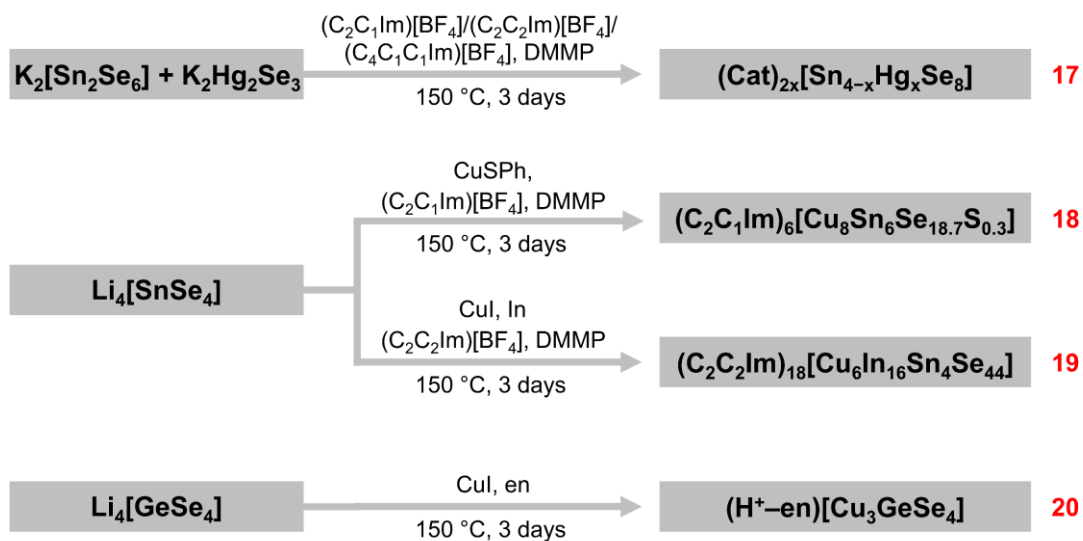
a heating rate of 30 °C/h, kept at 150 °C for 72 h, and then cooled down to room temperature at a cooling rate of 5 °C/h. Black, cubic crystals of **18** were obtained.

5.4.19 Synthesis of $(C_2C_2Im)_{18}[Cu_6In_{16}Sn_4Se_{44}]$ (19)

30 mg (0.065 mmol) of $Li_4[SnSe_4]$, 10 mg of (0.053 mmol) CuI , 10 mg (0.087 mmol) of In , 500 μL (2.358 mmol) of $(C_2C_2Im)[BF_4]$, and 100 μL (0.812 mmol) of DMMP were combined in a borosilicate glass ampoule, which was flash frozen in a liquid nitrogen filled dewar, evacuated to an internal pressure of 0.05 mbar and subsequently sealed air-tight thereupon. The ampoule was heated to 150 °C at a heating rate of 30 °C/h, kept at 150 °C for 72 h, and then cooled down to room temperature at a cooling rate of 5 °C/h. Black, cubic crystals of **19** were obtained.

5.4.20 Synthesis of $(H^+-en)[Cu_3GeSe_4]$ (20)

30 mg (0.065 mmol) of $Li_4[GeSe_4]$, 10 mg of (0.053 mmol) CuI , and 500 μL (8.333 mmol) of en were combined in a borosilicate glass ampoule, which was flash frozen in a liquid nitrogen filled dewar, evacuated to an internal pressure of 0.05 mbar and subsequently sealed air-tight thereupon. The ampoule was heated to 150 °C at a heating rate of 30 °C/h, kept at 150 °C for 72 h, and then cooled down to room temperature at a cooling rate of 5 °C/h. Black, plate crystals of **20** were obtained.



Scheme 5.8: Summary of the syntheses of compounds **17** – **20**. Cat represents cations in the formula of **17**, and to be characterized by elemental analysis (C, H, N) due to their moderate scattering at high angles.

5.4.21 Synthesis of $(C_2C_1Im)[Sb_3Se_5]$ (21)

30 mg of inseparable $K_3[SbSe_4]$ and $K_3[SbSe_3]$, and 500 μL (2.526 mmol) of $(C_2C_1Im)[BF_4]$, and 100 μL (0.812 mmol) of DMMP were combined in a borosilicate glass ampoule, which was flash

frozen in a liquid nitrogen filled dewar, evacuated to an internal pressure of 0.05 mbar and subsequently sealed air-tight thereupon. The ampoule was heated to 150 °C at a heating rate of 30 °C/h, kept at 150 °C for 72 h, and then cooled down to room temperature at a cooling rate of 5 °C/h. Black, plate crystals of **21** were obtained.



Scheme 5.9: Syntheses of compound **21**.

6 Additional information

6.1 Additional information on compounds discussed in Chapter 3

6.1.1 High-resolution mass spectra of the cluster anion in 1, 2a, and 3

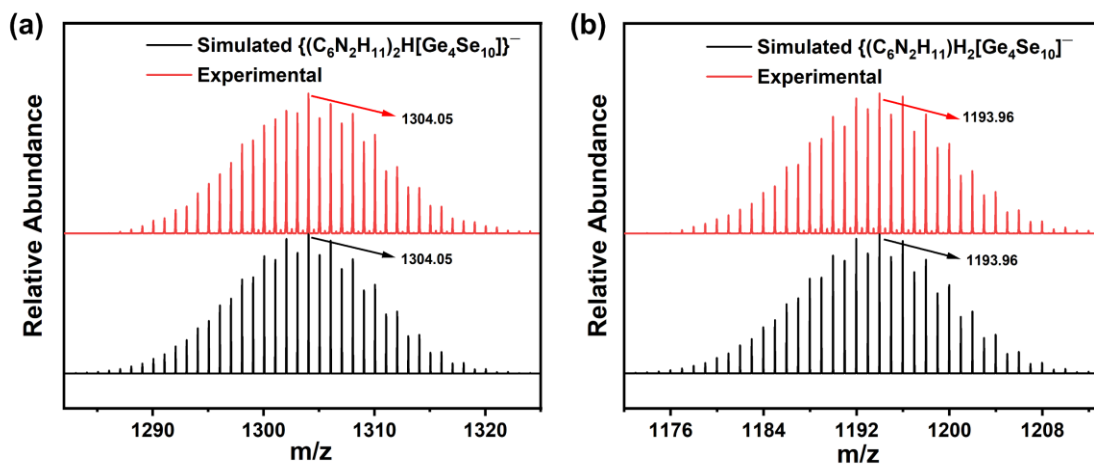


Figure 6.1: High-resolution mass peak of the cluster anions in **1**, detected along with two ionic liquid cations and one proton (a), one ionic liquid cation and two protons (b).

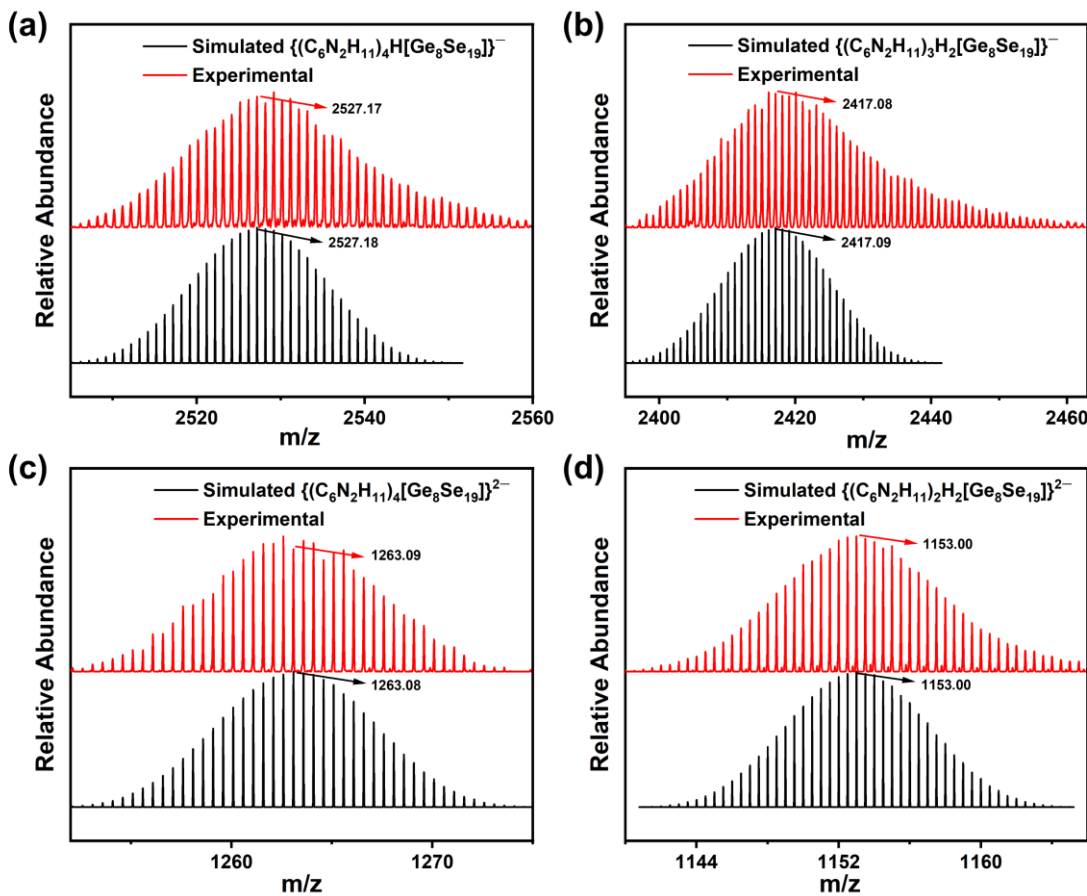


Figure 6.2: High-resolution mass peak of the cluster anions in **2a**, detected along with four ionic liquid cations and one proton (a), three ionic liquid cation and two protons (b), four ionic liquid cations (c), two ionic liquid cations and two protons (d).

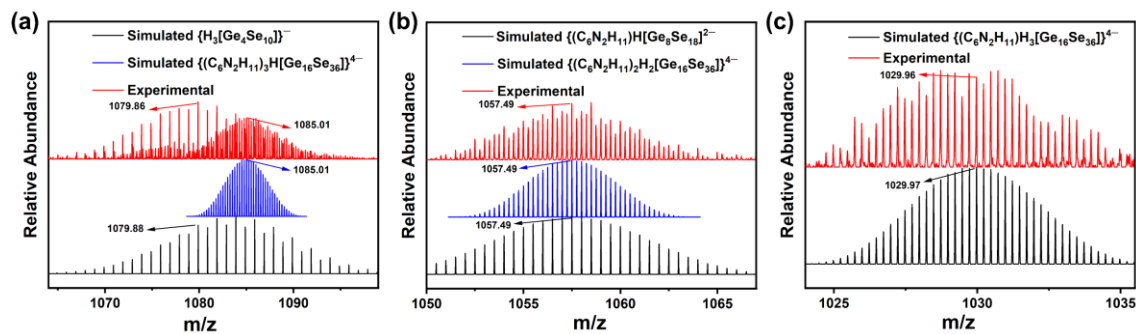


Figure 6.3: High-resolution mass peak of the cluster anions, with a total negative charge of 4, in **3**, detected along with three ionic liquid cations and one proton (a), two ionic liquid cations and two protons (b), one ionic liquid cation and three protons(c).

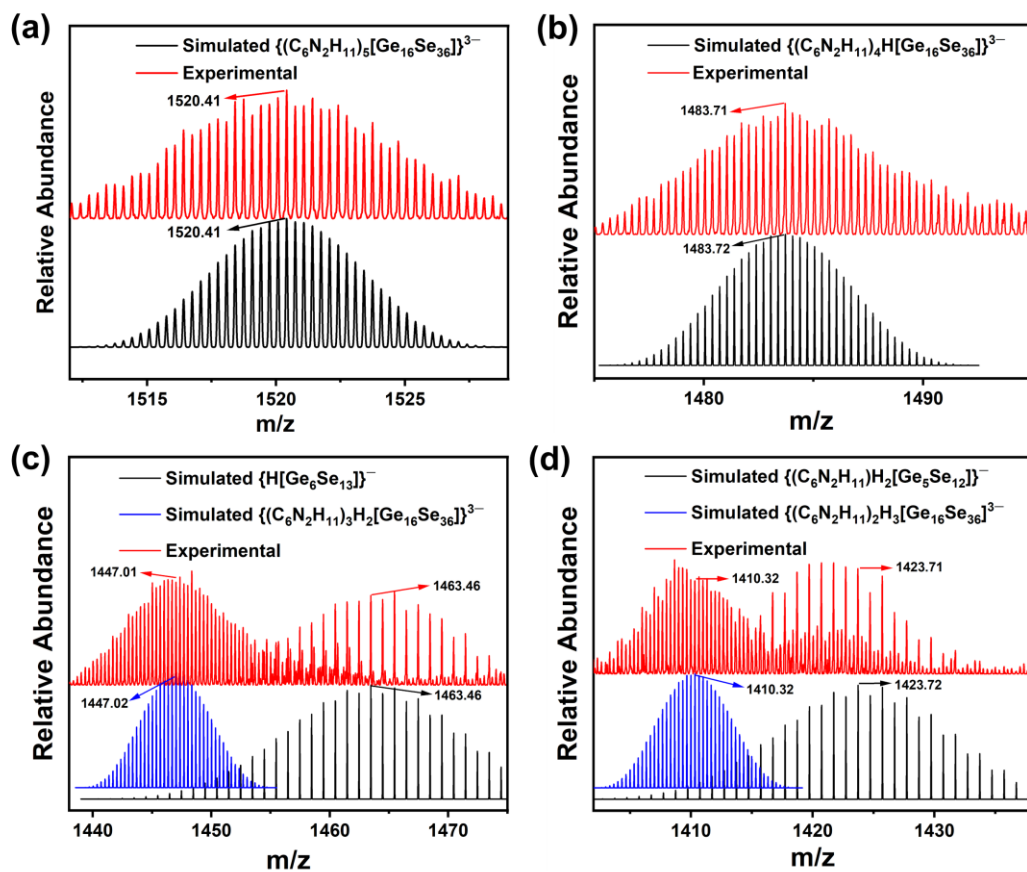


Figure 6.4: High-resolution mass peak of the cluster anions, with a total negative charge of 3, in **3**, detected along with five ionic liquid cations (a), four ionic liquid cations and one proton (b), three ionic liquid cations and two protons (c), two ionic liquid cations and three protons (d).

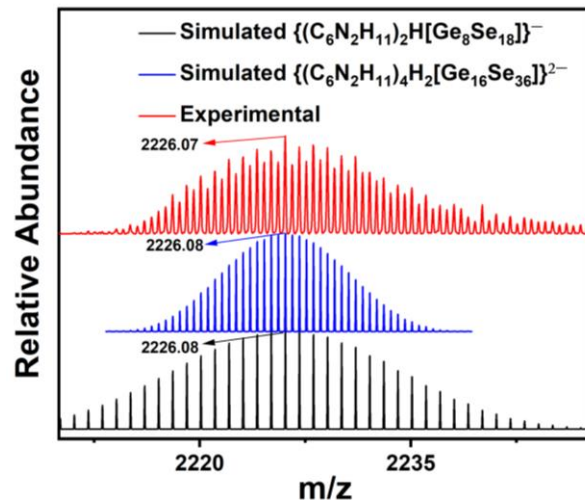


Figure 6.5: High-resolution mass peak of the cluster anions, with a total negative charge of 2, in **3**, detected along with four ionic liquid cations and two protons.

6.1.2 Stability study of solutions of the soluble compounds **1**, **2a**, and **3**

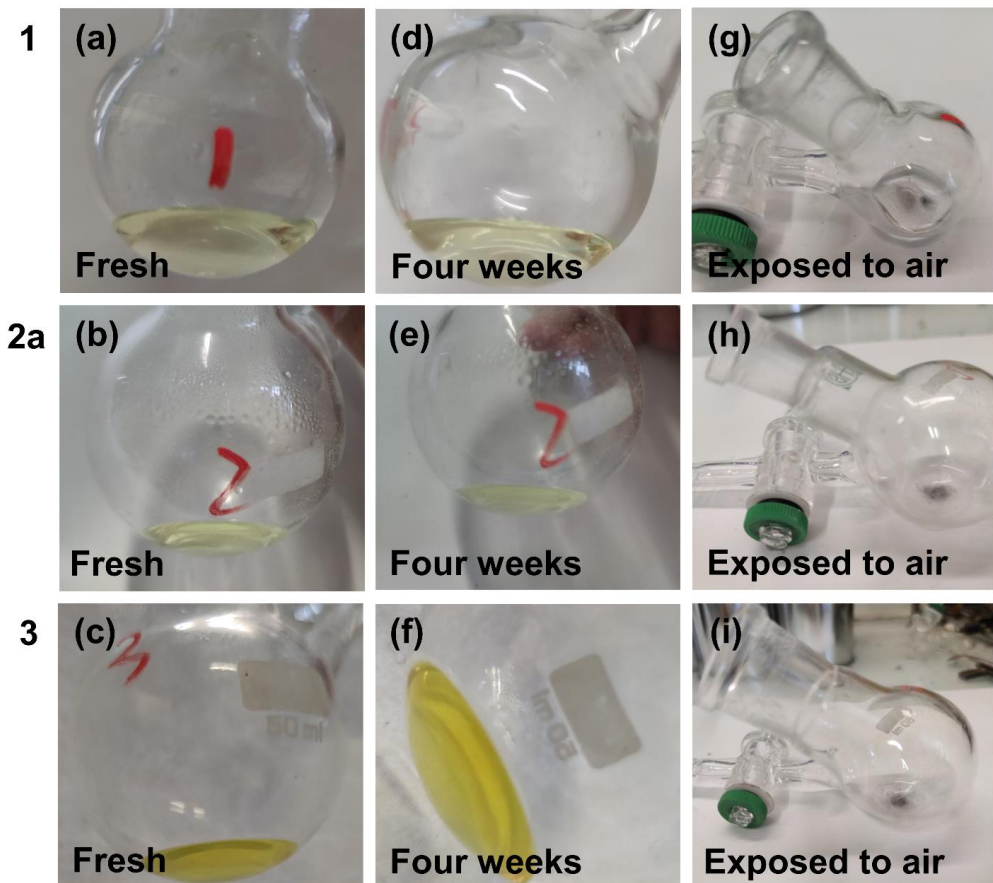


Figure 6.6: Photographs of fresh solutions of compound **1** (a), compound **2a** (b), and compound **3** (c) dissolved in DMF under inert conditions. Photographs of DMF solutions of compound **1** (d), compound **2a** (e), and compound **3** (f) after being kept under inert condition for four weeks. Photographs of DMF solutions of compound **1** (g), compound **2a** (h), and compound **3** (i) after being exposed to air for two hours. Corresponding experiments of compounds **2b** and **4** were impossible owing to the small yield of compound **2b** on the one hand, and the insolubility of the extended-network compound **4** on the other hand.

6.1.3 UV-visible diffuse-reflectance spectra of compounds **1**, **2a**, and **3**

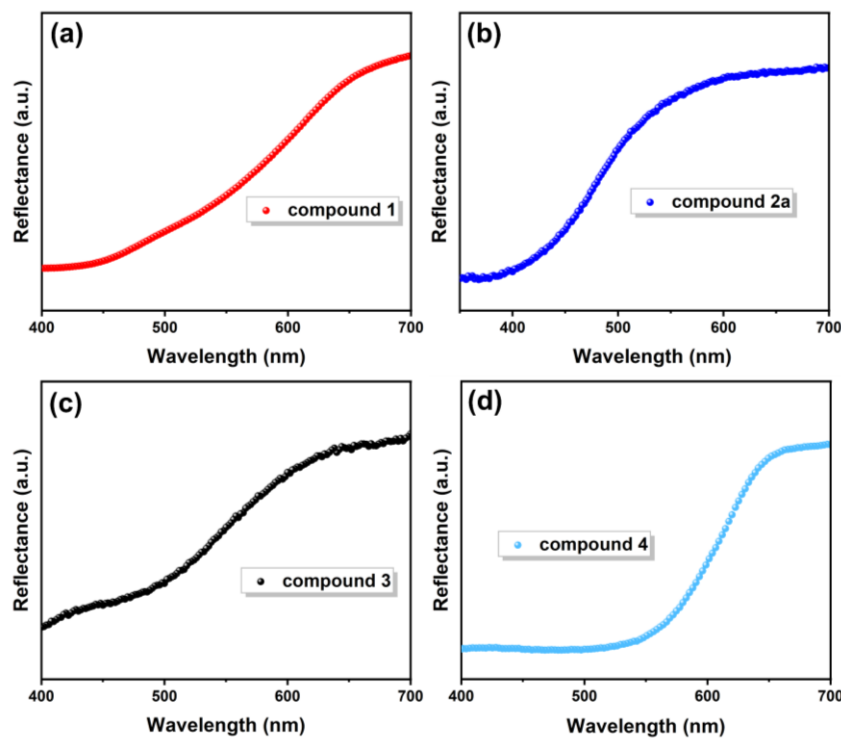


Figure 6.7: Solid-state UV-visible spectra of single-crystalline samples of **1** (a), **2a** (b), **3** (c) and **4** (d), recorded in diffuse-reflectance mode. Corresponding experiments of compound **2b** were hampered by the small yield of this compound.

6.1.4 Structural details of compound 5

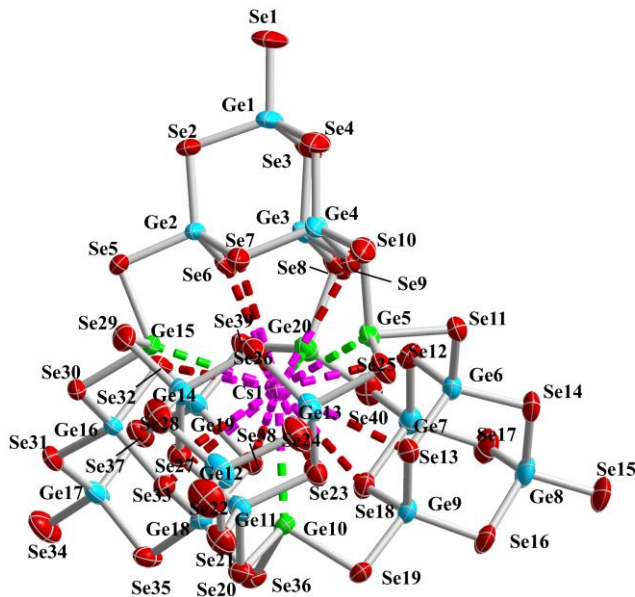


Figure 6.8: Asymmetric unit of compound 5. All the atoms are shown as thermal ellipsoids at the 50% probability level, imidazolium counterions are omitted for clarity. Ge^{IV}—sky blue; Ge^{II}—green; Se—red; Cs—pink.

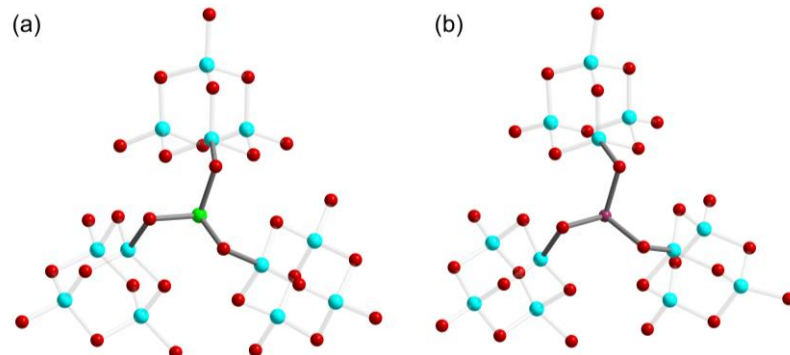


Figure 6.9: Ge^{II}–Se–Ge^{IV} bridging angle in compound 5 (a), and Sn^{II}–Se–Ge^{IV} bridging angle in reported compound $[\text{Cs}@\text{Sn}^{\text{IV}}_4(\text{Ge}^{\text{IV}}_4\text{Se}_{10})_4]^{7-}$ (b). The structural details of other parts are omitted for clarity. Ge^{IV}—sky blue; Ge^{II}—green; Sn^{II}—maroon; Se—red.

Table 6.1: Comparison of the bridging angle Ge^{II}–Se–Ge^{IV} in compound 5 with the Sn^{II}–Se–Ge^{IV} in reported $[\text{Cs}@\text{Sn}^{\text{IV}}_4(\text{Ge}^{\text{IV}}_4\text{Se}_{10})_4]^{7-}$ compound, and comparison of the Se–Ge^{II}–Se angle in 5 with the Se–Sn^{II}–Se angle in the reported analog.

Cluster	M ^{II}	M ^{II} –Se–Ge ^{IV}	Se–M ^{II} –Se
$[\text{Cs}@\text{Ge}^{\text{IV}}_4(\text{Ge}^{\text{IV}}_4\text{Se}_{10})_4]^{7-}$ (in 5)	Ge ^{II}	91.396(7) – 97.188(8)	92.84(9) – 96.05(8)
$[\text{Cs}@\text{Sn}^{\text{IV}}_4(\text{Ge}^{\text{IV}}_4\text{Se}_{10})_4]^{7-}$	Sn ^{II}	96.31(1)	92.82(8)

In both the Sn/Ge/Se and the Ge/Se superclusters, the $[\text{Ge}_4\text{Se}_{10}]^{4-}$ units are rotated with respect to the *pseudo-C*₃ axes of an idealized tetrahedral architecture to adopt the volume of the inner cavity to the size of the inner Cs⁺ cation. In case of the Sn/Ge/Se compound, this rotation is identical for all four $[\text{Ge}_4\text{Se}_{10}]^{4-}$ moieties, leading to a high crystallographic symmetry of the clusters (*D*₂). In

the smaller Ge/Se cluster, the subunits are rotated to slightly different extents, hence ending up with *pseudo-D*₂ symmetry only. The structural parameters of the anionic cluster structure also differ as a consequence of the (formal) replacement of Sn with Ge atoms, which is notable especially for the coordination environment of the divalent atoms: The Ge^{II}–Se–Ge^{IV} and Se–Ge^{II}–Se angles in **5** span ranges, 91.396(7)–97.188(8)° and 92.84(9)–96.05(8)°, respectively. Their mean values (approx. 94°) differ from the (larger) Sn^{II}–Se–Ge^{IV} angle (96.31(1)°) and the (smaller) Se–Sn^{II}–Se angle (92.82(8)°) in the Sn/Ge/Se analog, in which one value is found owing to the higher symmetry.

6.1.5 Structural details of compound **6**

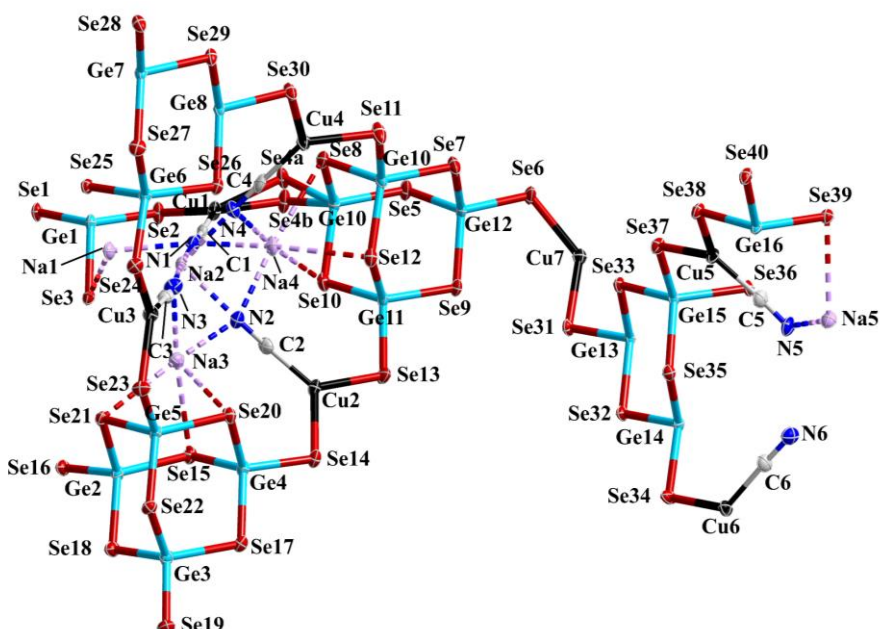


Figure 6.10: Asymmetric unit of compound **6a**. All the atoms are shown as thermal ellipsoids at the 50% probability level, imidazolium counterions are omitted for clarity. Atom color code: Ge–sky blue; Cu–black; Se–red; Na–lilac; C–grey; N–blue.

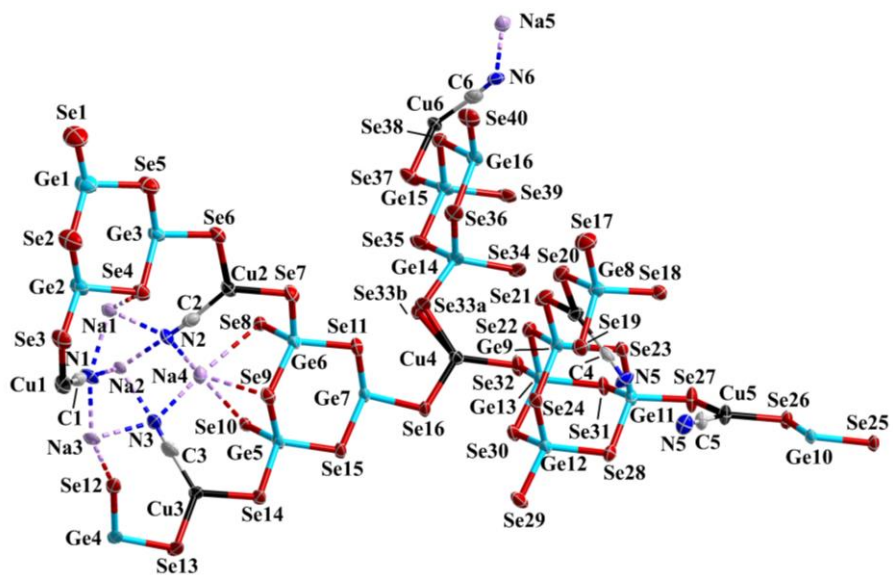


Figure 6.11: Asymmetric unit of compound **6b**. All the atoms are shown as thermal ellipsoids at the 50% probability level, imidazolium counterions are omitted for clarity. Atom color code: Ge—sky blue; Cu—black; Se—red; Na—lilac; C—grey; N—blue.

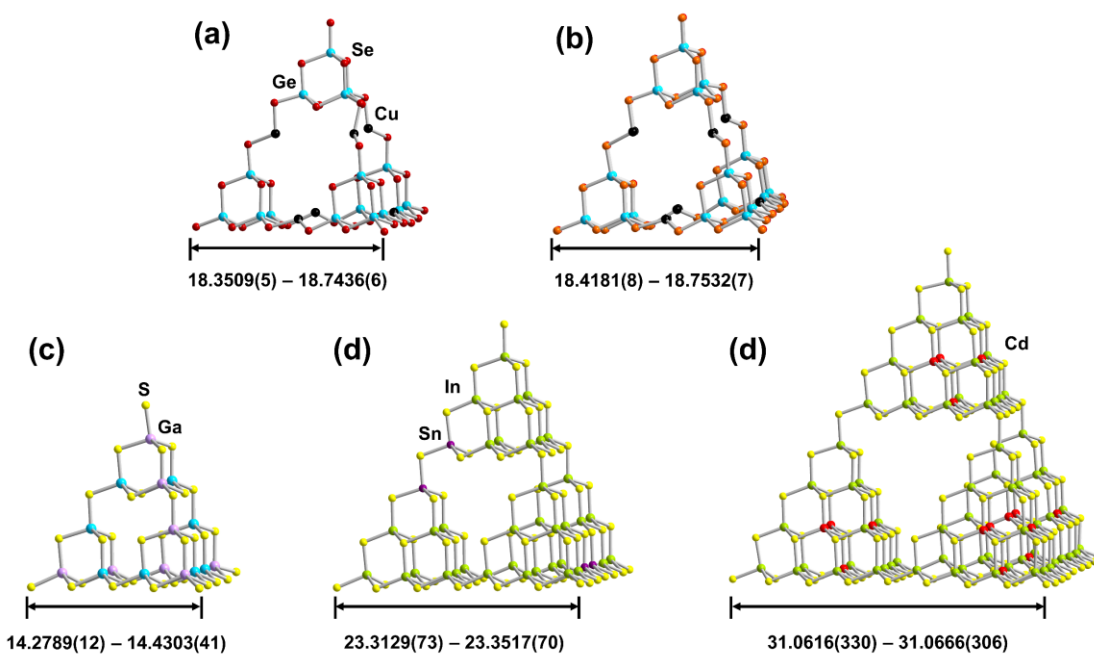


Figure 6.12: Comparison of the cluster size between T2,2-type supercluster in compound **6a** (a); in compound **6b** (b); T2,2 cluster in compound (AEP)_{2.41}[Ga_{2.13}Sn_{1.87}S₈] (c); T3,2 cluster in compound [(H⁺–DBU)_{16.5}(H⁺–AB)_{6.1}(H₂O)₄][In_{42.6}Sn_{7.4}S₉₀] (d); T4,2 cluster in compound [(H⁺)₂–DBN)₁₁((H⁺)₂–(DEM)(H₂O)₅₀][Cd₁₆In₆₄S₁₃₄] (e). Atom color code: Ge–sky blue, Cu–black, Se–wine red, S–yellow, Ga–lilac, Sn–purple, In–lime, Cd–red. AEP = 1-(2-aminoethyl)piperazine; DBU = 1,8-diazabicyclo(5.4.0)undec-7-ene; AB = 2-amino-1-butanol; DEM = 4-[2-(dimethylamino)ethyl]morpholine.

6.1.6 Mass weight and yield of the cross-experiments for compound 5

Table 6.2: Summary over the yield and weight of **5** from cross-experiments, **x** denotes that no target compound **5** was formed under the given reaction conditions.

	No additional ACl (yield + weight)	CsCl (yield + weight)	NaCl (yield + weight)	KCl (yield + weight)	RbCl (yield + weight)	NaCl + CsCl (yield + weight)
[Li ₄ (H ₂ O) _{20,33}][Ge ₄ Se ₁₀]	x	62.3% (17.2 mg)	x	x	x	56.2% (15.5 mg)
Na ₄ [Ge ₄ Se ₁₀]	x	66.5% (18.4 mg)	x	x	x	58.6% (16.2 mg)
[K ₄ (H ₂ O) ₃][Ge ₄ Se ₁₀]	x	69.8% (19.3 mg)	x	x	x	62.3% (17.2 mg)
Rb ₄ [Ge ₄ Se ₁₀]	x	64.1% (17.7 mg)	x	x	x	66.4% (18.3 mg)
[Cs ₄ (H ₂ O)][Ge ₄ Se ₁₀]	76.4% (20.7 mg)	72.5% (20.0 mg)	70.2% (19.4 mg)	71.9% (19.9 mg)	66.5% (18.4 mg)	73.2% (20.2 mg)

6.1.7 Structural details of compound 7

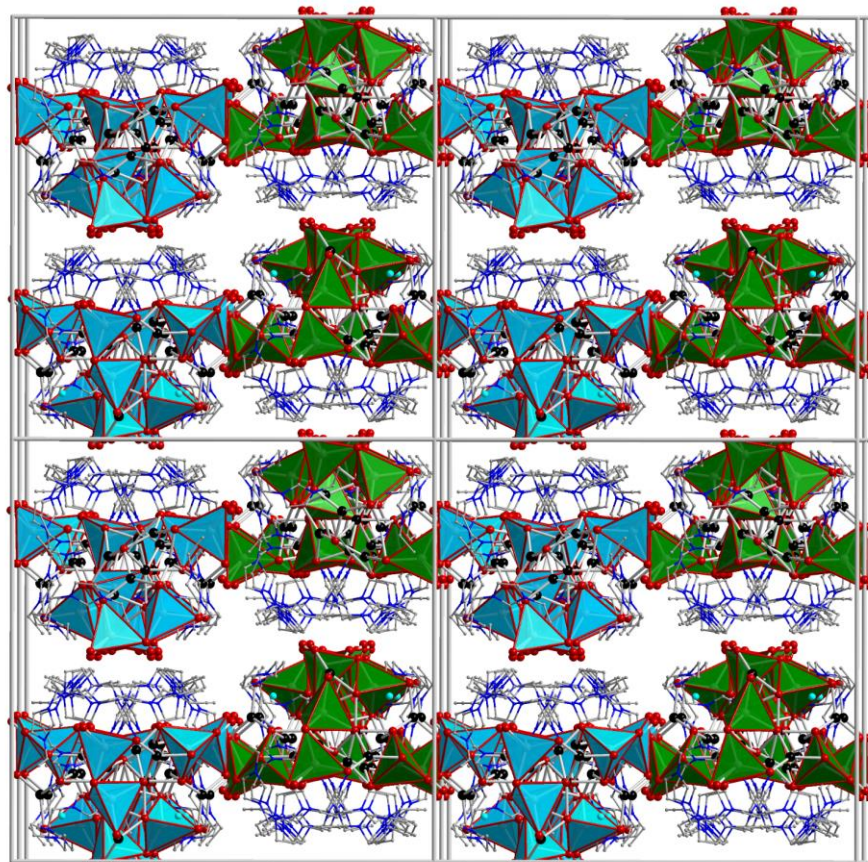


Figure 6.13: Arrangement of 64 anions in the crystal structure of compound **7**, accommodated in a 2 x 2 x 2 supercell.
Color code: Cu–Black; Se–Red; Sn–Gray; Li–Turquoise.

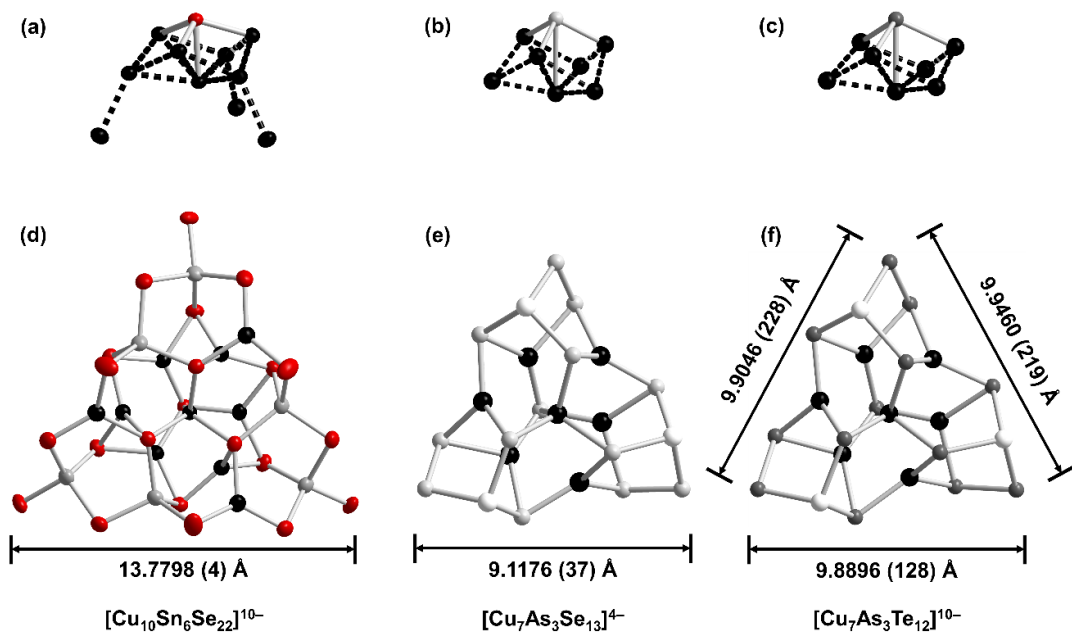


Figure 6.14: Comparison of the cluster core $\{\text{Cu}_{10}\text{Se}\}$ of the cluster anion of compound 7 (a), the cluster core $\{\text{Cu}_7\text{Se}\}$ in known $[\text{Cu}_7\text{As}_3\text{Se}_{13}]^{4-}$ anion (b) and the cluster core $\{\text{Cu}_7\text{Te}\}$ in known $[\text{Cu}_7\text{As}_3\text{Te}_{13}]^{4-}$ anion (c). The molecular structure and size of cluster anion in compound 7 (d), thermal ellipsoids are drawn at 50% probability level, disordered atoms are omitted for clarity; the molecular structure and size of cluster anion in reported $[\text{Cu}_7\text{As}_3\text{Se}_{13}]^{4-}$ (e) and $[\text{Cu}_7\text{As}_3\text{Te}_{13}]^{4-}$ (f). Color code: Cu–Black; Se–Red; Sn–Gray.

6.1.8 Structural details of compound 8

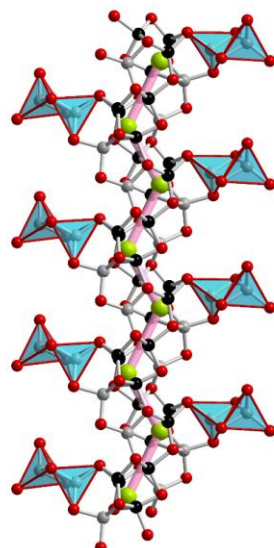


Figure 6.15: Infinite zigzag chain fragment in compound 8. Color code: Cu–Black; Se–Red; Sn–Gray, ionic liquid counterions are omitted for clarity; each $\{\text{Cu}_4\text{Sn}_2\text{Se}_6\}$ repeating unit is regarded as a node, illustrated as a pale green sphere for a simplified representation of the backbone-type strand.

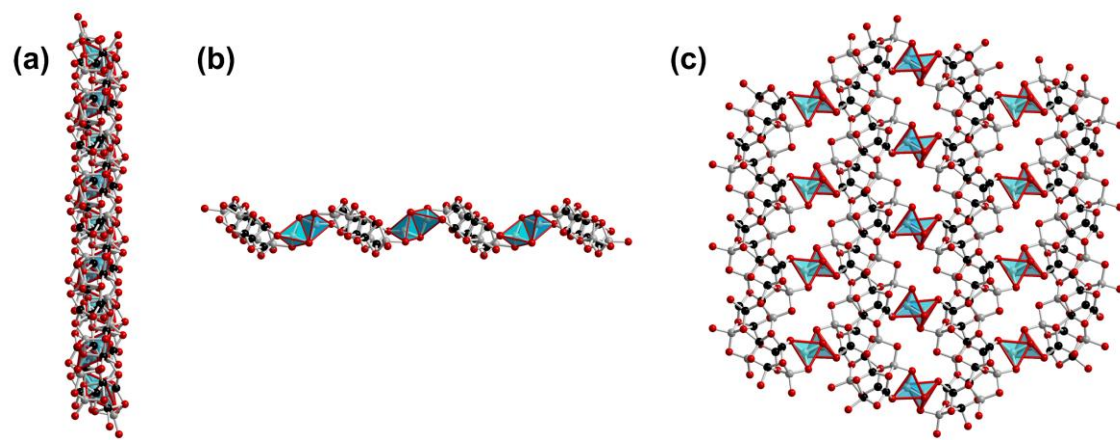


Figure 6.16: View of the single anionic layer in compound **8** from direction a (a); b (b); and c (c). Color code: Cu-Black; Se-Red; Sn-Grey, ionic liquid counterions are omitted for clarity.

6.1.9 Structural details of compound **9**

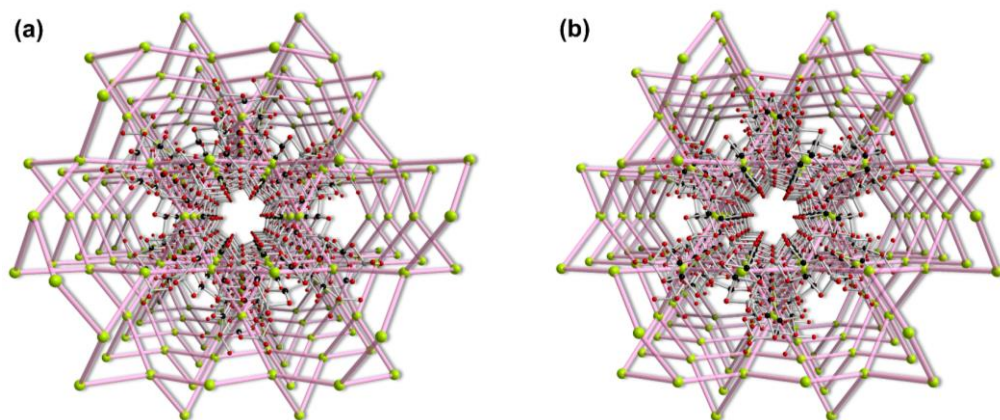


Figure 6.17: The *qtz* networks of compound **9a** (a) and **9b** (b) along c axis via regarding each cluster as a node (shown as a pale green sphere). Color code: Cu-Black; Se-Red; Sn-Grey.

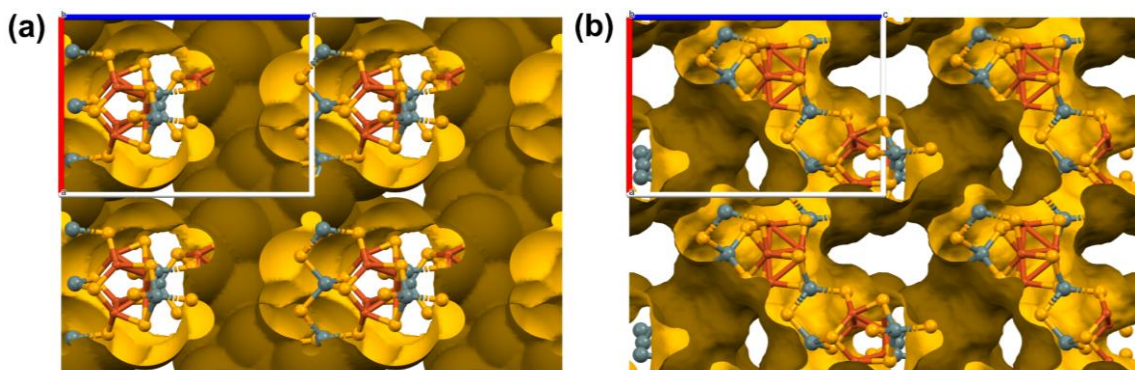


Figure 6.18: The solvent accessible surfaces show potential positions of structure directing cations in **9a** (a); and **9b** (b) along b axis.

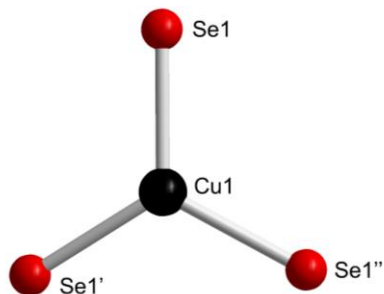


Figure 6.19: Three-connected Cu^+ observed in the asymmetric unit of compound **10**, shown for atom Cu1 as an example.

6.1.10 Structural details of compound 10

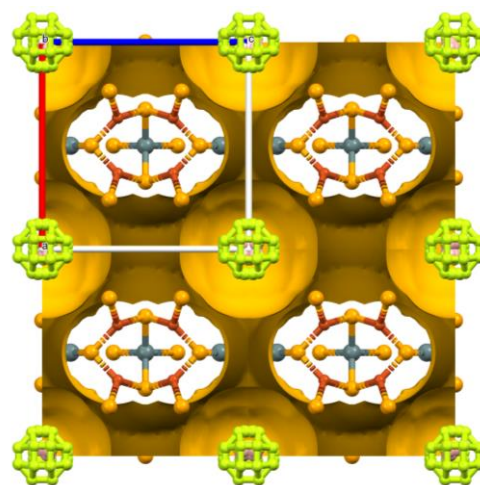


Figure 6.20: The solvent accessible surfaces show potential positions of structure directing cations in **10**.

6.1.11 Bond valence sum (BVS) of Cu atoms in compound 7 – 10

To verify the valence state of all Cu atoms in compound 7 – 10, BVS caculation is applied. The bond valence is defined as $S_{ij} = \exp[(R_0 - R_{ij})/B]$, where R_{ij} is the bond length between the two given atoms, R_0 and R_{ij} are empirical parameters as defined by Brown *et al.* We herein use $R_0 = 1.9$, $B = 0.37$. The BVS is defined as $\text{BVS} = \sum S_{ij}$ for the sum of all the bond valences around a given atom i .

Table 6.3: Bond length (Å) and result of a BVS calculation of the one tetra-coordinated and three tri-coordinated Cu atoms in the asymmetric unit of compound **7**.

	Se3	Se3	Se3	Se8	BVS
Cu1	2.5856	2.5856	2.5856	2.5017	0.6670
	Se4	Se7	Se8		
Cu2	2.3905	2.4428	2.3757		0.7727
	Se3	Se4	Se7		
Cu3	2.4219	2.3666	2.4289		0.7668
	Se2	Se3	Se5		
Cu4	2.3880	2.4652	2.3573		0.7751

Table 6.4: Bond length (Å) and result of a BVS calculation of the one tetra-coordinated and three tri-coordinated Cu atoms in the asymmetric unit of compound **8**.

	Se1	Se2	Se3	Se4	BVS
Cu1	2.6621	2.4631	2.4134	2.5955	0.7481
	Se1	Se2	Se4	Se5	BVS
Cu2	2.5448	2.3901	2.6221	2.5615	0.7503
	Se13	Se15	Se17	Se18	BVS
Cu7	2.6434	2.5533	2.3880	2.5449	0.7476
	Se13	Se16	Se17	Se18	BVS
Cu8	2.5984	2.4071	2.6640	2.4767	0.7427
	Se3	Se5	Se7		BVS
Cu3	2.3769	2.3555	2.4050		0.8230
	Se1	Se4	Se7		BVS
Cu4	2.3656	2.3705	2.4114		0.8155
	Se12	Se13	Se17		BVS
Cu5	2.4305	2.3738	2.3687		0.7980
	Se12	Se15	Se16		BVS
Cu6	2.4004	2.3523	2.3681		0.8353

Table 6.5: Bond length (Å) and result of a BVS calculation of the one tetra-coordinated and three tri-coordinated Cu atoms in the asymmetric unit of compound **9a**.

	Se4	Se5	Se6	BVS
Cu1	2.3609	2.3814	2.3661	0.8437
	Se3	Se5	Se7	BVS
Cu2	2.3496	2.3933	2.3648	0.8450
	Se3	Se9	Se10	BVS
Cu3	2.3538	2.3798	2.3734	0.8449
	Se4	Se8	Se9	BVS

Cu4	2.3565	2.3605	2.3935	0.8427
	Se7	Se8	Se10	BVS
Cu5A	2.5386	2.1600	2.8201	0.7564
	Se6	Se7	Se8	BVS
Cu5B	2.8368	2.1607	2.5255	0.7582

Table 6.6: Bond length (Å) and result of a BVS calculation of the one tetra-coordinated and three tri-coordinated Cu atoms in the asymmetric unit of compound **9b**.

	Se4	Se5	Se6	BVS
Cu1	2.3607	2.3578	2.3537	0.8715
	Se3	Se5	Se7	BVS
Cu2	2.3274	2.3479	2.4091	0.8657
	Se3	Se9	Se10	BVS
Cu3	2.3762	2.3496	2.3504	0.8688
	Se4	Se8	Se9	BVS
Cu4	2.3390	2.3893	2.3667	0.7427
	Se7	Se8	Se10	BVS
Cu5A	2.6699	2.0899	2.6921	0.8409
	Se6	Se7	Se8	BVS
Cu5B	2.7115	2.0720	2.6923	0.8573

Table 6.7: Bond length (Å) and result of a BVS calculation of the one tetra-coordinated and three tri-coordinated Cu atoms in the asymmetric unit of compound **10**.

	Se1	Se1	Se1	BVS
Cu1	2.3488	2.3488	2.3488	0.8919

6.1.12 Optical properties of compounds **8 – 11**

Optical absorption spectra of compounds **8–11** were measured in diffuse-reflectance mode on single crystals employing a Varian Cary 5000 UV/vis/NIR spectrometer from Agilent, equipped with a Praying Mantis accessory for the solid-state samples. Tauc plots were generated using the Kubelka–Munk function $(F(R\infty)hv)^{1/\gamma}$, with $\gamma = 0.5$, indicative for a direct allowed optical gap, or $\gamma = 2$, indicative for an indirect optical gap.

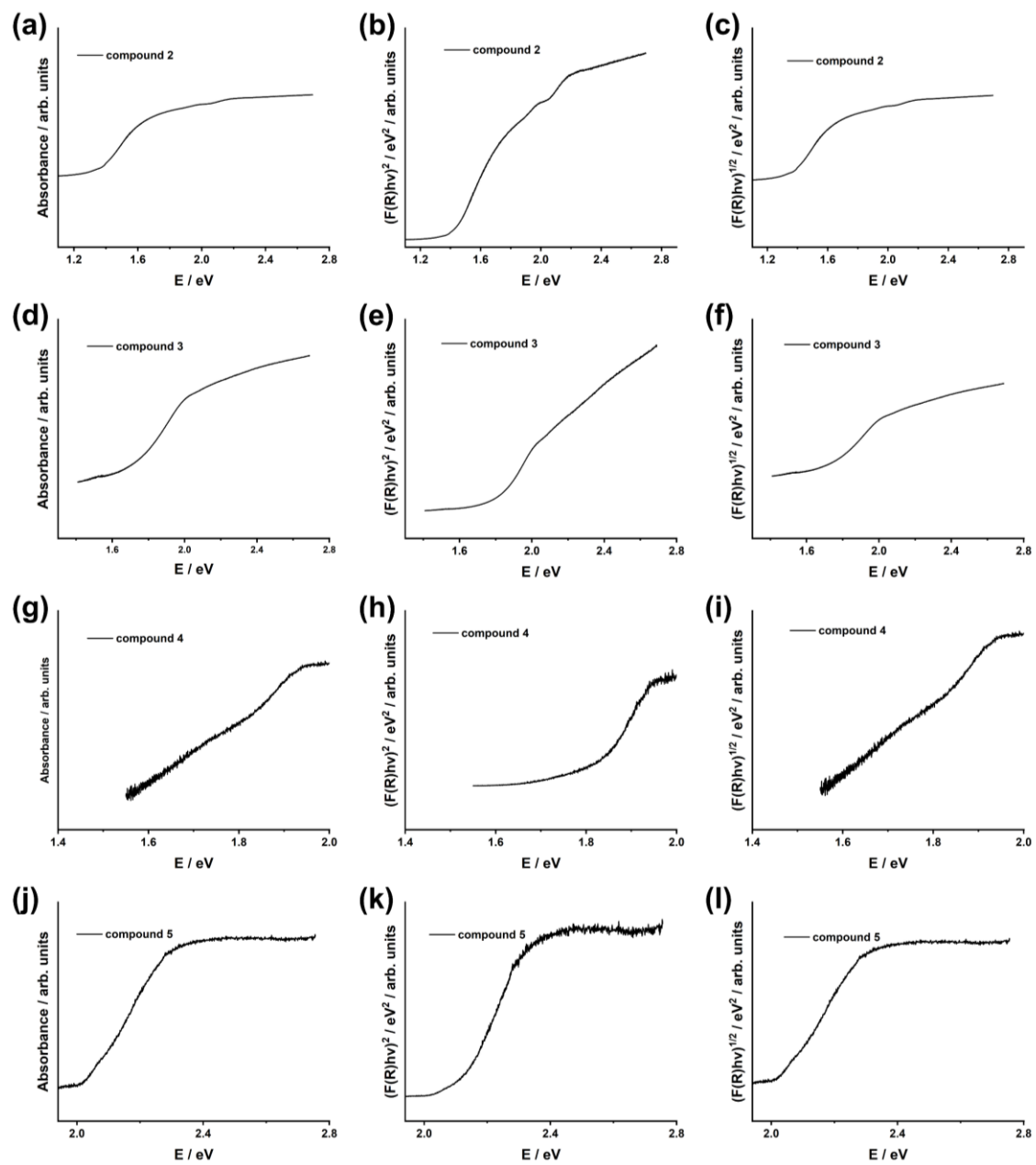


Figure 6.21: Tauc plots derived from the solid-state UV-visible spectra of samples of **8** (a), **9** (b), **10** (c); and **11** (d). Corresponding experiment of compound **7** was hampered by the small yield of this compound.

Table 6.8: Summary of the optical band gaps energies E_{gap} of chalcogenido metalate compounds comprising Cu^+ , as well as photovoltaic materials based on the Cu/Sn/Ch elemental combination (Ch = S, Se).

Compound	E_{gap} (eV)	Comment	Ref.
Cluster-based compounds			
Cu-Ge-S			
$[\text{Ni}(\text{en})_3]_4[\text{Cu}_{16}\text{Ge}_{12}\text{S}_{36}]\text{Cl}_{1.5}$	2.08		[200]
$(\text{H}^+\text{-en})_4[\text{Cu}_8\text{Ge}_5\text{S}_{16}]$	2.50		[198]
$(\text{H}^+\text{-C}_4\text{N}_2\text{H}_{10})_{0.5}[\text{Cu}_3\text{GeS}_4]$	2.30		[237]
$(\text{H}^+\text{-C}_3\text{N}_2\text{H}_{10})_{0.5}[\text{Cu}_3\text{GeS}_4]$	2.06		[237]
$\text{Na}_4[\text{Cu}_8\text{Ge}_5\text{S}_{12}] \bullet 2\text{H}_2\text{O}$	2.40		[238]
$\text{K}_4[\text{Cu}_8\text{Ge}_3\text{S}_{12}]$	2.20		[239]
$(\text{H}^+\text{-C}_6\text{N}_4\text{H}_{18})_4[\text{Cu}_8\text{Ge}_3\text{S}_{12}]$	2.45		[240]
Cu-Ge-Se			
$(\text{H}^+\text{-C}_5\text{NH}_{11})[\text{Cu}_8\text{Ge}_6\text{Se}_{19}]$	1.42		[200]
$(\text{H}^+\text{-C}_6\text{N}_4\text{H}_{18})_6[\text{Cu}_7\text{Ge}_4\text{Se}_{13}]$	1.40		[200]
$(\text{H}^+\text{-CNH}_6)_6[\text{Cu}_{10}\text{Ge}_8\text{Se}_{24}]$	1.76		[206]
Cu-Sn-S			
$(\text{H}^+\text{-C}_4\text{N}_2\text{H}_{12})_2[\text{Cu}_2\text{SnS}_4]$	2.15		[241]
$(\text{H}^+\text{-en})_2[\text{Cu}_8\text{Sn}_3\text{S}_{12}]$	2.00		[242]
	– 2.10		
$\text{Rb}_2[\text{Cu}_2\text{SnS}_4]$	2.08		[243]
$(\text{H}^+\text{-en})_2[\text{La}(\text{en})_4(\text{CuSn}_3\text{S}_9)] \bullet 0.5\text{en}$	2.13		[244]
$(\text{H}^+\text{-en})_4[\text{Nd}(\text{en})_4]_2(\text{Cu}_6\text{Sn}_6\text{S}_{20})] \bullet 3\text{en}$	2.29		[244]
Cu-Sn-Se			
$(\text{H}^+\text{-C}_5\text{NH}_{11})_{10}[\text{Cu}_{16}\text{Sn}_6\text{Se}_{19}(\text{Se}_2)_6]$	0.73	Contains polyselenide units	[191]
$(\text{H}^+\text{-C}_6\text{N}_2\text{H}_{11})_4[\text{Cu}_8\text{Sn}_6\text{Se}_{19}] \bullet 13\text{H}_2\text{O}$	1.19		[200]
$(\text{H}^+\text{-C}_4\text{N}_2\text{H}_{12})[\text{Cu}_2\text{SnSe}_4]$	1.61		[245]
Photovoltaic materials			
Cu_2SnS_3	1.88	Nanocrystals	[209]
Cu_2SnSe_3	1.50	Nanocrystals	[207]
$\text{Cu}_2\text{ZnSnS}_4$	1.50	Contains additional Zn^{2+}	[208]
$\text{Cu}_2\text{ZnSnSe}_4$	1.30	Contains additional Zn^{2+}	[208]

6.1.13 ESI(–) mass spectra of the solution upon extracting **13** with Cs^+

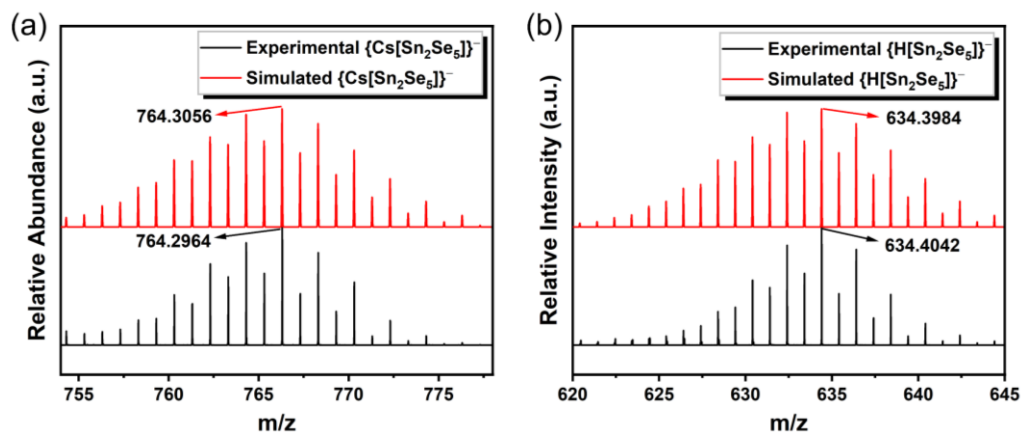


Figure 6.22: High resolution ESI(–) mass spectra of $\{\text{Cs}[\text{Sn}_2\text{Se}_5]\}^-$ (a), and $\{\text{H}[\text{Sn}_2\text{Se}_5]\}^-$ (b) detected in the solution after treating **13** with aqueous solution of CsCl .

6.1.14 Crystal structure measurement and optical photographs of compounds 1 – 21

Single-crystal diffraction data were collected at $T = 100$ K with Mo- $K\alpha$ radiation ($\lambda = 0.71073$ Å) on an area detector system Stoe IPDS-2T, or on a Bruker D8Quest with a CMOS detector, or on a Stoe StadiVari diffractometer using Cu- $K\alpha$ radiation ($\lambda = 1.54186$ Å) equipped with an Oxford Cryosystems module, or on a Stoe StadiVari diffractometer using Ga- $K\alpha$ radiation ($\lambda = 1.34134$ Å).

Measurement, structure solution, and refinement results are detailed in following Tables. The structures were solved by dual-space methods implemented in SHELXT from SHELXL-2018/136 and refined by full matrix least-squares methods against F^2 using the SHELXL program. Measurement, structure solution, and refinement results, as well as details on the back Fourier transform procedure using the SQUEEZE algorithm in the PLATON program package, are detailed in corresponding Tables. Figures were created with Diamond 4.5.

The following tables provide crystal data refinement details and photographs of single crystals on these compounds.

Table 6.9: Crystallographic data and refinement parameters for compound **1**.

Compound	1
Chemical formula	Ge ₄ Se ₁₀ C ₂₄ N ₈ H ₄₄
Formula weight	1524.63
Temperature/K	100(2)
Crystal system	Tetragonal
Space group	<i>P</i> 4 ₂ /n
<i>a</i> /Å	13.6752(14)
<i>b</i> /Å	13.6752(14)
<i>c</i> /Å	12.0415(15)
α /°	90
β /°	90
γ /°	90
Volume/Å ³	2251.9(5)
<i>Z</i>	2
ρ_{calc} g/cm ³	2.249
μ /mm ⁻¹	10.754
Radiation	MoK α (λ = 0.71073)
2 θ range for data collection/°	4.212 to 49.264
Reflections collected	13684
Independent reflections	1908
R _{int}	0.099
Data/restraints/parameters	1908/2/102
Goodness-of-fit on F^2	0.934
Final R indexed [$I \geq 2\sigma(I)$]	$R_1 = 0.0381$, $wR_2 = 0.1013$
Final R indexed [all data]	$R_1 = 0.0693$, $wR_2 = 0.1112$
Largest diff. peak/hole / e Å ⁻³	1.39/−0.61

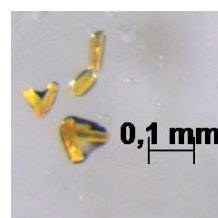
Figure 6.23: Crystal photograph of compound **1**.

Table 6.10: Crystallographic data and refinement parameters for compound **2a**.

Compound	2a
Chemical formula	Ge ₈ Se ₁₉ C ₃₆ N ₁₂ H ₆₆
Formula weight	2747.96
Temperature/K	100(2)
Crystal system	Triclinic
Space group	<i>P</i> 1̄
<i>a</i> /Å	10.2607(5)
<i>b</i> /Å	17.6852(9)
<i>c</i> /Å	21.9944(11)
$\alpha/^\circ$	100.8887(18)
$\beta/^\circ$	95.5998(18)
$\gamma/^\circ$	105.2396(18)
Volume/Å ³	3735.5(3)
<i>Z</i>	2
ρ_{calc} g/cm ³	2.443
μ/mm^{-1}	12.465
Radiation	MoK α ($\lambda = 0.71073$)
2 θ range for data collection/°	4.16 to 50.796
Reflections collected	75462
Independent reflections	13817
R_{int}	0.0516
Data/restraints/parameters	13817/75/596
Goodness-of-fit on F^2	1.236
Final R indexed [$I \geq 2\sigma(I)$]	$R_1 = 0.0999, wR_2 = 0.1962$
Final R indexed [all data]	$R_1 = 0.1130, wR_2 = 0.2021$
Largest diff. peak/hole / e Å ⁻³	3.20/-2.10

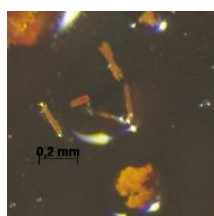


Figure 6.24: Crystal photograph of compound **2a**.

Table 6.11: Crystallographic data and refinement parameters for compound **2b**.

Compound	2b
Chemical formula	Ge ₈ Se ₁₉ C ₃₆ N ₁₂ H ₆₆
Formula weight	2747.96
Temperature/K	100(2)
Crystal system	Monoclinic
Space group	<i>P</i> 2 ₁ / <i>c</i>
<i>a</i> /Å	22.2060(2)
<i>b</i> /Å	9.5440(1)
<i>c</i> /Å	36.8230(4)
α°	90
β°	105.37(9)
γ°	90
Volume/Å ³	7524.8(9)
<i>Z</i>	4
ρ_{calc} g/cm ³	2.426
μ/mm^{-1}	14.373
Radiation	CuK α ($\lambda = 1.54186$)
2 θ range for data collection/°	5.56 to 152.852
Reflections collected	143325
Independent reflections	15777
R_{int}	0.1546
Data/restraints/parameters	15777/370/535
Goodness-of-fit on F^2	1.070
Final R indexed [$I \geq 2\sigma(I)$]	$R_1 = 0.0878, wR_2 = 0.2523$
Final R indexed [all data]	$R_1 = 0.1263, wR_2 = 0.2979$
Largest diff. peak/hole / e Å ⁻³	1.57/−1.73

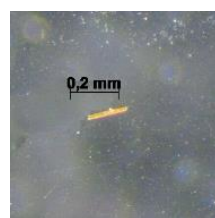
Figure 6.25: Crystal photograph of compound **2b**.

Table 6.12: Crystallographic data and refinement parameters for compound **3**.

Compound	3
Chemical formula	Ge ₁₆ Se ₃₆ C ₄₈ N ₁₆ H ₈₈
Formula weight	4893.34
Temperature/K	100(2)
Crystal system	Monoclinic
Space group	<i>C</i> 2/c
<i>a</i> /Å	20.5265(19)
<i>b</i> /Å	28.744(2)
<i>c</i> /Å	19.720(2)
α /°	90
β /°	94.640(8)
γ /°	90
Volume/Å ³	11596.6(18)
<i>Z</i>	4
ρ_{calc} g/cm ³	2.803
μ/mm^{-1}	15.417
Radiation	MoK α ($\lambda = 0.71073$)
2 θ range for data collection/°	3.098 to 53
Reflections collected	32924
Independent reflections	7582
R_{int}	0.1695
Data/restraints/parameters	7582/85/379
Goodness-of-fit on F^2	0.913
Final R indexed [$I \geq 2\sigma(I)$]	$R_1 = 0.0592, wR_2 = 0.1264$
Final R indexed [all data]	$R_1 = 0.1384, wR_2 = 0.1534$
Largest diff. peak/hole / e Å ⁻³	1.36/-0.87

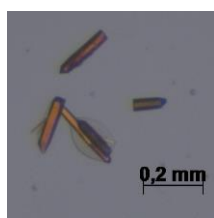


Figure 6.26: Crystal photograph of compound **3**.

Table 6.13: Crystallographic data and refinement parameters for compound 4.

Compound	4
Chemical formula	Ge ₂₄ Se ₅₄ C ₇₂ N ₂₄ H ₁₃₂
Formula weight	7340.01
Temperature/K	150(2)
Crystal system	Monoclinic
Space group	<i>P</i> 2 ₁ / <i>n</i>
<i>a</i> /Å	14.8339(11)
<i>b</i> /Å	30.6469(17)
<i>c</i> /Å	20.4654(16)
α°	90
β°	107.603(6)
γ°	90
Volume/Å ³	8868.2(11)
<i>Z</i>	2
ρ_{calc} g/cm ³	2.749
μ/mm^{-1}	12.090
Radiation	GaK α ($\lambda = 1.34143$)
2 θ range for data collection/°	4.672 to 89.994
Reflections collected	32408
Independent reflections	10733
R_{int}	0.1248
Data/restraints/parameters	10733/0/352
Goodness-of-fit on F^2	0.877
Final R indexed [$I \geq 2\sigma(I)$]	$R_1 = 0.0656, wR_2 = 0.1487$
Final R indexed [all data]	$R_1 = 0.1737, wR_2 = 0.1663$
Largest diff. peak/hole / e Å ⁻³	1.31/−0.75

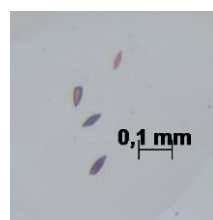


Figure 6.27: Crystal photograph of compound 4.

Table 6.14: Crystallographic data and refinement parameters for compound **5**.

Compound	5
Chemical formula	C ₄₂ N ₁₄ H ₇₇ CsGe ₂₀ Se ₄₀
Formula weight	5521.28
Temperature/K	150(2)
Crystal system	orthorhombic
Space group	<i>P</i> 2 ₁ 2 ₁ 2 ₁
<i>a</i> /Å	18.1595(7)
<i>b</i> /Å	18.5017(6)
<i>c</i> /Å	36.6323(13)
$\alpha/^\circ$	90
$\beta/^\circ$	90
$\gamma/^\circ$	90
Volume/Å ³	12307.8(8)
<i>Z</i>	4
ρ_{calc} g/cm ³	2.980
μ/mm^{-1}	14.194
Radiation	GaK α ($\lambda = 1.34143$)
2 θ range for data collection/°	6.294 to 99.982
Reflections collected	107357
Independent reflections	19191
R _{int}	0.0765
Data/restraints/parameters	19191/7/578
Goodness-of-fit on F^2	0.794
Final R indexed [$I \geq 2\sigma(I)$]	$R_1 = 0.0366, wR_2 = 0.0646$
Final R indexed [all data]	$R_1 = 0.0727, wR_2 = 0.0687$
Largest diff. peak/hole / e Å ⁻³	0.78/-0.66

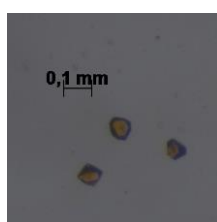


Figure 6.28: Crystal photograph of compound **5**.

Table 6.15: Crystallographic data and refinement parameters for compound **6a**.

Compound	6a
Chemical formula	C ₆₆ N ₂₆ H ₁₁₀ Na ₅ Cu ₇ Ge ₁₆ Se ₄₀
Formula weight	6147.36
Temperature/K	100(2)
Crystal system	triclinic
Space group	<i>P</i> ī
<i>a</i> /Å	19.2790(6)
<i>b</i> /Å	20.4268(7)
<i>c</i> /Å	23.2357(9)
α /°	105.2750(10)
β /°	93.6570(10)
γ /°	115.2060(10)
Volume/Å ³	7822.6(5)
<i>Z</i>	2
ρ_{calc} g/cm ³	2.610
μ /mm ⁻¹	13.312
Radiation	MoK α (λ = 0.71073)
2 θ range for data collection/°	4.026 to 50.712
Reflections collected	249496
Independent reflections	28621
R _{int}	0.0901
Data/restraints/parameters	28621/7/1442
Goodness-of-fit on F^2	1.046
Final R indexed [$I \geq 2\sigma(I)$]	$R_1 = 0.0317$, $wR_2 = 0.0724$
Final R indexed [all data]	$R_1 = 0.0526$, $wR_2 = 0.0766$
Largest diff. peak/hole / e Å ⁻³	2.17/−1.25

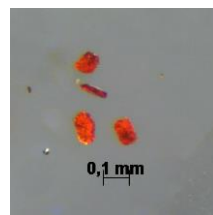
Figure 6.29: Crystal photograph of compound **6a**.

Table 6.16: Crystallographic data and refinement parameters for compound **6b**.

Compound	6b
Chemical formula	C ₆₆ N ₂₆ H ₁₁₀ Na ₅ Cu ₇ Ge ₁₆ Se ₄₀
Formula weight	6147.36
Temperature/K	100(2)
Crystal system	triclinic
Space group	<i>P</i> 1̄
<i>a</i> /Å	20.3457(8)
<i>b</i> /Å	20.8202(9)
<i>c</i> /Å	23.1199(11)
$\alpha/^\circ$	72.172(2)
$\beta/^\circ$	68.184(2)
$\gamma/^\circ$	60.802(1)
Volume/Å ³	7842.1(6)
<i>Z</i>	2
ρ_{calc} g/cm ³	2.472
μ/mm^{-1}	13.271
Radiation	MoK α ($\lambda = 0.71073$)
2 θ range for data collection/°	3.958 to 50.774
Reflections collected	119149
Independent reflections	28841
R _{int}	0.0897
Data/restraints/parameters	28841/114/1288
Goodness-of-fit on F^2	1.039
Final R indexed [$I \geq 2\sigma(I)$]	$R_1 = 0.0643, wR_2 = 0.1584$
Final R indexed [all data]	$R_1 = 0.1312, wR_2 = 0.1824$
Largest diff. peak/hole / e Å ⁻³	1.90/-1.24

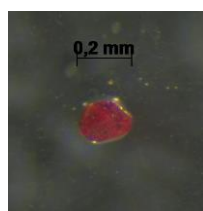


Figure 6.30: Crystal photograph of compound **6b**.

Table 6.17: Crystallographic data and refinement parameters for compound 7.

Compound	7
Chemical formula	C ₆₃ N ₁₈ H ₁₁₇ LiCu ₁₀ Sn ₆ Se ₂₂
Formula weight	4218.34
Temperature/K	100(2)
Crystal system	cubic
Space group	<i>P</i> a $\bar{3}$
<i>a</i> /Å	29.1431(12)
<i>b</i> /Å	29.1431(12)
<i>c</i> /Å	29.1431(12)
α /°	90
β /°	90
γ /°	90
Volume/Å ³	24752(3)
<i>Z</i>	8
ρ_{calc} g/cm ³	2.264
μ /mm ⁻¹	9.374
Radiation	MoK α (λ = 0.71073)
2 θ range for data collection/°	3.952 to 46.548
Reflections collected	425280
Independent reflections	5960
R _{int}	0.1177
Data/restraints/parameters	5960/15/236
Goodness-of-fit on F^2	1.058
Final R indexed [$I \geq 2\sigma(I)$]	$R_1 = 0.0626$, $wR_2 = 0.1548$
Final R indexed [all data]	$R_1 = 0.0824$, $wR_2 = 0.1715$
Largest diff. peak/hole / e Å ⁻³	2.17/-1.74

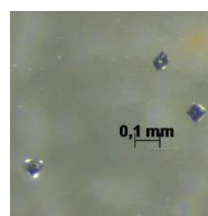


Figure 6.31: Crystal photograph of compound 7.

Table 6.18: Crystallographic data and refinement parameters for compound **8**.

Compound	8
Chemical formula	C ₅₆ N ₁₆ H ₁₀₄ Sn ₁₂ Cu ₁₆ Se ₃₆
Formula weight	6285.34
Temperature/K	100(2)
Crystal system	monoclinic
Space group	<i>P</i> 2 ₁ /c
<i>a</i> /Å	28.693(2)
<i>b</i> /Å	10.4788(6)
<i>c</i> /Å	23.2254(19)
α /°	90
β /°	111.748(6)
γ /°	90
Volume/Å ³	6486.0(8)
<i>Z</i>	2
ρ_{calc} g/cm ³	3.164
μ/mm^{-1}	32.578
Radiation	CuK α ($\lambda = 1.54186$)
2 θ range for data collection/°	6.634 to 99.962
Reflections collected	48294
Independent reflections	6652
R _{int}	0.1796
Data/restraints/parameters	6652/192/523
Goodness-of-fit on F^2	0.931
Final R indexed [$I \geq 2\sigma(I)$]	$R_1 = 0.0598, wR_2 = 0.1352$
Final R indexed [all data]	$R_1 = 0.1148, wR_2 = 0.1549$
Largest diff. peak/hole / e Å ⁻³	1.98/-1.46

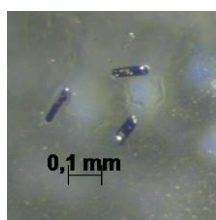


Figure 6.32: Crystal photograph of compound **8**.

Table 6.19: Crystallographic data and refinement parameters for compound **9a**.

Compound	9a
Chemical formula	C ₁₈ N ₆ H ₃₃ Cu ₅ Sn ₃ Se ₁₀
Formula weight	1796.87
Temperature/K	100(2)
Crystal system	trigonal
Space group	<i>P</i> 3 ₂
<i>a</i> /Å	14.0995(11)
<i>b</i> /Å	14.0995(11)
<i>c</i> /Å	17.2340(13)
α°	90
β°	90
γ°	120
Volume/Å ³	2967.0(5)
<i>Z</i>	3
ρ_{calc} g/cm ³	3.017
μ /mm ⁻¹	28.395
Radiation	CuK α (λ = 1.54186)
2 θ range for data collection/°	7.24 to 152.878
Reflections collected	33492
Independent reflections	7757
R _{int}	0.0683
Data/restraints/parameters	7757/13/172
Goodness-of-fit on F^2	0.719
Final R indexed [$I \geq 2\sigma(I)$]	$R_1 = 0.0320, wR_2 = 0.0493$
Final R indexed [all data]	$R_1 = 0.0643, wR_2 = 0.0555$
Largest diff. peak/hole / e Å ⁻³	0.54/−0.46

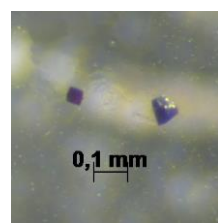
Figure 6.33: Crystal photograph of compound **9a**.

Table 6.20: Crystallographic data and refinement parameters for compound **9b**.

Compound	9b
Chemical formula	C ₁₈ N ₆ H ₃₃ Cu ₅ Sn ₅ Se ₁₀
Formula weight	1796.87
Temperature/K	100(2)
Crystal system	trigonal
Space group	<i>P</i> 3 ₁
<i>a</i> /Å	13.843(2)
<i>b</i> /Å	13.843(2)
<i>c</i> /Å	17.174(3)
$\alpha/^\circ$	90
$\beta/^\circ$	90
$\gamma/^\circ$	120
Volume/Å ³	2849.9(11)
<i>Z</i>	3
ρ_{calc} g/cm ³	3.141
μ/mm^{-1}	29.561
Radiation	CuK α ($\lambda = 1.54186$)
2 θ range for data collection/°	7.374 to 107.96
Reflections collected	18654
Independent reflections	4404
R_{int}	0.1274
Data/restraints/parameters	4404/19/142
Goodness-of-fit on F^2	0.842
Final R indexed [$I \geq 2\sigma(I)$]	$R_1 = 0.0867, wR_2 = 0.2189$
Final R indexed [all data]	$R_1 = 0.1540, wR_2 = 0.2515$
Largest diff. peak/hole / e Å ⁻³	1.41/-0.82

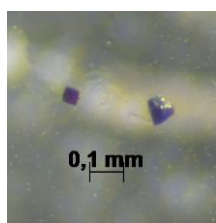


Figure 6.34: Crystal photograph of compound **9b**.

Table 6.21: Crystallographic data and refinement parameters for compound **10**.

Compound	10
Chemical formula	C ₄₂ N ₁₂ H ₇₈ B ₁ F ₅ Cu ₈ Sn ₆ Se ₁₈
Formula weight	3498.86
Temperature/K	100(2)
Crystal system	cubic
Space group	<i>Pm</i> $\overline{3}$
<i>a</i> /Å	12.384(2)
<i>b</i> /Å	12.384(2)
<i>c</i> /Å	12.384(2)
α /°	90
β /°	90
γ /°	90
Volume/Å ³	1899.3(11)
<i>Z</i>	1
ρ_{calc} g/cm ³	2.721
μ /mm ⁻¹	27.823
Radiation	CuK α (λ = 1.54186)
2 θ range for data collection/°	7.138 to 124.444
Reflections collected	12360
Independent reflections	587
R _{int}	0.1046
Data/restraints/parameters	587/0/20
Goodness-of-fit on F^2	1.017
Final R indexed [$I \geq 2\sigma(I)$]	$R_1 = 0.0565, wR_2 = 0.1754$
Final R indexed [all data]	$R_1 = 0.0731, wR_2 = 0.1830$
Largest diff. peak/hole / e Å ⁻³	1.88/−0.70

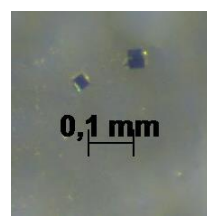
Figure 6.35: Crystal photograph of compound **10**.

Table 6.22: Crystallographic data and refinement parameters for compound **11**.

Compound	11
Chemical formula	C ₇₀ N ₂₀ Sn ₁₂ Se ₂₈ B ₂ F ₈ H ₁₃₀
Formula weight	5140.18
Temperature/K	100(2)
Crystal system	triclinic
Space group	<i>P</i> 1̄
<i>a</i> /Å	13.8832(13)
<i>b</i> /Å	20.2057(19)
<i>c</i> /Å	23.954(3)
α /°	95.208(8)
β /°	89.890(8)
γ /°	94.943(8)
Volume/Å ³	6666.9(11)
<i>Z</i>	2
ρ_{calc} g/cm ³	2.390
μ/mm^{-1}	26.700
Radiation	CuK α ($\lambda = 1.54186$)
2 θ range for data collection/°	6.012 to 119.998
Reflections collected	52281
Independent reflections	18873
R _{int}	0.0964
Data/restraints/parameters	18873/644/1162
Goodness-of-fit on F^2	1.026
Final R indexed [$I \geq 2\sigma(I)$]	$R_1 = 0.1099$, $wR_2 = 0.3403$
Final R indexed [all data]	$R_1 = 0.1991$, $wR_2 = 0.3767$
Largest diff. peak/hole / e Å ⁻³	4.66/-3.42

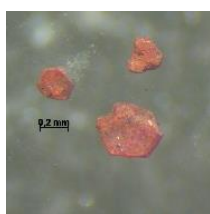


Figure 6.36: Crystal photograph of compound **11**.

Table 6.23: Crystallographic data and refinement parameters for compound **12**.

Compound	12
Chemical formula	$\text{Sn}_6\text{Se}_{14}\text{C}_{27}\text{N}_7\text{H}_{53}\text{O}$
Formula weight	2309.45
Temperature/K	100(2)
Crystal system	monoclinic
Space group	<i>Cc</i>
<i>a</i> /Å	13.9563(10)
<i>b</i> /Å	23.7774(12)
<i>c</i> /Å	18.5447(13)
$\alpha/^\circ$	90
$\beta/^\circ$	109.337(5)
$\gamma/^\circ$	90(3)
Volume/Å ³	5806.8(7)
<i>Z</i>	4
ρ_{calc} g/cm ³	2.558
μ/mm^{-1}	30.445
Radiation	$\text{CuK}\alpha$ ($\lambda = 1.54186$)
2 θ range for data collection/°	6.942 to 146.878
Reflections collected	215170
Independent reflections	6532
R_{int}	0.0299
Data/restraints/parameters	6532/136/478
Goodness-of-fit on F^2	1.089
Final R indexed [$I \geq 2\sigma(I)$]	$R_1 = 0.0371$, $wR_2 = 0.1024$
Final R indexed [all data]	$R_1 = 0.0383$, $wR_2 = 0.1037$
Largest diff. peak/hole / e Å ⁻³	1.48/−1.53

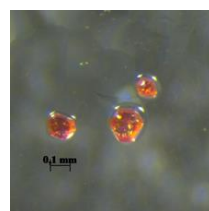
Figure 6.37: Crystal photograph of compound **12**.

Table 6.24: Crystallographic data and refinement parameters for compound **13**.

Compound	13
Chemical formula	Sn ₄ Se ₁₀ C ₂₄ N ₄ H ₅₆ O ₄
Formula weight	1729.16
Temperature/K	100(2)
Crystal system	triclinic
Space group	<i>P</i> 
<i>a</i> /	13.9007(4)
<i>b</i> /	13.9225(4)
<i>c</i> /	14.8731(5)
$\alpha/^\circ$	71.403(3)
$\beta/^\circ$	75.705(2)
$\gamma/^\circ$	60.472(2)
Volume/ ³	2359.69(14)
<i>Z</i>	1
ρ_{calc} g/cm ³	2.281
μ/mm^{-1}	9.829
Radiation	MoK α ($\lambda = 0.71073$)
2 θ range for data collection/°	3.458 to 69.376
Reflections collected	47156
Independent reflections	18902
R_{int}	0.0470
Data/restraints/parameters	18902/798/562
Goodness-of-fit on F^2	0.954
Final R indexed [$I \geq 2\sigma(I)$]	$R_1 = 0.0519$, $wR_2 = 0.1377$
Final R indexed [all data]	$R_1 = 0.1400$, $wR_2 = 0.1624$
Largest diff. peak/hole / e  ⁻³	2.35/−2.31

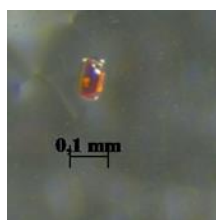


Figure 6.38: Crystal photograph of compound **13**.

Table 6.25. Crystallographic data and refinement parameters of compound **14**.

Compound	14
Chemical formula	Sn ₆ Se ₁₄ C ₄₀ N ₁₀ H ₇₅ Br
Formula weight	2593.59
Temperature/K	100(2)
Crystal system	triclinic
Space group	<i>P</i> 
<i>a</i> /	12.825(5)
<i>b</i> /	13.834(6)
<i>c</i> /	20.169(6)
$\alpha/^\circ$	89.44(3)
$\beta/^\circ$	86.56(3)
$\gamma/^\circ$	84.03(3)
Volume/ ³	3352.0(20)
<i>Z</i>	2
ρ_{calc} g/cm ³	2.425
μ/mm^{-1}	25.660
Radiation	CuK α (λ = 1.54186)
2 θ range for data collection/°	6.942 to 146.878
Reflections collected	48097
Independent reflections	13827
<i>R</i> _{int}	0.0405
Data/restraints/parameters	13827/0/532
Goodness-of-fit on <i>F</i> ²	1.047
Final R indexed [<i>I</i> ≥ 2 σ (<i>I</i>)]	<i>R</i> ₁ = 0.0475, <i>wR</i> ₂ = 0.1292
Final R indexed [all data]	<i>R</i> ₁ = 0.0497, <i>wR</i> ₂ = 0.1321
Largest diff. peak/hole / e  ⁻³	2.02/−2.37

Table 6.26. Crystallographic data and refinement parameters of compound **15**.

Compound	15
Chemical formula	$\text{Sn}_{12}\text{Se}_{28}\text{C}_{70}\text{N}_{20}\text{H}_{130}\text{Br}_2$
Formula weight	4431.44
Temperature/K	150(2)
Crystal system	monoclinic
Space group	$P2_1/n$
$a/\text{\AA}$	23.945(3)
$b/\text{\AA}$	13.8203(14)
$c/\text{\AA}$	40.650(7)
$\alpha/^\circ$	90
$\beta/^\circ$	91.645(13)
$\gamma/^\circ$	90
Volume/ \AA^3	13447 (3)
Z	8
ρ_{calc} g/cm ³	2.414
μ/mm^{-1}	18.339
Radiation	GaK α ($\lambda = 1.34143$)
2 θ range for data collection/°	3.68 to 107.994
Reflections collected	83258
Independent reflections	22202
R_{int}	0.1574
Data/restraints/parameters	22202/725/1225
Goodness-of-fit on F^2	0.892
Final R indexed [$I \geq 2\sigma(I)$]	$R_1 = 0.0644$, $wR_2 = 0.1448$
Final R indexed [all data]	$R_1 = 0.1432$, $wR_2 = 0.1592$
Largest diff. peak/hole / e \AA^{-3}	1.57/-1.64

Table 6.27. Crystallographic data and refinement parameters of compound **16**.

Compound	16
Chemical formula	$\text{Sn}_{10}\text{O}_4\text{Se}_{20}\text{C}_{72}\text{N}_8\text{H}_{136}$
Formula weight	3994.20
Temperature/K	150(2)
Crystal system	trigonal
Space group	<i>P</i> 31 c
<i>a</i> /Å	15.5794(12)
<i>b</i> /Å	15.5794(12)
<i>c</i> /Å	24.942(2)
$\alpha/^\circ$	90
$\beta/^\circ$	90
$\gamma/^\circ$	120
Volume/Å ³	5242.8(9)
<i>Z</i>	2
ρ_{calc} g/cm ³	1.793
μ/mm^{-1}	9.286
Radiation	MoK α ($\lambda = 0.71073$)
2 θ range for data collection/°	3.018 to 42.06
Reflections collected	24328
Independent reflections	3749
<i>R</i> _{int}	0.1100
Data/restraints/parameters	3749/13/103
Goodness-of-fit on <i>F</i> ²	1.047
Final R indexed [<i>I</i> ≥ 2 σ (<i>I</i>)]	<i>R</i> ₁ = 0.0878, <i>wR</i> ₂ = 0.2821
Final R indexed [all data]	<i>R</i> ₁ = 0.1250, <i>wR</i> ₂ = 0.3016
Largest diff. peak/hole / e Å ⁻³	1.18/-1.24

Table 6.28. Crystallographic data and refinement parameters of compound **17**.

Compound	17
Chemical formula	Hg _x Sn _{4-x} Se ₈
Formula weight	?
Temperature/K	100(2)
Crystal system	tetragonal
Space group	<i>I4₁/amd</i>
<i>a</i> /Å	7.8735(11)
<i>b</i> /Å	7.8735(11)
<i>c</i> /Å	47.184(11)
α°	90
β°	90
γ°	90
Volume/Å ³	2925.0(11)
<i>Z</i>	2
ρ_{calc} g/cm ³	?
μ/mm^{-1}	38.071
Radiation	CuK α ($\lambda = 1.54186$)
2 θ range for data collection/ $^{\circ}$	7.494 to 124.214
Reflections collected	4615
Independent reflections	671
<i>R</i> _{int}	0.1101
Data/restraints/parameters	671/0/20
Goodness-of-fit on <i>F</i> ²	1.044
Final R indexed [<i>I</i> ≥ 2 σ (<i>I</i>)]	<i>R</i> ₁ = 0.0782, <i>wR</i> ₂ = 0.2428
Final R indexed [all data]	<i>R</i> ₁ = 0.0988, <i>wR</i> ₂ = 0.2580
Largest diff. peak/hole / e Å ⁻³	2.16/-1.12

Table 6.29. Crystallographic data and refinement parameters of compound **18**.

Compound	18
Chemical formula	Cu ₆₄ Sn ₄₈ Se _{149.6} S _{2.4} N ₉₆ H ₅₂₈ C ₂₈₈
Formula weight	26989.07
Temperature/K	150(2)
Crystal system	cubic
Space group	<i>Im</i> 
<i>a</i> /	24.350(8)
<i>b</i> /	24.350(8)
<i>c</i> /	24.350(8)
$\alpha/^\circ$	90
$\beta/^\circ$	90
$\gamma/^\circ$	90
Volume/ ³	14438(14)
<i>Z</i>	1
ρ_{calc} g/cm ³	3.104
μ/mm^{-1}	30.976
Radiation	GaK α (λ = 1.34143)
2 θ range for data collection/°	4.464 to 107.392
Reflections collected	8816
Independent reflections	2300
<i>R</i> _{int}	0.1086
Data/restraints/parameters	2300/7/59
Goodness-of-fit on <i>F</i> ²	0.866
Final R indexed [<i>I</i> ≥ 2 σ (<i>I</i>)]	<i>R</i> ₁ = 0.0593, <i>wR</i> ₂ = 0.1638
Final R indexed [all data]	<i>R</i> ₁ = 0.1263, <i>wR</i> ₂ = 0.1796
Largest diff. peak/hole / e  ⁻³	0.75/-1.19

Table 6.30. Crystallographic data and refinement parameters of compound **19**.

Compound	19
Chemical formula	<chem>Cu6In16Sn4Se44C126N36H234</chem>
Formula weight	8421.17
Temperature/K	100(2)
Crystal system	cubic
Space group	<i>P</i> 23
<i>a</i> /Å	16.700(4)
<i>b</i> /Å	16.700(4)
<i>c</i> /Å	16.700(4)
α°	90
β°	90
γ°	90
Volume/Å ³	4657(4)
<i>Z</i>	1
ρ_{calc} g/cm ³	3.002
μ/mm^{-1}	30.639
Radiation	CuK α ($\lambda = 1.54186$)
2 θ range for data collection/°	5.292 to 86.918
Reflections collected	6609
Independent reflections	1154
<i>R</i> _{int}	0.1194
Data/restraints/parameters	1154/0/55
Goodness-of-fit on <i>F</i> ²	0.988
Final R indexed [<i>I</i> ≥ 2 σ (<i>I</i>)]	<i>R</i> ₁ = 0.1007, <i>wR</i> ₂ = 0.2332
Final R indexed [all data]	<i>R</i> ₁ = 0.2518, <i>wR</i> ₂ = 0.3365
Largest diff. peak/hole / e Å ⁻³	1.27/−0.53

Table 6.31. Crystallographic data and refinement parameters of compound **20**.

Compound	20
Chemical formula	Cu ₃ GeSe ₄ C ₂ N ₂ H _{8.5}
Formula weight	639.22
Temperature/K	180(2)
Crystal system	monoclinic
Space group	<i>P</i> 2 ₁ / <i>m</i>
<i>a</i> /Å	6.8553(18)
<i>b</i> /Å	7.6886(13)
<i>c</i> /Å	10.447(3)
α /°	90
β /°	102.90(2)
γ /°	90
Volume/Å ³	536.7(2)
<i>Z</i>	2
ρ_{calc} g/cm ³	3.905
μ /mm ⁻¹	43.996
Radiation	GaK α (λ = 1.34143)
2 θ range for data collection/°	11.522 to 116.244
Reflections collected	4906
Independent reflections	1201
<i>R</i> _{int}	0.0340
Data/restraints/parameters	1201/174/115
Goodness-of-fit on <i>F</i> ²	1.114
Final R indexed [<i>I</i> ≥ 2 σ (<i>I</i>)]	<i>R</i> ₁ = 0.0413, <i>wR</i> ₂ = 0.1195
Final R indexed [all data]	<i>R</i> ₁ = 0.0434, <i>wR</i> ₂ = 0.1209
Largest diff. peak/hole / e Å ⁻³	2.94/-1.26

Table 6.32. Crystallographic data and refinement parameters of compound **21**.

Compound	21
Chemical formula	Sb ₃ Se ₅ C ₆ N ₂ H ₁₁
Formula weight	871.22
Temperature/K	150(2)
Crystal system	monoclinic
Space group	<i>P</i> 2 ₁ / <i>a</i>
<i>a</i> /Å	7.0544(9)
<i>b</i> /Å	22.7913(19)
<i>c</i> /Å	10.5259(14)
α°	90
β°	104.025(10)
γ°	90
Volume/Å ³	1641.9(3)
<i>Z</i>	4
ρ_{calc} g/cm ³	3.524
μ/mm^{-1}	34.920
Radiation	GaK α (λ = 1.34314)
2 θ range for data collection/°	6.748 to 126.366
Reflections collected	23307
Independent reflections	4019
R_{int}	0.0494
Data/restraints/parameters	4019/36/167
Goodness-of-fit on F^2	0.999
Final R indexed [$I \geq 2\sigma(I)$]	$R_1 = 0.0388$, $wR_2 = 0.1048$
Final R indexed [all data]	$R_1 = 0.0445$, $wR_2 = 0.1067$
Largest diff. peak/hole / e Å ⁻³	2.04/−2.20

Bibliography

- [1] E. M. Flanigen, *Pure Appl. Chem.* **1980**, *52*, 2191–2211.
- [2] W. H. Taylor, *Z. Krist. - Cryst. Mater.* **1930**, *74*, 1–19.
- [3] L. Pauling, *Proc. Natl. Acad. Sci.* **1930**, *16*, 453–459.
- [4] J. Yu, in *Introd. to Zeolite Sci. Pract.* (Eds.: J. Čejka, H. van Bekkum, A. Corma, F.B.T.-S. in S.S. and C. Schüth), Elsevier, **2007**, pp. 39–103.
- [5] X. Meng, F.-S. Xiao, *Chem. Rev.* **2014**, *114*, 1521–1543.
- [6] C. Wu, K. Chao, *J. Chem. Soc. Faraday Trans.* **1995**, *91*, 167–173.
- [7] H. S. Sherry, *J. Phys. Chem.* **1968**, *72*, 4086–4094.
- [8] K. C. Kemp, J. G. Min, H. J. Choi, S. B. Hong, in *Struct. Bond.* (Eds.: S. Valencia, F. Rey), Springer International Publishing, Cham, **2020**, pp. 1–30.
- [9] A. Corma, *J. Catal.* **2003**, *216*, 298–312.
- [10] X. Bu, P. Feng, G. D. Stucky, *Science* **1997**, *278*, 2080–2085.
- [11] C. Baerlocher, L. B. McCusker, R. Chiappetta, *Microporous Mater.* **1994**, *2*, 269–280.
- [12] R. C. Rouse, D. R. Peacor, S. Merlino, *Am. Mineral.* **1989**, *74*, 1195–1202.
- [13] M. Mehring, in *Struct. Bond.* (Ed.: S. Dehnen), Springer International Publishing, Cham, **2017**, pp. 201–268.
- [14] W. H. Casey, M. M. Olmstead, C. R. Hazlett, C. Lamar, T. Z. Forbes, *Inorganics* **2015**, *3*, 21–26.
- [15] Z.-E. Lin, J. Zhang, S.-T. Zheng, G.-Y. Yang, *Microporous Mesoporous Mater.* **2004**, *74*, 205–211.
- [16] P. Feng, X. Bu, N. Zheng, *Acc. Chem. Res.* **2005**, *38*, 293–303.
- [17] X. Bu, N. Zheng, P. Feng, *Chem. Eur. J.* **2004**, *10*, 3356–3362.
- [18] N. Zheng, X. Bu, H. Vu, P. Feng, *Angew. Chem. Int. Ed.* **2005**, *44*, 5299–5303.
- [19] N. Zheng, X. Bu, B. Wang, P. Feng, *Science* **2002**, *298*, 2366–2369.
- [20] R. L. Bedard, S. T. Wilson, L. D. Vail, J. M. Bennett, E. M. Flanigen, in *Zeolites Facts, Fig. Futur. Part A - Proc. 8th Int. Zeolite Conf.* (Eds.: P.A. Jacobs, R.A.B.T.-S. in S.S. and C. van Santen), Elsevier, **1989**, pp. 375–387.
- [21] H. Li, A. Laine, M. O’Keeffe, O. M. Yaghi, *Science* **1999**, *283*, 1145–1147.
- [22] B. Krebs, D. Voelker, K.-O. Stiller, *Inorganica Chim. Acta* **1982**, *65*, L101–L102.

[23] S. Makin, P. Vaqueiro, *Molecules* **2021**, *26*, 5415–5421.

[24] W. Schiwy, B. Krebs, *Angew. Chem. Int. Ed.* **1975**, *14*, 436.

[25] A. Benkada, H. Reinsch, M. Poschmann, J. Krahmer, N. Pienack, W. Bensch, *Inorg. Chem.* **2019**, *58*, 2354–2362.

[26] C. Zimmermann, C. E. Anson, F. Weigend, R. Clérac, S. Dehnen, *Inorg. Chem.* **2005**, *44*, 5686–5695.

[27] H. Li, J. Kim, T. L. Groy, M. O’Keeffe, O. M. Yaghi, *J. Am. Chem. Soc.* **2001**, *123*, 4867–4868.

[28] X. Bu, N. Zheng, Y. Li, P. Feng, *J. Am. Chem. Soc.* **2002**, *124*, 12646–12647.

[29] X. Xu, W. Wang, D. Liu, D. Hu, T. Wu, X. Bu, P. Feng, *J. Am. Chem. Soc.* **2018**, *140*, 888–891.

[30] L. Zhang, C. Xue, W. Wang, D. Hu, J. Lv, D. Li, T. Wu, *Inorg. Chem.* **2018**, *57*, 10485–10488.

[31] O. Palchik, R. G. Iyer, J. H. Liao, M. G. Kanatzidis, *Inorg. Chem.* **2003**, *42*, 5052–5054.

[32] N. Zheng, X. Bu, P. Feng, *Angew. Chem. Int. Ed.* **2004**, *43*, 4753–4755.

[33] G. S. H. Lee, D. C. Craig, I. Ma, M. L. Scudder, T. D. Bailey, I. G. Dance, *J. Am. Chem. Soc.* **1988**, *110*, 4863–4864.

[34] X.-W. Zhao, L.-W. Qian, H.-C. Su, C.-J. Mo, C.-J. Que, Q.-Y. Zhu, J. Dai, *Cryst. Growth Des.* **2015**, *15*, 5749–5753.

[35] N. Zheng, X. Bu, P. Feng, *J. Am. Chem. Soc.* **2003**, *125*, 1138–1139.

[36] Y. Zhang, X. Wang, D. Hu, C. Xue, W. Wang, H. Yang, D. Li, T. Wu, *ACS Appl. Mater. Interfaces* **2018**, *10*, 13413–13424.

[37] L. Sun, H.-Y. Zhang, F.-Q. Zhang, L. Wang, X.-M. Zhang, *Mater. Chem. Front.* **2023**, *7*, 128–136.

[38] T. Wu, L. Wang, X. Bu, V. Chau, P. Feng, *J. Am. Chem. Soc.* **2010**, *132*, 10823–10831.

[39] T. Wu, X. Bu, X. Zhao, R. Khazhakyan, P. Feng, *J. Am. Chem. Soc.* **2011**, *133*, 9616–9625.

[40] P. Vaqueiro, M. L. Romero, *Chem. Commun.* **2007**, 3282–3284.

[41] P. Vaqueiro, M. L. Romero, *Inorg. Chem.* **2009**, *48*, 810–812.

[42] T. Wu, X. Bu, P. Liao, L. Wang, S.-T. Zheng, R. Ma, P. Feng, *J. Am. Chem. Soc.* **2012**, *134*, 3619–3622.

[43] G. Stuhrmann, J. Schneider, K. Schmidt, S. Dehnen, *Chem. Commun.* **2023**, *59*, 13171–13174.

[44] B. Peters, G. Stuhrmann, F. Mack, F. Weigend, S. Dehnen, *Angew. Chem. Int. Ed.* **2021**, *60*, 17622–17628.

[45] B. Peters, S. Santner, C. Donsbach, P. Vöpel, B. Smarsly, S. Dehnen, *Chem. Sci.* **2019**, *10*, 5211–5217.

[46] W.-Q. Mu, Q.-Y. Zhu, L.-S. You, X. Zhang, W. Luo, G.-Q. Bian, J. Dai, *Inorg. Chem.* **2012**, *51*, 1330–1335.

[47] X.-L. Sun, Q.-Y. Zhu, W.-Q. Mu, L.-W. Qian, L. Yu, J. Wu, G.-Q. Bian, J. Dai, *Dalton Trans.* **2014**, *43*, 12582–12589.

[48] J. Xu, L.-J. Xue, J.-L. Hou, Z.-N. Yin, X. Zhang, Q.-Y. Zhu, J. Dai, *Inorg. Chem.* **2017**, *56*, 8036–8044.

[49] F. Danker, C. Näther, F. Pielnhofer, W. Bensch, *Eur. J. Inorg. Chem.* **2017**, *2017*, 4317–4323.

[50] F. Zhang, X.-H. Yin, X. Liu, J. Zhou, *Z. Anorg. Allg. Chem.* **2011**, *637*, 1388–1393.

[51] R. Blachnik, A. Fehlker, *Z. Krist. - N. Cryst. Struct.* **2000**, *215*, 95–97.

[52] M. Wachhold, M. G. Kanatzidis, *Chem. Mater.* **2000**, *12*, 2914–2923.

[53] H.-Y. Luo, J. Zhou, *Dalton Trans.* **2018**, *47*, 14751–14759.

[54] J. Zhou, H. Xiao, H.-P. Xiao, T. Yang, H.-H. Zou, X. Liu, R.-Q. Zhao, Q. Tang, *Dalton Trans.* **2015**, *44*, 1350–1357.

[55] A. M. Pirani, H. P. A. Mercier, D. A. Dixon, H. Borrman, G. J. Schrobilgen, *Inorg. Chem.* **2001**, *40*, 4823–4829.

[56] C.-W. Park, M. A. Pell, J. A. Ibers, *Inorg. Chem.* **1996**, *35*, 4555–4558.

[57] Z.-X. Lei, Q.-Y. Zhu, X. Zhang, W. Luo, W.-Q. Mu, J. Dai, *Inorg. Chem.* **2010**, *49*, 4385–4387.

[58] Y.-P. Zhang, X. Zhang, W.-Q. Mu, W. Luo, G.-Q. Bian, Q.-Y. Zhu, J. Dai, *Dalton Trans.* **2011**, *40*, 9746–9751.

[59] D.-D. Yang, W. Li, W.-W. Xiong, J.-R. Li, X.-Y. Huang, *Dalton Trans.* **2018**, *47*, 5977–5984.

[60] X. Bu, N. Zheng, Y. Li, P. Feng, *J. Am. Chem. Soc.* **2003**, *125*, 6024–6025.

[61] X. Bu, N. Zheng, X. Wang, B. Wang, P. Feng, *Angew. Chem. Int. Ed.* **2004**, *43*, 1502–1505.

[62] H. Li, J. Kim, M. O’Keeffe, O. M. Yaghi, *Angew. Chem. Int. Ed.* **2003**, *42*, 1819–1821.

[63] P. Vaqueiro, M. L. Romero, *MRS Online Proc. Libr.* **2009**, *1148*, 1007.

[64] N.-N. Shen, B. Hu, C.-C. Cheng, G.-D. Zou, Q.-Q. Hu, C.-F. Du, J.-R. Li, X.-Y. Huang, *Cryst. Growth Des.* **2018**, *18*, 962–968.

[65] Y. Wang, Z. Zhu, Z. Sun, Q. Hu, J. Li, J. Jiang, X. Huang, *Chem. Eur. J.* **2020**, *26*, 1624–1632.

[66] W.-W. Xiong, J.-R. Li, B. Hu, B. Tan, R.-F. Li, X.-Y. Huang, *Chem. Sci.* **2012**, *3*, 1200–

[67] D.-Y. Chung, T. Hogan, P. Brazis, M. Rocci-Lane, C. Kannewurf, M. Bastea, C. Uher, M. G. Kanatzidis, *Science* **2000**, *287*, 1024–1027.

[68] W. S. Sheldrick, M. Wachhold, *Coord. Chem. Rev.* **1998**, *176*, 211–322.

[69] W. S. Sheldrick, M. Wachhold, *Angew. Chem. Int. Ed.* **1997**, *36*, 206–224.

[70] K. Biswas, Q. Zhang, I. Chung, J.-H. Song, J. Androulakis, A. J. Freeman, M. G. Kanatzidis, *J. Am. Chem. Soc.* **2010**, *132*, 14760–14762.

[71] J. D. Breshears, M. G. Kanatzidis, *J. Am. Chem. Soc.* **2000**, *122*, 7839–7840.

[72] T. J. McCarthy, M. G. Kanatzidis, *Chem. Mater.* **1993**, *5*, 1061–1063.

[73] M. G. Kanatzidis, in *Encycl. Inorg. Chem.*, **2005**.

[74] H. J. Deiseroth, C. Reiner, M. Schlosser, L. Kienle, *Z. Anorg. Allg. Chem.* **2002**, *628*, 1641–1647.

[75] K. O. Klepp, C. Weithaler, *J. Alloys Compd.* **1996**, *243*, 12–18.

[76] E. A. I. I. Axtell, J. H. Liao, Z. Pikramenou, Y. Park, M. G. Kanatzidis, *J. Am. Chem. Soc.* **1993**, *115*, 12191–12192.

[77] E. A. Axtell III, J.-H. Liao, Z. Pikramenou, M. G. Kanatzidis, *Chem. Eur. J.* **1996**, *2*, 656–666.

[78] I. Nußbruch, S. Dehnen, *Z. Anorg. Allg. Chem.* **2018**, *644*, 1897–1901.

[79] X. Zhou, V. S. C. Kolluru, W. Xu, L. Wang, T. Chang, Y.-S. Chen, L. Yu, J. Wen, M. K. Y. Chan, D. Y. Chung, M. G. Kanatzidis, *Nature* **2022**, *612*, 72–77.

[80] R. Xu, W. Pang, J. Yu, Q. Huo, J. Chen, *Chemistry of Zeolites and Related Porous Materials: Synthesis and Structure*, John Wiley & Sons, **2009**.

[81] O. M. Yaghi, H. Li, C. Davis, D. Richardson, T. L. Groy, *Acc. Chem. Res.* **1998**, *31*, 474–484.

[82] O. M. Yaghi, Z. Sun, D. A. Richardson, T. L. Groy, *J. Am. Chem. Soc.* **1994**, *116*, 807–808.

[83] S.-H. Feng, G.-H. Li, in (Eds.: R. Xu, Y.B.T.-M.I.S.C. (Second E. Xu)), Elsevier, Amsterdam, **2017**, pp. 73–104.

[84] A. Rabenau, *Angew. Chem. Int. Ed.* **1985**, *24*, 1026–1040.

[85] R. I. Walton, *Chem. Soc. Rev.* **2002**, *31*, 230–238.

[86] G. Li, Y. Liu, C. Liu, *Microporous Mesoporous Mater.* **2013**, *167*, 137–145.

[87] Z. Lei, B. Chen, Y.-M. Koo, D. R. MacFarlane, *Chem. Rev.* **2017**, *117*, 6633–6635.

[88] R. D. Rogers, G. A. Voth, *Acc. Chem. Res.* **2007**, *40*, 1077–1078.

[89] E. R. Cooper, C. D. Andrews, P. S. Wheatley, P. B. Webb, P. Wormald, R. E. Morris, *Nature* **2004**, *430*, 1012–1016.

[90] N. V. Plechkova, K. R. Seddon, *Chem. Soc. Rev.* **2008**, *37*, 123–150.

[91] E. R. Parnham, R. E. Morris, *Acc. Chem. Res.* **2007**, *40*, 1005–1013.

[92] Y. Lin, S. Dehnen, *Inorg. Chem.* **2011**, *50*, 7913–7915.

[93] H.-H. Tan, X. Liu, C.-M. Huang, J. Zhou, *Inorg. Chem.* **2023**, *62*, 11240–11247.

[94] M. Hao, Q. Hu, Y. Zhang, M. Luo, Y. Wang, B. Hu, J. Li, X. Huang, *Inorg. Chem.* **2019**, *58*, 5126–5133.

[95] Y. Lin, W. Massa, S. Dehnen, *J. Am. Chem. Soc.* **2012**, *134*, 4497–4500.

[96] J.-R. Li, Z.-L. Xie, X.-W. He, L.-H. Li, X.-Y. Huang, *Angew. Chem. Int. Ed.* **2011**, *50*, 11395–11399.

[97] J.-R. Li, W.-W. Xiong, Z.-L. Xie, C.-F. Du, G.-D. Zou, X.-Y. Huang, *Chem. Commun.* **2013**, *49*, 181–183.

[98] C.-F. Du, N.-N. Shen, J.-R. Li, M.-T. Hao, Z. Wang, X.-Y. Huang, *Chem. Asian J.* **2016**, *11*, 1555–1564.

[99] Y. Wang, Q. Hu, J. Jin, J. Li, J. Li, X. Huang, *Dalton Trans.* **2020**, *49*, 5020–5023.

[100] Y. Liu, Y. Wang, Y. Peng, Q. Hu, J. Li, X. Huang, *ChemistrySelect* **2022**, *7*, e202200585.

[101] H. Yin, Y. Liu, A. Ablez, Y. Wang, Q. Hu, X. Huang, *Catalyst* **2023**, *13*, 1160–1172.

[102] M. Melullis, M. K. Brandmayer, S. Dehnen, *Z. Anorg. Allg. Chem.* **2006**, *632*, 64–72.

[103] E. Ruzin, S. Dehnen, *Z. Anorg. Allg. Chem.* **2006**, *632*, 749–755.

[104] T. Kaib, P. Bron, S. Haddadpour, L. Mayrhofer, L. Pastewka, T. T. Järvi, M. Moseler, B. Roling, S. Dehnen, *Chem. Mater.* **2013**, *25*, 2961–2969.

[105] S. Santner, S. Yogendra, J. J. Weigand, S. Dehnen, *Chem. Eur. J.* **2017**, *23*, 1999–2004.

[106] Y. Lin, W. Massa, S. Dehnen, *Chem. Eur. J.* **2012**, *18*, 13427–13434.

[107] B. Peters, S. Reith, S. Dehnen, *Z. Anorg. Allg. Chem.* **2020**, *646*, 964–967.

[108] H. Yang, M. Luo, L. Luo, H. Wang, D. Hu, J. Lin, X. Wang, Y. Wang, S. Wang, X. Bu, P. Feng, T. Wu, *Chem. Mater.* **2016**, *28*, 8774–8780.

[109] H. Yang, M. Luo, X. Chen, X. Zhao, J. Lin, D. Hu, D. Li, X. Bu, P. Feng, T. Wu, *Inorg. Chem.* **2017**, *56*, 14999–15005.

[110] D.-D. Hu, J. Lin, Q. Zhang, J.-N. Lu, X.-Y. Wang, Y.-W. Wang, F. Bu, L.-F. Ding, L. Wang, T. Wu, *Chem. Mater.* **2015**, *27*, 4099–4104.

[111] N. Zheng, X. Bu, P. Feng, *Nature* **2003**, *426*, 428–432.

[112] T. Wu, Q. Zhang, Y. Hou, L. Wang, C. Mao, S.-T. Zheng, X. Bu, P. Feng, *J. Am. Chem.*

Soc. **2013**, *135*, 10250–10253.

[113] J. Lin, Q. Zhang, L. Wang, X. Liu, W. Yan, T. Wu, X. Bu, P. Feng, *J. Am. Chem. Soc.* **2014**, *136*, 4769–4779.

[114] Z.-Q. Li, C.-J. Mo, Y. Guo, N.-N. Xu, Q.-Y. Zhu, J. Dai, *J. Mater. Chem. A* **2017**, *5*, 8519–8525.

[115] Y. Wang, J. Li, Q. Hu, M. Hao, Y. Liu, L. Gong, R. Li, X. Huang, *ACS Appl. Mater. Interfaces* **2021**, *13*, 40562–40570.

[116] J.-N. Zhang, J.-X. Liu, H. Ma, X. Luo, C.-K. Han, R. Zhou, S.-F. Yuan, D.-S. Li, T. Wu, *J. Mater. Chem. A* **2024**, *12*, 14398–14407.

[117] Z. Wu, M. Luo, C. Xue, J. Zhang, J. Lv, X. Wang, T. Wu, *Cryst. Growth Des.* **2019**, *19*, 4151–4156.

[118] M.-B. Luo, S.-L. Huang, H.-D. Lai, J. Zhang, Q. Lin, *Chem. Commun.* **2020**, *56*, 8388–8391.

[119] B. Peters, C. Krampe, J. Klärner, S. Dehnen, *Chem. Eur. J.* **2020**, *26*, 16683–16689.

[120] C. Xue, L. Zhang, X. Wang, D. Hu, X.-L. Wang, J. Zhang, R. Zhou, D.-S. Li, H. Su, T. Wu, *Inorg. Chem.* **2020**, *59*, 15587–15594.

[121] V. N. Soloviev, A. Eichhöfer, D. Fenske, U. Banin, *J. Am. Chem. Soc.* **2001**, *123*, 2354–2364.

[122] V. N. Soloviev, A. Eichhöfer, D. Fenske, U. Banin, *J. Am. Chem. Soc.* **2000**, *122*, 2673–2674.

[123] B. Krebs, H.-J. Jacobsen, *Z. Anorg. Allg. Chem.* **1976**, *421*, 97–104.

[124] S. Santner, A. Wolff, M. Ruck, S. Dehnen, *Chem. Eur. J.* **2018**, *24*, 11899–11903.

[125] H. Ahari, A. Garcia, S. Kirkby, G. A. Ozin, D. Young, A. J. Lough, *J. Chem. Soc. Dalton Trans.* **1998**, 2023–2028.

[126] L. Sun, H.-Y. Zhang, J. Zhang, Y.-J. Jia, Y.-Z. Yu, J.-J. Hou, Y.-X. Wang, X.-M. Zhang, *Dalton Trans.* **2020**, *49*, 13958–13961.

[127] W. Jin, J. Bo, W. Xiang, D. Yayun, W. Xiao-Li, T. Dandan, L. Xiaohong, S. Jie, L. Dong-Sheng, L. Qipu, W. Yan-Bo, W. Tao, *CCS Chem.* **2020**, *3*, 2584–2590.

[128] C. Wang, X. Bu, N. Zheng, P. Feng, *J. Am. Chem. Soc.* **2002**, *124*, 10268–10269.

[129] A. L. Spek, *Acta Crystallogr., Sect. C Strut. Chem.* **2015**, *71*, 9–18.

[130] P. Pyykkö, M. Atsumi, *Chem. Eur. J.* **2009**, *15*, 186–197.

[131] J. Kielland, *J. Am. Chem. Soc.* **1937**, *59*, 1675–1678.

[132] A. Choudhury, S. Strobel, B. R. Martin, A. L. Karst, P. K. Dorhout, *Inorg. Chem.* **2007**, *46*, 2017–2027.

[133] B. R. Martin, L. A. Polyakova, P. K. Dorhout, *J. Alloys Compd.* **2006**, *408–412*, 490–495.

[134] Evenson, P. K. Dorhout, *Inorg. Chem.* **2001**, *40*, 2409–2414.

[135] N. Ma, L. Xiong, L. Chen, L.-M. Wu, *Sci. China Mater.* **2019**, *62*, 1788–1797.

[136] I. Csarnovics, M. Veres, P. Nemec, S. Molnár, S. Körkényesi, *J. Non-Crystalline Solids X* **2020**, *6*, 100045.

[137] Y. Yang, S.-C. Liu, W. Yang, Z. Li, Y. Wang, X. Wang, S. Zhang, Y. Zhang, M. Long, G. Zhang, D.-J. Xue, J.-S. Hu, L.-J. Wan, *J. Am. Chem. Soc.* **2018**, *140*, 4150–4156.

[138] A. R. Barik, M. Bapna, D. A. Drabold, K. V Adarsh, *Sci. Rep.* **2014**, *4*, 3686.

[139] Y. Liu, F.-Q. Shi, X. Hao, M.-Y. Li, L. Cheng, C. Wang, K.-Y. Wang, *J. Hazard. Mater.* **2023**, *458*, 132038.

[140] J. Yan, B. Zhang, J. Li, Y. Yang, Y.-N. Wang, Y.-D. Zhang, X.-Z. Liu, *Inorg. Chem.* **2023**, *62*, 12843–12850.

[141] B. Zhang, H.-Y. Sun, J. Li, L.-Z. Li, Y.-L. Deng, S.-H. Liu, M.-L. Feng, X.-Y. Huang, *Inorg. Chem.* **2019**, *58*, 11622–11629.

[142] H. Zhang, J. Hou, Y. Hu, P. Wang, R. Ou, L. Jiang, J. Z. Liu, B. D. Freeman, A. J. Hill, H. Wang, *Sci. Adv.* **2024**, *4*, eaaq0066.

[143] J. Lu, H. Zhang, J. Hou, X. Li, X. Hu, Y. Hu, C. D. Easton, Q. Li, C. Sun, A. W. Thornton, M. R. Hill, X. Zhang, G. Jiang, J. Z. Liu, A. J. Hill, B. D. Freeman, L. Jiang, H. Wang, *Nat. Mater.* **2020**, *19*, 767–774.

[144] G. M. Bögels, J. A. M. Lugger, O. J. G. M. Goor, R. P. Sijbesma, *Adv. Funct. Mater.* **2016**, *26*, 8023–8030.

[145] W. Ma, T.-T. Lv, J.-H. Tang, M.-L. Feng, X.-Y. Huang, *JACS Au* **2022**, *2*, 492–501.

[146] E. Han, Y.-G. Kim, H.-M. Yang, I.-H. Yoon, M. Choi, *Chem. Mater.* **2018**, *30*, 5777–5785.

[147] T. Hanada, M. Goto, *ACS Sustain. Chem. Eng.* **2021**, *9*, 2152–2160.

[148] Q. He, N. J. Williams, J. H. Oh, V. M. Lynch, S. K. Kim, B. A. Moyer, J. L. Sessler, *Angew. Chem. Int. Ed.* **2018**, *57*, 11924–11928.

[149] H. Gohil, S. Chatterjee, S. Yadav, E. Suresh, A. R. Paital, *Inorg. Chem.* **2019**, *58*, 7209–7219.

[150] Q. He, Z. Zhang, J. T. Brewster, V. M. Lynch, S. K. Kim, J. L. Sessler, *J. Am. Chem. Soc.* **2016**, *138*, 9779–9782.

[151] A. Razmjou, M. Asadnia, E. Hosseini, A. Habibnejad Korayem, V. Chen, *Nat. Commun.* **2019**, *10*, 5793.

[152] Y. Guo, Y. Ying, Y. Mao, X. Peng, B. Chen, *Angew. Chem. Int. Ed.* **2016**, *55*, 15120–15124.

[153] T. Ye, G. Hou, W. Li, C. Wang, K. Yi, N. Liu, J. Liu, S. Huang, J. Gao, *Nat. Commun.* **2021**, *12*, 5231.

[154] A. J. Celestian, J. D. Kubicki, J. Hanson, A. Clearfield, J. B. Parise, *J. Am. Chem. Soc.*

2008, 130, 11689–11694.

[155] W.-A. Li, Y.-C. Peng, W. Ma, X.-Y. Huang, M.-L. Feng, *Chem. Eng. J.* **2022**, 442, 136377.

[156] X.-M. Zhang, D. Sarma, Y.-Q. Wu, L. Wang, Z.-X. Ning, F.-Q. Zhang, M. G. Kanatzidis, *J. Am. Chem. Soc.* **2016**, 138, 5543–5546.

[157] X. Zeng, Y. Liu, T. Zhang, J.-C. Jin, J.-L. Li, Q. Sun, Y.-J. Ai, M.-L. Feng, X.-Y. Huang, *Chem. Eng. J.* **2021**, 420, 127613.

[158] C. Xiao, Z. Hassanzadeh Fard, D. Sarma, T.-B. Song, C. Xu, M. G. Kanatzidis, *J. Am. Chem. Soc.* **2017**, 139, 16494–16497.

[159] J. Zhang, P. Feng, X. Bu, T. Wu, *Natl. Sci. Rev.* **2022**, 9, nwab076.

[160] J. Zhang, X. Bu, P. Feng, T. Wu, *Acc. Chem. Res.* **2020**, 53, 2261–2272.

[161] Y. Liu, J. Zhang, B. Han, X. Wang, Z. Wang, C. Xue, G. Bian, D. Hu, R. Zhou, D.-S. Li, Z. Wang, Z. Ouyang, M. Li, T. Wu, *J. Am. Chem. Soc.* **2020**, 142, 6649–6660.

[162] Q. Lin, X. Bu, P. Feng, *Chem. Commun.* **2014**, 50, 4044–4046.

[163] J. Lv, J. Zhang, C. Xue, D. Hu, X. Wang, D.-S. Li, T. Wu, *Inorg. Chem.* **2019**, 58, 3582–3585.

[164] J. Zhang, C. Qin, Y. Zhong, X. Wang, W. Wang, D. Hu, X. Liu, C. Xue, R. Zhou, L. Shen, Y. Song, D. Xu, Z. Lin, J. Guo, H. Su, D.-S. Li, T. Wu, *Nano Res.* **2020**, 13, 2828–2836.

[165] A. Eichhöfer, D. Fenske, *J. Chem. Soc. Dalt. Trans.* **2000**, 941–944.

[166] D. Altermatt, I. D. Brown, *Acta Crystallogr., Sect. B Struct. Sci.* **1985**, 41, 240–244.

[167] I. D. Brown, K.-K. Wu, *Acta Crystallogr., Sect. B Struct. Sci.* **1976**, 32, 240–244.

[168] V. T. Almsick, S. W. Sheldrick, *Crystallogr. Commun.* **2005**, 61, 2348–2350.

[169] Z. Wu, I. Nußbruch, S. Nier, S. Dehnen, *JACS Au* **2022**, 2, 204–213.

[170] S. Zhan, T. Hong, B. Qin, Y. Zhu, X. Feng, L. Su, H. Shi, H. Liang, Q. Zhang, X. Gao, Z.-H. Ge, L. Zheng, D. Wang, L.-D. Zhao, *Nat. Commun.* **2022**, 13, 5937.

[171] T. Wang, X. Duan, H. Zhang, J. Ma, H. Zhu, X. Qian, J.-Y. Yang, T.-H. Liu, R. Yang, *InfoMat* **2023**, 5, e12481.

[172] R. Mannu, A. Basak, U. P. Singh, *J. Mater. Sci. Mater. Electron.* **2023**, 34, 2100.

[173] A. C. Lokhande, P. T. Babar, V. C. Karade, M. G. Gang, V. C. Lokhande, C. D. Lokhande, J. H. Kim, *J. Mater. Chem. A* **2019**, 7, 17118–17182.

[174] C. Ritchie, A. S. R. Chesman, J. Jasieniak, P. Mulvaney, *Chem. Mater.* **2019**, 31, 2138–2150.

[175] C. Yan, J. Huang, K. Sun, S. Johnston, Y. Zhang, H. Sun, A. Pu, M. He, F. Liu, K. Eder, L. Yang, J. M. Cairney, N. J. Ekins-Daukes, Z. Hameiri, J. A. Stride, S. Chen, M. A. Green, X. Hao, *Nat. Energy* **2018**, 3, 764–772.

[176] J. J. Scragg, P. J. Dale, L. M. Peter, G. Zoppi, I. Forbes, *Phys. status solidi* **2008**, *245*, 1772–1778.

[177] D. Nowak, F. Atlan, D. Pareek, M. Guc, A. Perez-Rodriguez, V. Izquierdo-Roca, L. Gütay, *Sol. Energy Mater. Sol. Cells* **2023**, *256*, 112342.

[178] G. S. Sahoo, M. Verma, S. Routray, G. P. Mishra, *IEEE Trans. Nanotechnol.* **2024**, *1*–8.

[179] T. Yokoi, M. Yoshioka, H. Imai, T. Tatsumi, *Angew. Chem. Int. Ed.* **2009**, *48*, 9884–9887.

[180] C. C. Freyhardt, M. Tsapatsis, R. F. Lobo, K. J. Balkus, M. E. Davis, *Nature* **1996**, *381*, 295–298.

[181] W. Wang, X. Wang, D. Hu, H. Yang, C. Xue, Z. Lin, T. Wu, *Inorg. Chem.* **2018**, *57*, 921–925.

[182] Z. Wu, F. Weigend, D. Fenske, T. Naumann, J. M. Gottfried, S. Dehnen, *J. Am. Chem. Soc.* **2023**, *145*, 3802–3811.

[183] A. Mathieson, S. Feldmann, M. De Volder, *JACS Au* **2022**, *2*, 1313–1317.

[184] M. Jin, Z. Zeng, H. Fu, S. Wang, Z. Yin, X. Zhai, Q. Zhang, Y. Du, *JACS Au* **2023**, *3*, 216–226.

[185] X.-L. Wang, Z. Wu, X. Wang, C. Xue, C. Liu, J. Zhang, R. Zhou, D.-S. Li, T. Wu, *Electrochim. Acta* **2021**, *376*, 138048.

[186] Q. Lin, X. Bu, C. Mao, X. Zhao, K. Sasan, P. Feng, *J. Am. Chem. Soc.* **2015**, *137*, 6184–6187.

[187] N. Zheng, X. Bu, P. Feng, *Chem. Commun.* **2005**, 2805–2807.

[188] Z. Wang, Y. Liu, J. Zhang, X. Wang, Z. Wu, J. Wu, N. Chen, D.-S. Li, T. Wu, *J. Mater. Chem. C* **2021**, *9*, 13680–13686.

[189] N. Rinn, L. Guggolz, H. Y. Hou, S. Dehnen, *Chem. Eur. J.* **2021**, *27*, 11167–11174.

[190] J. Zhang, X. Wang, J. Lv, D.-S. Li, T. Wu, *Chem. Commun.* **2019**, *55*, 6357–6360.

[191] H. Yang, L. Wang, D. Hu, J. Lin, L. Luo, H. Wang, T. Wu, *Chem. Commun.* **2016**, *52*, 4140–4143.

[192] S. Dehnen, A. Schäfer, D. Fenske, R. Ahlrichs, *Angew. Chem. Int. Ed.* **1994**, *33*, 746–749.

[193] C. Wang, R. C. Haushalter, *Inorganica Chim. Acta* **1999**, *288*, 1–6.

[194] C. Wang, R. C. Haushalter, *Chem. Commun.* **1997**, 1457–1458.

[195] O. M. Yaghi, *J. Am. Chem. Soc.* **2016**, *138*, 15507–15509.

[196] Y. Kong, Y. Ding, C. Liu, J. Zhang, R. Zhou, D.-S. Li, N. Chen, X. Wang, T. Wu, *Dalton Trans.* **2021**, *50*, 14985–14989.

[197] C. W. Liu, B. Sarkar, Y.-J. Huang, P.-K. Liao, J.-C. Wang, J.-Y. Saillard, S. Kahlal, *J. Am. Chem. Soc.* **2009**, *131*, 11222–11233.

[198] Z. Zhang, J. Zhang, T. Wu, X. Bu, P. Feng, *J. Am. Chem. Soc.* **2008**, *130*, 15238–15239.

[199] R.-C. Zhang, C. Zhang, D.-J. Zhang, J.-J. Wang, Z.-F. Zhang, M. Ji, Y.-L. An, Z. *Anorg. Allg. Chem.* **2012**, *638*, 2503–2507.

[200] M. Luo, D. Hu, H. Yang, D. Li, T. Wu, *Inorg. Chem. Front.* **2017**, *4*, 387–392.

[201] W.-A. Li, J.-R. Li, B. Zhang, H.-Y. Sun, J.-C. Jin, X.-Y. Huang, M.-L. Feng, *ACS Appl. Mater. Interfaces* **2021**, *13*, 10191–10201.

[202] B. Peters, M. Möbs, N. Michel, F. Tambornino, S. Dehnen, *ChemistryOpen* **2021**, *10*, 227–232.

[203] C.-F. Du, J.-R. Li, M.-L. Feng, G.-D. Zou, N.-N. Shen, X.-Y. Huang, *Dalton Trans.* **2015**, *44*, 7364–7372.

[204] W.-W. Xiong, J. Miao, K. Ye, Y. Wang, B. Liu, Q. Zhang, *Angew. Chem. Int. Ed.* **2015**, *54*, 546–550.

[205] T. Jiang, G. A. Ozin, R. L. Bedard, *Adv. Mater.* **1994**, *6*, 860–865.

[206] H.-W. Liu, K.-Y. Wang, D. Ding, M. Sun, L. Cheng, C. Wang, *Chem. Commun.* **2019**, *55*, 13884–13887.

[207] M. Ahmadi, S. S. Pramana, S. K. Batabyal, C. Boothroyd, S. G. Mhaisalkar, Y. M. Lam, *Inorg. Chem.* **2013**, *52*, 1722–1728.

[208] L. Shi, C. Pei, Y. Xu, Q. Li, *J. Am. Chem. Soc.* **2011**, *133*, 10328–10331.

[209] B. Li, Y. Xie, J. Huang, Y. Qian, *J. Solid State Chem.* **2000**, *153*, 170–173.

[210] X. Cai, H. Jing, H. Wuliji, H. Zhu, *J. Phys. Chem. C* **2023**, *127*, 5576–5583.

[211] J. M. Gonzalez, I. I. Oleynik, *Phys. Rev. B* **2016**, *94*, 125443.

[212] J. McKenzie, P. A. Kempler, C. K. Brozek, *Chem. Sci.* **2022**, *13*, 12747–12759.

[213] J. Tang, X. Wang, J. Zhang, J. Wang, W. Yin, D.-S. Li, T. Wu, *Nat. Commun.* **2021**, *12*, 4275.

[214] J. McKenzie, K. N. Le, D. J. Bardgett, K. A. Collins, T. Ericson, M. K. Wojnar, J. Chouinard, S. Golledge, A. F. Cozzolino, D. C. Johnson, C. H. Hendon, C. K. Brozek, *Chem. Mater.* **2022**, *34*, 1905–1920.

[215] K. A. Michalow, D. Logvinovich, A. Weidenkaff, M. Amberg, G. Fortunato, A. Heel, T. Graule, M. Rekas, *Catal. Today* **2009**, *144*, 7–12.

[216] P. Makuła, M. Pacia, W. Macyk, *J. Phys. Chem. Lett.* **2018**, *9*, 6814–6817.

[217] Y. Huang, E. Sutter, J. T. Sadowski, M. Cotlet, O. L. A. Monti, D. A. Rake, M. R. Neupane, D. Wickramaratne, R. K. Lake, B. A. Parkinson, P. Sutter, *ACS Nano* **2014**, *8*, 10743–10755.

[218] J. Zeng, E. Liu, Y. Fu, Z. Chen, C. Pan, C. Wang, M. Wang, Y. Wang, K. Xu, S. Cai, X. Yan, Y. Wang, X. Liu, P. Wang, S.-J. Liang, Y. Cui, H. Y. Hwang, H. Yuan, F. Miao, *Nano Lett.* **2018**, *18*, 1410–1415.

[219] A. Ahmed, M. Zahir Iqbal, A. Dahshan, S. Aftab, H. H. Hegazy, E. S. Yousef, *Nanoscale* **2024**, *16*, 2097–2120.

[220] B. Krebs, H. Uhlen, *Z. Anorg. Allg. Chem.* **1987**, *549*, 35–45.

[221] B. Krebs, S. Pohl, W. Schiwy, *Z. Anorg. Allg. Chem.* **1972**, *393*, 241–252.

[222] J. Li, J. Jin, Y. Zou, H. Sun, X. Zeng, X. Huang, M. Feng, M. G. Kanatzidis, *ACS Appl. Mater. Interfaces* **2021**, *13*, 13434–13442.

[223] L. Yang, X. Wen, T. Yang, Q.-Q. Hu, J.-T. Liu, H.-Y. Yin, A. Ablez, M.-L. Feng, X.-Y. Huang, *Dalton Trans.* **2024**, *53*, 6063–6069.

[224] S. Zhu, G. Zhou, W. Yuan, S. Mao, F. Yang, G. Fu, B. Sun, *J. Colloid Interface Sci.* **2020**, *560*, 565–571.

[225] L. Zheng, B. Sun, Y. Chen, T. Li, S. Mao, S. Zhu, H. Wang, Y. Zhang, M. Lei, Y. Zhao, *Mater. Today Chem.* **2018**, *10*, 167–174.

[226] Y. Lin, D. Xie, W. Massa, L. Mayrhofer, S. Lippert, B. Ewers, A. Chernikov, M. Koch, S. Dehnen, *Chem. Eur. J.* **2013**, *19*, 8806–8813.

[227] V. Spetzler, R. Kiebach, C. Näther, W. Bensch, *Z. Anorg. Allg. Chem.* **2004**, *630*, 2398–2404.

[228] J. P. Perdew, K. Burke, M. Ernzerhof, *Phys. Rev. Lett.* **1996**, *77*, 3865.

[229] D. Peng, N. Middendorf, F. Weigend, M. Reiher, *J. Chem. Phys.* **2013**, *138*, 184105.

[230] Y. J. Franzke, N. Middendorf, F. Weigend, *J. Chem. Phys.* **2018**, *148*, 104110.

[231] P. Pollak, F. Weigend, *J. Chem. Theory Comput.* **2017**, *13*, 3696–3705.

[232] A. Schäfer, A. Klamt, D. Sattel, J. C. W. Lohrenz, F. Eckert, *Phys. Chem. Chem. Phys.* **2000**, *2*, 2187–2193.

[233] K. O. Klepp, *Z. Naturforsch. B* **1992**, *47*, 411–417.

[234] M. Duchardt, S. Haddadpour, T. Kaib, P. Bron, B. Roling, S. Dehnen, *Inorg. Chem.* **2021**, *60*, 5224–5231.

[235] B. Eisenmann, J. Hansa, *Z. Krist. - Cryst. Mater.* **1993**, *205*, 325–326.

[236] K. O. Klepp, F. Fabian, *Z. Naturforsch. B* **1999**, *54*, 1499–1504.

[237] Q. Lin, Z. Zhang, X. Bu, P. Feng, *Inorg. Chem.* **2014**, *53*, 13207–13211.

[238] R.-C. Zhang, J.-C. Zhang, Z. Cao, J.-J. Wang, S.-S. Liang, H.-J. Cong, H.-J. Wang, D.-J. Zhang, Y.-L. An, *Inorg. Chem.* **2018**, *57*, 13128–13136.

[239] R.-C. Zhang, H.-G. Yao, S.-H. Ji, M.-C. Liu, M. Ji, Y.-L. An, *Inorg. Chem.* **2010**, *49*, 6372–6374.

[240] S. Tang, J. Zhou, X. Liu, H.-P. Xiao, *Mater. Today Commun.* **2018**, *15*, 88–93.

[241] N. Pienack, C. Näther, W. Bensch, *Solid State Sci.* **2007**, *9*, 100–107.

[242] R.-C. Zhang, H.-G. Yao, S.-H. Ji, M.-C. Liu, M. Ji, Y.-L. An, *Chem. Commun.* **2010**, *46*, 4550–4552.

[243] J. H. Liao, M. G. Kanatzidis, *Chem. Mater.* **1993**, *5*, 1561–1569.

[244] R. Chen, F. Wang, C. Tang, Y. Zhang, D. Jia, *Chem. Eur. J.* **2013**, *19*, 8199–8206.

[245] M. Baiyin, J. Naren, G. Gang, X. Wang, X. Xu, *Inorg. Chem. Commun.* **2013**, *35*, 135–139.

Declaration

I hereby declare that the present work was written independently by myself and I have not used any sources other than those specified and cited in the whole thesis. This thesis has not been published or submitted to other universities.

The thesis was initiated and half conducted at Philipps-Universität Marburg from 2020.11 to 2022.11, and was subsequently improved and finalized at Karlsruher Institut für Technologie between 2022.12 and 2024.10, due to the academic movement of my Ph.D. advisor, Prof. Dr. Stefanie Dehnen, who has supervised the entire thesis.

Zhou Wu

Curriculum Vitae

Name	Zhou Wu
Date of birth	21.08.1994
Place of birth	Anqing, Anhui Province
Gender	Male
Nationality	Chinese
Address	Gerwigstraße 43, 76131, Karlsruhe, Germany
E-Mail	zhou.wu@partner.kit.edu

12/2022 – 12/2024	Ph.D. in Chemistry Institute of Nanotechnology (INT), Karlsruhe Institute of Technology (KIT), Germany
11/2020 – 11/2022	Ph.D. in Chemistry Department of Chemistry and Material Sciences Center, Philipps-Universität Marburg, Germany Supervisor: Prof. Dr. Stefanie Dehnen
09/2017 – 06/2020	M.Sc. in Chemistry College of Chemistry, Chemical Engineering and Materials Science, Soochow University, China Supervisor: Prof. Dr. Tao Wu
09/2013 – 06/2017	B. Eng. in Pharmaceutical Engineering College of Biological Chemical Sciences and Engineering, Jiaxing University, China Supervisor: Assistant Prof. Dr. Li-Qiu Zhang

Publications

1. Zhou Wu, Benjamin Peerless, Panpan Wang, Wolfgang Schuhmann, Stefanie Dehnen* Structural Expansion and Enhanced Photocurrent Conversion of Selenido Stannates with Cu⁺ Ions. *JACS Au.* **2024**, 4, 3788–3799.
2. Zhou Wu[†], Mirko Tallu[†], Gina Stuhrmann[†], Stefanie Dehnen* Ligand-Functionalized and Ligand-Bridged or Organyl-Separated Chalcogenido Metalate-Based Clusters, *Coord. Chem. Rev.* **2023**, 497, 215424. ([†] equal contribution)
3. Zhou Wu, Florian Weigend, Dieter Fenske, Tim Naumann, J. Michael Gottfried, Stefanie Dehnen* Ion-Selective Assembly of Supertetrahedral Selenido Germanate Clusters for Alkali Metal Ion Capturing and Separation, *J. Am. Chem. Soc.* **2023**, 145, 3802–2811.
4. Zhou Wu[†], Gina Stuhrmann[†], Stefanie Dehnen* Crystalline Chalcogenidometalate-based Compounds from Uncommon Reaction Media, *Chem. Commun.* **2022**, 58, 11609–11624. ([†] equal contribution)
5. Zhou Wu, Isabell Nußbruch, Simon Nier, Stefanie Dehnen* Ionothermal Access to Defined Oligomers of Supertetrahedral Selenido Germanate Clusters, *JACS Au.* **2022**, 2, 204–213.

Acknowledgement

Time flies! These past four years have been wonderful, fruitful, and unforgettable. I still remember the first day I arrived in Germany—I was nervous and anxious but also excited and full of anticipation as I embarked on my Ph.D. journey at the Dehnen Lab. While I knew pursuing a Ph.D. would be challenging, I am proud to have tackled many obstacles along the way. Now, I am grateful for the chance to thank everyone who has helped, supported, and believed in me throughout this journey.

I would like to express my heartfelt gratitude to my Ph.D. supervisor, Prof. Dr. Stefanie Dehnen. I appreciate that she welcomed me into her group and gave her all to support me throughout my studies. Her dedication to creating the best working conditions for the group and putting students at the forefront of her efforts has made all the difference. Thanks to her guidance, I had the chance to explore and validate my ideas in the lab—which to me is the happiest things in the last four years.

Many thanks to...

... PD Dr. Masooma Ibrahim, for serving as the second supervisor of my thesis.

... all the collaborators: Prof. Dr. Dieter Fenske for the single crystal XRD measurements, Prof. Dr. Florian Weigend (Philipps-Universität Marburg) for the DFT calculations, Prof. Dr. J. Michael Gottfried (Philipps-Universität Marburg) for the XPS investigation, Prof. Dr. Wolfgang Schuhmann (Ruhr University Bochum) for the photocurrent measurements, Prof. Dr. Jasmin Aghassi-Hagmann for the electrical property measurements.

... Dr. Olaf Fuhr, Dr. Bastian Weinert, Dr. Peerless Benjamin, and Dr. Niklas Rinn for all your kind help in the lab, especially to Dr. Peerless Benjamin, for proof-reading and revising my thesis and research paper.

... Dr. Svetlana Klementyeva and Dr. Pierre Picchetti for all the kind suggestions.

...our IL group members—Dr. Gelen Gomez Jaimes, Dr. Arijit Jana, Gina Stuhrmann, Mirko Tallu, Marvin Szabo, Maryam Ahmadi, Dr. Bertram Peters, and Peer Räke, for the joyful time in the lab and outside the lab, it has been wonderful to work with you guys together. To work everything out with you guys together is so cool!

... Dr. Yaofeng Wang, Dr. Mingting Hao, Dr. Lukas Guggolz, Dr. Asha Pankajakshan, Dr. Irán Rojas León, and Dr. Fu-Xing Pan for all your suggestions in the lab.

...Jie Wang, Shangxin Wei, Katrin Beuthert, Jan Christmann, Kimon Flosdorf, Chloé Krampe, Yannick Lohse, Simon Nier, Julia Rienmüller, Andreas Schmidt, Nils Spang, Nikolai Bartnick, Franziska Ganslmaier, Martina Kämpfe, David Kistner, Damian Klein, and Shen Chen for all the fun we had together.

...Uwe Justus, and Andrea Tschirch for your work to create better working conditions for me. And many previous group members at Philipps-Universität Marburg, it is great to meet and know you guys.

...Friends that not only in Germany, but also those in China, for your friendship, and kind suggestions in life and in career. And all of those who helped me, who supported me along this journey, it has been a great honor to know all of you!

Of course, I would also like to thank the China Scholarship Council for granting me a four-year scholarship.

The biggest thanks definitely go to my family. My parents, my sister, my brother-in-law, thank you for your support, your understanding, and your love without any reason. My nephews and niece, you three are great and brought a lot of fun to me (although via video-call).